UNIVERSITY OF CALIFORNIA

Santa Barbara

Next-Generation End Functional Polymers through Living Anionic Polymerization

A dissertation submitted in partial satisfaction of the

requirements for the degree Doctor of Philosophy

in Chemistry

by

Allison Christine Abdilla

Committee in charge:

Professor Craig J. Hawker, Co-Chair

Professor Javier Read de Alaniz, Co-Chair

Professor Christopher Bates

Professor Lior Sepunaru

Professor Ram Seshadri

March 2022

The dissertation of Allison Christine Abdilla is approved.

_____
Christopher M. Bates

_____
Lior Sepunaru

_____
Ram Seshadri

_____
Javier Read de Alaniz, Committee Co-Chair

_____
Craig J. Hawker, Committee Co-Chair

March 2022

Next-Generation End Functional Polymers through Living Anionic Polymerization

Copyright © 2022
by
Allison Christine Abdilla

This thesis is dedicated to all the young STEM graduate students, undergraduates and other future scientists. May you continue to dream big and never give up on the pursuit of happiness.

ACKNOWLEDGEMENTS

I would like to express my deepest gratitude to my advisors Craig Hawker and Javier Read de Alaniz. They both have been incredibly supportive mentors throughout my time at UCSB and inspired me in more ways than I can count. Craig not only gave me incredible freedom to explore my own ideas as a graduate student, but also when I was a young undergraduate during my internship in his group. He has taught me to take pride in my work and how to effectively communicate my research to almost any audience (I will forever be chasing the next "Manny Award"). Craig has inspired me to continuously challenge myself to become a better scientist and has worked tirelessly to create a fun, innovative, and collaborative environment for *everyone*. It has been an absolute joy to work in your group and I will forever be thankful.

Javier has been a wonderful co-advisor to Craig during grad school and he is the most patient man I have ever met. Javier always took the time listen to my wild project ideas and believed in me to make them a reality. He has always had my back and helped me any time I needed his support even when he had a million other things on his plate already. Javier has been a spectacular source to go to when things aren't working and has taught me an incredible amount organic chemistry, reaction mechanisms and how to be a better mentor to others. Your enthusiasm for science and positive attitude has inspired me to keep working harder and clear any obstacles in my way.

I also could have never made it this far without the immense support my lab mates in the Hawker & Read de Alaniz groups, especially my mentors Jimmy Lawrence and Jing Ming Ren who taught me almost everything I know in lab and a great deal about life. Jing, you are truly a gifted individual and made anionic polymerizations look easy. I learned a great deal

about how to be rigorous yet efficient in my research while maintaining a healthy work-life balance. Jimmy, I will forever appreciate how you made all the late nights in lab so much fun. Your incredible drive to succeed gave me the courage to keep my “energizer bunny” going and never stop pursuing my dreams.

Although I graduated years ago, I would also like to thank the McMaster Chemistry Department for teaching me a great deal about how to think critically and be an independent scientist. Especially to my undergraduate advisor Harald Stöver who let me take on my own project as a first year undergraduate and endlessly supported me. You always encouraged me to keep going no matter how many mistakes I made, even when I confidently said free radical polymerization was a “step growth” mechanism (I put the correct version in the intro of this thesis just for you). You have cheered me on every step of the way in my career and I am eternally grateful. Thank you to also Nick Burke and the rest of the Stöver lab for giving me the foundation I needed to pursue my Ph.D.

I have been also incredibly fortunate to have some of the best friends and family anybody could have ever asked for. Thank you to Allie, Eric, and “Mr. and Mrs. bbqurl” Ryan and Shelby for all of the good times as well as to my “NMR triplets” Fariha and Krystle for all the late nights trading cat pictures and watching Nic Cage movies. Thank you to my mom Janice, my siblings Jess and Joe, and the Shynns for all your love and support. Thank you to all my friends in Santa Barbara who were my family away from home especially Angelique, Manny, Meghan, Zongheng, Sophia, the Hawker D&D crew, the BDL ladies, my partner Chris and my cat Mia. I also want to extend my gratitude everyone who gave me food, shelter and a shoulder to lean on during difficult times in my life so that I could continue in school, you are all truly guardian angels.

None of the work I have done during graduate school would have been possible without the help of my colleagues. Thank you to Chris and Morgan Bates for all of your support in the Dow Project and teaching me the "ABC's" of block copolymers, and Ram and Lior who were incredible to have on my committee. A special shout out goes to all the Chemistry, MRL and CNSI staff including Rachel Behrens, Amanda Strom, Jaya Nolt, Youli Li, Aidan Taylor, Hongjun Zhou, Dmitriy Uchenik, India Madden, Samantha Crossono, Jess Henry, Sara Bard and Sylvia Vogel. I would also like to express my gratitude to Vani Singhania, Gregg Kent, Ann Williams, Olivia Hwang, Songi Han and the rest of the ChemPD team for their immense help in organizing during Career Day and other professional development opportunities. Finally, I would like to thank all my coauthors listed below, including talented undergraduates I was fortunate to work with, for their help the research in this thesis:

Chapter 2: Neil Dolinski, Puck de Roos, Jing Ming Ren, Erika van der Woude, Soyoung (Eileen) Seo, Manuel Zayas, Jimmy Lawrence, Javier Read de Alaniz, Craig Hawker.

Chapter 3: Yoichi Okayama, Taejun Eom, Michael Czuczola, David Goldfeld, Elizabeth Murphy, Christopher Bates, Javier Read de Alaniz and Craig Hawker.

Chapter 4: Patrick Getty, Colton D'Ambra, Michael Czuczola, David Goldfeld, Souvagya Biswas, Jodi Mecca, Steven Swier, Thomas Bekemeier, David Laitar, Morgan Bates, Christopher Bates, and Craig Hawker.

VITA OF ALLISON CHRISTINE ABDILLA
March 2022

EDUCATION

University of California, Santa Barbara, CA, USA 2017 – Present
Ph.D. Materials Chemistry (Expected Graduation: April 2022) Research
Advisors: Professor Craig Hawker and Professor Javier Read de Alaniz

McMaster University, Hamilton, ON, Canada 2012 – 2017
H.B.Sc. Chemistry, *Summa Cum Laude*
Research Advisor: Professor Harald Stöver

HONORS AND AWARDS

2021	Phillip Joshua Chase Mabe Memorial Fellowship
2018-	NSERC Graduate Research Fellowship (NSERC PGSD3)
2019	UCSB Chemistry: Outstanding Service to the Department
2019	Chemical Sciences Student Seminar Best Graduate Student Speaker Travel
2018	Phi Lambda Upsilon Award (National Honorary Chemical Society)
2018	UCSB Robert H. Wolfe Graduate Teaching Fellow
2018	Canadian Society of Chemistry Graduate Poster Award – Materials Science
2016	NIMS International Internship Award
2016	McMaster University Hypercube Scholar Award
2015	John and Helen Maxwell Award
2013	McMaster University Chemistry Summer Research Scholarship

PROFESSIONAL EMPLOYMENT

University of California, Santa Barbara Santa Barbara, CA, USA
Undergraduate & Graduate Student Researcher 2015 – Present

- Designed and synthesized chain-end functionalized stereocontrolled methacrylate and siloxane polymers
- Structurally characterized self-assembled Au nanoparticles and microphase separated diblock copolymers
- Lead teams of PhD students and postdocs to develop industrially relevant polymers for Dow Chemical
- Prepared polymeric comb particles within a GMP facility for arteriosclerosis imaging in humans
- Managed laboratory safety by training workers on the potential hazards of chemicals and equipment

McMaster University Hamilton, ON, Canada
Undergraduate Student Researcher 2013 – 2017

- Synthesized pH responsive zwitterionic polymers to encapsulate therapeutic cells in polymer networks
- Analyzed the 3D arrangement and viability of encapsulated cells by confocal microscopy

National Institute of Materials Science (NIMS) Tsukuba, IB, Japan
International Research Intern 2016

- Fabricated portable hemodialysis membranes by electrospinning polymer-zeolite nanofiber composites onto aluminum substrates and measured their selective adsorption of urea
- Collaborated with Japanese scientists to image zeolite particle distributions with fibers

MENTORSHIP AND OUTREACH

University of California, Santa Barbara
Chemistry Professional Development (ChemPD), Co-President 2019 - 2021

- Interface with UCSB faculty, chemistry graduate students, department administrators and external companies to provide professional development opportunities for the department
- Lead a 25+ person team to host two annual virtual Chemistry Career Day for over 250 participants and 70 industrial representatives

Hawker & Read de Alaniz Groups, Graduate Mentor 2017 - Present

- Designed individual research projects for 6 undergraduate, high school, first-year graduate students and visiting scientists based on their research interests and career goals
- Taught each mentee how to plan, conduct and characterize their experiments in an effective and safe manner, then communicate their results to a broad audience with diverse scientific backgrounds

Graduate Students for Diversity in Science (GSDS), Outreach Director 2017 - 2020

- Organized the Outreach team to teach underrepresented California State University undergrads about graduate life and research
- Worked with other GSDS executives to provide diversity seminars and discussion sessions

Department of Chemistry and Biochemistry, Head Teaching Assistant 2017 – 2018

- Supervised a team of teaching assistants to proctor and grade weekly labs, monthly mid-terms tests and quarterly exams
- Provided written and hands-on feedback on students' technical skills in organic chemistry labs and communication in scientific reports

McMaster University
Department of Chemistry, Science Communicator 2014 – 2017

- Educated local high school students and families on how chemistry played a critical role in their daily life
- Safely carried out various chemistry demonstrations with great enthusiasm in the "Magic of Molecules!" show for 375 people

National Institute of Materials Science
International Center for Materials Nanoarchitectonics, Smart Polymer Ranger. 2016

- Performed as the "Smart Polymer Yellow" Ranger at the Tsukuba Capio arena for local Japanese elementary school children
- Assisted NIMS staff in preparing demonstrations to display the unique properties of stimuli-responsive polymeric materials

PUBLICATIONS

1. **A. Abdilla**, C. A. D'Ambra, Z. Geng, J. J. Shin, M. Czuczola, D. J. Goldfeld, S. Biswas, J. M. Mecca, S. Swier, T. D. Bekemeier, D. S. Laitar, M. W. Bates,* C. M. Bates,* C. J. Hawker.* Silicone-based Polymer Blends: Enhancing Properties through Compatibilization. *J. Polym. Sci.* **2021**, DOI: 10.1002/pol.20210453.
2. L. Detering†, **A. Abdilla†**, H. P. Luehmann, J. W. Williams, L.-H. Huang, D. Sultan, A. Elvington, G. S. Heo, P. K. Woodard, R. J. Gropler, G. J. Randolph, C. J. Hawker,* Y. Liu.* CC Chemokine Receptor 5 Targeted Nanoparticles Imaging the Progression and Regression of Atherosclerosis Using Positron Emission Tomography/Computed Tomography. *Mol. Pharmaceutics,* **2021**, *18,* 1386.
3. Y. Kim, H. Park, **A. Abdilla**, H. Yun, J. Han, G. G. Stein, C. J. Hawker,* B. J. Kim.* Chain-Length-Dependent Self-Assembly Behaviors of Discrete Conjugated Oligo(3-hexylthiophene). *Chem. Mater.* **2020,** *32*, 3597.
4. **A. Abdilla**, N. D. Dolinski, P. de Roos, J. M. Ren, E. van der Woude, S. E. Seo, M. Zayas, J. Lawrence,* J. Read de Alaniz,* C. J. Hawker.* Polymer Stereocomplexation as a scalable platform for nanoparticle assembly. *J. Am. Chem. Soc.* **2020,** *142*, 1667. (Highlighted in a *JACS Spotlight*)
5. M. S. Zayas, N. D. Dolinski, J. L. Self, **A. Abdilla**, C. J. Hawker, C. M. Bates, J. Read de Alaniz.* Tuning Merocyanine Photoacid Structure to Enhance Solubility and Temporal Control: Application in Ring Opening Polymerization. *ChemPhotoChem,* **2019**, *3*, 467.
6. D. J. Lunn, S. Seo, S. Lee, R. B. Zerdan, K. Mattson, N. J. Treat, A. J. McGrath, W. R. Gutekunst, J. Lawrence, **A. Abdilla**, A. Anastasaki, A. S. Knight, B. V. K. J. Schmidt, M. W. Bates, P. G. Clark, J. P. DeRocher, A. K. Van Dyk,* C. J. Hawker.* Scalable Synthesis of an architectural library of well-defined poly(acrylic acid) derivatives: Role of structure on dispersant performance. *J. Polym. Sci. A. Polym. Chem.* **2019**, *57*, 716.
7. J. M. Ren, A. S. Knight, B. G. P. van Ravensteijn, P. Kohl, R. B. Zerdan, Y. Li, D. J. Lunn, **A. Abdilla**, G. Qiao,* C. J. Hawker.* DNA-Inspired Strand-Exchange for Switchable PMMA-Based Supramolecular Morphologies, *J. Am. Chem. Soc.* **2019**, *141,* 6, 2630.
8. J. M. Ren, J. Lawrence, A. S. Knight, **A. Abdilla**, R. B. Zerdan, A. E. Levi, B. Oschmann, W. R. Gutekunst, S. Lee, Y. Li, A. J. McGrath, C. M. Bates, G. Qiao,* C. J. Hawker.* Controlled Formation and Binding Selectivity of Discrete Oligo(methyl methacrylate) Stereocomplexes. *J. Am. Chem. Soc.* **2018**, *140*, 1945.
9. W. Gutekunst, A. Anastasaki, D. J. Lunn, N. P. Truong, R. Whitfield, G. R. Jones, N. Treat, **A. Abdilla**, B. E. Barton, P. G. Clark, D. M. Haddleton, T. P. Davis, C. J. Hawker.* Practical Chain-End Reduction of Polymers Obtained with ATRP. *Macromol. Chem. Phys.* **2017**, *218*, 1700107.
10. J. Lawrence, S. Lee, **A. Abdilla**, M D. Nothling, J. M. Ren, A. S. Knight, C. Fleischmann, Y. Li, A. S. Abrams, B. V. K. J. Schmidt, M. C. Hawker, L. A. Connal, A. J. McGrath, P. G. Clark, W. R. Gutekunst,* C. J. Hawker.* A Versatile and Scalable Strategy to Discrete Oligomers. *J. Am. Chem. Soc.* **2016,** *138*, 6306.
11. **A. Abdilla**, S. Shi, N. A. D. Burke, H. D. H. Stöver.* Multistimuli Responsive Ternary Polyampholytes: Formation and Crosslinking of Coacervates. *J. Polym. Sci. A. Polym. Chem.* **2016,** *54,* 2109.

PRESENTATIONS

1. **A. Abdilla**, N. D. Dolinski, P. de Roos, J. M. Ren, E. van der Woude, S. E. Seo, J. Lawrence, J. Read de Alaniz, C. J. Hawker. Polymer Stereocomplexation as a Scalable Platform for Nanoparticle Assembly, *Invited Speaker - Materials Research Outreach Program Symposium,* January 27, **2022**, Santa Barbara, CA, USA.

2. **A. Abdilla**, N. D. Dolinski, P. de Roos, J. M. Ren, E. van der Woude, S. E. Seo, J. Lawrence, J. Read de Alaniz, C. J. Hawker. Polymer Stereocomplexation as a Platform for Nanoparticle Assembly, *Chemical Sciences Student Seminar,* October 7 – January 13, **2019 – 2020**, Santa Barbara, CA, USA.
3. **A. Abdilla,** P. de Roos, N. D. Dolinski, S. E. Seo, J. M. Ren, J. Lawrence, E. van der Woude, J. Read de Alaniz, C. J. Hawker. Polymer Stereocomplexation as a Platform for Inter-Nanoparticle Coupling. *Canadian Chemistry Conference and Exhibition*, June 3 – 7, **2019**, Québec City, QC, Canada.
4. **A. Abdilla,** P. de Roos, J. M. Ren, J. Lawrence, N. D. Dolinski, S. E. Seo, E. van der Woude, J. Read de Alaniz, C. J. Hawker. Polymer Stereocomplexation as a Platform for Nanoparticle Assembly. *ACS National Meeting and Exposition*, March 31 – April 4, **2019**, Orlando, Fl, USA.
5. **A. Abdilla,** J. M. Ren, J. Lawrence, J. Read de Alaniz, C. J. Hawker. Stereocomplex Driven Nanoparticle Assemblies, *Canadian Chemistry Conference and Exhibition*, May 27 – 31, **2018**, Edmonton, AB, Canada.
6. **A. Abdilla,** S. Shi, N. A. D. Burke, H. D. H. Stöver. Ternary Polyampholytes: Preparation, Properties and Crosslinked Hydrogels, *Canadian Chemistry Conference and Exhibition*, June 13 – 17, **2017**, Ottawa, ON, Canada.
7. **A. Abdilla**, S. Shi, N. A. D. Burke, H. D. H. Stöver. Multistimuli Responsive Ternary Polyampholytes, *PolyMac Conference*, December 9, **2014**, Hamilton, ON, Canada.

ABSTRACT

Next-Generation End Functional Polymers through Living Anionic Polymerization

by

Allison Christine Abdilla

A grand challenge in polymer chemistry is the development of methods for constructing functional macromolecules with control over the molecular weight, composition, stereoregularity and chain-end fidelity. In particular, living anionic polymerization is a powerful technique to prepare well-defined high molecular weight macromolecules with extremely narrow dispersities and controlled stereochemistries on industrial scales. However, state-of-the art anionic polymerization techniques greatly sensitive to many functional substituents, limiting their chain-end functionalization strategies and subsequent incorporation into advanced materials.

In **Chapter 2** and **Appendix A**, the development of new synthetic methods to prepare end-functional, tacticity-controlled polymers are described. In particular, versatile and scalable synthetic strategy to obtain stereocontrolled poly(methyl metacrylate) with diverse chain-ends through living anionic polymerization with precise termination reactions and post-polymerization modifications is presented. The utility of such polymers was demonstrated through their use as nanoparticle ligands, allowing for a new self-assembly platform via stereocomplexation. The synthetic availability of these functional stereocontrolled building blocks presents new opportunities to create designer materials for both industrial applications and fundamental interests.

In **Chapter 3** and **Appendix B** of this thesis, a new approach for synthetizing heterotelechelic polydimethylsiloxane (PDMS) through the anionic ring opening of

hexamethylcylclotrisiloxane, initiated with a bifunctional H-($SiOMe_2$)$_4$-OH oligomer is discussed. Careful control of the reaction conditions followed by termination with various silyl chlorides yields PDMS with both Si-H moieties and a wide range of chain ends (eg: alkyl chlorides, methacrylates and norbornenes) with high fidelities. Further end-functionalization by hydrosilylation with terminal olefins (alcohols, epoxides and esters) opens a diverse plethora of asymmetric PDMS materials for use in advanced silicone-based systems.

The utility of end functional PDMS materials from living anionic polymerizations is presented in **Chapter 4** and **Appendix C**. In particular, well-defined PDMS-based "block random" structures were developed by the controlled radiclal copolymerization of novel silicone-methacrylate monomers from bromine-terminated PDMS macroinitiators. The physical properties and phase behavior vary dramatically depending on the composition of the random methacrylate block ranging from disordered viscous liquids to glassy solids with well-ordered lamellar structures. This technique presents an exciting platform to prepare PDMS-based block copolymers with tunable segregations strengths for applications in silicone-organic blend-compatibilization.

Finally, **Appendix D** and **Appendix E** are supplementary provided to describe state-of-the-art strategies to compatibilize silicone-based polymer blends and novel comb nanoparticle radiotracers derived from heterotelechelic poly(ethylene glycol) building blocks.

TABLE OF CONTENTS

Chapter 1. Introduction 1

1.1 Radical Polymerization 1
1.1.1 Free Radical Polymerization 1
1.1.2 Controlled Radical Polymerization 4

1.2 Living Anionic Polymerization 7
1.2.1 Stereocontrolled Polymerizations 8
1.2.2 Ring Opening Polymerizations 11
1.2.3 Chain-End Transformations to Controlled Radical Polymerizations 15

1.3 References 16

Chapter 2. Polymer Stereococomplexation as a Scalable Platform for Nanoparticle Assembly 21

2.1 Abstract 21

2.2 Introduction 21

2.3 Results and Discussion 24

2.4 Conclusion 31

2.5 References 32

Chapter 3. A Si-H Functionalized Initiator for the Precise Synthesis of Heterotelechelic Polysiloxanes 34

3.1 Abstract 34

3.2 Introduction 34

3.3 Results and Discussion 38

3.4 Conclusions & Future Work 47

3.5 References 48

Chapter 4. PDMS-based Block Random Copolymers with Tunable Segregation Strengths 53

4.1 Abstract 53

4.2 Introduction 53

4.3 Results and Discussion 57

4.4 Conclusion & Future Work 65

4.5 References 65

Chapter 5. Conclusions 69

Appendix A. Supporting Information for Chapter 2 72

Appendix B. Supporting Information for Chapter 3 103

Appendix C. Supporting Information for Chapter 4 116

Appendix D. Silicone-based polymer blends: Enhancing Properties Through Compatibilization 125

Appendix E. CC Chemokine Receptor 5 Targeted Nanoparticles Imaging the Progression and Regression of Atherosclerosis using PET/CT 141

Chapter 1. Introduction

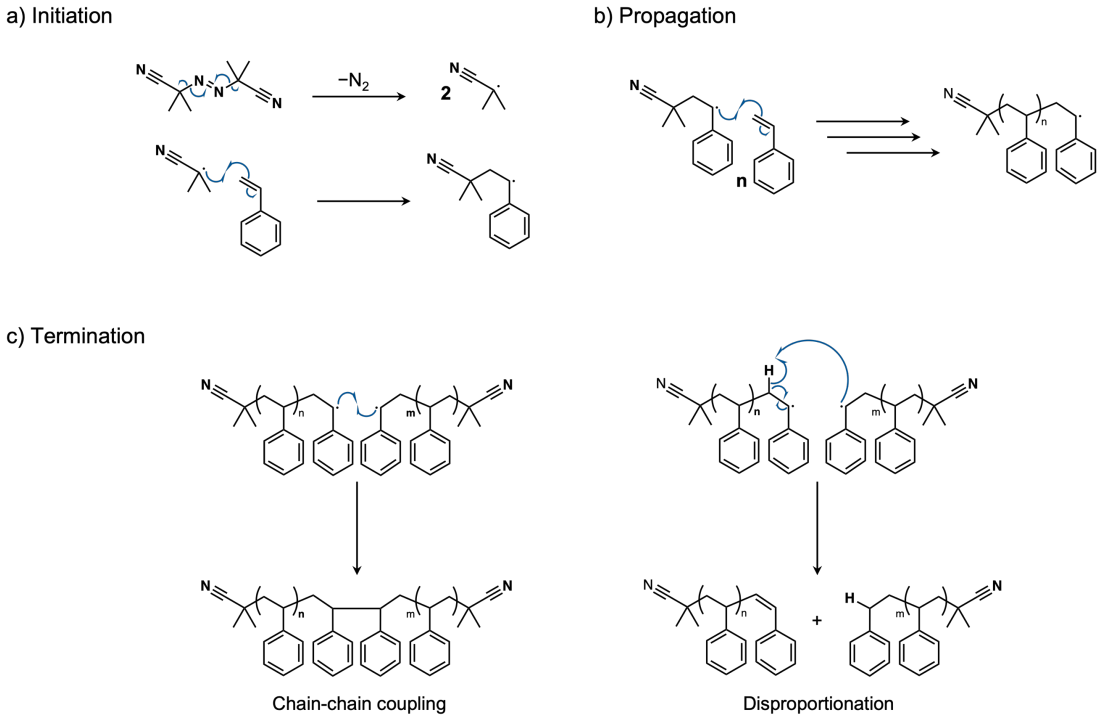
1.1 Radical Polymerization

1.1.1 Free Radical Polymerization

"*Dear Colleague, abandon your idea of large molecules, organic molecules with molecular weights exceeding 5000 do not exist. Purify your products such as rubber, they will crystallize and turn out to be low molecular weight compounds*." H. Wieland to H. Staudinger, early 1920s[1,2]

On December 10th, 1953 Hermann Staudinger was awarded the Nobel Prize in Chemistry for his revolutionary research on macromolecules, marking a new era of molecular design of high molecular weight structural and functional polymeric materials.[1,3] Today, synthetic polymers are omnipresent in our society with over 200 million tons produced worldwide each year.[4] Polymeric materials are unmatched with respect to their unique combination of cost/performance ratio, low-energy demand during preparation and processing, and exceptionally versatile properties and applications.[1]

The vast macromolecular structures that entangle our everyday lives can be synthesized by "step growth" or "chain growth" polymerization mechanisms.[5] Free radical polymerization, a chain-growth technique, is one of the most important polymerization industrial methods accounting for 40-50% of all synthetic polymers produced.[6] The process can be divided into initiation, propagation and termination steps as shown in Scheme 1 below.



Scheme 1. Representative mechanism for the free radical polymerization of styrene initiated by Azobisisobutyronitrile (AIBN). The homolytic cleavage of AIBN may be driven thermally at elevated temperatures or by UV light irradiaton.[5]

The initiation of polymer growth is most often driven by the homolytic cleavage of the initiator into highly reactive radicals.[5] The generated initiator radical fragments react with nearby species such as the unsaturated carbon-carbon double bonds of vinyl monomers. This begins a polymer chain which continues to propagate in the presence of monomer until the radical chain end is terminated by radical recombination (chain-chain coupling) or disproportionation. It is important to note that termination via chain-chain coupling results in a doubling of the molecular weight and polymer chains that are symmetric at the point of combination.[5] In contrast, disproportionation retains the molecular weight of the propagating radicals but produces one polymer with a terminal unsaturated group and another with a terminal saturated group. Termination by combination with initiator radicals or impurities such as oxygen or inhibitors may also generate additional chain-end structures.[5] As chain-

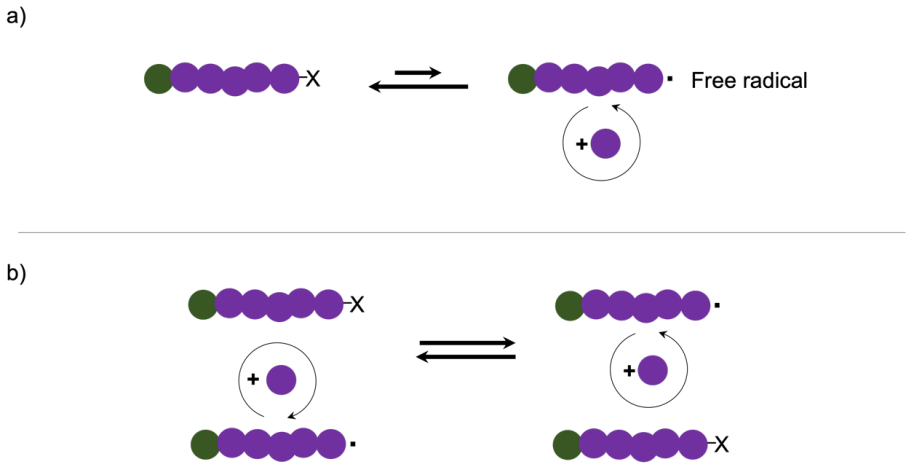
propagation and termination reactions between growing radicals are rapid while initiation is slow, high-molecular weight polymers form almost immediately and then remain relatively unchanged despite increasing monomer conversion.[5,6,7]

Although free radical polymerization is a powerful technique, a significant drawback to these polymerizations is that they yield polymers with uncontrolled molecular weights with high dispersities ($Đ > 1.5$).[7] In addition, termination reactions often compete with several chain-transfer processes that involve the abstraction of hydrogen from monomer, solvent or polymer chains that produce branched polymers occurs as monomers add to newly produces radicals along the polymer backbone.[5,8] This effect is especially pronounced in low-density polyethylene where material properties are critically determined by the amount of chain transfer to polymer that takes place.[8]

As a result of irreversible termination and chain-transfer processes that rapidly occur in free radical polymerization, the resulting materials are highly complex mixtures with thousands of different compositions, significantly limiting the design of structure-property relationships commonly observed in nature.[9] In addition to broad molecular weight distributions, free radical polymerizations also have poor chain-end fidelities with their end group structures dictated via the various termination processes at play. This significantly hinders the ability to install chain-end functionalities at polymer termini that modify solubility, chain-association, adsorption, rheological and surface properties or give the capability to synthesize materials with complex architectures such as block, star, cyclic and dendritic polymers.[10-17] In addition, physical hydrogels made from end-functionalized polymers show enhanced mechanical properties, improved responses to external stimuli, and self-healing capabilities by end-group mediated supramolecular assembly.[18-22]

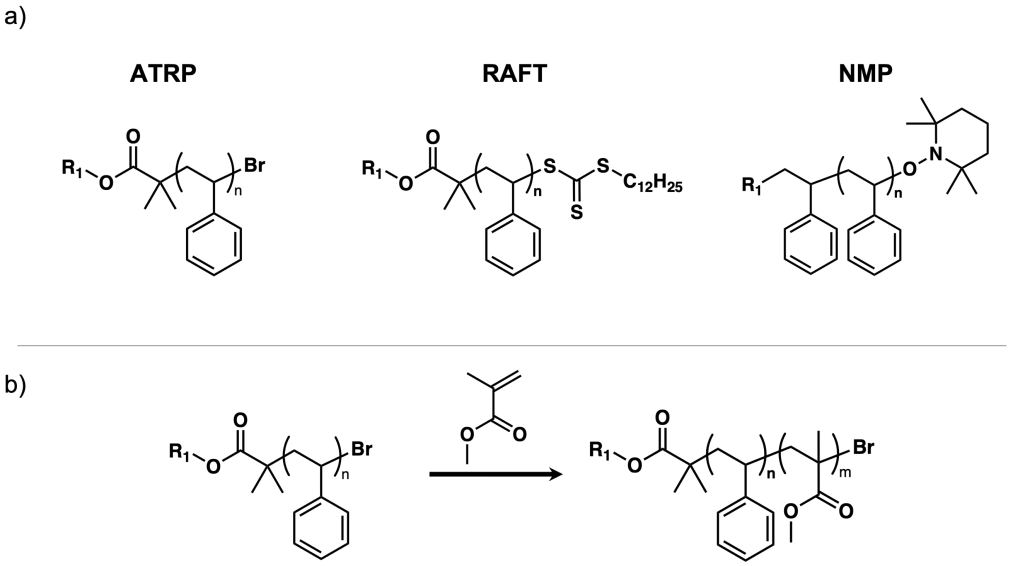
1.1.2 Controlled Radical Polymerization

The drive to address the aforenoted challenges with free radical polymerization in the polymer chemistry community yielded to the development of controlled radical polymerization (also known referred to as living radical or reversible-deactivation radical polymerization).[2,23] In a controlled polymerization, the rate of initiation is greater than the rate of propagation and the addition of monomer to polymer chain ends occurs irreversibly, leading to polymers with narrow molecular weight distributions. In addition, the development of reversible termination of active chain-ends or rapid degenerate exchange between dormant and active chain ends result in essentially "living" polymerizations where all polymer chains grow at the same rate with minimal irreversible termination reactions (Scheme 2).[2] As such, controlled radical polymerizations lead to polymers with well-defined molecular weights and high chain-end fidelities.[2,23]



Scheme 2. Controlled radical polymerization driven by a) reversible deactivation in which equilibrium between dormant and active chain ends. Upon completion of the polymerization, most chains are terminated by the reversible deactivating moiety (X). b) Reversible deactivation by rapidly exchanging chain transfer between propagating chains. Upon completion of the polymerization, most chains are capped with the chain-transfer agent (X).[2]

The end groups of polymers synthesized by controlled radical polymerization are determined by whichever initiating and terminating species are used. Several different controlled radical polymerization techniques such as atom transfer radical polymerization (ATRP), nitroxide mediated polymerization (NMP), reversible addition fragmentation chain transfer (RAFT) polymerization and other processes have been developed based on various mechanisms resulting in a wide variety of chain-end structures (Scheme 3,a).[2,6,24-27] Furthermore, as termination processes in controlled radical polymerization are reversible, dormant chain-ends may be converted back to active species to re-initiate polymerization in the presence of a second, different monomer, resulting in a covalently linked block copolymer (Scheme 3,b).[2,28] Incompatibility of the blocks results in microphase separation with nanostructured morphologies used in a variety of applications ranging from mundane plastics to high-tech devices.[29]



Scheme 3. a) Examples of α- and ω- end functional polystyrene attainable by ATRP, RAFT, and NMP. In all cases, R_1 chain-ends may be capped with functionalities that do not interfere in radical polymerizations such as carboxylic acids, esters, alcohols, ethers, disulfides, etc.[2,6,24-27] b) Re-initiation of isolated end-functional homopolymers by controlled radical for the preparation of diblock copolymers.[2,28]

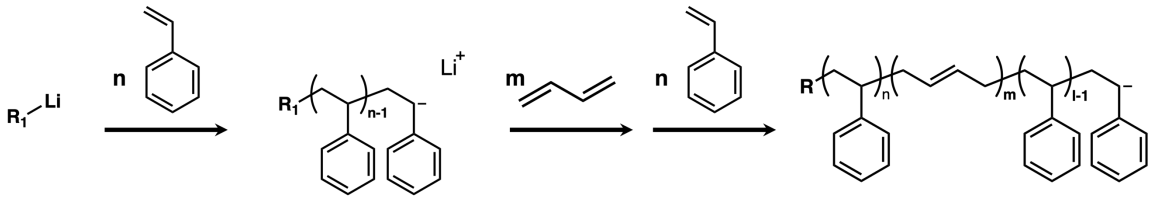
The reactive end-groups resulting from controlled radical techniques may also be transformed through a wide variety of post-polymerization techniques.[10,30,31] Although several examples for chain-end modification via RAFT exist, the alkyl halide obtained from ATRP is arguably the most versatile with its electrophilic character allowing for a wide range of functionalization strategies.[31,32] Functional initiators may also be used, allowing for the preparation of α-, ω- or α,ω-telechelic (symmetric end groups) or heterotelechelic (asymetric end-groups) functionalized polymers. The ease and versatility of this technique opened access to precise macromolecular building blocks for the preparation of polymers with complex architectures.

Although controlled radical polymerization has revolutionized macromolecular research over the past 20 years, it still suffers significant drawbacks that limits its use in industrial settings.[2] Many controlled radical polymerizations require the optimization of various parameters such as initiators, suitable catalyst structures, solvent, temperature, and added salts, deactivators or reducing agents in order to achieve a high degree of control over molecular weight, dispersity and chain-end fidelity.[33,34] This is often challenging for both experts and non-experts alike as choosing appropriate conditions for successful polymerizations is often a time consuming, arduous task. Ever after careful optimization of the reaction conditions, often one has to stop the polymerization at moderate/low conversions (e.g., 60%) in order to maintain high end group fidelities and narrow dispersity followed by extensive purification that limits commercial exploitation.[34] Furthermore, control over the stereochemistry of the polymer backbone (i.e. tacticity) is extremely challenging with radical polymerizations due to the planar geometry of the propagating radicals.[35] Finally, certain

monomer families such as dienes or cyclic epoxides, lactides, siloxanes, and amino acid N-carboxyanhydrides are either highly challenging or inaccessible to polymerize via radical chain-growth mechanisms.[5,36]

1.2 Living Anionic Polymerization

Controlled radical polymerization techniques produce narrow disperse polymers through reversible termination processes that minimize irreversible chain-chain coupling and disproportionation processes.[2] Anionic polymerization, which follows a chain-growth mechanism using anionic propagating species, imparts control by eliminating termination reactions commonly observed in radical systems.[2,5,36] First described by Szwarc, propagating anionic chain-ends during polymerization are incapable of recombining and termination or transfer processes do not occur.[2,36,37] In the absence of impurities, chain-end anions are maintained even at 100% conversion, allowing for the precise control of molecular weights up to 10^6 g/mol with extremely narrow molecular weight distributions ($Đ < 1.05$) and essentially quantitative chain-end fidelities (Scheme 4).[17,36] The "living" nature of this polymerization allows for the synthesis of block copolymers or other complex architectures in one pot simply by sequential monomer or coupling agent additions without the need to isolate and purify the polymerization before chain-extension.[17,38] Significant advances in precisely controlled functional polymer syntheses and various structurally elaborate complex macromolecular architectures by living anionic polymerization has been extensively reviewed by Hirao and coworkers.[17]



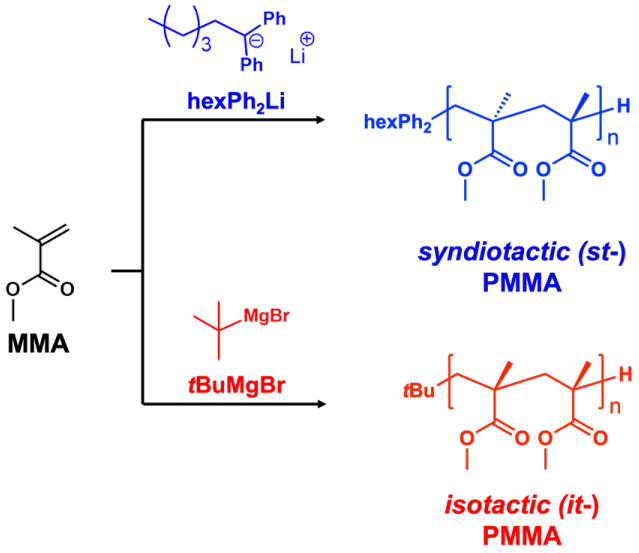
Scheme 4. Example living anionic polymerization of poly(styrene)-poly(butadiene)-poly(styrene) triblock copolymers by sequential monomer additions. The highly living anionic chain-ends continue to propagate until quenched with a proton source or terminating agent.[36]

Chain-end functionalization of α-, ω- polymer ends groups by living anionic polymerizations can be achieved utilizing functional initiators or terminating agents although often requires the use of protecting strategies as functional groups with active hydrogen(s) and carbonyls such as OH, SH, SiOH, NH_2, CHO, COR and COOH are not compatible with high reactive anions.[17] Nonetheless, living anionic polymerization remains the preferred method for the precise synthesis of large, extremely well-defined macromolecules in both academic and industrial settings.[17,36] New chain-end functionalization strategies without the use of protecting groups for highly desirable polymers by living anionic polymerization and their use in materials application are described in this thesis.

1.2.1 Stereocontrolled Polymerizations

Unlike radical polymerization, the stereoregularity of vinyl polymers that significantly impacts thermal and/or mechanical properties of their resulting materials can be tuned in living anionic systems by altering the coordination states of the propagating species.[17] One primary example of this is the stereoregulated polymerization of poly(methyl methacrylate) PMMA where highly *isotactic* (*it*-) or *syndiotactic* (*st*-) isomers can be prepared by carefully selecting the initiator and solvent (Scheme 5).[17,39-41] For organolithium initiators in THF, each MMA monomer unit forms a single coordination site with Li^+ counterions resulting in a

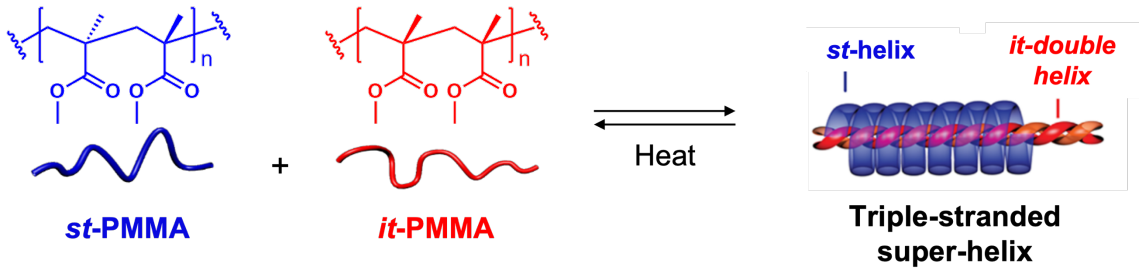
syndiotactic rich polymer (rr > 75%), whereas multisite coordination of the PMMA chain to Mg^{2+} counterions during polymerizations from Grignard initiators in toluene results in highly isotactic materials (mm > 90%).[17,39-41] The addition of aluminum-based lewis acids in hydrocarbon media can also further enhance stereoregularity resulting in highly syndiotactic (rr > 90%) or heterotactic (mr = 68%) PMMA.[17]



Scheme 5. Synthesis of *syndiotactic* (*st*-) or *isotactic* (*it*-) poly(methyl methacrylate)s (PMMA)s.[39-41] Adapted from reference 41 with permission. Copyright 2018 American Chemical Society.

Very interestingly, stereoregular PMMA strands can form a synthetic multi-stranded triple-helix that is structurally similar to biological helices (Scheme 6).[41] This supramolecular assembly forms in common organic solvents and consists of an inner double-stranded of *it*-PMMA, wrapped by a single-stranded *st*-PMMA chain.[42,43] Additionally, the stereocomplexation is reversible where the triple-helix is able to revert to its individual components upon heating or dissolution in nonpolar solvents like chloroform. Unlike natural helices such as DNA, the PMMA triple-helix does not require site-specific interactions such as hydrogen bonding to form and is driven by van der Waals forces along PMMA backbones.[43]

Based on the unique structural features of triple-helix PMMA stereocomplexes, a wide range of applications have been examined including templates for inclusion complexes, stereospecific polymerization, peptide recognition systems, and "smart" nanosystems based on the phenomenon of selective strand-exchange only previously observed in natural helices such as DNA.[44-50]



Scheme 6. Illustration of PMMA triple-helix stereocomplex formation.[41] Adapted from reference 41 with permission. Copyright 2018 American Chemical Society.

To expand the utility of PMMA stereocomplexation for advanced materials applications, synthetic strategies for the preparation of end-functional stereoregular PMMA are required. The halogenation of *st-/it-* PMMA was reported by the Kamigaito group by terminating stereospecific living anionic polymerizations with several halogenating agents aided by common basic additives such as 1,8-diazabicyclo[5.4.0]undec-7-ene (DBU).[51] Although bromide and chloride terminated *st-/it-* PMMA with controlled molecular weights and high chain-end fidelities were achieved, their tertiary halide end groups are unreactive by nucleophilic substitution, limiting their post-polymerization modification strategies. Nonetheless, the azidation of halogenated *st-/it-* PMMA via radical mechanisms and subsequent copper-mediated click reactions with alkynes has been reported for the preparation of stereospecific bottlebrushes and block copolymers.[50,52] In addition to this strategy,

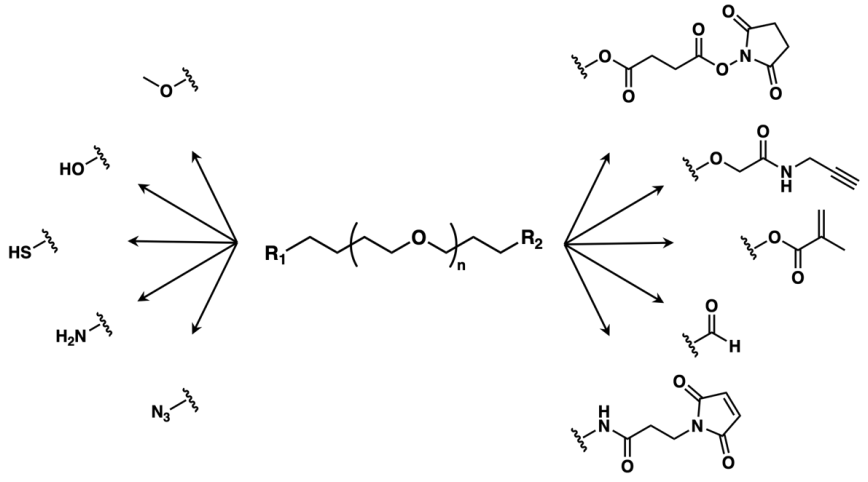
Kitayama and coworkers reported the synthesis *st-/it-* PMMA with clickable C=C chain-ends by quenching their living anionic polymerizations driven by methylaluminum bis(2,6-di-t-butylphenoxide) or isopropyl α-lithioisobutyrate and lithium trimethylsilanoate with α-(halomethl)acrylates.[53,54] The terminal C=C bonds activated by an electron withdrawing carbonyl group can be modified by base catalyzed thiol-Michael additions to yield end-functional stereospecific PMMA with a variety of chain-ends.[54] Inspired by these reports from Kamigaito and Kitayama, a new synthetic strategy for the preparation of alkene-terminated *st-/it-* PMMA on multigram scales with common initiators and their modification into nanoparticle ligands is described in **Chapter 2** and **Appendix A** of this thesis.

1.2.2 Ring Opening Polymerizations

In addition to vinyl monomers, anionic mitigated ring opening polymerization has become a powerful tool for the synthesis of various polymers including polyethers, polyesters, polyamides, polysiloxanes and polycarbonates.[36] Ring strain coming from distortion of ring angles and stretching bonds is generally responsible for driving the propagation of monomers into polymer chains. Although ring opening polymerizations may also be performed via cationic, coordination-insertion or other mechanisms, living anionic techniques are generally preferred for the preparation of well-defined high molecular weight materials and precise macromolecular architectures.[36]

Of the monomer families mentioned above, the anionic ring opening polymerization of cyclic ethers such as ethylene oxide enables the synthesis of poly(ethylene oxide) (PEO, also known as poly(ethylene glycol) or PEG).[36] The several million tons of PEG are produced by anionic polymerization per year for use in a variety of commercial products ranging from commodity laxatives and cosmetics to high-performance PEG functionalized pharmaceuticals

such as mRNA COVID-19 vaccines.[36,55-57] The increased hydrodynamic size and improved aqueous solubility by the covalent attachment of reactive PEG derivates (referred to PEGylation) to hydrophobic drugs, lipids, or therapeutic proteins prolongs their circulatory time in patients by reducing their renal clearance.[55,56] The pharmaceutical advantages and FDA approval of PEGylated technology has laid the foundation for a growing multibillion-dollar industry[55]. For scalable and effective PEGylation to be achieved, the quantitative and selective functionalization of PEG at one or both chain-ends are crucial. Thus, several reported strategies to synthesize α-, ω- monofunctional and α,ω-telechelic or heterotelechelic chemically activated end-functionalized PEG macromolecules derived from anionic polymerization have been commercialized (Scheme 7).[55,56] The development of Chemokine Receptor 5 (CCR5) targeted nanoparticles derived from heterotelechelic PEG-peptide conjugates and their use as *in vivo* imaging agents to visualize the progression and regression of atherosclerosis is described **Appendix E** of this thesis.

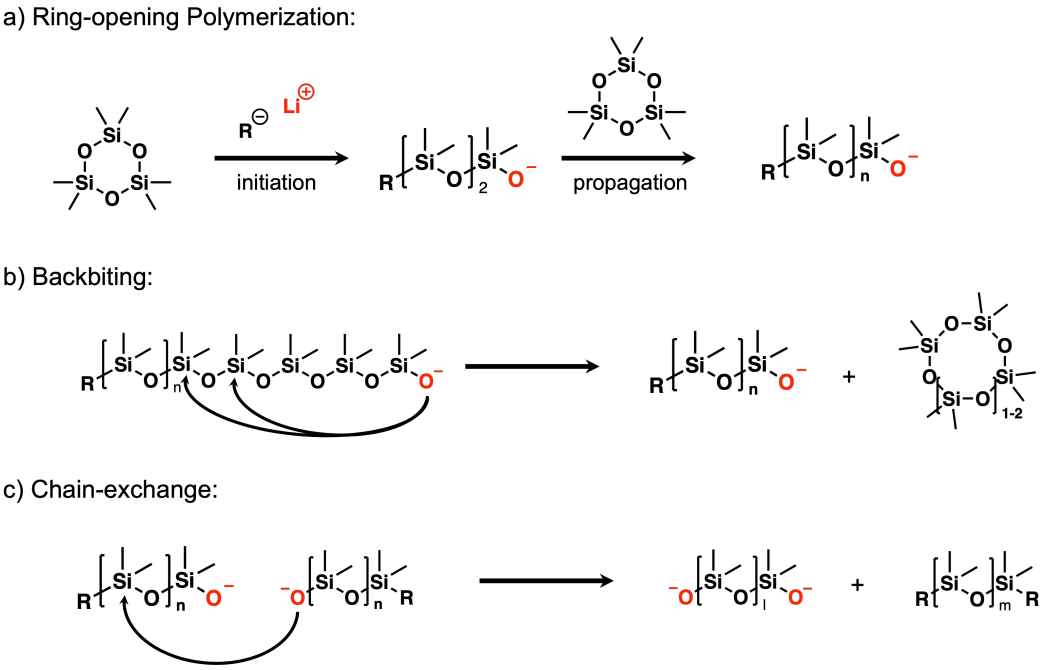


Scheme 7. Representative example of commercially available end-functionalities for PEG synthesized by anionic ring opening polymerization.[36,55,56]

Polysiloxanes, also referred to as silicones, are high value polymers with exceptional properties unmatched by organic materials such as their chain-flexibility imparted by the wide Si-O bond angle paired with high bond strength.[58] These unique attributes stemming from the substantial dipolar nature of Si-O-Si bonds along polysiloxane backbones and the facile control over organic substituents at each silicone atom give rise to their low Tg, low surface energy, high thermal stability, gas permeability and excellent biocompatibility.[58,59] Many polysiloxane-based materials have been manufactured in the form of fluids, resins, and crosslinked elastomers for thousands of commercial products ranging from high performance aerospace adhesives to pharmaceuticals and biomedical devices.[60-65] There is also considerable interest in blending polysiloxanes with organic materials as a cost-effective method to obtain new materials with improved properties, but the propensity for silicones to macrophase separate motivates the development compatibilization strategies. State-of-the-art polysiloxane compatibilization strategies for silicone-organic polymer blends are described in **Appendix D**.

Although many strategies to synthesize polysiloxanes have been previously described elsewhere, the ring opening polymerization of cyclic oligomers allows better precision in terms of molecular weight and dispersity than the polycondensation of functional precursors.[36] It is important to note that although the anionic polymerization of several cyclic siloxane monomers has been reported, careful control of the reaction conditions is required in order to avoid the reformation of cyclic oligomers or other byproducts.[36,66] Unlike previously described anionic polymerizations, many side reactions including backbiting, chain-scrambling and condensations, known as equilibration or redistribution processes, are thermodynamically during the ring opening polymerizations of siloxanes and have significant

consequences on the product distribution and chain-end structures (Scheme 8).[36,66] However, these side reactions may be minimized via kinetic control where selective cleavage of highly strained tricyclosiloxane monomers and their chain-propagation occur almost exclusively at low conversions.[66] Kinetically controlled anionic ring opening polymerizations provide access to well-defined high molar polysiloxanes with narrow molecular weight distributions and high chain-end fidelities.[66] However, the intolerance of propagating anions to many functional groups and potential to re-initiate acid or base catalyzed equilibrium pathways during post-polymerization modifications makes the synthesis of chain-end functional polysiloxanes extremely challenging.[17,66,67] Thus, a new strategy to prepare α,ω-telechelic and heterotelechelic poly(dimethyl siloxane) (PDMS) by living anionic polymerization and their quantitative chain-end transformations under mild conditions to install a wide variety of functional groups is described in **Chapter 3** and **Appendix B** or this thesis.

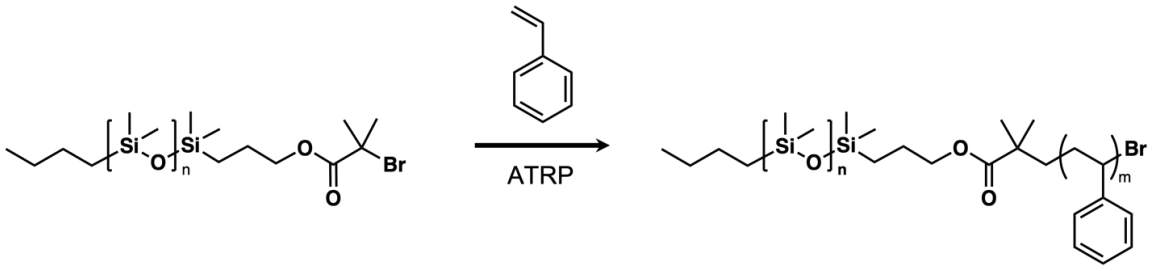


Scheme 8. a) Kinetically controlled polymerization of strained cyclotrisiloxane monomers and thermodynamic redistribution mechanisms by b) backbiting or c) chain-exchange during anionic ring opening polymerizations of polysiloxanes.[36,66]

1.2.3 Chain-End Transformations to Controlled Radical Polymerizations

Although much of this thesis discusses anionic polymerization as an attractive method to prepare well-defined end-functionalized polymers, it is important to note that there are still many classes of materials where radical techniques reign supreme.[5] In particular, the reactivity of propagating anions is extremely sensitive to their monomer substituents, limiting anionic polymerization of vinyl monomers to materials with electron withdrawing or aromatic groups that can stabilize negative charges.[5] This effect is magnified in the case of copolymerizations with two or more different monomers as their reactivity ratios vary wildly depending on the polymerization conditions.[68] In contrast, a significantly broader spectrum of monomers can be polymerized by radical mechisms and the statistical copolymerizaton of vinyl monomers within the same family (eg: acrylates, methacrylates, styrenics, etc) is facile.[5,23,69]

As both anionic and controlled radical polymerizations are important tools in polymer chemistry, these two techniques may be combined through chain-end transformations to facilitate the synthesis of hybrid materials with exciting properties.[51,70] One example is the preparation of well-defined polysiloxane macroinitiators with terminal alkyl bromides through living anionic polymerizations subsequently followed by controlled radical polymerizations of vinyl monomers (Scheme 9).[70] The resulting silicone-organic block copolymers exhibit remarkably high Flory-Huggins interaction parameters (χ) and segregation strengths enabling their microphase separation into sub-10 nm domains for lithographic techniques.[71] However, the development of low χ-polysiloxane-BCPs that enhance their compatibility with organic materials for applications such as blend compatibilization is required. The preparation of PDMS-based "block random" copolymers with tunable segregation strengths via the ATRP driven copolymerization of MMA and a new hybrid silicone-methacrylate monomer from PDMS-Br macroinitiators is presented in **Chapter 4** and **Appendix D**.



Scheme 9. Synthesis of hybrid PDMS-based block copolymers by chain-extension of end-functionalized PDMS-Br macroinitiatiors with vinyl monomers via ATRP.

1.3 References

(1) Mülhaupt, R. *Angew. Chem., Int. Ed.* **2004**, *43*, 1054.

(2) Grubbs, R. B.; Grubbs, R. H. *Macromolecules*, **2017**, *50*, 6979.

(3) The web page of the Nobel Foundation contains Prof. A. Fredgas “Presentation Speech” (http ://www.nobel.se/chemistry/laureates/1953/press.html), the Staudinger Biography (http://www.nobel.se/chemistry/laureates/1953/staudinger-bio.html), as well as Staudinger's Nobel Lecture (http://www.nobel.se/chemistry/ laureates/1953/staudinger-lecture.html) and his “Banquet Speech” (http ://www.nobel.se/chemistry/laureates/1953/ staudinger-speech.html).

(4) Matyjaszewski, K.; Tsarevsky, N. V. *Nature Chemistry*, 2009, *1*, 276.

(5) Odian, G. *Principles of Polymerization*. John Wiley & Sons, 4 ed., **2004**.

(6) Yamago, S.; Nakamura, Y. *Polymer*, 2013, *54*, 981.

(7) Matyjaszewski, K.; Tsarevsky, N. V. *J. Am. Chem. Soc.* 2014, *136*, 6513.

(8) Rudin, A.; Choi, O. *The Elements of Polymer Science and Engineering*, Academic Press, **2012**.

(9) Matyjaszewski, K. *Macromolecules*, 2012, 45, 4015.

(10) Kim, J.; Jung, Y. Park, M. J. *Macromolecules*, **2020**, *53, 746.*

(11) Pispas, S.; Hadjichristidis, N. *Macromolecules*, **1994**, *27*, 1891.

(12) Charlier, P.; Jeŕôme, R.; Teyssie,́ P.; Utracki, L . A. *Macromolecules*, **1990**, *23*, 3313.

(13) Ito, K.; Tanaka, K.; Tanaka, H.; Imai, G.; Kawaguchi, S.; Itsuno, S. *Macromolecules*, **1991**, *24*, 2348.

(14) Fleischer, C. A.; Koberstein, J. T.; Krukonis, V.; Wetmore, P. *Macromolecules*, **1993**, *26*, 4172.

(15) Lundberg, D. J.; Brown, R. G.; Glass, J. E.; Eley, R. R. *Langmuir,* **1994**, *10*, 3027.

(16) Song, T.; Dai, S.; Tam, K. C.; Lee, S. Y.; Goh, S. H. *Langmuir*, **2003**, *19*, 4798.

(17) Hirao, A.; Goseki, R.; Ishizone, T. *Macromolecules*, **2014**, *6*, 1883.

(18) Chang, R.; Huang, Y.; Shan, G.; Bao, Y.; Yun, X.; Dong, T.; Pan, P. *Polym. Chem.* **2015**, *6*, 5899.

(19) Herbst, F.; Döhler, D.; Michael, P.; Binder, W. H. *Macromol. Rapid Commun.* **2013**, *34*, 203.

(20) Folmer, B. J. B.; Cavini, E. *Chem. Commun.* **1998**, *17*, 1847.

(21) Sijbesma, R. P.; Beijer, F. H.; Brunsveld, L.; Folmer, B. J. B.; Hirschberg, J. H. K. K.; Lange, R. F. M.; Lowe, J. K. L.; Meijer, E. W. *Science* **1997**, *278*, 1601.

(22) Guo, M.; Pitet, L. M.; Wyss, H. M.; Vos, M.; Dankers, P. Y. W.; Meijer, E. W. J. *Am. Chem. Soc. 2014*, *136*, 6969.

(23) Braunecker, W. A.; Matyjaszewski, K.; *Progress in Polymer Science*, 2007, *32*, 93.

(24) Boyer, C.; Corrigan, N. A.; Jung, K.; Nguyen, D.; Nguyen, T.-K.; Adnan, N. N. M.; Oliver, S.; Shanmugam, S.; Yeow, J. *Chem. Rev.* **2016**, *116*, 1803.

(25) Anastasaki, A.; Nikolaou, V.; Nurumbetov, G.; Wilson, P.; Kempe, K.; Quinn, J. F.; Davis, T. P.; Whittaker, M. R.; Haddleton, D. M. *Chem. Rev.* **2016**, *116*, 835.

(26) Perrier, S. *Macromolecules*, **2017**, *50*, 7433.

(27) Hawker, C. J.; Bosman, A. W. Harth, E. *Chem. Rev.* **2001**, *101*, 3661.

(28) Engelis, N. G.; Anastasaki, A.; Nurumbetov, G.; Truong, N. P.; Nikolaou, V.; Shegiwal, A.; Whittaker, M. R.; Davis, T. P.; Haddleton, D. M. *Nat. Chem.* **2016**, *9*, 171.

(29) Bates, C. M.; Bates, F. M. *Macromolecules*, **2017**, *50*, 3.

(30) Blasco, E.; Sims, M. B.; Goldmann, A. S.; Sumerlin, B. S.; Barner-Kowolik, C. *Macromolecules*, **2017**, *50*, 5215.

(31) Lunn, D. J.; Discekici, E. H.; Read de Alaniz, J.; Gutekunst, W. R.; Hawker, C. J. *J. Polym. Sci. A. Polym. Chem.* **2017**, *55*, 2903.

(32) Anastasaki, A.; Willenbacher, J.; Fleischmann, C.; Gutekunst, W. R.; Hawker, C. J. *Polym. Chem.* **2017**, *8*, 689.

(33) Matyjaszewski, K. *Macromolecules*, **2012**, *45*, 4015.

(34) Whitfield, R.; Anastasaki, A.; Nikolaou, V.; Jones, G. R.; Engelis, N. G.; Discekici, E. H.; Fleischmann, C.; Willenbacher, J.; Hawker, C. J.; Haddleton, D. M. *J. Am. Chem. Soc.* **2017**, *139*, 1003.

(35) Satoh, K.; Kamigaito, M. *Chem. Rev.* **2009**, *109*, 5120.

(36) Hadjichristidis, N.; Hirao, A. *Anionic Polymerization: Principles, Practice, Strength, Consequences and Applications.* Springer, Tokyo, **2015**.

(37) Szwarc, M, *Nature*, 1956, 178, 1168.

(38) Szwarc, M.; Levy, M.; Milkovich, R. *J. Am. Chem. Soc.* **1956**, *78*, 2656.

(39) Hatada, K.; Ute, K.; Tanaka, K.; Kitayama, T.; Okamoto, Y. *Polym. J.* **1985**, *17*, 977.

(40) Cao, Z.-K.; Okamoto, Y.; Hatada, K. *Kobunshi Ronbunshu*, **1986**, *43*, 857.

(41) Ren, J. M.; Lawrence, J.; Knight, A. S.; Abdilla, A.; Zerdan, R. B.; Levi, A. E.; Oschmann, B.; Gutekunst, W. R.; Li, Y.; McGrath, A. J.; Bates, C. M.; Qiao, G. G.; Hawker, C. J. J. *Am. Chem. Soc.* **2018**, *140*, 1945.

(42) Kumaki, J.; Kawauchi, T.; Okoshi, K.; Kusanagi, H.; Yashima, E. *Angew. Chem., Int. Ed.* **2007**, *46*, 5348.

(43) Christofferson, A. J.; Yiapanis, G.; Ren, J. M.; Qiao, G. G.; Satoh, K.; Kamigaito, M.; Yarovsky, I. *Chem. Sci.* **2015**, *6*, 1370.

(44) Kawauchi, T.; Kitaura, A.; Kumaki, J.; Kusanagi, H.; Yashima, E. *J. Am. Chem. Soc.* **2008**, *130*, 11889.

(45) Vidal, F.; Falivene, L.; Caporaso, L.; Cavallo, L.; Chen, E. Y. X. *J. Am. Chem. Soc.* **2016**, *138*, 9533.

(46) Kawauchi, T.; Kumaki, J.; Kitaura, A.; Okoshi, K.; Kusanagi, H.; Kobayashi, K.; Sugai, T.; Shinohara, H.; Yashima, E. *Angew. Chem., Int. Ed.* **2008**, *47*, 515.

(47) Serizawa, T.; Hamada, K.; Akashi, M. *Nature* **2004**, *429*, 52.

(48) Serizawa, T.; Sawada, T.; Kitayama, T. *Angew. Chem., Int. Ed.* **2007**, 46, 723.

(49) Serizawa, T.; Sawada, T.; Matsuno, H.; Matsubara, T.; Sato, T. *J. Am. Chem. Soc.* **2005**, *127*, 13780.

(50) Ren, J. M.; Knight, A. S.; van Ravensteijn, B. G. P.; Kohl, P.; Bou Zerdan, R.; Li, Y.; Lunn, D. J.; Abdilla, A.; Qiao, G. G.; Hawker, C. J. *J. Am. Chem. Soc.* **2019**, *141*, 2630.

(51) Aoshima, H.; Satoh, K.; Kamigaito, M. *ACS Macro Lett.* **2013**, *2*, 72.

(52) Ren, J. M.; Ishitake, K.; Satoh, K.; Blencowe, A.; Fu, Q.; Wong, E. H. H.; Kamigaito, M.; Qiao, G. G. *Macromolecules* **2016**, *49*, 788.

(53) Kohsaka, Y.; Kurata, T.; Kitayama, T. *Polym. Chem.* **2013**, *4*, 5043.

(54) Kohsaka, Y.; Kurata, T.; Yamamoto, K.; Ishihara, S.; Kitayama, T. *Polym. Chem.* **2015**, *6*, 1078.

(55) Knop, K.; Hoogenboom, R.; Fisher, D.; Schubert, U. *Angew. Chem. Int. Ed.* **2010**, *49*, 6288.

(56) Damodaran, V. B.; Fee, C. J. *Eur. Pharm. Rev.* **2010**, *15*, 18.

(57) Cabanillas, B.; Akdis, C. A.; Novak, N. *Allergy*, **2020**, *76*, 1617.

(58) Voronkov, M. G.; Mileshkevich, V. P.; Yuzhelevskii, Y. A. Studies in Soviet Science. The Siloxane Bond, Physical Properties and Chemical Transformations, Plenum Publishing Corporation, New York, USA **1978**.

(59) Pouget, E.; Tonnar, J.; Lucan, P.; Lacroix-Desmazes, P.; Ganachaud, F.; Boutevin, B.; *Chem. Rev.* **2010**, *110*, 1233.

(59) Centre Européen des Silicones, http://www.silicones.eu 2020.

(60) Zimmermann, C. G.; *MRS Bull.* **2010**, *35*, 48.

(61) Aziz, T.; Waters, M.; Jagger, R.; *J. Dentist*. **2003**, *31*, 67.

(62) Holzapfel, B. M.; Reichert, J. C.; Schantz, J.-T.; Gbureck, U.; Rackwitz, L.; Nöth, U.; Jakob, F.; Rubert, M.; Groll, J.; Hutmacher, D. W. *Adv. Drug Delivery Rev*. **2013**, *65*, 581.

(63) Hassler, C.; Boretius, T.; Stieglitz, T.; J. *Polym. Sci., Part B: Polym. Phys.* **2011**, *49*, 18.

(64) Abbasi, F.; Mirzadeh, H.; Katbab, A.-A.; *Polym. Int.* **2001**, *50*, 1279.

(65) Mojsiewicz-Pieńkowska, K. *Handbook of Polymers for Pharmaceutical Technologies*, Scrivener, Beverly, Massachusetts, **2015**.

(66) Chojnowski, J. *J. Inorg. Organomet. Polym.* **1991**, *1*, 299.

(67) Brook, M. A. *Chem. Eur. J.* **2018**, *24,* 8458.

(68) Beckingham, B. S.; Register, R. A. *Macromolecules* **2011**, *44*, 4313.

(69) Matyjaszewski, K. *Adv. Mater.* **2018**, *30*, 1706441.

(70) Miller, P. J.; Matyjaszewski, K. *Macromolecules*, **1999**, *32*, 87.

(71) Luo, Y.; Montarnal, D.; Kim, S.; Shi, W.; Barteau, K. P.; Pester, C. W.; Hustad, P. D.; Christianson, M. D.; Fredrickson, G. H.; Kramer, E. J.; Hawker, C. J. *Macromolecules* **2015**, *48*, 3422.

Chapter 2. Polymer Stereococomplexation as a Scalable Platform for Nanoparticle Assembly

This chapter was initially published in *Journal of the American Chemical Society*. Adapted with permission *J. Am. Chem. Soc.* **2020**, *142*, 4, 1667 – 1672.
Copyright 2020, American Chemical Society.

2.1 Abstract

DNA-mediated assembly of inorganic particles has demonstrated to be a powerful approach for preparing nanomaterials with a range of interesting optical and electrical properties. Building on this inspiration, we describe a generalizable gram-scale method to assemble nanoparticles through the formation of poly(methyl methacrylate) (PMMA) triple-helices. In this work, alkene-terminated *syndiotactic* (*st*-) and *isotactic* (*it*-) PMMA polymers were prepared and subsequently functionalized to afford nanoparticle ligands. Nanoparticles with complementary *st*- and *it*-PMMA ligands could then be spontaneously assembled upon mixing at room temperature. This process was robust and fully reversible through multiple heating and cooling cycles. The versatility of PMMA stereocomplexation was highlighted by assembling hybrid structures composed of nanoparticles of different compositions (e.g., Au and quantum dots) and shapes (e.g., spheres and rods). These initial demonstrations of nanoparticle self-assembly from inexpensive PMMA-based materials present an attractive alternative to DNA-based nanomaterials.

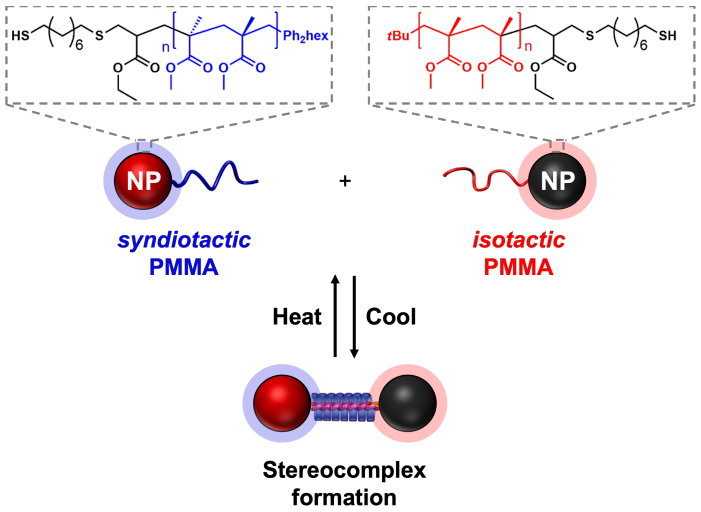
2.2 Introduction

There has been growing interest in broadening the range of colloidal crystals derived from inorganic nanoparticles, driven in part by applications in nanoelectronics and photonics.[1] The properties of these materials are dictated by the chemical composition, shape, size, and

relative three- dimensional arrangement of nanoparticles. In particular, manipulating the assembly process results in nanoparticle structures with properties that are highly desirable for optics, catalysis and metamaterial applications.[2–4] Different strategies to obtain such assemblies have been developed, such as brick- and-mortar procedures,[5] covalent coupling,[6] or "sticky" nanoparticles,[7] leading to control over nanoscale assembly. DNA has emerged as an attractive surface ligand to direct nanoparticle assembly into ordered structures due to their programmable interactions and highly tunable structure. Pioneered by the Mirkin group, nanoparticles coated with a dense shell of DNA strands act as programmable atom equivalents, where DNA "bonds" arrange nanoparticle "atoms" of arbitrary composition into superlattices with well-defined spacing, symmetry, and, in some cases, crystal habit.[8–11] Despite the high level of structural control afforded by DNA-mediated assembly, limitations do exist. These include (1) restriction to aqueous conditions, (2) cost of surface- binding DNA derivatives, and (3) difficulty in scaling to multigram quantities which hinders use in many materials applications.[12] In contrast, synthetic polymers provide scalability, are processable in organic media, and are easily produced on multigram scales. Prior studies have shown that polymeric ligands show significant promise for tuning particle interactions, providing access to entropically and enthalpically driven structures.[13–16] However, the challenge with polymeric systems includes a limited toolbox of stimuli responses and decreased precision in molecular interactions/nanoscale assembly when compared to DNA.[17,18]

To bridge DNA and polymer-based technologies, we turned our attention to synthetic helical polymers as they are known to mimic the semicrystalline structure, rigidity, and selective interactions of DNA.[19,20] One such synthetic multistranded system is the stereoregular poly(methyl methacrylate) (PMMA) triple-helix.[21] This supramolecular

assembly forms in common organic solvents and consists of an inner double- stranded helix of *isotactic* (*it*-) PMMA, wrapped by a single- stranded *syndiotactic* (*st*-) PMMA chain.[22,23] Additionally, the stereocomplexation is reversible where the triple-helix is able to revert to its individual components upon heating or dissolution in nonpolar solvents like chloroform. Unlike natural helices such as DNA, the PMMA triple-helix does not require site- specific interactions such as hydrogen bonding to form and is driven by van der Waals force along PMMA backbones.[23] Most importantly, stereoregular PMMA can be synthesized on multigram scale from commodity materials using industrially practiced techniques.[24] Despite these advances, the controlled self-assembly of hybrid materials bearing such polymers has remained unexplored. Herein, we report a versatile strategy to obtain *st*- and *it*-PMMA with thiol chain-ends on multigram scales (Scheme 1). The utility of stereospecific PMMA ligands was then demonstrated through their use as nanoparticle ligands, where complementary nanoparticles could be assembled through stereocomplexation in organic solvents. The specificity and reversibility of stereocomplexation is demonstrated to offer a facile and scalable pathway to form unique nanostructures.



Scheme 1. Nanoparticle Assembly via PMMA Stereocomplexation.

2.3 Results and Discussion

To expand the utility of PMMA stereocomplexation for nanoparticle assembly, we first developed a synthetic strategy for the preparation of thiol-terminated stereoregular PMMA on multigram scales. Inspired by reports from Kohsaka and Kamigaito,[25−27] we first conducted a standard *st*-specific polymerization of MMA initiated by hexPh_2Li at −78 °C in THF.[22] An excess of ethyl 2-(bromomethyl)acrylate and 1,8- diazabicyclo[5.4.0]undec-7-ene (DBU) were added to the polymerization mixture after 1 h, reacted overnight under vigorous stirring, and quenched with degassed methanol. The polymers synthesized for this study had molecular weights ranging from 2−10 kDa with a high degree of stereocontrol (racemo triad rr > 75%), narrow dispersities ($Đ$ < 1.20), and near quantitative incorporation of the alkene chain functionality. The complementary alkene-terminated *it*-PMMA system was synthesized by anionic polymerization of MMA with tBuMgBr in toluene (meso triad mm > 92%, $Đ$ < 1.20).[19] Subsequent chain-end functionalization to produce thiol- terminated *st*- and *it*-PMMA pairs was accomplished via thiol-Michael addition with a large excess of 1,8-octanedithiol and DBU as a catalyst (Figure 1a). Quantitative consumption of alkene chain-ends for both *st*- and *it*- systems was observed within 1 h, regardless of the polymer molecular weight. High thiol chain-end fidelity with little-to-no chain−chain coupling was confirmed by size-exclusion chromatography (SEC) and matrix-assisted laser desorption/ionization (MALDI) mass spectral analysis (Figures A6, A8, A15, and A17). To demonstrate scaling of this approach, the anionic polymerization and subsequent Michael-addition of stereoregular PMMA ligands were conducted on a multigram scale (∼5 g) at a high yield (96%) with no impact on the dispersity or chain-end functionality (Figure A9).

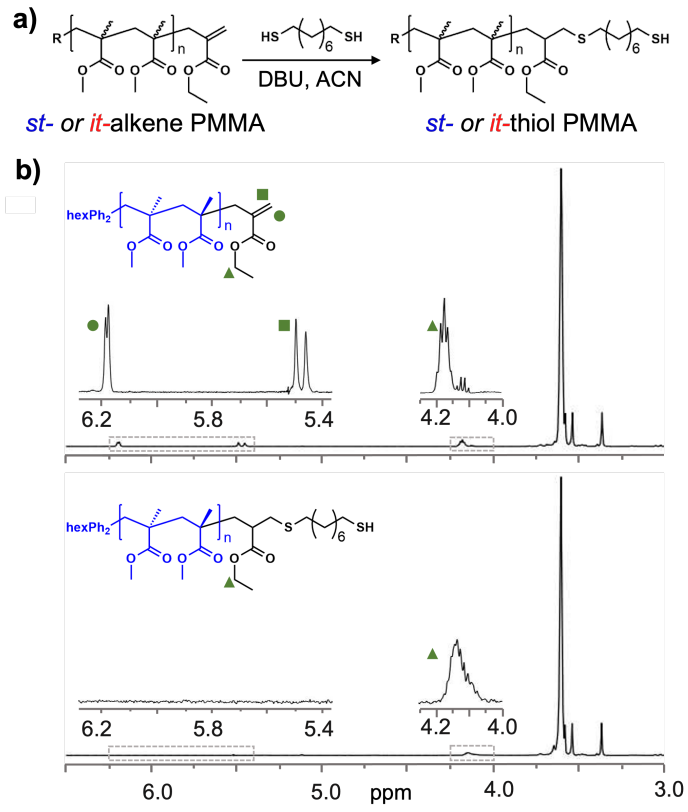


Figure 1. a) Michael-addition of alkene-terminated *st*-/*it*-PMMA to give thiol-functionalized PMMA ligands. b) NMR traces of alkene-terminated *st*-PMMA-2K (top) and thiol-terminated *st*-PMMA-2K (bottom).

To demonstrate triple-helix driven assembly, complementary *st*-/*it*-PMMA-grafted gold nanoparticles (Au NPs) were initially prepared. Au NPs were chosen as a model system based on the sensitivity of surface plasmon resonance (SPR) to the AuNP aggregation state and the facile functionalization of Au NPs via gold−thiol chemistry. A modified procedure from Stucky and co-workers yielded 5−10 nm *st*-/*it*-PMMA- functionalized Au NPs with a clear SPR band between 520 and 530 nm (Figure A18).[28] The PMMA−Au NPs could be readily dispersed in common organic solvents with ligand densities between 2.0 and 2.5 chains/nm^2 as determined by thermal gravimetric analysis (Table A3). To induce triple-helix formation, complementary *st*- and *it*-PMMA−Au NPs were dispersed in acetonitrile, a strong

complexation solvent. Upon mixing solutions of *st*-PMMA6K−Au NPs and *it*-PMMA3K− Au NPs in a 1:1 ratio, rapid precipitation from solution was observed (Figure 2a). In contrast, no particle assembly or precipitation was observed for the individual *st*-/*it*-PMMA−Au NPs as they remained dispersed in acetonitrile. Further evidence of this assembly process was demonstrated by transmission electron microscopy (TEM), dynamic light scattering (DLS), Fourier-transform infrared spectroscopy (FTIR), and wide-angle X-ray scattering (WAXS) which revealed that large nanoparticle clusters only form in *st*-/*it*- mixtures. Spectroscopic changes were also characteristic of helix formation (Figures 2b, A29, A32, and A33).

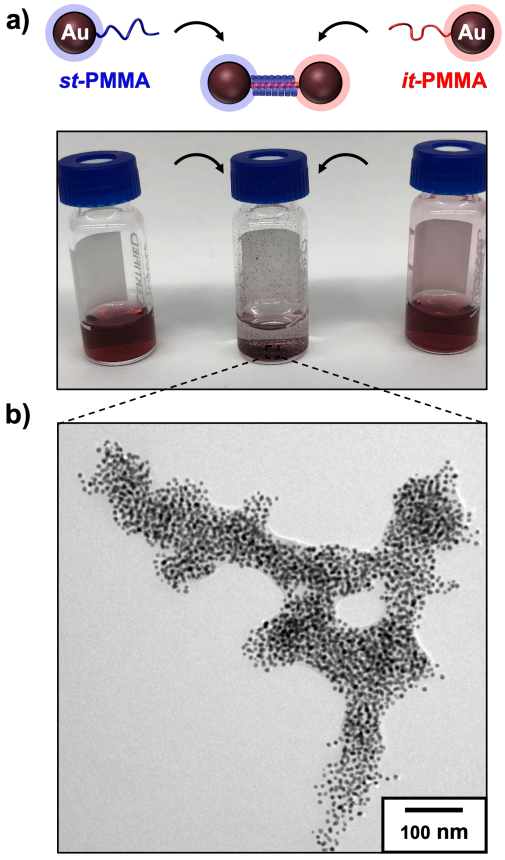


Figure 2. a) Schematic (top) and a photo (bottom) of *st*-PMMA6K-Au NPs (left), *it*-PMMA3K−Au NPs (right), and 1:1 *st*-PMMA6K−Au NPs + *it*-PMMA3K−Au NPs after mixing (15 min) (center). b) TEM image of stereocomplexed 1:1 *st*-PMMA6K−Au NPs + *it*-PMMA3K−Au NPs.

To understand the assembly kinetics for these systems, the SPR band of the *st*-/*it*-PMMA−Au NPs was monitored by UV−vis spectroscopy after the complementary nanoparticles were mixed. As expected for rapid complexation, noticeable red-shifting and broadening of the extinction peak were observed as the interparticle distance between Au NPs decreased. Over time, the extinction peak diminished as the nanoparticles formed larger aggregates and underwent precipitation (Figure 3a). Only a subtle change in extinction peak was observed after 8 min, indicating that most particles underwent stereocomplexation. A kinetic profile of the particle assembly process was generated by monitoring absorbance at 530 nm and showed a rapid decrease in absorbance upon particle mixing (Figure A26). This decay in the SPR extinction continued until an equilibrium is reached after 10 min.

While the particle stereocomplexation demonstrated desirable kinetics, an ideal property for nanoparticle assemblies is the ability to "melt" the system with increasing temperature to regenerate the starting nanoparticles. To investigate the thermal properties of stereocomplexed nanoparticles, *st*- + *it*- PMMA-Au NPs were allowed to fully assemble at room temperature. The precipitated particles were then monitored by UV−vis spectroscopy at 530 nm while heating at a rate of 1 °C/min. Significantly, this results in a curve with a character- istic melting temperature between 62 and 64 °C (Figure 3b), higher than for typical DNA-based systems (approximately 30−50 °C), indicating the formation of robust yet reversible assemblies.[29] Above the melting temperature, PMMA-Au NP aggregates redispersed and the solution color turned red, demonstrating the dynamic and reversible nature of the stereocomplex directed assembly process (Figure A25). Additionally, melted *st*- + *it*-PMMA-Au NPs reprecipitated from solution upon cooling to room temperature, indicating that PMMA triple-helices were able to reform. To test the robustness of stereocomplexed

nanoparticle assemblies, precipitated particles were then heated at 70 °C for 5 min and subsequently cooled to 25 °C for 20 min while monitoring the SPR band by UV−vis spectroscopy. This process was repeated for multiple heating and cooling cycles with little alteration of the assembly behavior or optical properties, illustrating the thermal stability of these ligands under these conditions (Figure 3c).

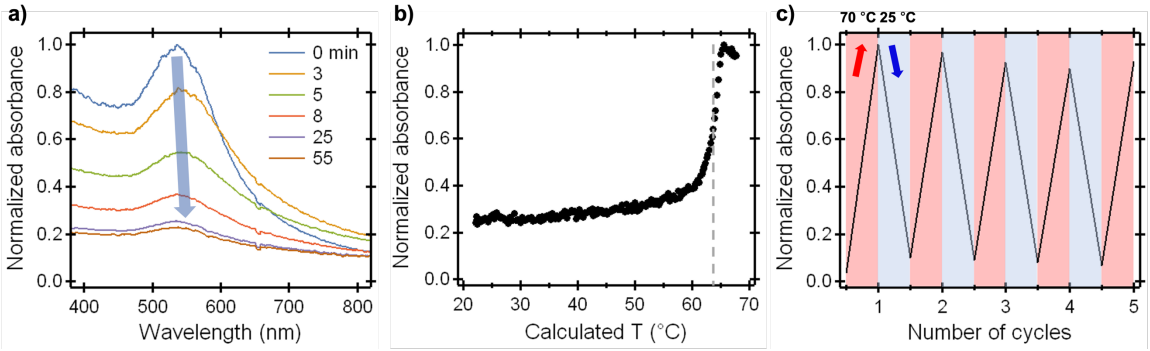


Figure 3. a) UV−vis spectra of 1:1 *st*-PMMA6K−Au NPs + *it*-PMMA3K−Au NPs taken at different time points after mixing. A rapid decay in absorbance demonstrates nanoparticle assembly via stereocomplexation. b) Kinetics of the melting process of stereocomplexed assemblies at 530 nm. c) Normalized extinction of stereocomplexed nanoparticles during several heating/cooling cycles at 530 nm.

In addition to homogeneous materials, nanoparticle assemblies made from anisotropic nanoparticles such as nanorods (NRs) are desirable as they possess directional dependent interactions, allowing for assemblies with advanced morphologies.[30] To investigate the versatility of *st*-/*it*-PMMA for assembly of anisotropic nanoparticles, *st*-PMMA10K−Au NRs were prepared via a ligand exchange process. The *st*-PMMA10K−Au NRs were then dispersed in acetonitrile and mixed with *it*-PMMA3K−Au NPs at a 1:10 ratio. Upon mixing, significant broadening and red-shifting of the longitudinal SPR band were observed by absorbance spectroscopy (Figure A27). TEM images of the stereocomplexed *it*-PMMA3K−Au NPs + *st*-PMMA10K−Au NRs showed that multiple Au NPs were selectively bound to the Au NRs (Figure 4). It is interesting to note that the *it*-PMMA3K−Au NPs were

evenly arranged at the *st*-PMMA10K−Au nanorod surface with no free Au NPs or Au NRs. To demonstrate that the assembly is driven by stereocomplexation, *it*-PMMA10K−Au NRs were mixed with *it*-PMMA3K−Au NPs, where a random scattering of Au NPs and Au NRs were observed across the carbon grid with no distinct assemblies under TEM, indicating no stereocomplex- ation or assembly (Figure A28).

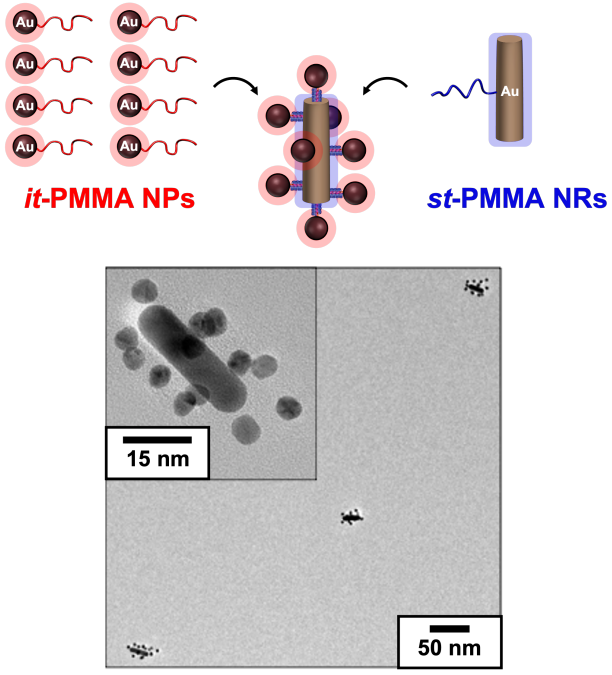


Figure 4. Schematic (top) and TEM image (bottom) of advanced morphologies by stereocomplexation of *it*-PMMA3K−Au NPs + *st*-PMMA10K−Au NRs.

Building on the success of assembling mixtures of Au NPs/ Au NRs, the versatility of this strategy was further demonstrated by expanding this concept to a wide variety of metals or semiconducting materials. In particular, assemblies with CdSe-based quantum dots were of interest due to their photoluminescent properties providing a unique diagnostic tool to probe the particle assembly process.[6,31] Red emitting oleic acid CdSe@ZnS quantum dots (QDs) were therefore synthesized via previously reported methods and functionalized via ligand exchange with thiol-terminated *it*-PMMA in chloroform at 60 °C.[32] The *it*-PMMA3K−QDs

were well dispersed in acetonitrile and retained a strong emission peak at 630 nm (Figure A22). Composite assembly of Au NPs and QDs was then conducted by mixing *st*-PMMA6K−Au NPs with *it*-PMMA3K−QDs in a 1:1 particle ratio in acetonitrile. Stereochemical formation of PMMA triple-helices was then observed leading to the formation of precipitates in analogy with the original Au−Au nanoparticle experiments (Figure 5a). In agreement with earlier Au NP UV−vis studies, the emission spectrum of the stereocomplexed supernatant showed a complete reduction in the photoluminescence (PL) intensity, indicating that no free *it*-PMMA3K−QDs are present in solution (Figure 5b). In contrast, *it*-PMMA3K−QDs mixed with *it*-PMMA3K−Au NPs remained dispersed in acetonitrile at the same QD/AuNP ratio and retained a strong red emission peak with a partial decrease in intensity due to quenching by close-proximity Au NPs.

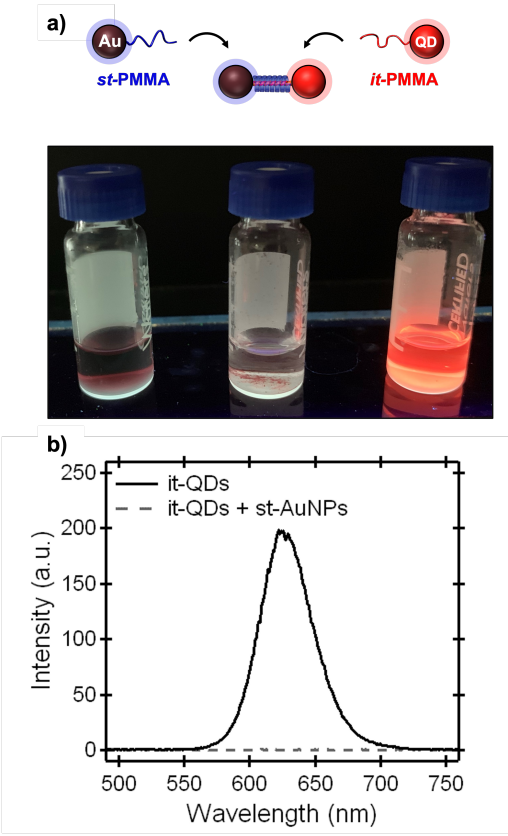


Figure 5. a) Schematic (top) and an image (bottom) of *st*-PMMA6K−Au NPs (left), stereocomplexed *it*-PMMA3K−QDs + *st*-PMMA6K−Au NPs (center) and red emitting *it*-PMMA3K−QDs (right) under irradiation. b) PL spectrum of *it*-PMMA3K−QDs and *it*-PMMA3K−QDs + *st*-PMMA6K−Au NPs.

2.4 Conclusion

In summary, we have described an effective and scalable strategy for the assembly of *st*- and *it*-PMMA nanoparticle building blocks via triple-helix formation. The *st*- and *it*-PMMA ligands prepared in this study can be easily synthesized from commodity materials and can greatly expand the utility of nanoparticle assemblies. The resulting stereocomplexed nano- particle systems are thermally reversible in organic solvents with similar optical and assembly behavior to previous DNA- based coupling strategies. Furthermore, a variety of hybrid nanoparticle structures can be formed by combining stereo- specific PMMA Au NPs, Au NRs, and QDs. The data presented here provide the first example of nanoparticle assembly

via synthetic multistranded helices and demonstrate an exciting new platform for nanoparticle coupling.

2.5 References

(1) Gabrys, P. A.; Zornberg, L. Z.; Macfarlane, R. J. *Small*, **2019**, *15*, 1805424.

(2) Park, D. J.; Zhang, C.; Ku, J. C.; Zhou, Y.; Schatz, G. C.; Mirkin, C. A. *Proc. Natl. Acad. Sci. U. S. A.* **2015**, *112*, 977.

(3) Auyeung, E.; Morris, W.; Mondloch, J. E.; Hupp, J. T.; Farha, O. K.; Mirkin, C. A. *J. Am. Chem. Soc.* **2015**, *137*, 1658.

(4) Ross, M. B.; Mirkin, C. A.; Schatz, G. C. *J. Phys. Chem. C*, **2016**, *120*, 816.

(5) Boal, A. K.; Ilhan, F.; Derouchey, J. E.; Thurn-Albrecht, T.; Russell, T. P.; Rotello, V. M. *Nature* **2000**, *404*, 746.

(6) Lawrence, J.; Emrick, T. *ACS Appl. Mater. Interfaces*, **2016**, *8*, 2393.

(7) Lukach, A.; Liu, K.; Therien-Aubin, H.; Kumacheva, E. *J. Am. Chem. Soc.* **2012**, *134*, 18853.

(8) Mirkin, C. A.; Letsinger, R. L.; Mucic, R. C.; Storhoff, J. J. *Nature*, **1996**, *382*, 607.

(9) Park, S. Y.; Lytton-Jean, A. K. R.; Lee, B.; Weigand, S.; Schatz, G. C.; Mirkin, C. A. *Nature*, **2008**, *451*, 553.

(10) Laramy, C. R.; O'Brien, M. N.; Mirkin, C. A. *Nat. Rev. Mater.* **2019**, *4*, 201.

(11) Seo, S. E.; Girard, M.; Olvera de la Cruz, M.; Mirkin, C. A. *Nat. Commun.* **2018**, *9*, 4558.

(12) Yang, D.; Hartman, M. R.; Derrien, T. L.; Hamada, S.; An, D.; Yancey, K. G.; Cheng, R.; Ma, M.; Luo, D. *Acc. Chem. Res.* **2014**, *47*, 1902.

(13) Zhang, J.; Santos, P. J.; Gabrys, P. A.; Lee, S.; Liu, C.; Macfarlane, R. J. *J. Am. Chem. Soc.* **2016**, *138*, 16228.

(14) Ye, X.; Zhu, C.; Ercius, P.; Raja, S. N.; He, B.; Jones, M. R.; Hauwiller, M. R.; Liu, Y.; Xu, T.; Alivisatos, A. P. *Nat. Commun.* **2015**, *6*, 10052.

(15) Santos, P. J.; Cao, Z.; Zhang, J.; Alexander-Katz, A.; Macfarlane, R. J. *J. Am. Chem. Soc.* **2019**, *141*, 14624.

(16) Santos, P. J.; Cheung, T. C.; Macfarlane, R. J. *Nano Lett.* **2019**, *19*, 5774.

(17) Nayak, S.; Horst, N.; Zhang, H.; Wang, W.; Mallapragada, S.; Travesset, A.; Vaknin, D. *J. Phys. Chem. C*, **2019**, *123*, 836.

(18) Wang, Y.; Santos, P. J.; Kubiak, J. M.; Guo, X.; Lee, M. S.; Macfarlane, R. J. *J. Am. Chem. Soc.* **2019**, *141*, 13234.

(19) Yashima, E.; Maeda, K.; Iida, H.; Furusho, Y.; Nagai, K. *Chem. Rev.* **2009**, *109*, 6102.

(20) Ren, J. M.; Knight, A. S.; van Ravensteijn, B. G. P.; Kohl, P.; Bou Zerdan, R.; Li, Y.; Lunn, D. J.; Abdilla, A.; Qiao, G. G.; Hawker, C. J. *J. Am. Chem. Soc.* **2019**, *141,* 2630.

(21) Hatada, K.; Kitayama, T. Structurally Controlled Polymer- izations of Methacrylates and Acrylates. Polym. Int. 2000, 49, 11−47. (22) Kumaki, J.; Kawauchi, T.; Okoshi, K.; Kusanagi, H.; Yashima, E. *Angew. Chem., Int. Ed.* **2007**, *46*, 5348.

(22) Kumaki, J.; Kawauchi, T.; Okoshi, K.; Kusanagi, H.; Yashima, E. *Angew. Chem., Int. Ed.* **2007**, *46*, 5348.

(23) Christofferson, A. J.; Yiapanis, G.; Ren, J. M.; Qiao, G. G.; Satoh, K.; Kamigaito, M.; Yarovsky, I. *Chem. Sci.* **2015**, *6*, 1370.

(24) Ren, J. M.; Lawrence, J.; Knight, A. S.; Abdilla, A.; Zerdan, R. B.; Levi, A. E.; Oschmann, B.; Gutekunst, W. R.; Li, Y.; McGrath, A. J.; Bates, C. M.; Qiao, G. G.; Hawker, C. J. *J. Am. Chem. Soc.* **2018**, *140*, 1945.

(25) Kohsaka, Y.; Kurata, T.; Kitayama, T. *Polym. Chem.* **2013**, *4*, 5043.

(26) Kohsaka, Y.; Kurata, T.; Yamamoto, K.; Ishihara, S.; Kitayama, T. *Polym. Chem.* **2015**, *6*, 1078.

(27) Aoshima, H.; Satoh, K.; Kamigaito, M. *ACS Macro Lett.* **2013**, *2*, 72.

(28) Zheng, N.; Fan, J.; Stucky, G. D. *J. Am. Chem. Soc.* **2006**, *128*, 6550.

(29) Macfarlane, R. J.; Lee, B.; Jones, M. R.; Harris, N.; Schatz, G. C.; Mirkin, C. A. *Science*, **2011**, *334*, 204.

(30) Jones, M. R.; Macfarlane, R. J.; Lee, B.; Zhang, J.; Young, K. L.; Senesi, A. J.; Mirkin, C. A. *Nat. Mater.* **2010**, *9*, 913.

(31) Zhang, Y.; Lu, F.; Yager, K. G.; Van Der Lelie, D.; Gang, O. A *Nat. Nanotechnol.* **2013**, *8*, 865.

(32) Bae, W. K.; Char, K.; Hur, H.; Lee, S. *Chem. Mater.* **2008**, *20*, 531.

Chapter 3. A Si-H Functionalized Initiator for the Precise Synthesis of Heterotelechelic Polysiloxanes

3.1 Abstract

Silicones are high value polymers that exhibit properties which are unmatched by organic polymers due in large part to the unusual behavior of the Si-O bond. Although monofunctional or symmetric linear polysiloxanes with the same functional group at both termini are commonly made on industrial scales, very few reports have explored their heterotelechelic analogues (two different functional groups) due to limitations in the asymmetric polymerization of cyclicsiloxane oligomers. Here, we present a versatile and scalable strategy to obtain heterotelechelic PDMS through the anionic ring opening polymerization of hexamethylcyclotrisiloxane (D_3) initiated by a bifunctional H-$(SiOMe_2)_4$-OH oligomer after lithiation with LiHMDS, a commonly used non-nucleophilic base. Careful control of the reaction conditions followed by termination with various silyl chlorides yields PDMS with both Si-H moieties and a wide range of chain ends (eg: alkyl chlorides, methacrylates and norbornenes) with high fidelities (Fig. 2). Further end-functionalization by hydrosilylation with terminal olefins (alcohols, esters, and epoxides) opens new opportunities for asymmetric PDMS materials for use in advanced materials applications.

3.2 Introduction

The preparation of synthetic polymers with precise structures, compositions, and functions is a grand challenge for polymer and material chemists. The advent of convenient and robust synthetic protocols for living polymerizations (e.g. ATRP, RAFT, ROMP)[1-4] allow the preparation of well-defined macromolecules on multigram scales rather than complex

mixtures. Recent studies in this area directed towards the development of polymers with control over monomer sequence, molecular weight distribution (*Đ*), architecture, and chain-ends have shown exquisite structure-property relationships and functions complementary to biopolymers found in nature.[6-12]

Silicones are high value polymers that exhibit properties which are unmatched by organic polymers including their very low T_g, low surface energy, high interfacial activity, high thermal stability, high gas permeability and excellent biocompatibility.[13] These unique properties arise from the substantial dipolar character of Si–O–Si bonds situated along a polysiloxane backbone, coupled with an ability to readily control the organic substituents at each silicon atom.[14] However, unlike recent trends in organic polymers, the vast majority of commercial silicones are complex mixtures. This is due in large part to thermodynamically favored acid or base-catalyzed metathesis/redistribution of Si-O bonds along the polymer backbone that occur during the polymerization of siloxane monomers, leading to the formation of undesired cyclic oligomers and loss of structural integrity.[15]

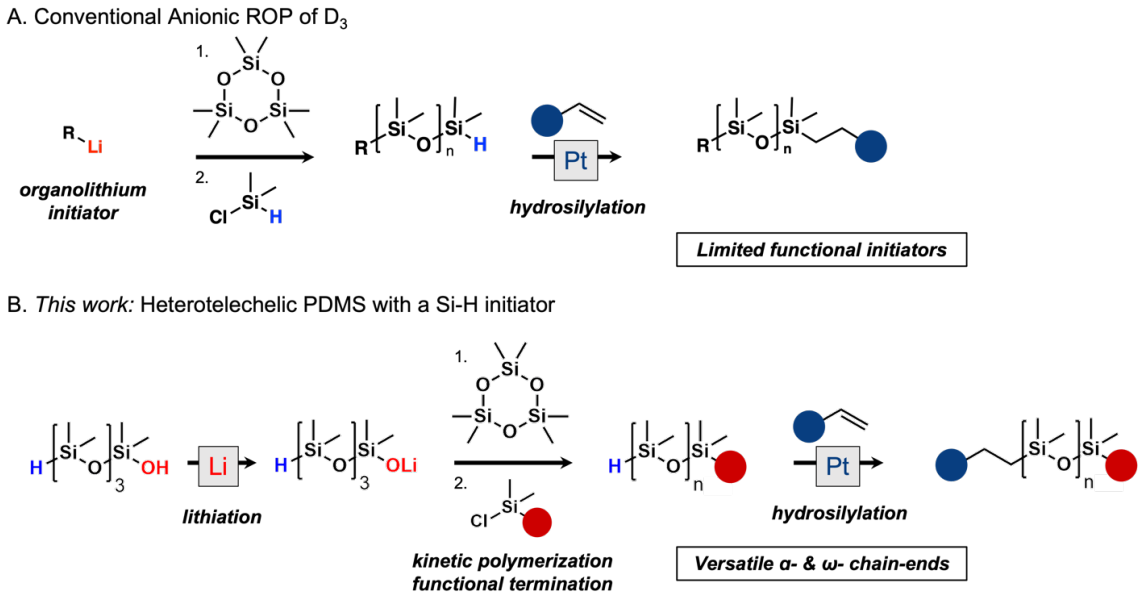
While many strategies for have been developed for the synthesis of precise silicones, the most successful approach is kinetically controlled anionic ring opening polymerization (AROP) of strained tricyclosiloxane monomers initiated by organolithium compounds or lithium silanoates.[16,17] Under kinetic control, propagation proceeds much faster than redistribution processes allowing polysiloxanes with narrow molecular weight distributions and tailored microstructures if the polymerization is quenched at low conversions.[18] In addition, well-defined polysiloxanes selectively functionalized at one chain end may be obtained by using functional chlorosilane terminators.[19,20]

Although a myriad of chain-ends for narrow-disperse PDMS can be accessed through termination and subsequent post-polymerization transformations, only a few reports have explored the use of functional initiators for polysiloxanes.[21,22] Each functionalized initiator molecule will produce a macromolecule with the desired functionality at the chain end regardless of molar mass, facilitating the synthesis of telechelic materials, functionalized block copolymers and star-branched polymers with functional groups at each arm terminus.[23] Furthermore, combining functional initiation and termination allows the synthesis of heterotelechelic polymers with different functional groups at each chain-end that have widespread applications in protein conjugation, imaging, crosslinking, and self-assembly.[24-30] Although the synthesis heterotelechelic polysiloxanes initiated vinyl and methacrylate silanoates have been reported, most functionalities of interest such as hydroxyl, carboxyl, or amino require a protecting group as they are not stable in the presence of organolithium reagents.[21,31-35] Furthermore, subsequent deprotection conditions are highly limited for end-functionalized polysiloxanes as any exposure to acid or base will catalyze equilibration reactions and lead to loss of structural control. Thus, new chemistry needs to be developed to permit the synthesis of precise heterotelechelic silicone structures without degradation via redistribution.

The Si-H group provides a synthetic handle that permits exquisite control at the silicon atom.[36] The reactivity of Si-H groups can be unlocked by transition metal such as Pt, Pd and Rh, and Lewis acids such as $B(C_6F_5)_3$, catalyzing their conversion to Si-C or Si-O bonds under mild, practical conditions for the synthesis of structurally controlled polysiloxanes. In particular, platinum-based hydrosilylations of Si-H groups with terminal olefins is one of the most important reactions in the silicone industry.[37,38] In addition, commercially available well-

defined, monofunctional silicones with a wide variety of chain-ends are produced by AROP and subsequent hydrosilylation of Si-H terminated polysiloxanes (Scheme 1, a).[13,21,39]

Although Si-H moieties are known to undergo hydrolysis or nucleophilic substitution under basic conditions, some literature reports remarkably indicate their stability during kinetically controlled AROPs with favorable propagation rates.[40,41] In this work, we investigate the AROP of hexamethylcyclotrisiloxane (D_3) initiated with Si-H functionalized lithium silanoate. Through careful control of the polymerization and redistribution kinetics allows for the retention of Si-H groups with high chain-end fidelities. The introduction of Si-H through initiation in combination with termination with various chlorosilanes gives a versatile and scalable strategy to obtain heterotelechelic PDMS with a wide variety of functional chain-ends. Further end-functionalization by hydrosilylation with terminal olefins opens a diverse plethora of well-defined, asymmetric poly(dimethylsiloxane) (PDMS) materials for use in advanced materials applications.



Scheme 1. Synthesis of α- and ω-functionalized heterotelechelic PDMS building blocks through initiation with a Si-H functional lithium silanoate in combination with functional termination, followed by the subsequent hydrosilylation of α-Si-H groups.

3.3 Results and Discussion

To investigate the AROP initiation of D_3 with a Si-H functionalized lithium silanoate, we first synthesized a discrete bifunctional octamethyltetrasiloxanol (H-Si_4-OH) according to the method reported by Meijer and coworkers.[42] The synthesis starts with the ring-opening of commercially available D_3 with chlorodimethylsilane in acetonitrile with a catalytic amount of dimethylformamide (DMF) to generate chloro-octamethyltetrasiloxane (H-Si_4-Cl) in followed by hydrolysis under basic conditions. This scalable synthesis can be performed in large quantities (~100g, > 60 % yield) with high structural purity from industrial purification techniques.

The conditions of the initiation step are of prime importance for the anionic polymerization of D_3 as a low rate of ring opening limits kinetic control.[18,43] One method to prepare well-defined polysiloxanes is the "seeding technique" were the lithium silanoate

initiator is first formed in a non-polymer solvent such as hexanes or benzene. Polymerization only occurs following the addition of polar complexing or chelating additives for alkali metal ions, allowing better solvation of the silanoate centers. As the Si-H group is known to undergo nucleophilic substitution under basic conditions and/or in the prescience of silaphilic nucleophiles, we first examined the lithiation of H-Si_4-OH with various organolithium bases in hexanes. A 1:1 stoichiometry of the lithium agent to H-Si_4-OH was employed as excess base may compete to ring open D_3, whereas leftover Si-OH may catalyze condensation side reactions during the polymerization.[31] The lithium base was allowed to react with H-Si_4-OH in hexanes for 5 minutes prior to the addition of D_3 and DMF to promote the polymerization. The AROPs were then quenched with methacryloxypropyldimethylchlorosilane (MAPrSiCl) after 30 minutes to examine the structure of the α- and ω- chain ends. As shown in Appendix B (Figure B4), AROPs utilizing strong organolithium agents such as *n*-BuLi showed a mixture of Si-H, Si-PrMA, and Si-*n*-Bu chain-ends likely due to nucleophilic attack of Si-H and Si-O bonds in H-Si_4-OH. Thus, we turned our attention to lithium bis(trimethylsilyl)amide as a sterically hindered non-nucleophilic base.[44] In contrast to *n*-BuLi, the ^{1}H and ^{29}Si NMR of AROPs with LiHMDS showed only Si-H, Si-PrMA chain ends with a 0.9:1 integration ratio, indicating the selective formation a lithium octamethyltetrasilanoate (H-Si_4-OLi) initiating species.

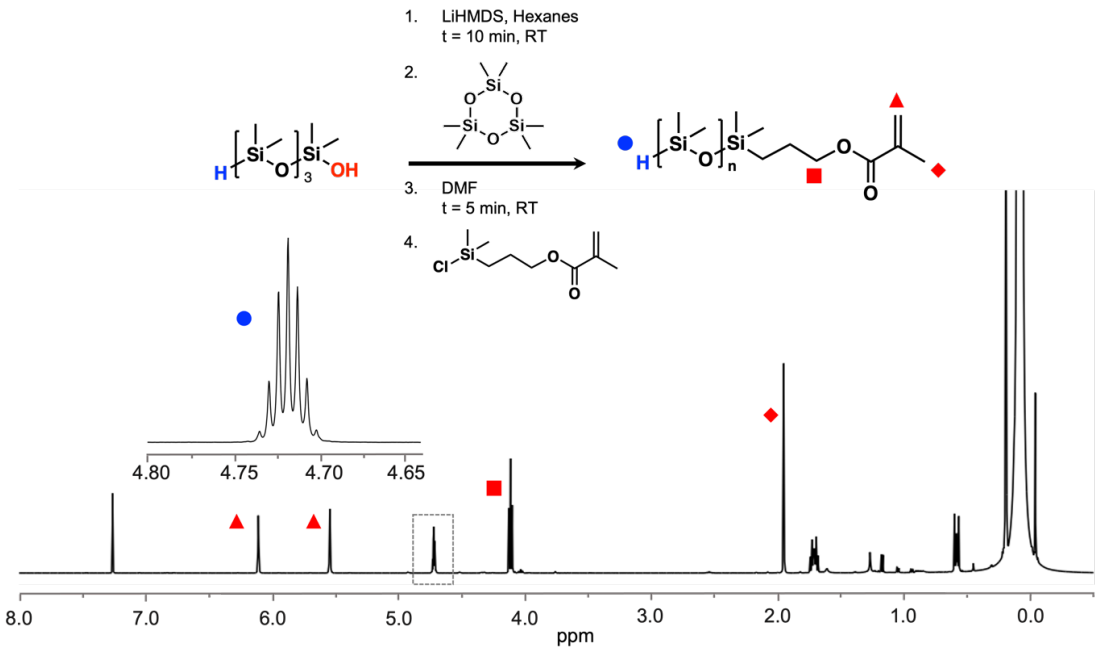


Figure 1. a) AROP conditions of D_3 initiated H-Si_4-OLi with LiHMDS. b) ^{1}H NMR trace confirming the presence of Si-H and Si-PrMA chain ends.

In addition to the enhanced reactivity of cyclotrisiloxanes, the kinetics of anionic polymerization is strongly affected by ion-ion, ion-siloxane and additive-ion association.[18,43] The active propagation center during the polymerization is the silanoate ion pair that may form unreactive aggregates that slow down the polymerization kinetics depending on the polarity of the medium. The course of initiation of siloxane AROPs is also particularly affected by ion association as ionic species appear in both the initiator and the active propagating center.[45,46] In order for kinetic polymerizations with narrow molecular weight distributions ($Đ < 1.3$) to be achieved, the activity of the living lithium silanoate centers must be properly adjusted by the addition of polar promoters. To examine the impact of solvent polarity on AROPs of D_3 initiated by H-Si_4-OLi, we employed either DMF or THF as polar promoters to enhance the polymerization kinetics. In particular, very fast polymerization kinetics were observed when 15 wt% DMF (relative to hexanes) was used to promote the

polymerization, achieving > 70% conversion in 30 minutes. Size exclusion chromatography analysis (SEC) of polymerizations quenched with MAPrSiCl at varying time points showed that narrow dispersity ($Đ$ < 1.3) was maintained at high conversions, indicating the living nature of the system (Figure 2). In contrast, no polymerization was observed when 15wt% THF was added despite THF-Li^+ interactions commonly utilized to promote AROP of D_3 in previous literature.[18,43]

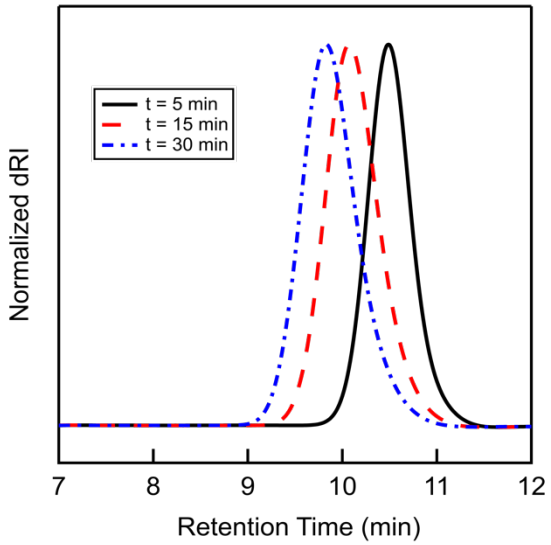


Figure 2. SEC-RI trace in chloroform of D_3 polymerizations initiated by H-Si_4-OLi with DMF as a promoter after various reaction times (30 – 77% conversion, M_n^{SEC} = 1.9 – 4.4 kDa, $Đ$ < 1.3). PDMS traces show negative RI values in chloroform and have been reversed for clarity.

Although narrow molecular weight distributions are achieved for kinetically controlled polymerizations of D_3, a number of side reactions such as backbiting and/or inter-chain exchange may still occur that do not significantly impact the dispersity of the system. In particular, Haddleton and coworkers revealed through matrix-assisted laser desorption ionization time-of-flight mass spectrometry (MALDI-ToF) that under living polymerization conditions of D_3 in THF, significant equilibrium interchain-exhange processes such as the

exchange of terminal silanoate units occur albeit slowed compared to the rate of polymerization, resulting in a trimodal molecular weight distribution as opposed to monomodal.[47] Narrow dispersity is maintained in these polymerizations despite chain-end scrambling as the Li^+ promoted siloxane-silanoate redistribution mechanism favors propagating chain termini.[48] MALDI-ToF analysis shown in Figure 4 of D_3 initiated by H-Si_4-OLi in hexanes/DMF and quenched with MAPrSiCl showed complex molecular weight distributions stemming from PDMS with three different terminal structures: the desired heterotelechelic H-PDMS-MA, as well as telechelic H-PDMS-H and MA-PDMS-MA. A trimodal mass distribution for H-PDMS-MA similar to those described by Haddleton was also observed.[47] Furthermore, the relative peak intensities for H-PDMS-H and MA-PDMS-MA increased with longer reaction times relative to H-PDMS-MA, indicating their formation by specific redistribution reactions occurring during propagation as opposed to the initiation step. Based on the MALDI-ToF molecular weight distributions of each species, it is likely that two inter-molecular chain-end exchange processes occur during the polymerization – one between propagating silaonate groups to produce H-PDMS-MA with different degrees of polymerization (DP) and the other resulting in the transfer of a terminal dimethylsilyl ($HSiMe_2$) group (Figure B5). A similar phenomenon was reported by Fuchise and coworkers for organocatalytic ring opening polymerizations of cyclotrisiloxanes initiated by Si-H functional silanols, with MALDI-ToF distributions indicating the inter-molecular transfer of $HSiMe_2$ was favored. The inter-molecular exchange between Si-H and Si-OLi chain-ends is likely facilitated by the preferential interaction of Li^+ counterions with the dimethylsilyl chain-end, as lithium *n*-butoxypropyloctamethyltetrasilanoate (*n*-BuOPr-Si_4-OLi) initiated AROPs

only showed evidence of redistribution reactions between propagating silanoate termini (Figure B10).

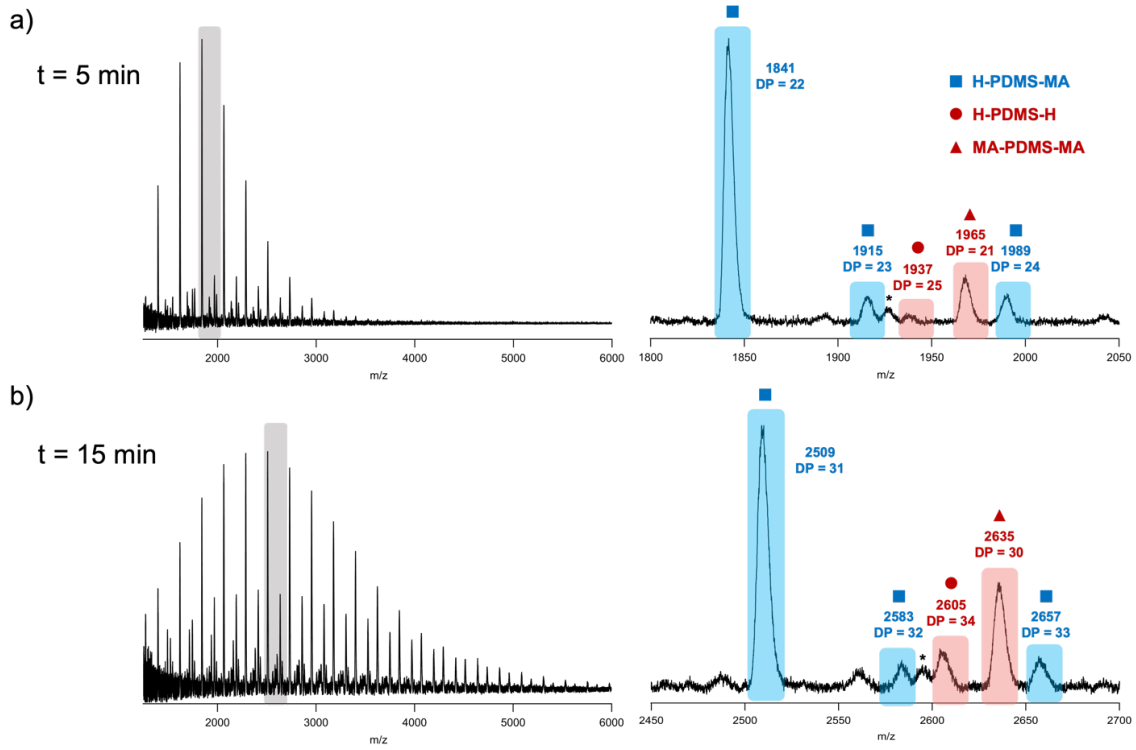


Figure 3. MALDI-ToF mass spectra of H-PDMS-MA after a) 5 minutes (30% conversion) and b) 15 minutes (52% conversion) polymerization times showing the chain-end exchange of the Si-OLi and Si-H chain ends during propagation.

Since the ring opening of cyclosiloxanes is unimolecular with respect to the active silanoate chain-ends, one would expect that the redistribution of chain-termini would become unimportant relative to propagation as the concentration of active ends decreased.[48] As a consequence, formation of high molecular weight polysiloxanes from D_3 proceed with minimal redistribution. In contrast, low molecular weight polysiloxanes where the concentration of active ends is much higher would produce redistributed products under the same conditions. Thus, higher molecular weight H-PDMS-MA was targeted by increasing the equivalents of D_3 relative to H-Si_4-OLi and the MALDI-ToF molecular weight distribution

was examined. As shown in Figure 4, AROPs initiated with a [H-Si$_4$-OLi]:[D$_3$] ratio of 1:92 showed significantly decreased intensities of H-PDMS-H and MA-PDMS-MA biproducts with high α- and ω- H-PDMS-MA chain-end fidelities relative to polymerizations targeting lower molecular weights quenched at similar conversions.

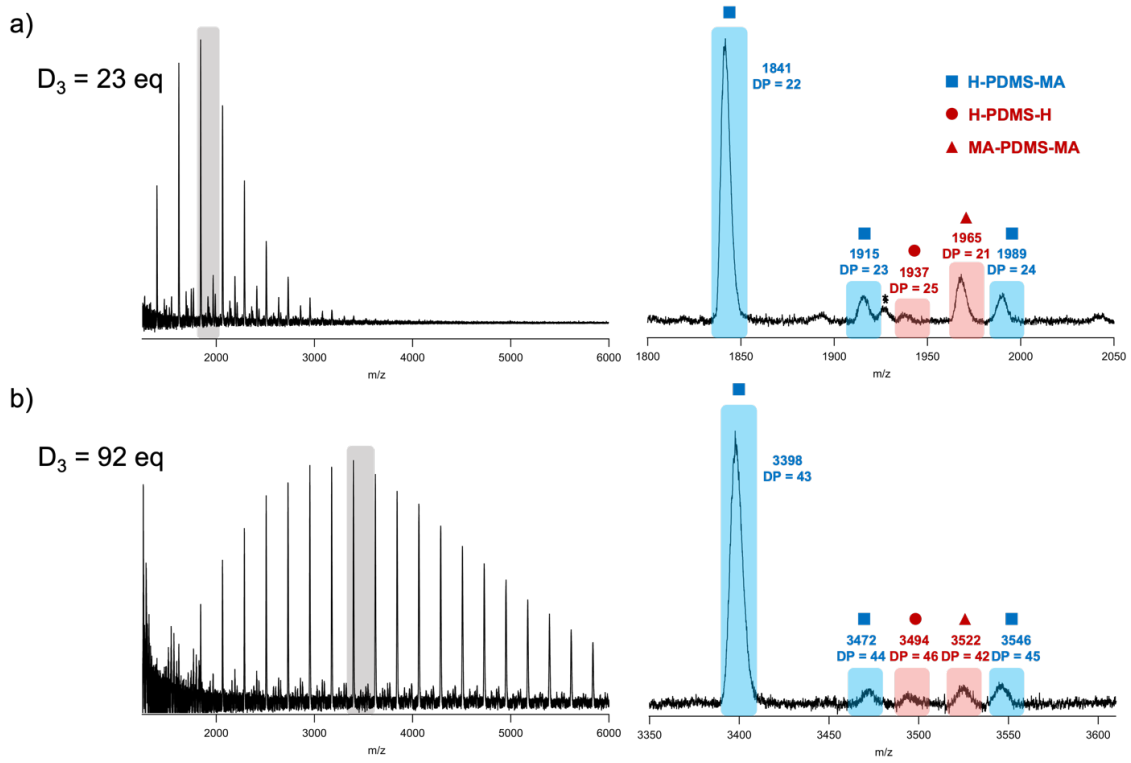


Figure 4. MALDI-ToF mass spectra of H-PDMS-MA after 5 minutes reaction time (20-30% conversion) with a) 23 equivalents of D$_3$ and b) a) 92 equivalents of D$_3$ showing lower degrees of exchange between Si-OLi and Si-H chain ends when targeting higher molecular weights.

With D$_3$ polymerization conditions with minimal chain-end scrambling in hand, we sought to expand the potential of α- and ω- chain-ends accessible by combining functional termination with post-polymerization transformation of Si-H groups from initiation. First, a wide variety of functional groups were installed by quenching D$_3$ AROPs initiated by H-Si$_4$-OLi with commercially available hydride-, vinyl-, chloropropyl-, and norbornene-substituted chlorosilanes (Figure 5, b). Similar to earlier polymerizations quenched by MAPrSiCl,

quantitative terminations of propagating lithium silanoate species were observed with minimal chain-end scrambling. It is important to note that higher polymerization conversions could be achieved in the case of termination with chlorodimethylsilane as chain-end scrambling during propagation still produces pure telechelic bis-hydride capped PDMS (H-PDMS-H). Furthermore, α-Si-H chain ends introduced via initiation (or ω-Si-H by termination) can be selectively modified post-polymerization under mild conditions through platinum-based hydrosilylations with terminal olefins.[37,38] As shown in Figure 5, hydrosilylations of Si-H capped heterotelechelic PDMS with Karstedt's catalyst allowed for quantitative α- chain-end transformations with a myriad of functional moieties including mono and difunctional alcohols, epoxides, trialkoxysilyl groups and esters in a single step without the use of protecting groups. It is important to note that platinum hydrosilylation reactions can remarkably tolerate a variety of functionalities including nitro, cyano, amine, sulfonate, phenol, ether, thioether, phenylthiol and perfluoroalkyl groups.[38,49,50] The diverse plethora of α- and ω- functional end groups available via H-Si_4-OLi initiated D_3 polymerizations opens new opportunities for orthogonal transformations at each chain-end including epoxide opening, ROP, controlled radical polymerizations, ROMP, surface functionalization, thiol-ene click reactions, and nucleophilic substitutions.[13, 51-62]

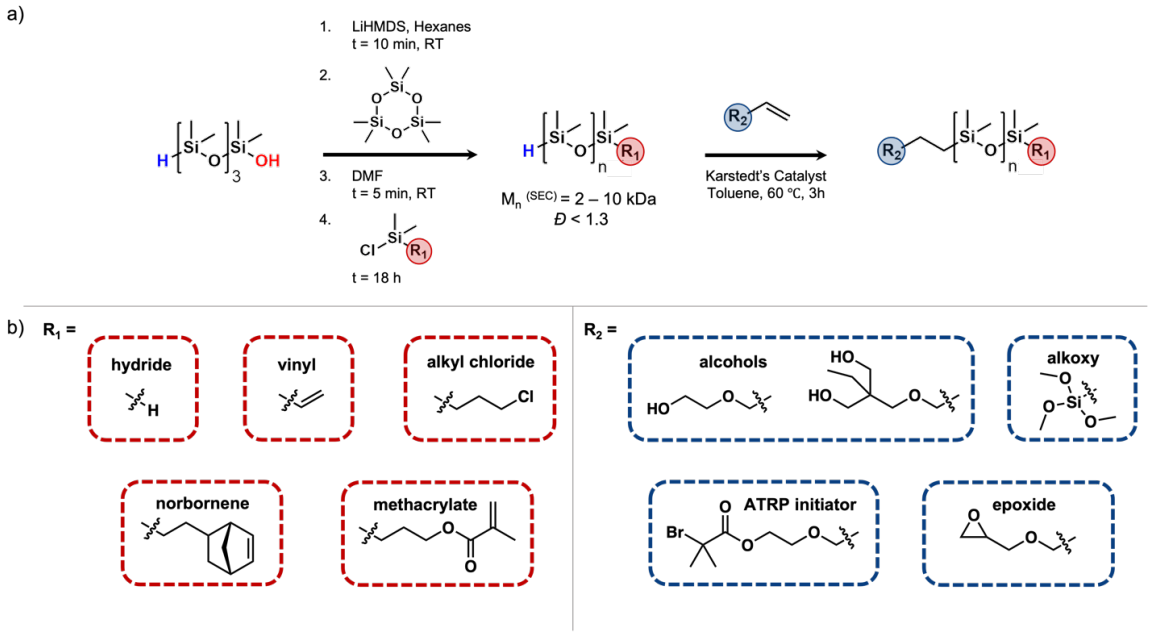


Figure 5. a) Synthetic scheme for the preparation of α- and ω- heterotelechelic PDMS materials by combining functional initiation and termination followed by hydrosilylation of Si-H groups. b) Substrate scope of α- and ω- functional groups explored in this work.

To expand the utility of α- and ω- heterotelechelic PDMS materials, we explored their use as building blocks in crosslinked silicone networks. In particular, networks formed from tetrahedron-like polymeric crosslinkers have gained significant interest due to their ideal homogeneous structure with minimal spatial homogeneities that inhibit their mechanical strength and elasticity.[63-66] As a proof of concept, tetrahedral PDMS-norbornene crosslinkers were synthesized via hydrosilylation with tetrakis (vinyl dimethylsiloxy)silane and Karstedt's catalyst. The terminal norbornene groups were then crosslinked via a light-driven thiol-ene chemistry with highly functionalized thiolated PDMS in an ambient atmosphere (Figure 6, b). Efficient curing was achieved with a thick, transparent crosslinked film formed after irradiating with a UV nail lamp. It is important to note however that the thiolated PDMS structure in this initial experiment is highly disperse, and future work will explore well-

defined tetrahedral PDMS-thiol macromonomers that decrease the degree of freedom in the microconnected network.[63] Furthermore, exchanging α- and ω- hetereotelechelic PDMS chains ends may open new pathways for A-B type connected crosslinked networks that limit self-reaction.

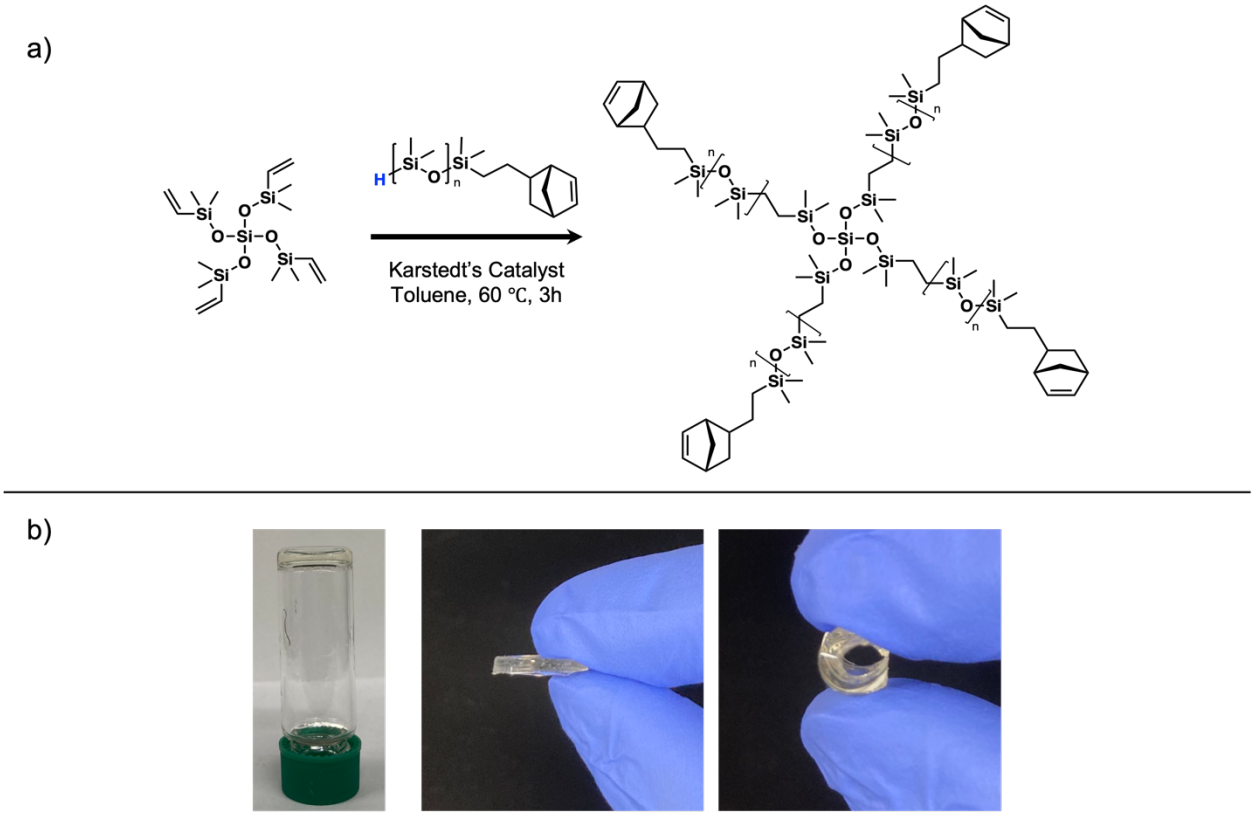


Figure 6. a) Formation of tetrahedral PDMS-Norbornene crosslinkers by hydrosilylation of heterotelechelic H-PDMS-Norbornene and b) UV-driven thiol-Norbonene crosslinking of PDMS films.

3.4 Conclusions & Future Work

In this work, a versatile and scalable strategy to obtain well defined α-,ω-heterotelechelic PDMS with a variety of functional groups through the anionic ring opening polymerization of D_3 initiated by a bifunctional H-$(SiOMe_2)_4$-OH oligomer with LiHMDS and subsequent Pt-catalyzed hydrosilylation post-polymerization modifications under mild

conditions. Kinetic control of the polymerization by targeting higher molecular weights and quenching the polymerizations at low conversions with various functional chlorosilanes allows α-Si-H groups to be retained with high-chain-end fidelities by minimizing intermolecular transfer of dimethylsilyl end groups. The utility of α-Si-H functional heterotelechelic PDMS was demonstrated through the preparation of tetrahedral PDMS-Norbornene crosslinkers and their photo-driven thiol-ene gelation. In future work, well-defined tetrahedral PDMS-thiol macromonomers that can form A-B crosslinks tetrahedral PDMS-Norbornenes will be employed to the degree of freedom in the microconnected network and limit defects that impact mechanical properties. It is also interesting to note that no Si-H bond scission was observed during chain-scrambling of Si-OLi chain-ends at higher conversions as only the adjacent Si-O units were cleaved. With these important factors in mind, it may be possible to deliberately design novel Si-H functional silane-based initiating systems which may eliminate α-chain-end exchange processes. These systems are currently under investigation and should favor kinetic propagation of strained cyclotrisiloxanes, thereby significantly increasing the yield and scalability of highly pure α-,ω- heterotelechelic polysiloxanes prepared via this method.

3.5 References

(1) Boyer, C.; Corrigan, N. A.; Jung, K.; Nguyen, D.; Nguyen, T.-K.; Adnan, N. N. M.; Oliver, S.; Shanmugam, S.; Yeow, J. *Chem. Rev.* **2016**, *116*, 1803.

(2) Anastasaki, A.; Nikolaou, V.; Nurumbetov, G.; Wilson, P.; Kempe, K.; Quinn, J. F.; Davis, T. P.; Whittaker, M. R.; Haddleton, D. M. *Chem. Rev.* **2016**, *116*, 835.

(3) Moad, G.; Rizzardo, E.; Thang, S. H. *Chem. - Asian J.* **2013**, *8*, 1634.

(4) Bielawski, C. W.; Grubbs, R. H. *Prog. Polym. Sci.* **2007**, *32*, 1.

(5) Grubbs, R. B.; Grubbs, R. H. *Macromolecules* **2017**, *50*, 6979.

(6) Lutz, J.-F.; Ouchi, M.; Liu, D. R.; Sawamoto, M. *Science* **2013**, *341*, 1238149.

(7) Rosales, A. M.; Segalman, R. A.; Zuckermann, R. N. *Soft Matter* **2013**, *9*, 8400.

(8) Lawrence, J.; Lee, S.-H.; Abdilla, A.; Nothling, M. D.; Ren, J. M.; Knight, A. S.; Fleischmann, C.; Li, Y.; Abrams, A. S.; Schmidt, B. V. K. J.; Hawker, M. C.; Connal, L. A.; McGrath, A. J.; Clark, P. G.; Gutekunst, W. R.; Hawker, C. J. *J. Am. Chem. Soc.* **2016**, *138*, 6306.

(9) Gentekos, D. T.; Dupuis, L. N.; Fors, B. P. *J. Am. Chem. Soc.* **2016**, *138*, 1848.

(10) Polymeropoulos, G.; Zapsas, G.; Ntetsikas, K.; Bilalis, P.; Gnanou, Y.; Hadjichristidis, N. *Macromolecules* **2017**, *50*, 1253.

(11) Konkolewicz, D.; Monteiro, M. J.; Perrier, S. *Macromolecules* **2011**, *44*, 7067.

(12) Kim, J.; Jung, H. Y.; Park, M. J. *Macromolecules,* **2020**, *53,* 746.

(13) Pouget, E.; Tonnar, J.; Lucan, P.; Lacroix-Desmazes, P.; Ganachaud, F.; Boutevin, B.; *Chem. Rev.* **2010**, *110*, 1233.

(14) Voronkov, M. G.; Mileshkevich, V. P.; Yuzhelevskii, Y. A. Studies in Soviet Science. The Siloxane Bond, Physical Properties and Chemical Transformations, Plenum Publishing Corporation, New York, USA **1978**.

(15) Graiver, D.; Farminer, K. W.; Narayan, R. *J. Polym. Environ.* **2003**, *11*, 129.
(16) Frye, C. L.; Salinger, R. M.; Fearon, F. W. G.; Klosowski, J. M.; DeYoung, T. *J. Org. Chem.* **1970**, *35*, 1308.

(17) Carlotti, S.; Peruch, F.; *Anionic Polymerization: Principles, Practice, Strength, Consequences and Applications*, ed. Hadjichristidis, N.; Hirao, A. Springer, Japan, Tokyo, **2015**.

(18) Chojnowski, J. *J. Inorg. Organomet. Polym.* **1991**, *1*, 299.

(19) Peters, M. A.; Belu, A. M.; Linton, R. W.; Dupray, L.; Meyer, T. J.; DeSimone, J. M. *J. Am. Chem. Soc.* **1995**, *117*, 3380.

(20) Chojnowksi, J.; Cyrpryk, M.; Fortuniak, W.; Ścibiorek, M.; Rózga-Wijas, K. *Macromolecules,* **2003**, *36,* 3890.

(21) Goff, J.; Sulaiman, S.; Arkles, B. *Molecules,* **2021**, *26*, 2755.

(22) Fuchise, K.; Kobayashi, T.; Sato, K.; Igarashi, M. *Polym. Chem.* **2020**, *11*, 7625.

(23) Quirk, R. P.; Jang, S. H.; Yang, H.; Lee, Y. *Macromol. Symp.* **1998**, *132*, 281.

(24) Heredia, K. L.; Grover, G. N.; Tao, L.; Maynard, H. D. *Macromolecules* **2009**, *42*, 2360.

(25) Roth, P. J.; Jochum, F. D.; Zentel, R.; Theato, P. *Biomacromolecules,* **2010**, *11*, 238.

(26) Detering, L.; Abdilla, A.; Luehmann, H. P.; Williams, J. W.; Huang, L.-H.; Sultan, D.; Elvington, A.; Heo, G. S.; Woodard, P. K.; Gropler, R. J.; Randolph, G. J.; Hawker, C. J.; Liu, Y. *Mol. Pharmaceutics* **2021,** *18,* 1386.

(27) Brassinne, J.; Stevens, A. M.; Van Ruymbeke, E.; Gohy, J. F.; Fustin, C. A. *Macromolecules* **2013**, *46*, 9134.

(28) Hong, J.; Kwon, Y.; Kwon, M. S.; Cha, C. *ACS Appl. Polym. Mater.* **2022**, https://doi.org/10.1021/acsapm.1c01894

(29) Taribagil, R. R.; Hillmyer, M. A.; Lodge, T. P. *Macromolecules* **2010**, *43*, 5396.

(30) Matyjaszewski, K.; Tsarevsky, N. V. *Nat. Chem.* **2009**, *1*, 276.

(31) Suzuki, T. *Polymer,* **1989**, *30*, 333.

(32) Goff, J.; Sulaiman, S.; Arkles, B.; Lewicki, J. P. *Adv. Mater.* **2016**, *28*, 2393.

(33) Rheingans, O.; Hugenberg, N.; Harris, J. R.; Fischer, K.; Maskos, M. *Macromolecules* **2000**, *33*, 4780.

(34) Elkins, C. L.; Long, T. E. *Macromolecules,* **2004**, 6657.

(35) Greene, T. W.; Wuts, P. G. M. *Protective Groups in Organic Synthesis*, 3rd ed.; John Wiley & Sons: New York, 1999.

(36) Brook, M. A. *Chem. Eur. J.* **2018**, *24,* 8458.

(37) Marciniec, B.; Maciejewski, H.; Pietraszuk, P. P. *Hydrosilylation: A Comprehensive Review On Recent Advances*, Springer, Poland, **2013**.

(38) Brook, M. A. *Silicones. Silicon in Organic, Organometallic and Polymer Chemistry*, Wiley, New York, **2000**.

(39) Goff, J.; Kimble, E.; Arkles, B. *Progress in Silicones and Silicone-Modified Materials,* ACS Symposium Series, **2013**.

(40) Paulasaari, J. K.; Weber, W. P. *Macromolecules*, **1999**, *32*, 6574.

(41) Cai, G. P.; Weber, W. P. *Macromolecules*, **2000**, *33*, 8976.

(42) Lamers, B. A. G.; de Waal, B. F. M.; Meijer, E. W. *J. Polym. Sci.* **2020**, *59*, 1142.

(43) Maschke, U.; Wagner, T. *Makromol. Chem.* **1992**, *193*, 2453.

(44) Gray, M.; Snieckus, V.; Lebel, H. *Encyclopedia of Reagents for Organic Synthesis*, **2004**.

(45) Chojnowski J.; Mazurek, M.; *Makromol. Chem.* 1975, *176*, 2999.

(46) Mazurek, M.; Chojnowski, J. *Macromolecules* **1978**, *11*, 347.

(47) Haddleton, D. M.; Bon, S. A. F.; Robinson, K. L.; Emery, J.; Moss, I. *Macromol. Chem. Phys.* **2000**, *201*, 694.

(48) Fessler, W. A.; Juliano, P. C. *Ind. Eng. Chem. Prod. Res. Develop.* **1972**, *11*, 407.

(49) Marciniec, B. *Comprehensive Handbook on Hydrosilation*, Pergamon Press, Oxford, **1992**.

(50) Marciniec, B. *Hydrosilylation*, Springer, Dordrecht, **2009**, 3.

(51) Biria, S.; Malley, P. P. A.; Kahan, T. F.; Hosein, I. D. *ACS Macro. Lett.* **2016**, *5*, 1237.

(52) Rodwogin, M. C.; Spanjers, C. S.; Leighton, C.; Hillmyer, M. A.; *ACS Nano,* **2010**, *4*, 725.

(53) Shinoda, H.; Miller, P. J.; Matyjaszewski, K. *Macromolecules*, 2001, *34*, 3186.

(54) Miller, P. J.; Matyjaszewski K. *Macromolecules*, **1999**, *32*, 8760.

(55) Cushman, K.; Keith, A.; Tanaka, J.; Sheiko, S. S.; You, W. *Macromolecules*, **2021**, *54*, 8365.

(56) Liu, Q.; Nian, G.; Yang, C.; Qu., S.; Suo, Z. *Nat. Commun.* **2018**, *9*, 846.

(57) Novak, B. *Adv. Mater.* **1993**, *5*, 422.

(58) Nikolaev, A.; Richardson, P. M.; Xie, S.; Llanes, L. C.; Jones, S. J.; Nordness, O.; Wang, H.; Bazan, G. C.; Segalman, R. A.; Clément, R. J.; Read de Alaniz, J. *Macromolecules*, **2022**. *55*, 971.

(59) Lusterio, A.; Melendez-Zamudio, M.; Brook, M. A. *Ind. Eng. Chem. Res.* **2021**, *60*, 3830.

(60) Luo, Y.; Montarnal, D.; Kim, S.; Shi, W.; Barteau, K. P.; Pester, C. W.; Hustad, P. D.; Christianson, M. D.; Fredrickson, G. H.; Kramer, E. J.; Hawker, C. J. *Macromolecules* **2015**, *48*, 3422.

(61) Madsen, F. B.; Javakhishvili, I.; Jensen, R. E.; Daugaard, A. E.; Hvilsted, S.; Skov, A. L. *Polym. Chem.* **2014**, *5*, 7054.

(62) Gonzaga, F.; Yu, G.; Brook, M. A. *Chem. Commun.* **2009**, 1730.

(63) Sakai, T.; Matsunaga, T.; Yamamoto, Y.; Ito, C.; Yoshida, R.; Suzuki, S.; Sasaki, N.; Shibayama, M.; Chung, U. I. *Macromolecules* **2008**, *41*, 5379.

(64) Akagi, Y.; Matsunaga, T.; Shibayama, M.; Chung, U.; Sakai, T. *Macromolecules*, **2010**, *43*, 488.

(65) Arona, A.; Lin, T.-S.; Olsen, B. D. *Macromolecules*, **2022**, *55*, 4.

(66) Heine, D. R.; Grest, G. S.; Lorenz, C. D.; Tsige, M.; Stevens, M. J. *Macromolecules*, **2004**, *37*, 3857.

Chapter 4. PDMS-based Block Random Copolymers with Tunable Segregation Strengths

4.1 Abstract

"Block-random" copolymers-wherein one of more blocks is a random copolymer- is a useful variation of typical block copolymers with continuously variable physical properties and phase behaviors depending on their composition. We report herein the modular synthesis of PDMS-based block random copolymers though the copolymerization of methyl methacrylate (MMA) and a compatibilizing silicone-methacrylate co-monomer (MD'M-ALMA). As MMA/MD'M-ALMA copolymerizations from PDMS-Br macroinitiators show reactivity ratios near unity, the preparation of well-defined PDMS-*b*-P[MD'M-ALMA-*r*-MMA] libraries with could be prepared. The compatibility, glass transitions (T_g) and the segregation strengths of the PDMS-*b*-P[MD'M-ALMA-*r*-MMA] copolymers varied dramatically depending on MD'M-ALMA incorporation with materials ranging from viscous disordered liquids to glassy solids with well-ordered lamellar structures. The use of MD'M-ALMA random blocks provides a first step toward the design of low χ PDMS-based block copolymers as potential compatibilzers for silicone-organic blends.

4.2 Introduction

Blending polymers is a powerful technique to obtain materials with improved properties,[1-4] often at a lower cost than the design of novel monomers and/or polymerization routes. The exceptional properties of silicones,[5] like the chain flexibility imparted by the wide silicon-oxygen bond angle paired with high bond strength, are key drivers for investigating the preparation of polymer blends based on mixtures of silicones with a wide variety of

organic polymers.[6] These unique properties arise from the substantial dipolar character of Si–O–Si bonds situated along a polysiloxane backbone, coupled with an ability to readily control the organic substituents at each silicon atom.[7] This versatile molecular design toolbox provides excellent tunability over surface properties, the glass transition temperature, flexibility, biocompatibility, chemical resistance, and thermal/oxidative stability.[8] Consequently, many polysiloxane-based materials have been manufactured in the form of fluids, resins, and as crosslinked elastomers for thousands of commercial products ranging from high performance aerospace adhesives to pharmaceuticals and advanced biomedical devices.[9-15]

Although the unique nature of Si–O bonds gives rise to the enhanced properties of silicones, polysiloxanes are known to be highly immiscible with other polymers, limiting their processing in blended materials.[16] When incorporated into blends, macrophase separation usually yields undesirable mechanical properties, and although good dispersions can sometimes be obtained with careful control of mixing conditions, the resulting blends are often thermodynamically unstable and undergo further phase separation over time.[17] Strategies to compatibilize polysiloxanes with organic polymers are therefore needed to develop novel, hybrid blends for advanced materials applications.

The emulsification of immiscible polymer blends by the addition of an interfacial modifier can lead to controllable morphologies with good mechanical properties and thermal stability.[18] These modifiers, referred to as compatibilizers, are often BCPs where each block is miscible with one of the blend components.[19] BCP compatibilizers typically segregate to the interface between immiscible homopolymers, resulting in increased interfacial adhesion, decreased interfacial tension and domain size, and minimal coalescence during subsequent

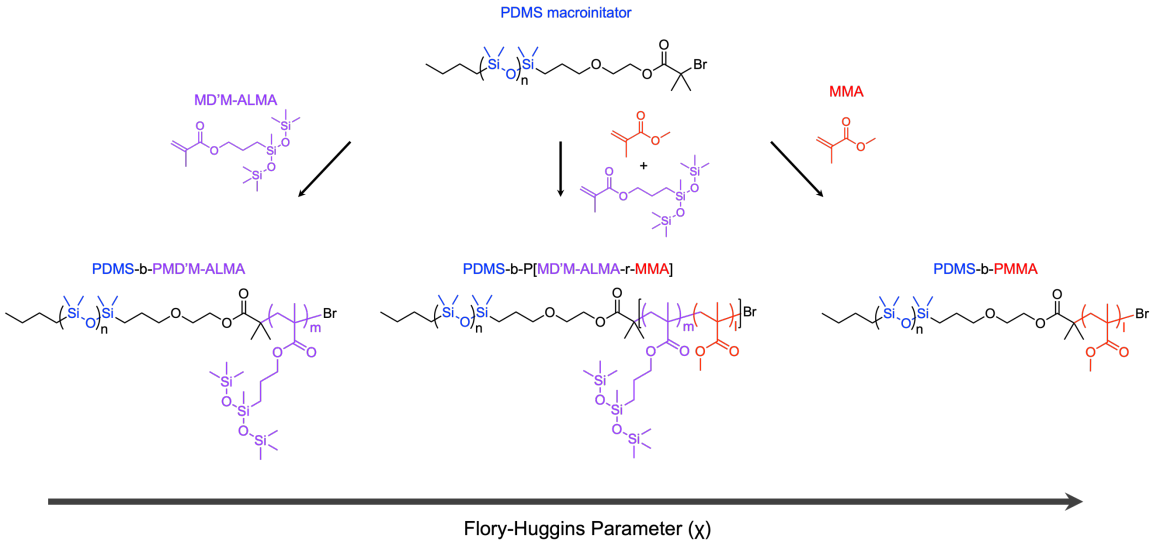
processing.[20,21] BCP additives that sufficiently reduce interfacial tension can also prevent brittle fracture due to debonding, allowing for toughening mechanisms such as shear yielding and crazing to occur while limiting crack propagation.[21] This interfacial toughening effect can be enhanced if the molecular weight of the copolymer is high enough to form entanglements with the surrounding homopolymer matrix.

Useful insights regarding the miscibility and phase behavior of polymers can be inferred from the Flory– Huggins interaction parameter, χ, which captures the binary interactions between chemically dissimilar polymers.[22] Polysiloxanes are generally incompatible with organic materials and silicone-based BCPs are widely studied as strongly segregating, high-χ systems.[23-26] While the high-χ nature of polysiloxanes with organic polymers facilitates the development of small features in applications such as photolithography and patterning, strong segregation presents a challenge for blend compatibilization.[9,27] Therefore, the development of low χ-polysiloxane-BCPs that enhance their compatibility with organic materials is required.

One method toward tuning BCP segregation strength is to incorporate compatibilizing comonomers into one or both blocks.[28,29] Controlling the comonomer composition allows for greatly reduced order-disorder transition temperatures ($T_{ODT}s$) at arbitrarily high molecular weights.[29,30] Composition profiles across the polymer chain length such as comonomer gradients, tapered block junctions or sequence-control also greatly impact block copolymer interfacial width and segmental mixing as well as enhance blend compatibilization.[31-35] A useful modification of these architectures are “block-random” copolymers, wherein one or more blocks have a random comonomer distribution, as the interblock interactions and

physical properties can be continuously modified through the random block's compostition.[28,29,36,37]

Here, we report the synthesis and self-assembly of block-random poly(dimethylsiloxane) (PDMS)-poly(methacrylate) copolymers with systematically tunable χ values by controlling the composition of the methacrylate block. Specifically, we incorporate heptamethyltrisiloxane-propyl methacrylate (MD'M-ALMA) as a compatibilizing comonomer with methyl methacrylate (MMA) through atom transfer radical polymerization (ATRP) from a PDMS macroinitiator (Scheme 1). The MD'M-ALMA/MMA monomer pair show reactivity ratios close to unity, allowing for gradient-free block copolymer libraries to be prepared across wide composition ranges. The low glass transition temperature of MD'M-ALMA monomer units and their enhanced compatibility with PDMS results in dramatically different physical properties and segregation strength of the final diblock random copolymers ranging from viscous disordered liquids to well-ordered lamellar structures.



Scheme 1. Random copolymerization-based tuning of the Flory-Huggins interaction parameter (χ) of PDMS-methacrylate block copolymers with MD'M-ALMA.

4.3 Results and Discussion

To develop a fundamental understanding of MD'M-ALMA's interactions with PDMS, we first developed a synthetic strategy to obtain PDMS-*b*-PMD'M-ALMA diblocks by ATRP – a versatile technique that produces polymers with low molar mass dispersities and high chain-end fidelity. In particular, near-symmetric PMD'M-ALMA-*b*-PDMS diblock copolymers were synthesized via chain-extension from a PDMS-Br macroinitiator. As shown in Figure 1, MD'M-ALMA was polymerized on a 4 g scale from 10k PDMS-Br utilizing Cu(I) catalyzed ATRP in chlorobenzene, with 6 vol% DMF added to improve the CuBr solubility. A well-controlled ATRP of MD'M-ALMA was achieved with these conditions up to 60-70% conversion, with size exclusion chromatography (SEC) analysis showing a clear shift to higher molecular weights while maintaining a narrow dispersity ($Đ < 1.2$). PMD'M-ALMA homopolymers were also prepared under the same ATRP conditions at > 10 g scales utilizing 2-ethylbromoisobutyrate as an initiator and showed similar results (Figure C3 & C4) The successful synthesis of PDMS-*b*-PMD'M-ALMA was confirmed with ^{1}H NMR with a resulting PDMS volume fraction (f_{PDMS}) of 0.45. Detailed characterization and NMR integrations utilized for this calculation are provided in appendix D.

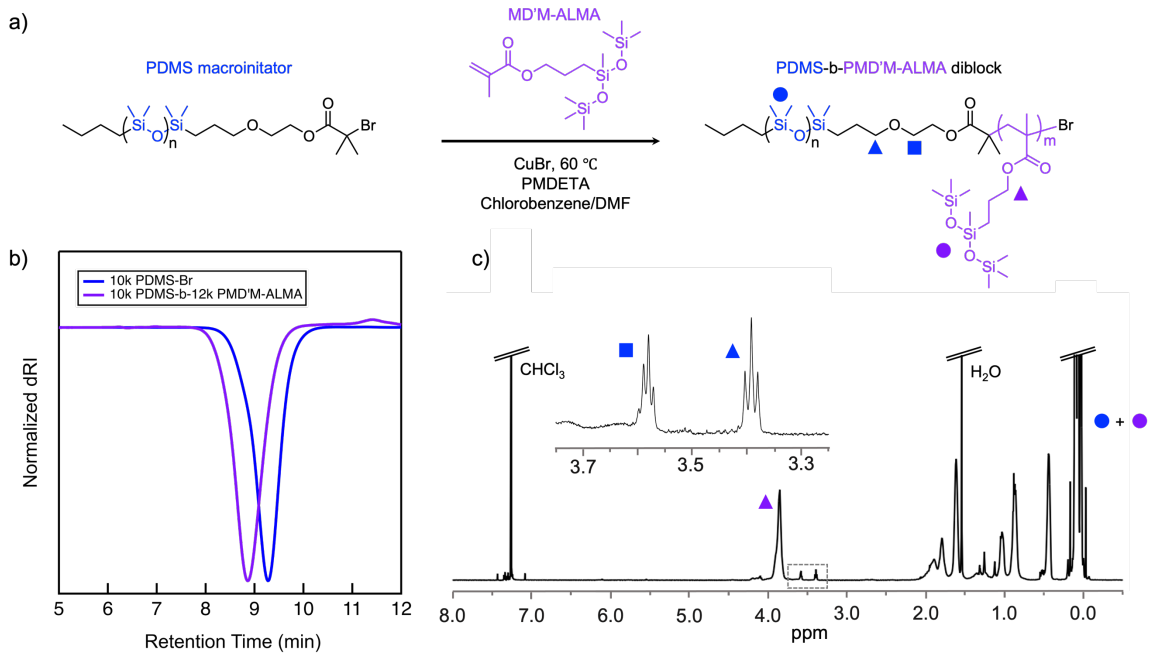


Figure 1. a) Cu (I) conditions for ATRP of MD'M-ALMA initiated by 10k PDMS-Br. b) SEC-RI trace of PDMS-*b*-PMD'M-ALMA in chloroform (M_n^{SEC} = 19.0 kDa, $Đ$ = 1.2) showing successful chain-extension and c) ^{1}H NMR trace confirming the synthesis of PDMS-b-PMD'M-ALMA.

Interestingly, the isolated 10k PDMS-*b*-12k PMD'M-ALMA was a clear, colorless viscous liquid at room temperature, qualitatively like PMD'M-ALMA homopolymer (Figure 2, C5). This is significant as even low T_g microphase separated block copolymers often exhibit viscoelastic-like behavior below their T_{ODT} due to the interconnected 3D networks of ordered domains.[38-40] Thus, the liquid-like nature of 10k PDMS-*b*-12k PMD'M-ALMA implies the system is disordered at room temperature. This qualitative observation was confirmed by small-angle X-ray scattering (SAXS) measurements as no scattering peaks were observed at all q values. The disordered nature of 10k PDMS-*b*-12k PMD'M-ALMA is quite shocking as PDMS-based BCPs with other methacrylates typically exhibit strong segregation at molecular weights as low as 3 – 4 kDa due to their high-χ nature.[27,41] As far as we are aware, low-χ PDMS-methacrylate block copolymers that are disordered at molecular weights > 20 kDa

have never been reported. We postulate that the oligomeric siloxane side-chain of MD'M-ALMA introduces favorable interactions with the PDMS block, greatly enhancing the compatibility of the system.

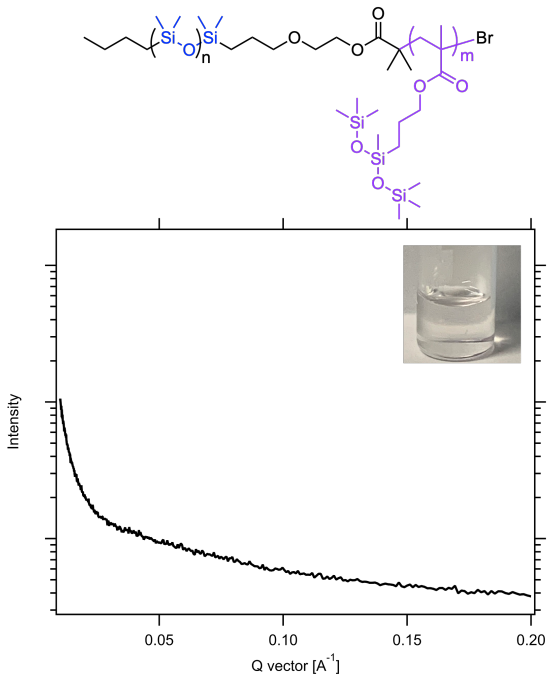


Figure 2. SAXS 1-D profile and image (inset) of 10k PDMS-*b*-12k PMD'M-ALMA at 25 °C showing complete disorder.

Inspired by the low-χ nature of PDMS-*b*-PMD'M-ALMA, we hypothesized that MD'M-ALMA could be copolymerized with other methacrylates to tune the segregation of their block copolymers with PDMS. In particular, "block-random" copolymers with a random block composed of MD'M-ALMA with other methacrylates were targeted to continuously tune χ and their resulting physical properties without gradient or tapered interfaces that strongly influence microphase separation behavior.[31, 32, 42] To investigate this, the reactivity ratios of MD'M-ALMA copolymerized with other methacrylates were studied through ^{1}H NMR kinetic experiments. Specifically, MMA was chosen as a comonomer in this study as PDMS-*b*-PMMA is known have high-χ values at low molecular weights. The reactivity ratios

of MMA and MD'M-ALMA via ATRP initiated by 10k PDMS-Br were calculated using the Jaacks model with a coefficient of determination.[43] (R^2) of 0.99 for both monomers. The calculated *r*-parameters are defined as follows: $r_1 = k_{11}/k_{12}$ and $r_2 = k_{22}/k_{21}$ with the rate constant *k*, 1 representing MMA and 2 representing MD'M-ALMA. The results show that the copolymerization of MMA and MD'M-ALMA displays a slight preferred propagation of MMA over MD'M-ALMA with *r*-parameters of $r_{MMA} = 1.29 \pm 0.04$ and $r_{MD'M\text{-}ALMA} = 0.81 \pm 0.05$. Both copolymerizations yielded equally narrow dispersities ($Đ < 1.2$) proving the reproducibility of the system as well as the absence of undesired termination reactions (Figure C8).

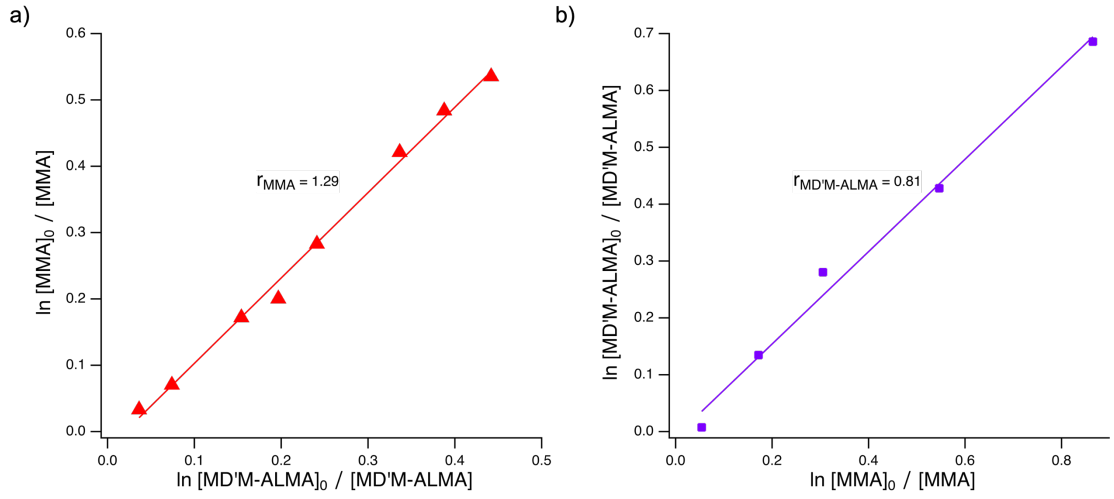


Figure 3. Linear fit of data calculated by the Jaacks equation for the evaluation of reactivity ratios of a) r_{MMA} and $r_{MD'M\text{-}ALMA}$ initiated by 10k PDMS-Br.

At large, the investigated copolymerization initiated by 10k PDMS-Br shows an almost ideally random character with a slight preference for incorporation of MMA over MD'M-ALMA. The random nature of the copolymerization allows for the incorporation of evenly distributed MD'M-ALMA compatibilizing segments along the backbone of the

methacrylate block. Thus, we sought to synthesize a library of near symmetric PDMS-b-P[MD'M-ALMA-r-MMA] block random copolymers by ATRP with composition-dependent physical properties and segregation strengths. Detailed characterization data including molecular weight, dispersity and volume fractions of each component are summarized in Table 1 below and Appendix C. In all cases, narrow dispersities, polymer compositions and molecular weights of each block close to their targeted values were achieved simply by modifying their monomer feed ratios. The ease of synthesis illustrates the power of this strategy for the preparation of PDMS-PMD'M-ALMA based block random copolymer libraries.

Table 1 – Summary of PDMS-based block random copolymer characterization

Entry	Monomer Feed[a]	Target DP[b]	Actual DP[b]	f_{PDMS}	$f_{MD'M\text{-}ALMA}$	Conv. (%)	$M_{n,SEC}$ (kDa)[c]	$Đ$[c]
1	[1]:[74]:[0]	142:30:0	142:38:0	0.45	0.55	50	26.9	1.14
2	[1]:[66]:[30]	144:26:12	144:35:20	0.44	0.49	48	27.2	1.19
3	[1]:[59]:[61]	142:23:24	142:22:29	0.51	0.37	44	26.9	1.16
4	[1]:[51]:[92]	142:20:37	142:20:40	0.51	0.33	47	30.4	1.18
5	[1]:[44]:[122]	142:18:49	142:17:55	0.51	0.28	46	35.7	1.18
6	[1]:[37]:[152]	142:15:61	142:13:63	0.52	0.22	44	33.8	1.17
7	[1]: [29]:[183]	142:12:73	142:12:88	0.48	0.19	48	33.3	1.20
8	[1]:[22]:[213]	142:9:86	142:9:95	0.50	0.14	48	36.7	1.21
9	[1]:[15]:[244]	142:6:98	142:5:96	0.52	0.09	46	33.8	1.20

In addition to tuning the segregation strength, one advantage of block random copolymer architectures is that the physical properties such as glass transition temperatures (T_gs) of the overall material can also be continuously varied depending on the incorporation of compatibilizing comonomers. In contrast to diblocks or gradient systems, perfectly random copolymers exhibit a single, narrow T_g indicating the absence of ordered structures or microphase separation.[44,45] Futhermore, the T_g of the resulting random copolymer can be

predicted via the Fox equation if no specific or very weak intermolecular interactions between comonomers are present.[46] As PDMS, PMD'M-ALMA and PMMA have very different glass transition temperatures ($T_{g,PDMS}$ = – 125 °C, $T_{g,PMD'M\text{-}ALMA}$ = – 45 °C and $T_{g,PMMA}$= 110 °C), the physical properties of the PDMS-*b*-P[MD'M-ALMA-*r*-MMA] diblock random copolymers varied dramatically from viscous liquids to glassy solids depending on the incorporation of MD'M-ALMA into the methacrylate block (Figure 4).

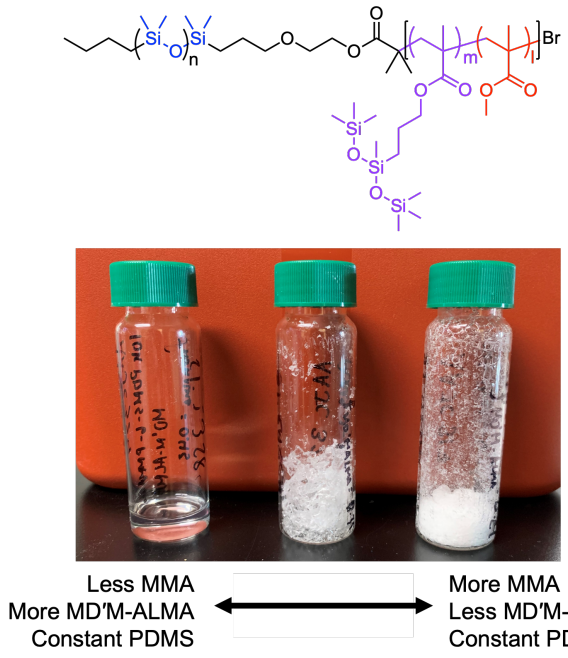


Figure 4. Image of PDMS-*b*-P[MD'M-ALMA-*r*-MMA] copolymer with (left) $f_{MD'M\text{-}ALMA}$ = 0.49, (middle) $f_{MD'M\text{-}ALMA}$ = 0.33 and (right) $f_{MD'M\text{-}ALMA}$ = 0.22 with tunable physical properties depending on composition.

The thermal properties of the PDMS-*b*-P[MD'M-ALMA-*r*-MMA] were evaluated by differential scanning calorimetry (DSC) at a ramp rate of 20 °C/min as shown in Figure 5. Interestingly, although a T_g for the PDMS block was observed for most of the PDMS-*b*-P[MD'M-ALMA-*r*-MMA] copolymers, the PDMS crystallization (T_c = – 85 °C - – 60 °C) and melting (T_m = – 55 °C - – 35 °C) were notably absent for MD'M-ALMA rich materials

indicating potential favorable interactions with PDMS domains, increasing their compatibility (Figure 5, a). In contrast, PDMS melting and crystallization was clearly observed for symmetric PDMS-*b*-P[MD'M-ALMA-*r*-MMA] with $f_{MD'M\text{-}ALMA} < 0.30$ indicating microphase separation (Figure 4b). This was confirmed by the appearance of a second T_g corresponding to methacrylate domains. As expected for a block random copolymer, a single T_g for the P[MD'M-ALMA-*r*-MMA] block was observed that shifted to higher temperatures with decreasing MD'M-ALMA content. The T_gs for the methacrylate block were notably higher than predicted via the Fox equation, indicating repulsive intermolecular interactions between MD'M-ALMA and MMA units along the polymer backbone that warrant further investigation. [47]

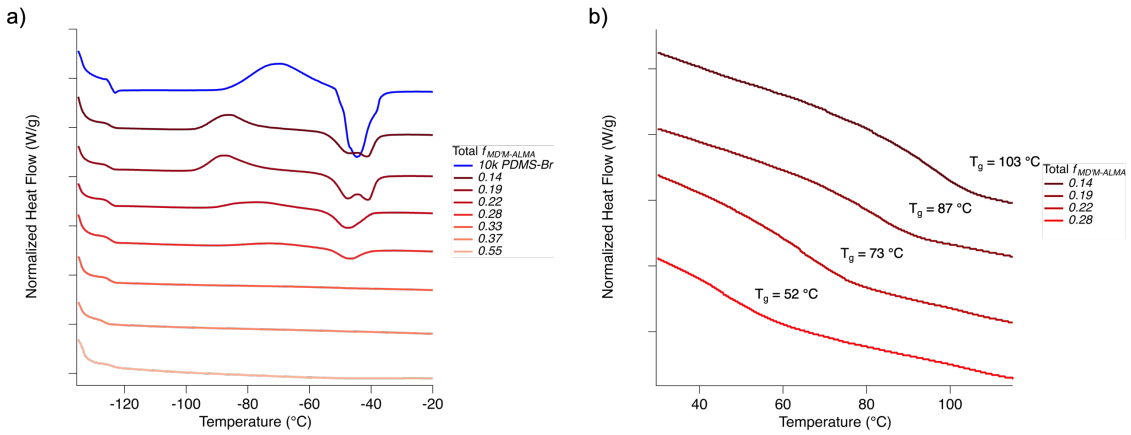


Figure 5.DSC traces of PDMS-*b*-P[MD'M-ALMA-*r*-MMA] at 20 °C/min (Exo up) showing a) the suppression of PDMS melting and crystallization for MD'M-ALMA rich block random copolymers and b) tunable T_gs for the methacrylate block depending on MD'M-ALMA incorporation.

Finally, the morphology and domain periods of the symmetric PDMS-*b*-P[MD'M-ALMA-*r*-MMA] block random copolymers were determined by SAXS measurements. Transmission SAXS data are summarized in Figure 6 with the domain period calculated for each sample through the expression $d_0 = 2\pi/q^*$ where q* is the position of the principal (first-

order) SAXS peak. For PDMS-*b*-P[MD'M-ALMA-*r*-MMA] with $f_{MD'M\text{-}ALMA}$ = 0.37, only a weak and broad principal peak was observed, and no secondary scattering peaks could be identified. This is clear evidence that the block random copolymers $f_{MD'M\text{-}ALMA}$ < 0.37 were disordered at the annealing temperature 160 °C. As MD'M-ALMA incorporation decreased, a clear sharp principal scattering appeared from q* = 0.035 A^{-1} - 0.029 A^{-1} PDMS-*b*-P[MD'M-ALMA-*r*-MMA] for $f_{MD'M\text{-}ALMA}$ = 0.33 – 0.22, with the shift to lower q* values at higher MMA content. Further decreasing MD'M-ALMA content to $f_{MD'M\text{-}ALMA}$ = 0.19 showed the emergence of secondary and tertiary scattering peaks at 2q* = 0.05 A^{-1} and 3q* = 0.07 A^{-1} indicative of a lamellar morphology. The combination of well-ordered lamella and strong segregation allowed all MD'M-ALMA poor PDMS-*b*-P[MD'M-ALMA-*r*-MMA] diblock copolymers to have d_0 < 30 nm.

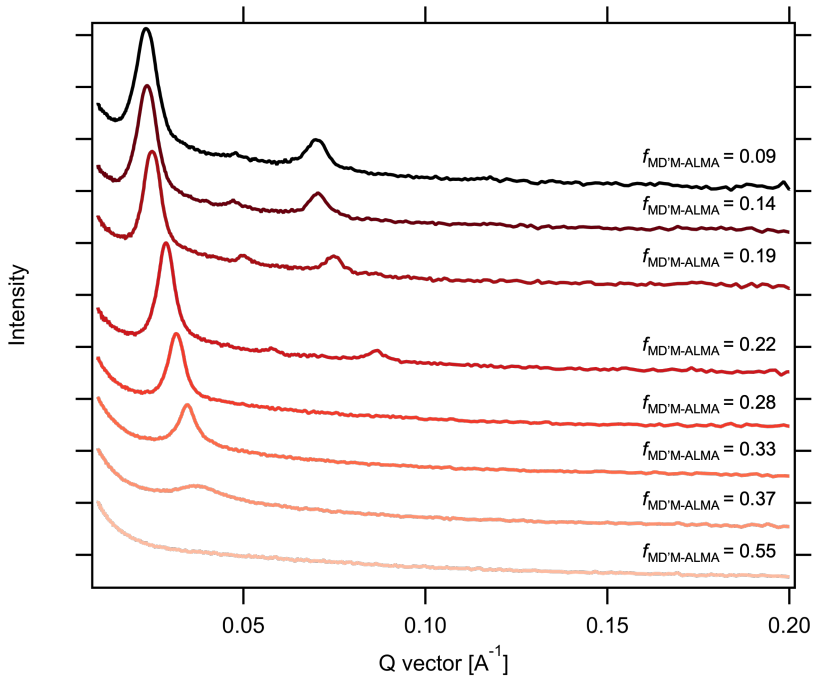


Figure 6. SAXS 1-D profiles PDMS-*b*-P[MD'M-ALMA-*r*-MMA] block random copolymers at 25 °C ordered by decreasing MD'M-ALMA content.

4.4 Conclusion & Future Work

In this work, a modular strategy for the synthesis of PDMS-based block random copolymer libraries through statistical copolymerization of hybrid silicone-methacrylate monomers from PDMS-Br macroinitiaors was developed. The physical properties and segregation strengths of near-symmetric PDMS-*b*-P[MD'M-ALMA-*r*-MMA] copolymers varied dramatically depending on the amount of MD'M-ALMA incorporation ranging from low T_g viscous disordered liquids to high T_g glassy solids with well-ordered lamellar structures. Although the use of MD'M-ALMA random blocks provides an important first step toward the design of low χ PDMS-based block copolymers, significant more work is required to fully understand the relationship between MD'M-ALMA content and χ. Towards this end, variable temperature SAXS and rheology studies are currently being conducted to measure the T_{ODT}s of MD'M-ALMA rich PDMS-*b*-P[MD'M-ALMA-*r*-MMA] to estimate their χ values. It is important to note however that C-*b*-[A-*r*-B] previously described by Register and workers often do not follow regular mixing models and the χ values between each monomer pair are required in order to fully understand their phase behavior.[36,37] Thus, a separate study of PMD'M-ALMA-*b*-PMMA diblock copolymers is underway to determine their χ parameters. The χ values of PDMS-*b*-P[MD'M-ALMA-*r*-MMA] copolymers reported in this chapter are also being investigated though DSC studies at Dow Chemical via Couchman-Karasz calculations.[47]

4.5 References

(1) Binder, K. Theories and Mechanism of Phase Transitions, Heterophase Polymerizations, Homopolymerization, Addition Polymerization, Springer-Verlag, Berlin, Germany, **1994**, p. 4.

(2) Koning, C.; van Duin, M.; Pagnoulle, R.; Jerome, R. Prog. Polym. Sci. **1998**, 23, 707.

(3) Paul, D. R.; Barlow, J. W.; Keskkula, H. Encyclopedia of Polymer Science and Engineering, 2nd ed., Vol. 12, Wiley-Interscience, New York, USA **1998**.

(4) Thomas, A. A. R. S. Compatibilization of Polymer Blends, Elsevier, Amsterdam, Netherlands **2020**.

(5) Silicone and polysiloxane is used interchangeably and siloxane is used to refer to the Si-O functional group.

(6) Abdilla, A.; D'Ambra, C. A.; Geng, Z.; Shin, J. J.; Czuczola, M.; Goldfeld, D. J.; Biswas, S.; Mecca, J. M.; Swier, S.; Bekemeier, T. D.; Laitar, D. S.; Bates, M. W.; Bates, C. M.; Hawker, C. J. J. Polym. Sci. **2021**, 59, 2114.

(7) Voronkov, M. G.; Mileshkevich, V. P.; Yuzhelevskii, Y. A. Studies in Soviet Science. The Siloxane Bond, Physical Properties and Chemical Transformations, Plenum Publishing Corporation, New York, USA **1978**.

(8) Pouget, E.; Tonnar, J.; Lucan, P.; Lacroix-Desmazes, P.; Ganachaud, F.; Boutevin, B.; *Chem. Rev.* **2010**, *110*, 1233.

(9) Centre Européen des Silicones, http://www.silicones.eu **2020**.

(10) Zimmermann, C. G. *MRS Bull.* **2010**, *35*, 48.

(11) Aziz, T.; Waters, M.; Jagger, R.; *J. Dentist.* **2003**, *31*, 67.

(12) Holzapfel, B. M.; Reichert, J. C.; Schantz, J.-T.; Gbureck, U.; Rackwitz, L.; Nöth, U.; Jakob, F.; Rubert, M.; Groll, J. D.; Hutmacher, D. W. *Adv. Drug Delivery Rev.* **2013**, *65*, 581.

(13) Hassler, C.; Boretius, T.; Stieglitz, T. *J. Polym. Sci., Part B: Polym. Phys.* **2011**, 49, 18.

(14) Abbasi, F.; Mirzadeh, H.; Katbab, A.-A. *Polym. Int.* **2001**, *50*, 1279.

(15) Mojsiewicz-Pieńkowska, K. *Handbook of Polymers for Pharmaceutical Technologies*, Scrivener, Beverly, Massachusetts **2015**, p. 13.

(16) Lucas, P.; Robin, J. J. *Functional Materials and Biomaterials*, Springer, Berlin, Heidelberg **2007**, p. 3.

(17) Sundararaj, U.; Macosko, C. W.; *Macromolecules* **1995**, *28*, 2647.

(18) Macosko, C. W.; Guégan, P.; Khandpur, A. K. *Macromolecules* **1996**, *29*, 5590.

(19) Noolandi, J.; Hong, K. M.; *Macromolecules* **1982**, *15*, 482.

(20) Ruzette, A. V.; Leibler, L.; *Nat. Mater.* **2005**, *4*, 19.

(21) Creton, C.; E. Kramer, J.; Brown, H. R.; Hui, C. Y.; *Adv. Polym. Sci.* **2002**, *156*, 53.

(22) Schwahn, D.; *Adv. Polym. Sci.* **2005**, *183*, 1.

(23) Pitet, L. M.; Wuister, S. F.; Peeters, E.; Kramer, E. J.; Hawker, C. J.; Meijer, E. W. *Macromolecules* **2013**, *46*, 8289.

(24) Tavakkoli, A.; Gotrik, K. W.; Hannon, A. F.; Alexander-Katz, A.; Ross, C. A.; Berggren, K. K.; *Science* **2012**, *336*, 1294.

(25) Durand, W. J.; Blachut, G.; Maher, M. J.; Sirard, S.; Tein, S.; Carlson, M. C.; Asano, Y.; Zhou, S. X.; Lane, A. P.; Bates, C. M.; Ellison, C. J.; Willson, C. G. *J. Polym. Sci.* **2014**, *53*, 344.

(26) Maher, M. J.; Bates, C. M.; Blachut, G.; Sirard, S.; Self, J. S.; Carlson, M. C.; Dean, L. M.; Cushen, J. D.; Durand, W. J.; Hayes, C. O.; Ellison, C. J.; Willson, C. J. *Chem. Mater.* **2014**, *26*, 1471.

(27) Luo, Y.; Montarnal, D.; Kim, S.; Shi, W.; Barteau, K. P.; Pester, C. W.; Hustad, P. D.; Christianson, M. D.; Fredrickson, G. H.; Kramer, E. J.; Hawker, C. J. *Macromolecules* **2015**, *48*, 3422.

(28) Beckingham, B. S.; Register, R. A. *Macromolecules* **2011**, *44*, 4313.

(29) Quinn, J. D.; Register, R. A. *J. Polym. Sci., Part B: Polym. Phys.* **2009**, *47*, 2106.

(30) Smith, S. D.; Ashraf, A.; Satkowski, M. M.; Spontak, R. *J Polym Prepr (Am Chem Soc Div Polym Chem)* **1994**, *35*, 651.

(31) Patterson, A. L.; Danielsen, S. P. O.; Yu, B.; Davidson, E. C.; Fredrickson, G. H.; Segalman, R. A. *Macromolecules* **2019**, *52*, 1277.

(32) Patterson, A. L.; Yu, B.; Danielsen, S. P. O.; Davidson, E. M.; Fredrickson, G. H.; Segalman, R. A. *Macromolecules* **2020**, *53*, 3262.

(33) Singh, N.; Tureau, M. S.; Epps, T. H. *Soft Matter* **2009**, *5*, 4757.

(34) Mastroianni, S. E.; Epps, T. H. *Langmuir* **2013**, *29*, 3864.

(35) Kim, J.; Gray, M. K.; Zhou, H. Y.; Nguyen, S. T.; Torkelson, J. M. *Macromolecules* **2005**, *38*, 1037.

(36) Beckingham, B. S.; Burns, A. B.; Register, R. A. *Macromolecules* **2013**, *46*, 2760.

(37) Beckingham, B. S.; Register, R. A. *Macromolecules* **2013**, *46*, 3084.

(38) Ekong, E. A.; Jayaraman, K. *J. Rheol.* **1984**, *28*, 45.

(39) Hahn, H.; Lee, J. H.; Balsara, N. P.; Garetz, B. A.; Wantanabe, H. *Macromolecules* **2001**, *34*, 8701.

(40) Xie, R.; Mukherjee, S.; Levi, A. E.; Self, J. L.; Wang, H.; Chabinyc, M. L.; Bates, C. M. *Macromolecules* **2021**, *54*, 5636.

(41) Oschmann, B.; Lawrence, J.; Schulze, M. W.; Ren, J. M.; Anastasaki, A.; Luo, Y.; Nothling, M. D.; Pester, C. W.; Delaney, K. T.; Connal, L. A.; McGrath, A. J.; Clark, P. G.; Bates, C. M.; Hawker, C. J. *ACS Macro Lett.* **2017**, *6*, 668.

(42) Mok, M. M.; Pujari, S.; Burghardt, W. R.; Dettmer, C. M.; Nguyen, S. T.; Ellison, C. J.; Torkelson, J. M. *Macromolecules* **2008**, *41*, 5818.

(43) Jaacks, V. A. *Makromol. Chem.* **1972**, *161*, 161.

(44) Kim, J.; Mok, M. M.; Sandoval, R. W.; Woo, D. J.; Torkelson, J. M. *Macromolecules* **2006**, *39*, 6152.

(45) Wong, C. L. H.; Kim, J.; Torkelson, J. M. *J. Polym. Sci., Part B: Polym. Phys.* **2007**, *45*, 2842.

(46) Fox, T. G.; *Bull. Am. Phys. Soc.* **1956**, *1*, 123.

(47) Lu, X.; Weiss, R. A. *Macromolecules* **1992**, *25*, 3242.

Chapter 5. Conclusions

In summary, well-defined end-functional polymers by living anionic polymerizations have a wide range of applications in materials science, and new synthetic platforms to install versatile reactive chain-ends can be developed through understanding of the polymerization mechanisms. The DBU catalyzed functional termination of stereospecific PMMA anionic polymerizations with α-(halomethl)acrylates in Chapter 2 demonstrated a versatile and scalable platform to prepare *st-/it*-PMMA nanoparticle ligands on multigram scales for stereocomplexation driven assembly platforms. The Michael-accepting alkene chain ends were highly reactive towards thiols, and thus a wide variety of functional *st-/it*-PMMA building blocks can be prepared with this technique. Furthermore, stereocomplexated nanoparticle assemblies showed remarkably similar properties to previously reported DNA-mediated methods, making this an exciting platform to develop hybrid organic-inorganic nanostructures. The development of highly crystalline nanoparticle superlattices may also be possible through careful control of the *st-/it*-PMMA dispersity, stereochemical purity, molecular weights and solution-mediated assembly kinetics. Further control over the assembly structure and dynamic morphologies can be attained by utilizing stereoselective PMMA strand-displacement phenomenon previously described by the Hawker group (*JACS,* **2018**, *140*, 1945 & *JACS,* **2019**, *141,* 6, 2630). This concept can also be extended to other polymeric systems known to form stereocompelxes such as end-functional highly crystalline poly(lactic acid) although further research in this area is required.

The end functionalization strategies for living anionic polymerizations described in this thesis can also be expanded to a wide variety of monomer families. In particular, the introduction of α-Si-H functionalities through initiation of anionic ring opening

polymerizations in combination with highly effective functional chlorosilane termination agents described in Chapter 3 opens new doors for the development of advanced silicone materials. This is particularly exciting as the development of well-defined end functionalized polysiloxanes has been especially challenging due to thermodynamically favored redistribution mechanisms that occur during polymerization or post-modifications that lead to a loss of structural control. Si-H functional groups are also known to be especially sensitive to nucleophilic substitution under basic conditions, however this thesis shows their retention with high chain-end fidelities through kinetic control. It is particularly interesting to note that although intermolecular exchange of dimethylsilyl groups occurs at high conversions, the α-Si-H bond itself remains intact and only the adjacent Si-O bonds are cleaved. The exchange mechanism described in Appendix C is also likely aided by the formation of Li^+ aggregates which are known to favor chain-end redistribution reactions. With these important factors in mind, it may be possible to deliberately design novel Si-H functional initiating systems which eliminate α-chain-end exchange processes with Na^+ and K^+ counterions or the replacement of H-Si-O units with H-Si-C. These systems are currently under investigation and should favor kinetic propagation of strained cyclotrisiloxanes, thereby significantly increasing the yield and scalability of highly pure α-,ω- heterotelechelic polysiloxanes prepared via this method. This will enable preparation of advanced silicone-based systems on multigram scales such as tetrahedral PDMS crosslinkers that undergo ideal alternate A-B reactions (limiting A-A or B-B self-reactions create network defects) or novel ABC triblock (or multiblock) copolymers with polysiloxane based B segments. It is also interesting to note that α-Si-H moieties through initiation of monomer families other than polysiloxanes may be possible.

Finally, well-defined chain-end functionalized polymers via living anionic polymerizations open opportunities to novel hybrid materials when combined with controlled radical polymerizations. The "block random" copolymers prepared by ATRP mediated copolymerization of MMA and MD'M-ALMA from PDMS-Br macroinitiators show remarkably different physical properties and segregation strengths depending on their compositions. It is especially remarkable that PDMS-*b*-PMD'M-ALMA diblock copolymers at molecular weights > 20 kDa and the low-χ nature of this system warrants further investigation. Although MMA was chosen as a model co-monomer for this system, MD'M-ALMA should exhibit reactivity ratios near unity for a wide variety of other methacrylates allowing for further tunability of this system. Novel blend BCP compatibilizers may also be possible through PDMS-*b*-P[MD'M-ALMA-*r*-MMA]-*b*-PMMA triblock copolymers with a random MD'M-ALMA midblock that broadens silicone-organic interfaces and homopolymer end blocks that entangle with polymer matrices.

In closing, this thesis demonstrates that thorough understanding of living anionic polymerization mechanisms can lead directly to the development of new and efficient end functionalization strategies without the use of protecting groups and greatly enhances the incorporation of their resulting polymers into advanced materials systems.

Appendix A. Supporting Information for Chapter 2

GENERAL EXPERIMENTAL SECTION

Materials

Magnesium turnings (Aldrich, >99.5%), *t*-butylbromide (Alfa Aesar, >98%), *n*-butyllithium solution (Aldrich, 1.6M in hexanes), *t*-butylamine borane complex (Aldrich, 97%), 1,8-octanedithiol (Acros Organics, 99%), sodium trifluoroacetate (NaTFA, Fluka ≥ 99.0%) and *trans*-2-[3-(4-*t*-butylphenyl)-2-methyl-2-propenylidene]-malononitrile (DCTB, Fluka, puriss) were used as received. Methyl Methacrylate (MMA, TCI, >99%), 1,1-diphenylethylene (DPE, Alfa Aesar, 98%), 1,8-diazabicyclo[5.4.0]undec-7-ene (DBU, Fisher Scientific, 99%) and ethyl 2-(bromomethyl)acrylate (EBMA, Aldrich, 98%) were distilled under reduced vacuum over calcium hydride (CaH_2, Aldrich, ≥ 97%) before use. Triphenylphosphonegold(I) chloride ($Au(PPh_3)Cl$) was prepared according to literature procedures and recrystallized from dichloromethane/ethanol before use. Toluene, tetrahydrofuran (THF) and acetonitrile were collected under an Ar atmosphere from a solvent purification system (PureSolv, Innovative Technology Inc.) for polymerization and chain-end functionalization use. Other solvents including diethyl ether (anhydrous, Aldrich, ≥ 99%), dichloromethane (DCM, Fisher Scientific, ≥99.5%), ethanol (Aldrich, 200 proof, anhydrous), ethyl acetate (Aldrich, 99.5%), *n*-hexane (Fisher Scientific, 55% as hexane), anhydrous methanol (Alfa Aesar, 99.9%), were used as received. *Atactic* α-thiol terminated poly(methyl methacrylate) (*at*-PMMA6K-SH, M_n^{SEC} = 6.5 kDa, $Đ_M$ = 1.25) was purchased from Polymer Source and purified prior to use by dissolution in THF, filtering through basic alumina (Aldrich, standard grade) and precipitation into cold methanol (100 mL).

Characterization Methods

^{1}H and ^{13}C NMR spectroscopy measurements were conducted in $CDCl_3$ at 20 °C or 45 °C on a Varian spectrometer operating at 600 (or 500) and 125 MHz for ^{1}H and ^{13}C, respectively. For PMMA, the triad tacticity was estimated by the integration under the C=O carbon resonance at 175-180 ppm in the ^{13}C NMR spectra of the polymers. The number-average molecular weight (M_n), weight-average molecular weight (M_w) and dispersity ($Đ_M$) were determined by Size Exclusion Chromatography (SEC) in 0.25 wt% triethylamine/chloroform using a Waters e2695 separation module with a Waters 2414 differential refractive index detector. The columns were calibrated against PMMA standards (Agilent Technologies; Mp = 550-1568000 Da; M_w/M_n = 1.02-1.09). PMMA's mass spectra were obtained using a Bruker Microflex LRF MALDI TOF mass spectrometer in positive reflectron mode; the analyte, matrix (DCTB) and cationization agent (NaTFA) were dissolved in THF at concentrations of 10, 10 and 1 mg/mL, respectively, and then mixed in a volume ratio of 10 : 1 : 0.3 μL of this solution was spotted onto a ground steel target plate and the solvent was allowed to evaporate prior to analysis. TEM micrographs were acquired without prior staining on a FEI Tecnai G2 Sphera Microscope with an accelerating voltage of 200 kV and particle size analyses were conducted using ImageJ software. All TEM samples were dispersed in acetonitrile (2.3×10^{13} or 2.3×10^{12} particles/mL) drop casted onto Carbon Film 300 Mesh Cu grids (Electron Microscopy Sciences) and fast dried by absorbing excess solvent with a filter paper. Stereocomplexed samples were mixed for at least 24 hours prior to imaging to ensure complete self-assembly. FTIR spectra were recorded on a Perkin Elmer Spectrum 100 FT-IR Spectrometer. UV-Vis spectra were recorded on an Agilent UV-Vis Spectrometer or using a home-built setup (details provided in previous literature).[1,2] Thermogravimetric analysis was

conducted using a TA Instruments Discovery TGA. Small angle X-ray scattering (SAXS) and Wide-angle X-ray scattering (WAXS) measurements were conducted using a custom constructed SAXS instrument in the X-ray diffraction facility in the Materials Research Laboratory (MRL) at University of California, Santa Barbara (UCSB). The instrument used a 50 micron microfocus, Cu target X-ray source with a parallel beam multilayer optics and monochromator (Genix from XENOCS SA, France), high efficiency scatterless hybrid slits collimator developed in house,1 and Pilatus100k and Eiger 1M solid state detectors (Dectris, Switzerland). SAXS data was collected at a sample-to-detector distance of 1.7 m or 0.15 m and calibrated with a silver behenate standard. The 2D data were reduced by azimuthal averaging to give I(q), where I is intensity and q is the momentum transfer vector $q = (4\pi/\lambda) \sin \theta$. For SAXS measurements, data reduction was carried out using the NIKA and IRENA software packages developed at Argonne National Laboratory. Dynamic Light Scattering (DLS) measurements were performed using a DynaPro NanoStar from Wyatt Technology with a 662 nm, 100mW laser and a 1μL quartz cuvette.

Polymer Synthesis Procedures

Alkene end-functionalized syndiotactic poly(methyl methacrylate) (*st*-PMMA-Alkene)

The *st*-PMMA-Alkene was synthesized according to previous procedures with modifications:[3] the initiator 1,1-diphenyl-*n*-hexyllithium (*n*-Hex$(Ph)_2$Li) was prepared *in-situ* by adding DPE (500 mM in THF, 3.4 mL) and *n*-butyllithium (1.6M in hexane, 0.7 mL) to anhydrous THF in a Schlenk tube with a stir bar at room temperature under Ar. The initiator solution stirred for 3 hours then cooled to -78 °C in a dry ice/MeOH bath. MMA (2.2 mL over 5 min) was then added dropwise to start the polymerization. The reaction solution was kept at -78 °C for 1 hour, then EBMA (2.5M in THF, 2.2 mL) and DBU (1.5M in THF, 3.5 mL) were

consecutively. The reaction was kept at -78 °C overnight (approx. 15h) and then quenched with degassed anhydrous methanol (2 mL). The crude solution was concentrated down to 1-2mL by rotatory evaporation and then purified with Hexanes/Ethyl Acetate using a Biotage Isolera One unit coupled with a Biotage ELSD-A120 detector, then precipitated twice into cold methanol (200 mL) to obtain *st*-PMMA-Alkene as a white powder, 1.8g (90% yield); ^{13}C NMR: mm/mr/rr(%) = 4/21/75. SEC data and ^{1}H and ^{13}C NMR spectra are provided in Figures A1-3. The same synthesis was repeated to yield higher MW materials by changing the monomer-to-initiator ratio and the final materials are summarized in Table S1. Additionally, a large-scale polymerization was conducted based on the procedure above to yield 5.2g (97%) of *st*-PMMA5K-Alkene and SEC-RI and ^{1}H NMR traces are provided in Figure A9.

Thiol end-functionalized syndiotactic poly(methyl methacrylate) (*st*-PMMA-SH)

The *st*-PMMA-SH was synthesized via thiol-Michael addition chemistry: *st*-PMMA2K-Alkene (1g, 0.4 mmol) and 1,8-octanedithiol (770 μL, 4 mmol) was dissolved in anhydrous acetonitrile (10 mL) in a 20 mL white cap screw vial with a stir bar and the solution was degassed by bubbling Ar for 15 minutes. The reaction mixture was then charged with DBU (1.5 mM in THF, 140 μL) and stirred for 1 hour at room temperature. The reaction solution was then concentrated down to 1-2mL by rotatory evaporation and purified with Hexanes/Ethyl Acetate using a Biotage Isolera One unit coupled with a Biotage ELSD-A120 detector to yield *st*-PMMA2K-SH as a white powder, 0.95g (95% yield) ^{13}C NMR: mm/mr/rr(%) = 4/21/75. SEC-RI data and ^{1}H and ^{13}C NMR spectra are provided in Figures A4-6. The same synthesis was repeated to yield different MW materials by adjusting the amounts of 1,8-octanedithiol and DBU. Additionally, a large-scale polymerization was

conducted based on the procedure above to yield 5.0g (96%) of *st*-PMMA5K-SH and SEC-RI and ^{1}H NMR traces are provided in Figure A9.

Alkene end-functionalized isotactic poly(methyl methacrylate) (*it*-PMMA-Alkene)

The *it*-PMMA-Alkene was synthesized according to previous procedures with modifications:[4,5] The Grignard reagent *t*-BuMgBr was prepared as follows: anhydrous Et_2O (28 mL) and t-butylbromide (14 g, 0.10 mol) were added consecutively into a dry addition funnel under N2. Separately, Mg turnings (3.7 g, 0.15 mol) were added to a dry round bottom flask under N2 via a funnel with a flushing adapter, followed by the addition of anhydrous Et_2O (60 mL). The t-butylbromide solution was then added slowly at 25 °C over 1 h. The solution was stirred for an additional hour and then left to stand for 12 h. The Grignard reagent ([*t*-BuMgBr]eff = 285 mM determined via polymerization) was stored in a dry round-bottom flask equipped with a 3-way stopcock under Ar atmosphere at 0 °C before use.

The general procedure for anionic polymerization *it*-PMMA-Alkene was as follows: The initiator solution (3.5 mL) was added to anhydrous toluene in a Schlenk tube under Ar with a stir bar and then cooled to -78 °C in a dry ice/MeOH bath. MMA (2.2 mL over 5 min) was then added dropwise to start the polymerization. The reaction solution was kept at -78 °C for 24 hours, then EBMA (2.5M in THF, 2.2 mL) and DBU (1.5M in THF, 3.5 mL) were consecutively. The reaction was kept at -78 °C overnight (approx. 15h) and then quenched with degassed anhydrous methanol (2 mL). The crude solution was concentrated down to 1-2mL by rotatory evaporation and then purified with Hexanes/Ethyl Acetate using a Biotage Isolera One unit coupled with a Biotage ELSD-A120 detector, then precipitated twice into cold methanol (200 mL) to obtain *it*-PMMA-Alkene as a white powder, 1.7g (85% yield); ^{13}C NMR: mm/mr/rr(%) = 1/7/92. SEC data and ^{1}H and ^{13}C NMR spectra are provided in Figures

S9-11. The same synthesis was repeated to yield different MW materials by changing the monomer-to-initiator ratio and the final materials are summarized in Table S2.

Thiol end-functionalized isotactic poly(methyl methacrylate) (*it*-PMMA-SH)

The *it*-PMMA-SH was synthesized via thiol-Michael addition chemistry: *it*-PMMA3K-Alkene (1g, 0.3 mmol) and 1,8-octanedithiol (610 μL, 3.3 mmol) was dissolved in anhydrous acetonitrile (10 mL) in a 20 mL white cap screw vial with a stir bar and the solution was degassed by bubbling Ar for 15 minutes. The reaction mixture was then charged with DBU (1.5 mM in THF, 110 μL) and stirred for 1 hour at room temperature. The reaction solution was then concentrated down to 1-2mL by rotatory evaporation and purified with Hexanes/Ethyl Acetate using a Biotage Isolera One unit coupled with a Biotage ELSD-A120 detector to yield *st*-PMMA-SH as a white powder, 0.95g (95% yield) ^{13}C NMR: mm/mr/rr(%) = 1/7/92. SEC data and ^{1}H and ^{13}C NMR spectra are provided in Figures S12-14. The same synthesis was repeated to yield different MW materials by adjusting the amounts of 1,8-octanedithiol and DBU.

Nanoparticle Synthesis Procedures

Synthesis of stereospecific poly(methyl methacrylate) functionalized Au NPs (*st-, at- or it*-PMMA-Au NPs)

Syndiotactic, *atactic or isotactic* PMMA stabilized gold nanoparticles with target size of 5 nm were prepared according to the method reported by Zheng et al.[6] Au NPs were prepared by dissolving [Au(PPh_3)Cl] (10 mg, 0.02 mmol) and *st*-PMMA6K-SH, *at*-PMMA6K-SH or *it*-PMMA3K-SH (240 or 120mg, 0.04 mmol) in anhydrous toluene (1.7 mL) in a 4 mL vial. Borane *tert*-butyl amine complex powder (17.6 mg, 0.2 mmol) was added and stirred rapidly for 2 minutes, then stirred slowly for 5 hours. The reaction mixture was then precipitated into

hexanes (100mL), collected by centrifugation (3000 rpm, 10 minutes). The Au NPs were then re-suspended in acetone and purified three times by ultra-centrifugation (15,000 rpm, 1 hour). The Au NPs were then re-suspended in acetonitrile prior to use.

Synthesis of stereospecific poly(methyl methacrylate) functionalized Au NRs (*st*- or *it*-PMMA-Au NRs)

CTAB stabilized gold nanorods were first synthesized according to previously reported methods and used immediately after preparation.[7] Either *st*-PMMA10K-SH or *it*-PMMA12K-SH (85 or 100 mg, 0.008 mmol) was then dissolved in THF (3 mL). CTAB Au NRs suspended in MilliQ water (0.5 mL) was quickly added while stirring and the solution was sonicated for 2 minutes. The reaction mixture was then left to stir overnight at room temperature and subsequently precipitated into hexanes. The Au NRs were then re-suspended in acetone and purified three times by ultra-centrifugation (15,000 rpm, 1 hour). The Au NRs were then re-suspended in acetonitrile prior to use.

Synthesis of isotactic poly(methyl methacrylate) functionalized CdSe@ZnS QDs (*it*-PMMA-QDs)

Red emitting oleic acid stabilized CdSe@ZnS quantum dots were first synthesized according to previously reported methods.[8] *It*-PMMA3k-SH (200 mg, 0.07 mmol) was then dissolved in chloroform (3 mL). Red CdSe@ZnS QDs (15 mg) suspended in chloroform (0.5 mL) were quickly added while stirring and the solution was sonicated for 2 minutes. The reaction mixture was then left to stir overnight at room temperature and subsequently precipitated into hexanes. The QDs were then re-suspended in acetone and purified three times by ultra-centrifugation (15,000 rpm, 1 hour). The QDs were then re-suspended in acetonitrile prior to use.

CHARACTERIZATION DATA

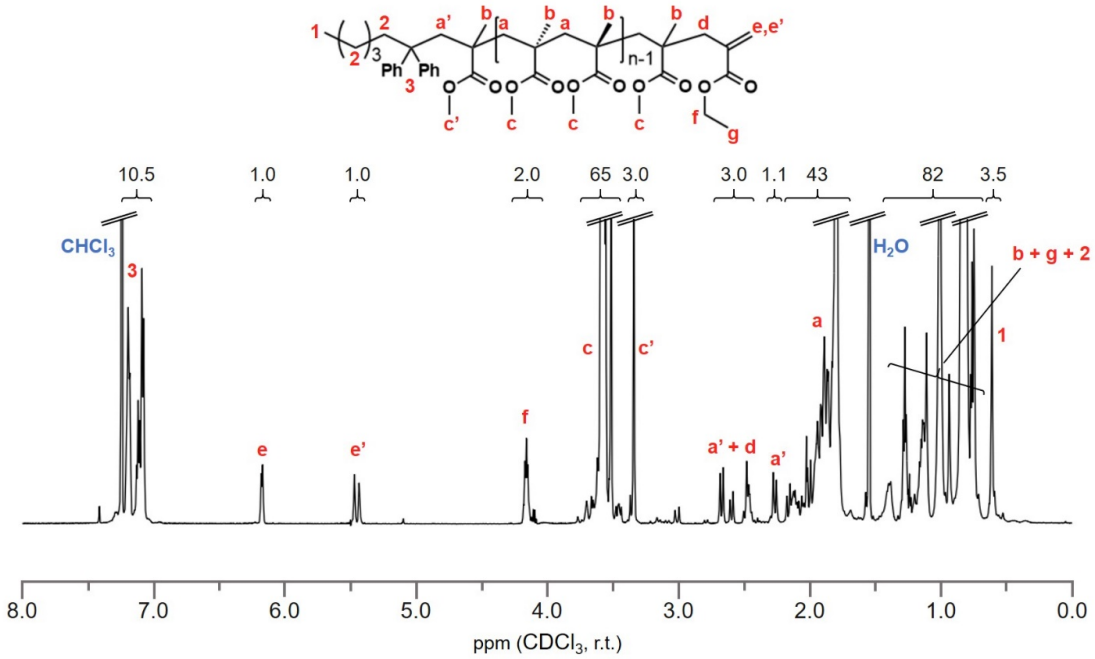


Figure A1. Representative ^{1}H NMR trace of *st*-PMMA2K-Alkene.

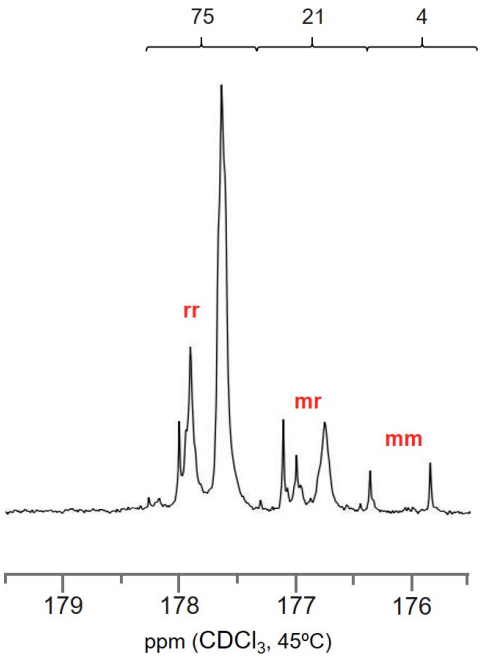


Figure A2. Partial ^{13}C NMR spectrum of *st*-PMMA2K-Alkene illustrating the tacticity determination.

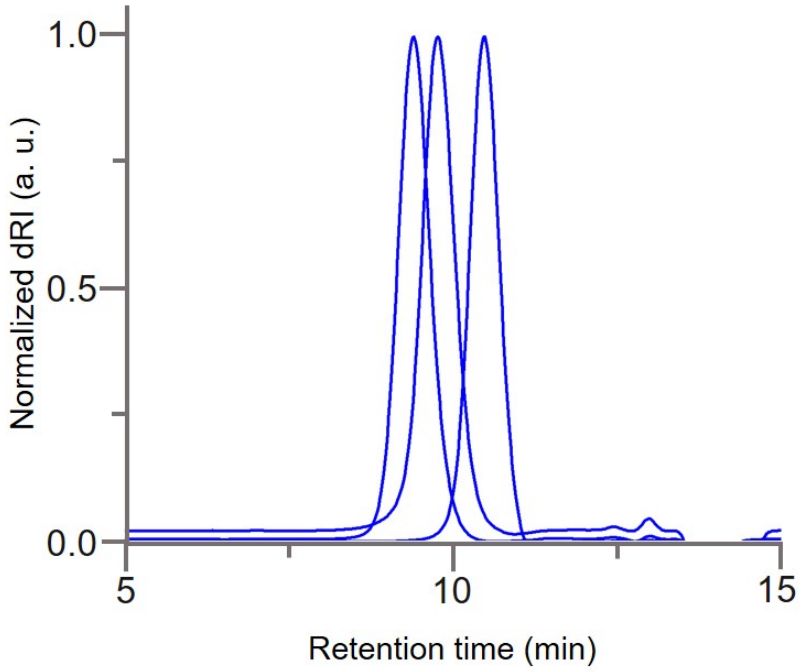


Figure A3. SEC-RI traces of isolated *st*-PMMA2K, 6K and 10K-Alkene.

Table A1. Result summary of alkene-terminated *st*-PMMA

Sample	SEC		NMR		
	M_n^{SEC}(Da)	$Đ_M$	M_n^{NMR}(Da)	mm/mr/rr	F_n (C=C)
st-PMMA2K	2500	1.1	2200	4/21/75	0.97
st-PMMA6K	6300	1.1	6100	1/22/77	0.95
st-PMMA10K	10500	1.1	10100	1/18/81	0.93

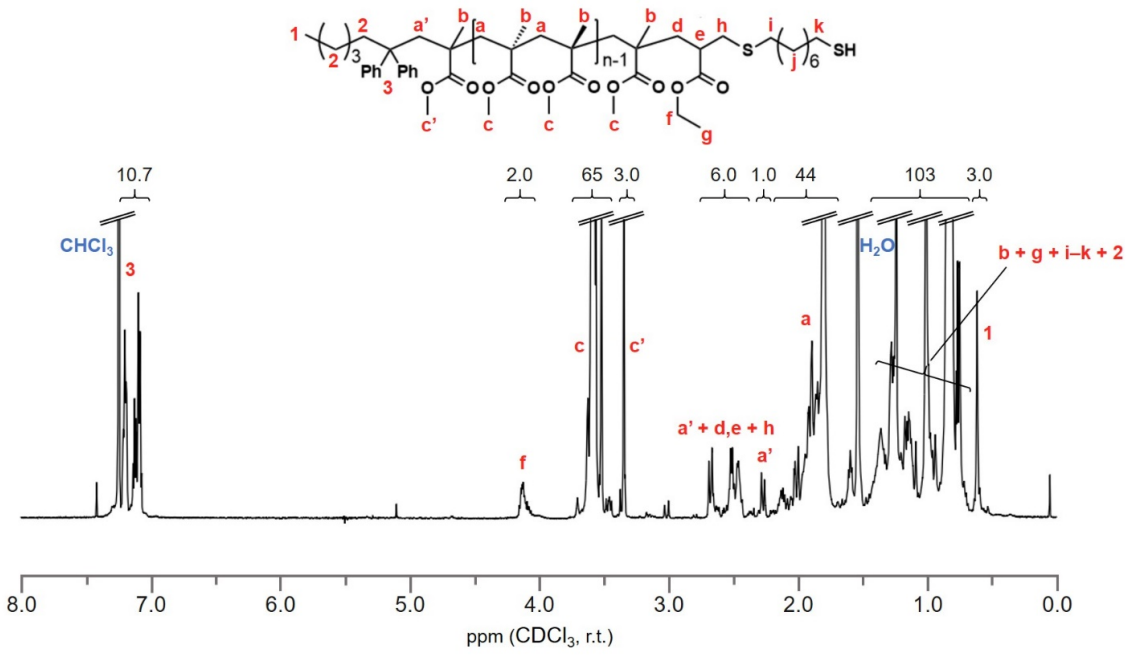


Figure A4. Representative ^{1}H NMR trace of *st*-PMMA2K-SH.

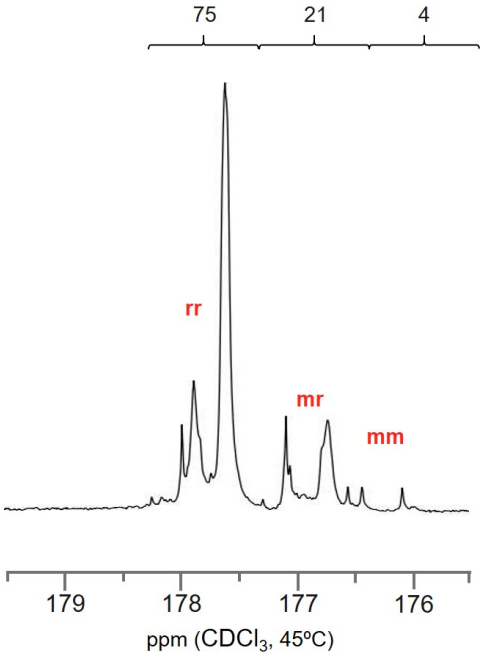


Figure A5. Partial ^{13}C NMR spectrum of *st*-PMMA2K-SH illustrating the tacticity determination.

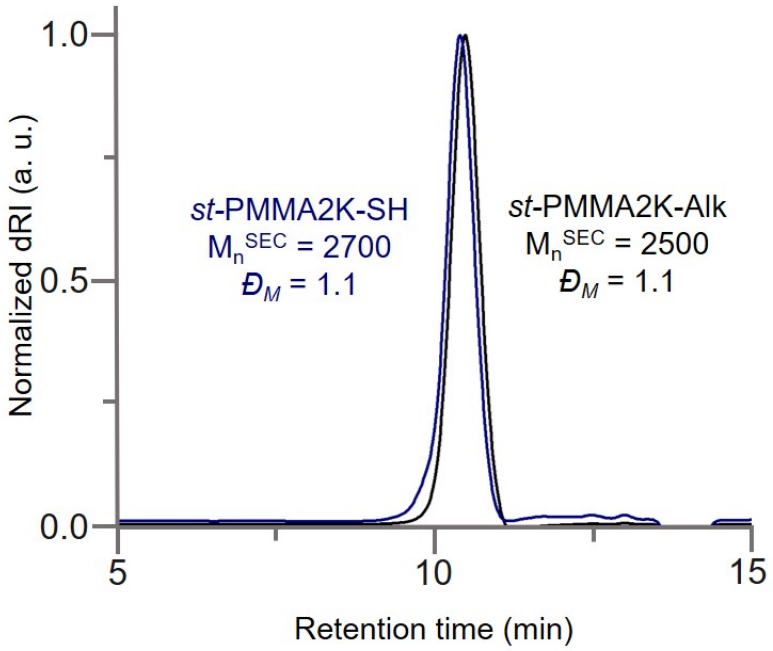


Figure A6. SEC-RI trace overlay of *st*-PMMA2K-Alkene before and *st*-PMMA2K-SH after the chain end modification.

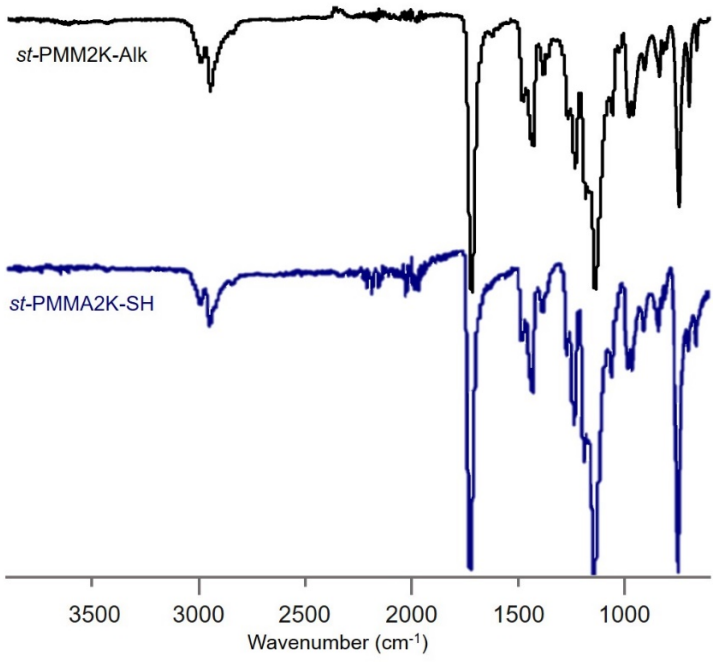


Figure A7. FT-IR spectra of *st*-PMMA2K-Alkene before and *st*-PMMA2K-SH after the chain end modification.

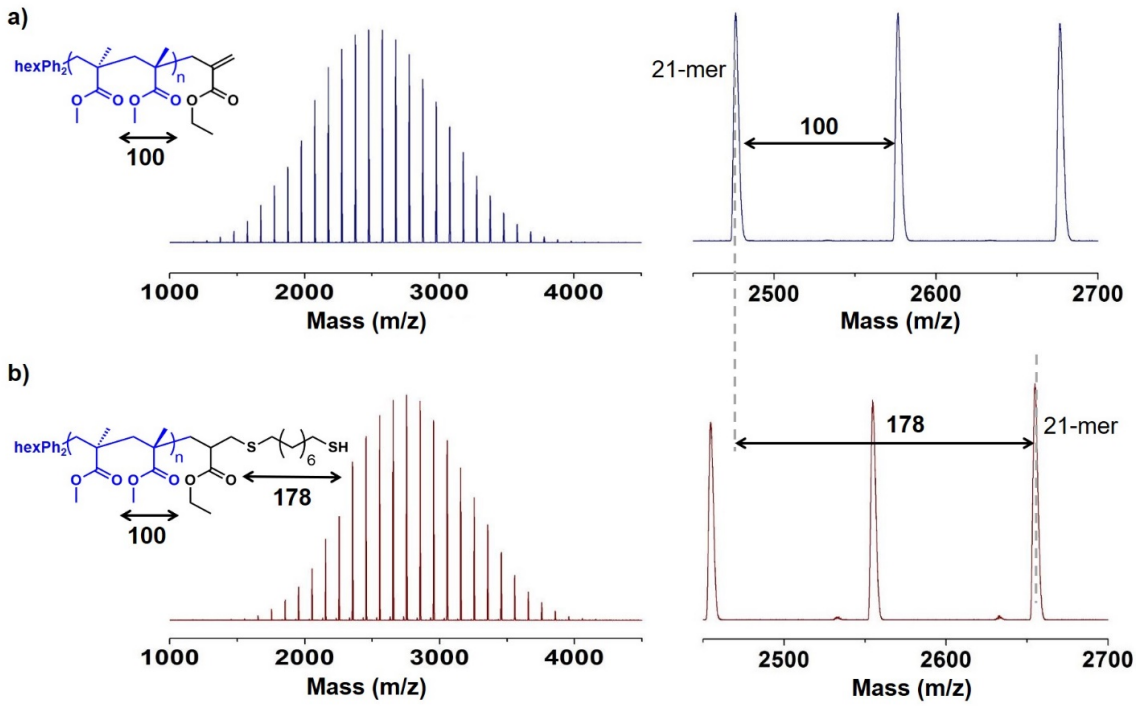


Figure A8. MALDI-ToF mass spectra *st*-PMMA2K-Alkene before and *st*-PMMA2K-SH after the chain end modification.

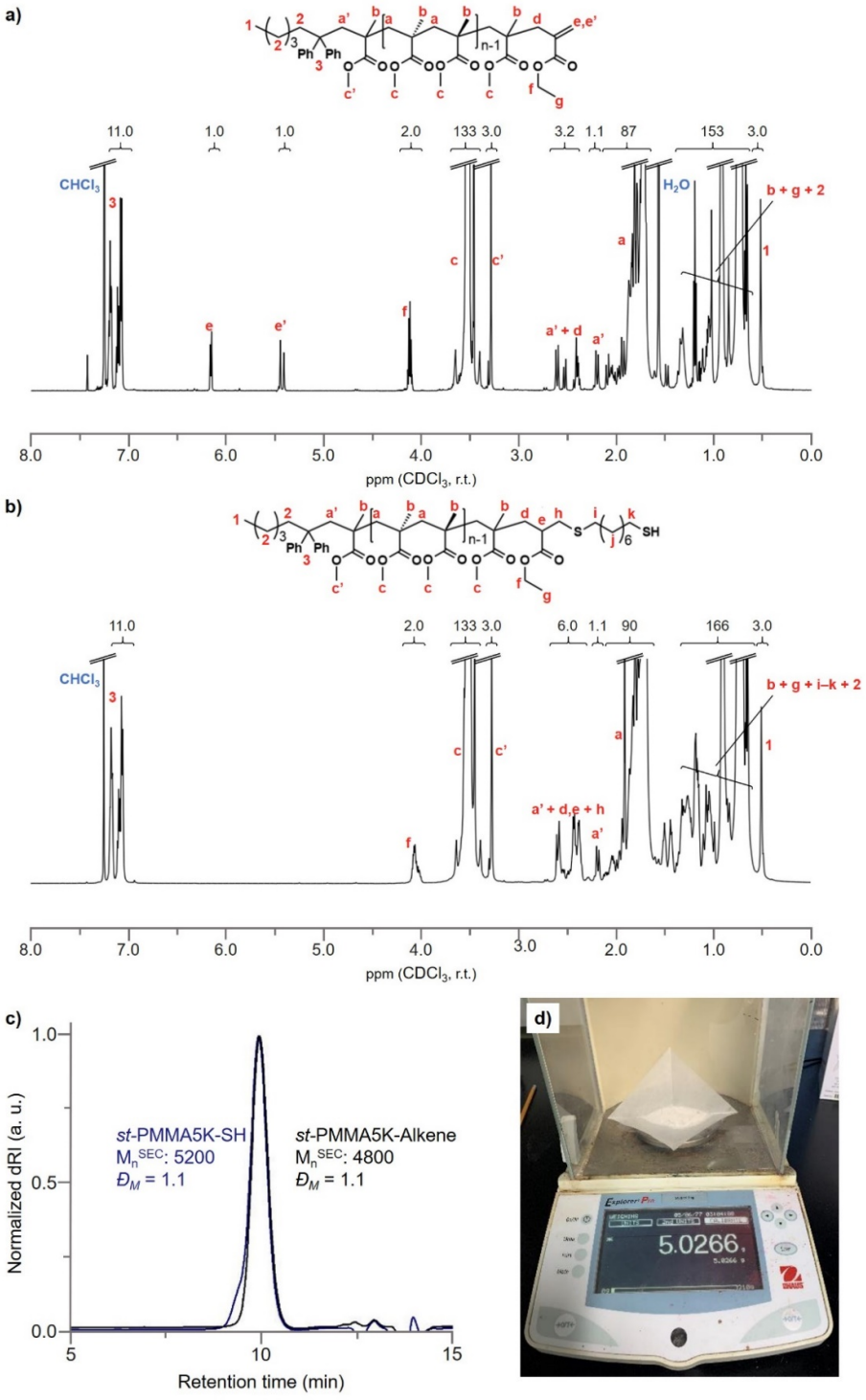


Figure A9. [1]H NMR traces show successful large-scale synthesis of a) *st*-PMMA5K-Alkene and b) *st*-PMMA5K-SH. c) SEC-RI traces show narrow dispersity for *st*-PMMA5K-Alkene and *st*-PMMA5K-SH (some disulfide coupling is observed, but it does not affect functionalization). d) Image of final yield for *st*-PMMA5K-SH.

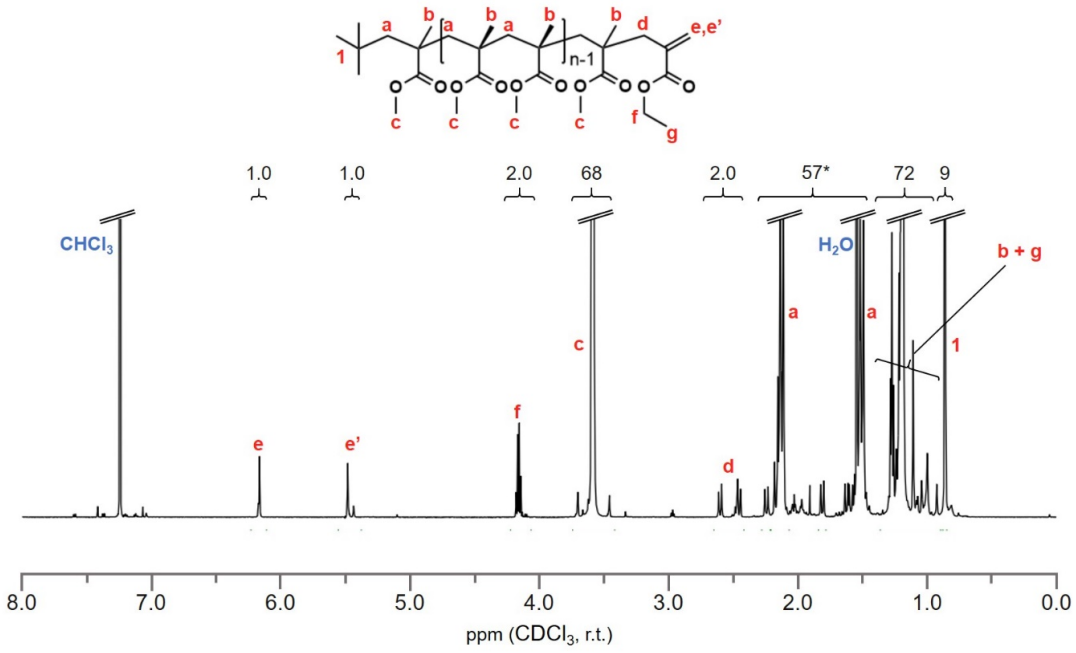


Figure A10. Representative ^{1}H NMR trace of *it*-PMMA3K-Alkene.

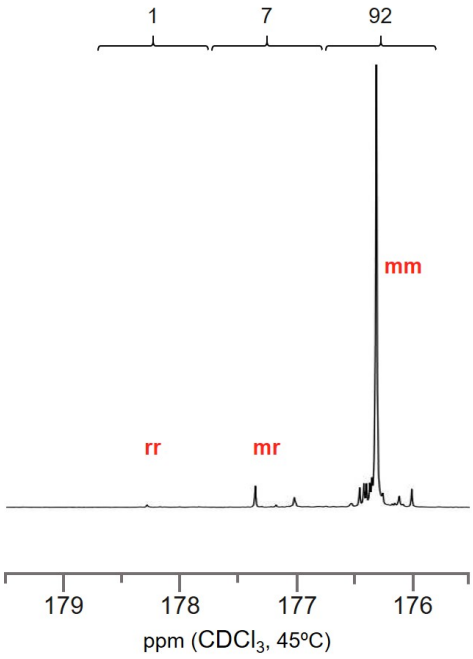


Figure A11. Partial ^{13}C NMR spectrum of *it*-PMMA3K-Alkene illustrating the tacticity determination.

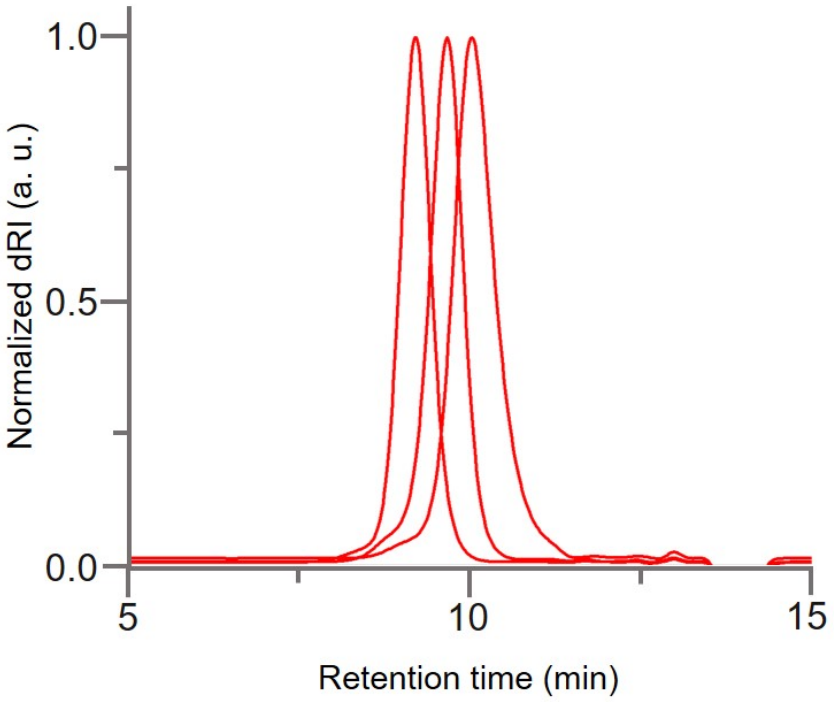


Figure A12. SEC-RI traces of isolated *it*-PMMA3K, 6K and 12K-Alkene.

Table A2. Result summary of alkene-terminated *it*-PMMA.

Sample	SEC		NMR		
	M_n^{SEC}(Da)	$Đ_M$	M_n^{NMR}(Da)	mm/mr/rr	F_n (C=C)
it-PMMA3K	3300	1.2	2200	92/7/1	0.97
it-PMMA6K	7300	1.2	5400	93/6/2	0.90
it-PMMA12K	14000	1.1	10500	94/4/2	0.80

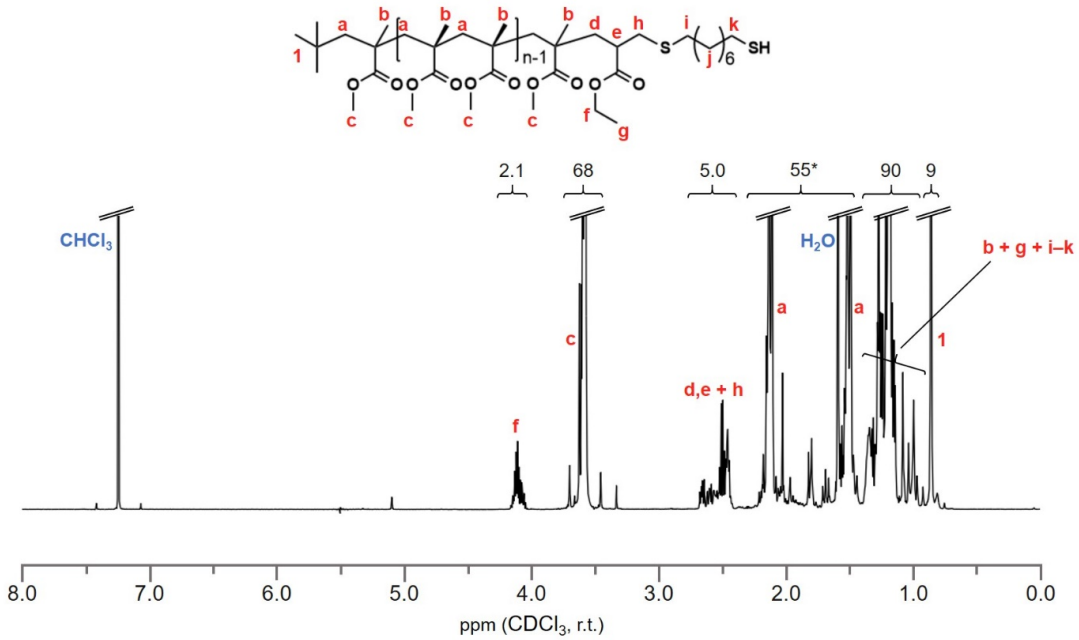


Figure A13. Representative ^{1}H NMR trace of *it*-PMMA3K-SH.

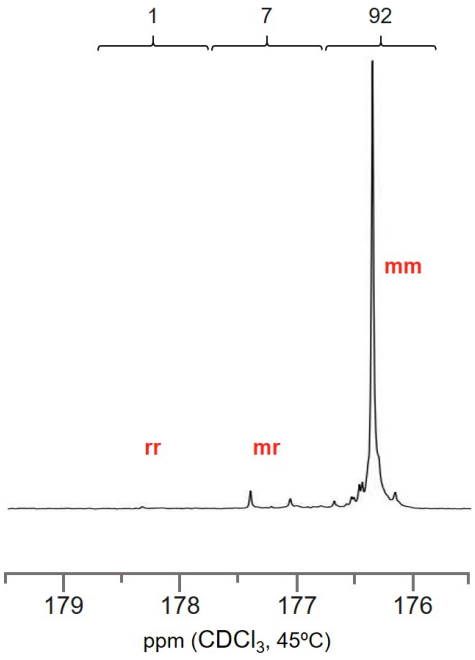


Figure A14. Partial ^{13}C NMR spectrum of *it*-PMMA3K-SH illustrating the tacticity determination.

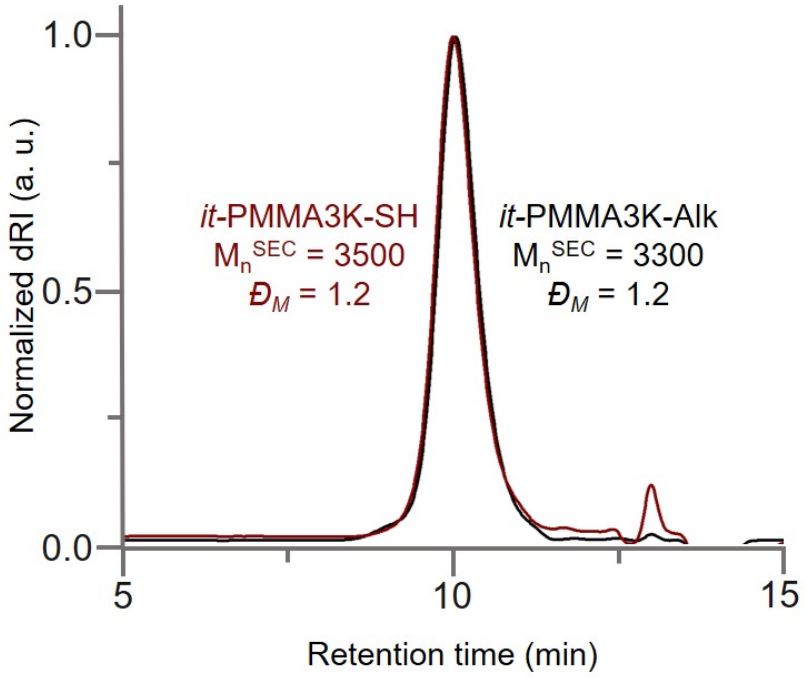


Figure A15. SEC-RI trace overlay of *it*-PMMA3K-Alkene before and *it*-PMMA3K-SH after the chain end modification.

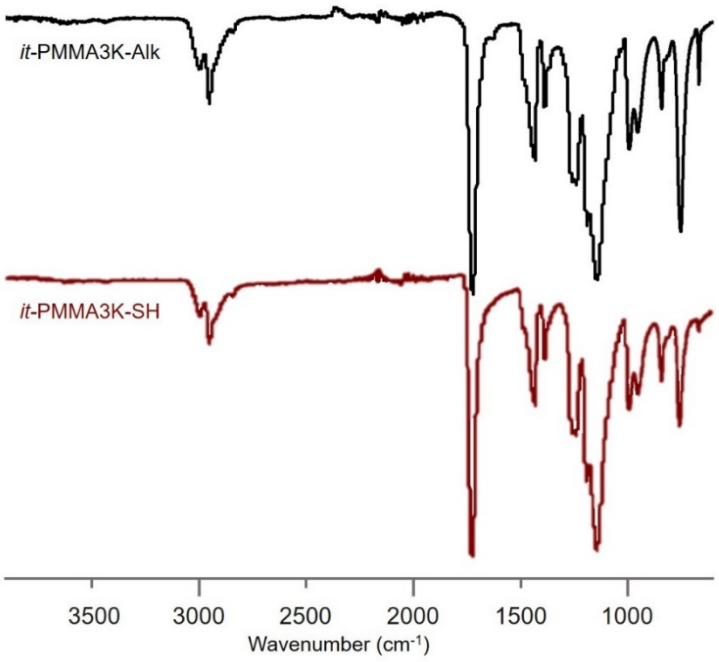


Figure A16. FT-IR spectra of *it*-PMMA3K-Alkene before and *it*-PMMA3K-SH after the chain end modification.

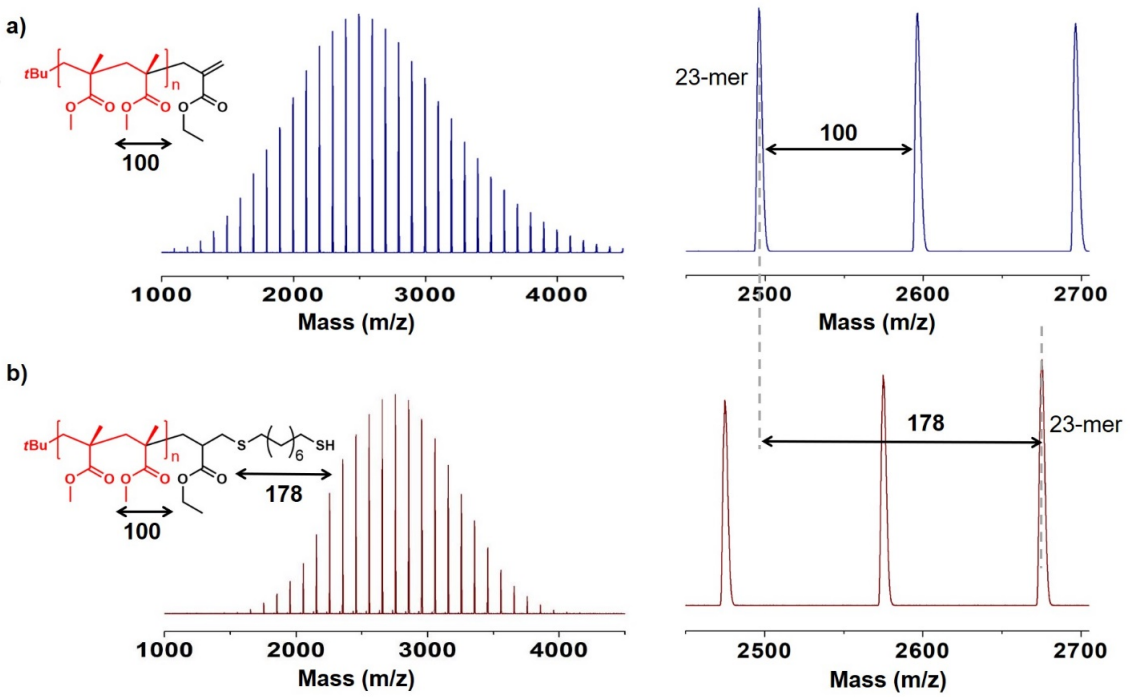


Figure A17. MALDI-ToF mass spectra of *it*-PMMA3K-Alkene before and *it*-PMMA3K-SH after the chain end modification.

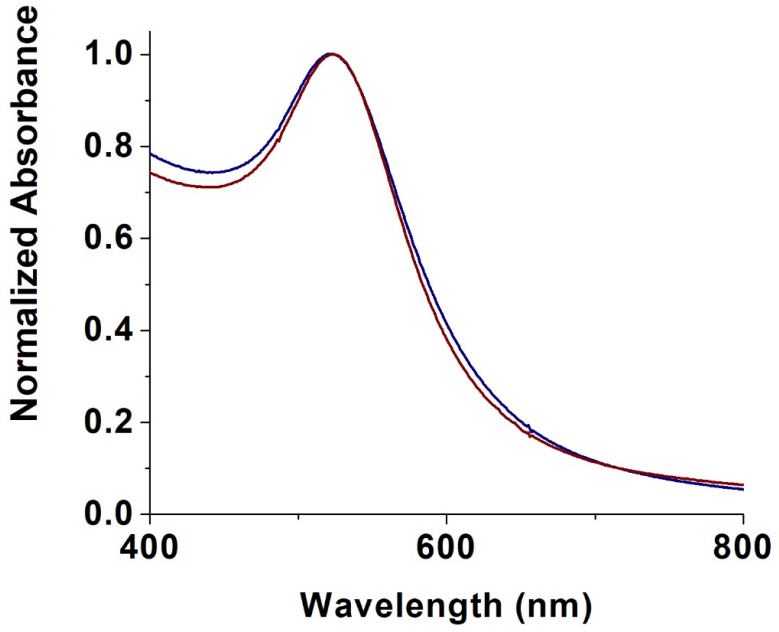


Figure A18. UV-Vis spectra of *st*-PMMA6K-Au NPs (blue) and i*t*-PMMA3K-Au NPs (red).

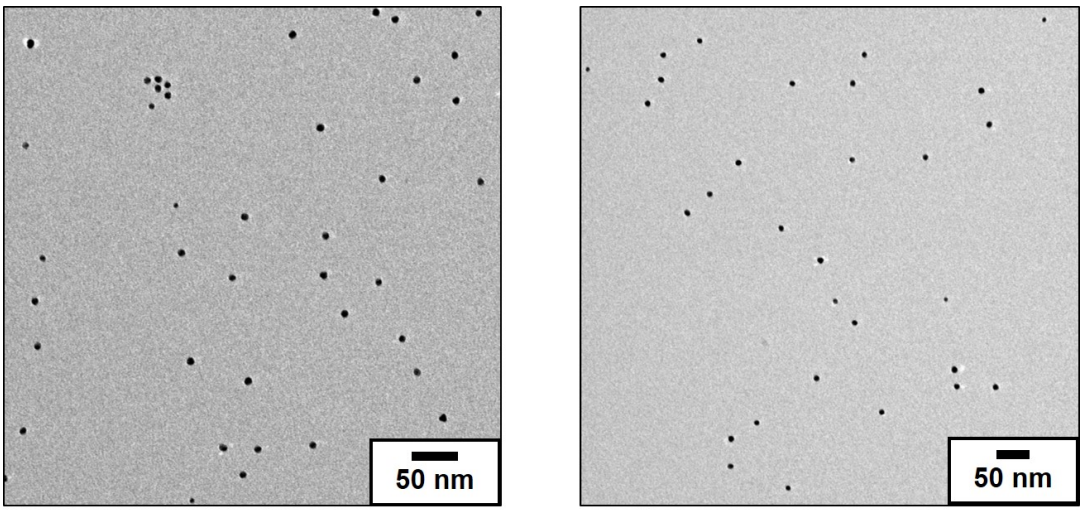


Figure A19. TEM images of *it*-PMMA3K-Au NPs (left) and *st*-PMMA6K-Au NPs (right).

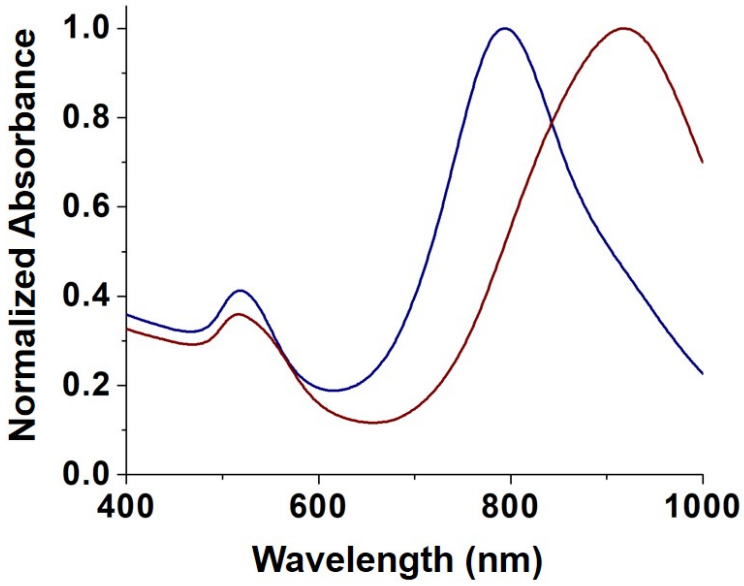


Figure A20. UV-Vis spectra of *st*-PMMA10K-Au NRs (blue) and *it*-PMMA12K-Au NRs (red).

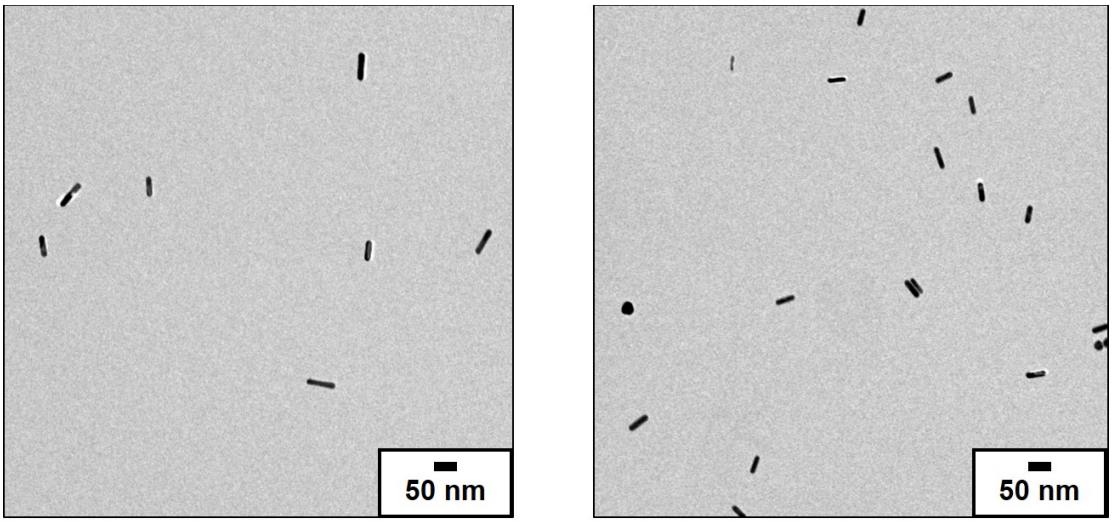


Figure A21. TEM images of *it*-PMMA12K-Au NRs (left) and *st*-PMMA10K-Au NRs (right).

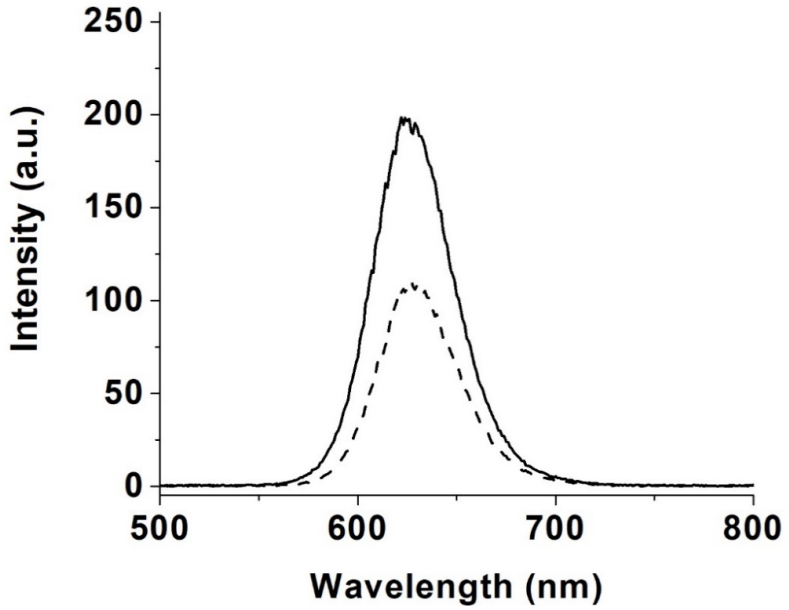


Figure A22. PL spectra of *it*-PMMA3K-QDs (solid) and *it*-PMMA3K-QDs + *it*-PMMA3K-Au NPs (dashed).

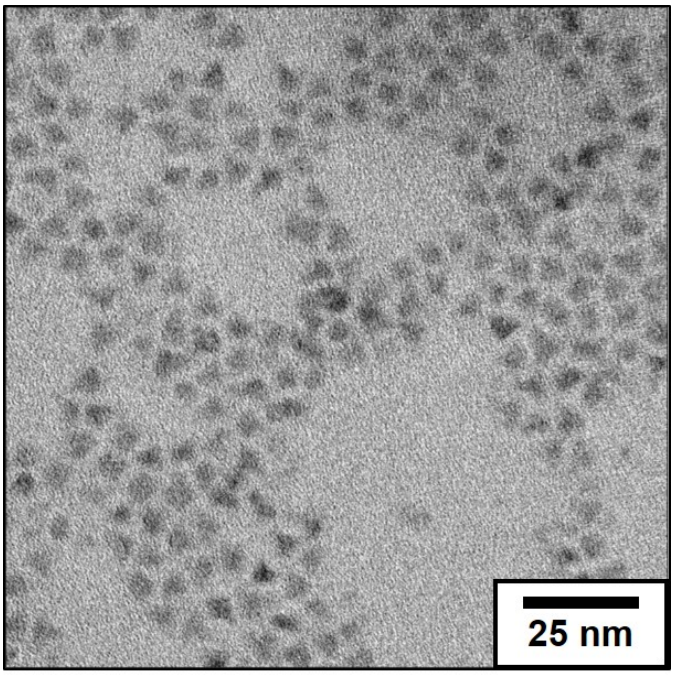


Figure A23. TEM image of *it*-PMMA3K-QDs.

Table A3. Ligand Densities of stereoregular nanoparticles from TGA analysis.

Sample	Average Diameter by TEM (nm)	Ligand Density (chains/nm^2)
it-PMMA3K-Au NPs	7.5 ± 0.7	2.5
st-PMMA6K-Au NPs	8.0 ± 0.8	2.0
it-PMMA12K-Au NRs	(58 ± 8) × (12 ± 1)	0.7
st-PMMA10K-Au NRs	(43 ± 5) × (12 ± 1)	0.8
it-PMMA3K-QDs	5.0 ± 1.1	1.2

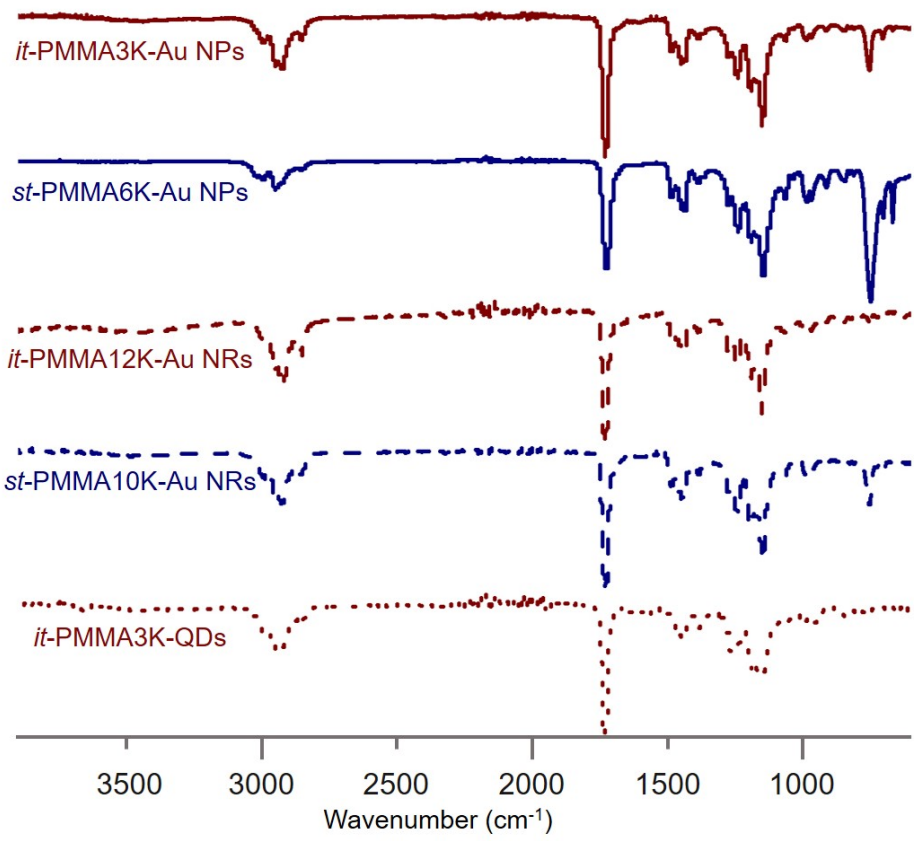


Figure A24. FT-IR spectra of stereoregular PMMA nanoparticles.

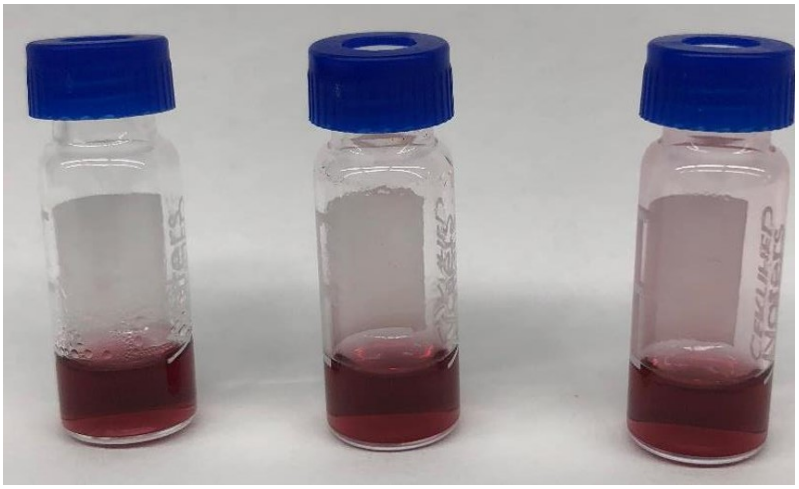


Figure A25. Image of *st*-PMMA6K-Au NPs (left), 1:1 *st*-PMMA6K-Au NPs + *it*-PMMA3K Au NPs (center) and *it*-PMMA3K-Au NPs (right) after heating for 5 minutes at 70 °C.

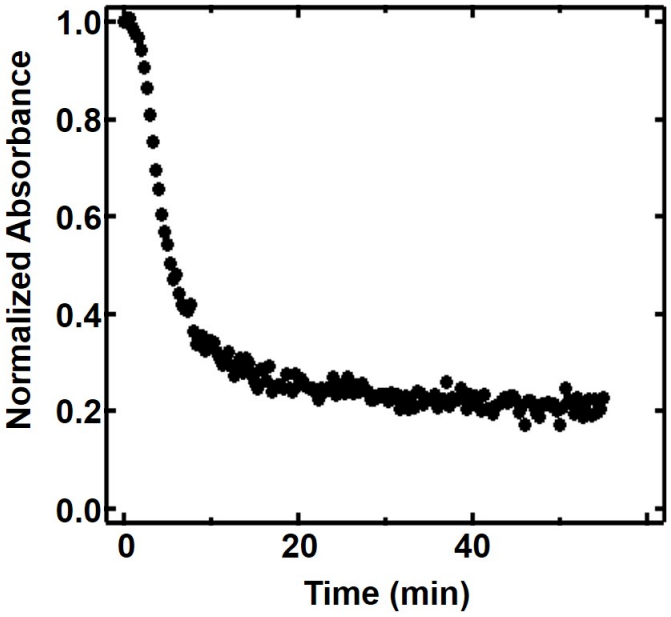


Figure A26. Normalized extinction at 530 nm of *st*-PMMA6K-Au NPs + *it*-PMMA3K-Au NPs during stereocomplexation.

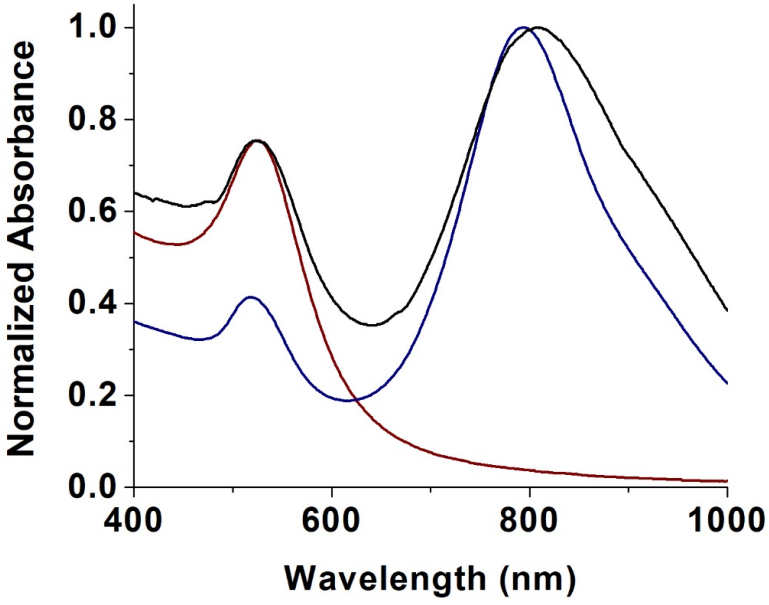


Figure A27. UV-Vis spectra of *it*-PMMA3K-Au NPs (red), *st*-PMMA10K-Au NRs (blue) and *it*-PMMA3K-Au NPs + *st*-PMMA10K-Au NRs (black).

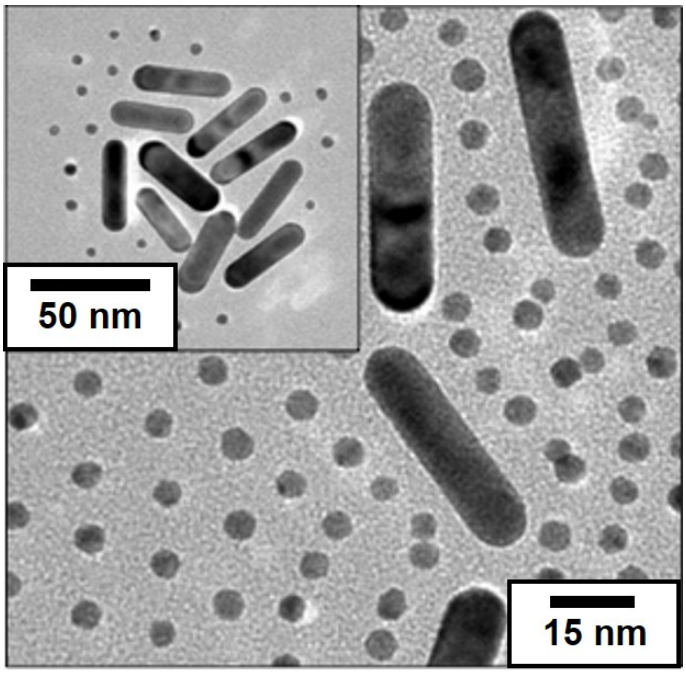


Figure A28. TEM image of *it*-PMMA3K-Au NPs + *it*-PMMA12K-Au NRs showing no stereocomplexation.

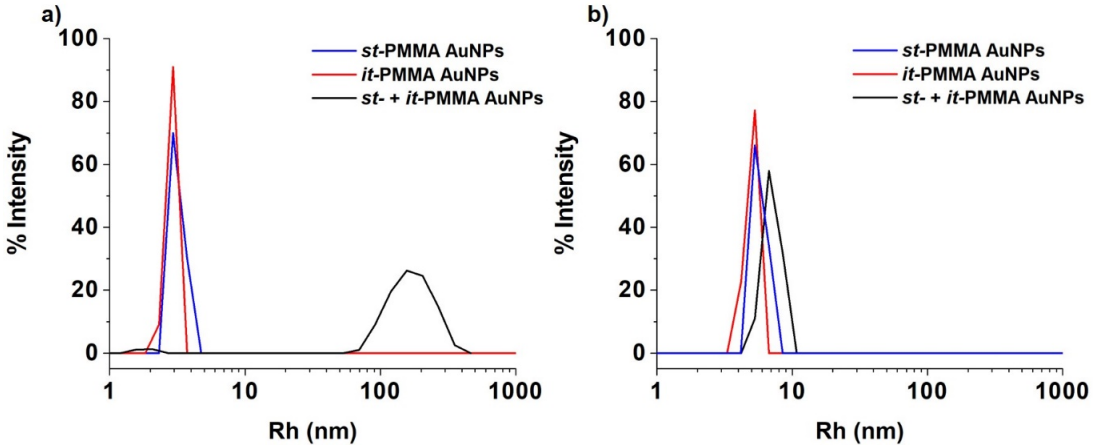


Figure A29. DLS traces of a) *st*-PMMA6K-Au NPs, *it*-PMMA3K-Au NPs and 1:1 *st*-PMMA6K-Au NPs + *it*-PMMA3K-Au NPs (30 seconds after mixing) at 25 °C and b) *st*-PMMA6K-Au NPs, *it*-PMMA3K-Au NPs and 1:1 *st*-PMMA6K-Au NPs + *it*-PMMA3K-Au NPs (after 5 minutes of heating) at 70 °C. All measurements are made in acetonitrile.

Table A4. Size distribution of stereoregular nanoparticles by DLS analysis.

Sample	Temperature (°C)	Rh (nm)
it-PMMA3K-Au NPs	25	2.9 ± 0.5 nm
	70	5.1 ± 0.5 nm
st-PMMA6K-Au NPs	25	3.2 ± 0.7 nm
	70	5.8 ± 0.7 nm
1:1 *st*-PMMA6K-Au NPs + *it*-PMMA3K-Au NPs	25	181 ± 102 nm
	70	7.1 ± 1.0 nm

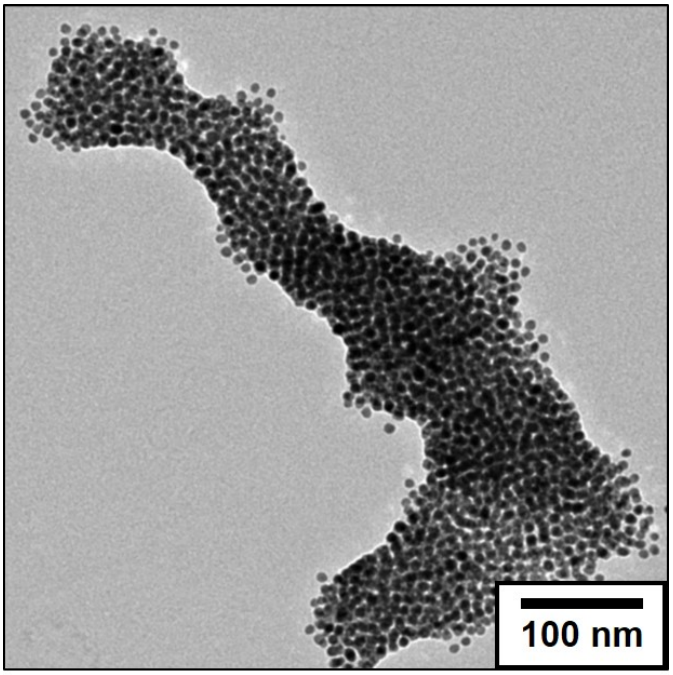


Figure A30. TEM image of 1:1 *st*-PMMA6K-Au NPs + *it*-PMMA3K-Au NPs after five heating/cooling cycles (70 °C for 5 minutes and 25 °C for 20 minutes).

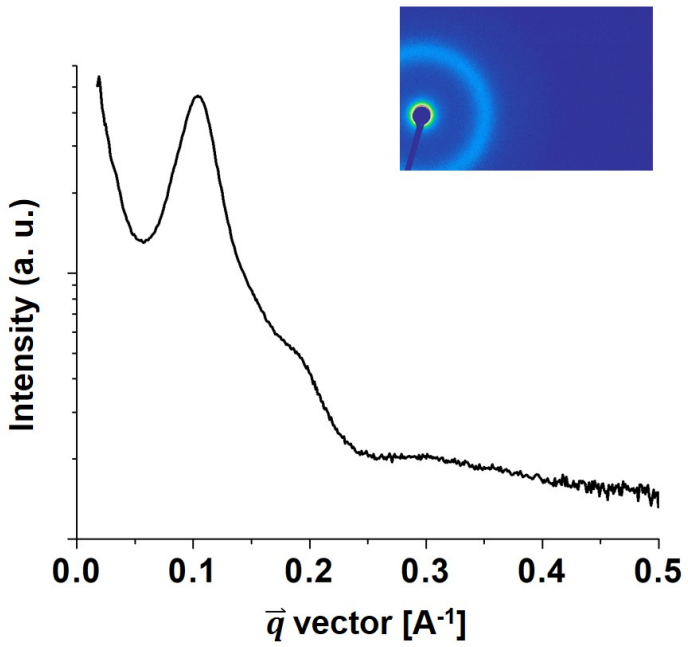


Figure A31. SAXS 1D plot (2D picture inset) for 1:1 *st*-PMMA6K-Au NPs + *it*-PMMA3K-Au NPs in acetonitrile.

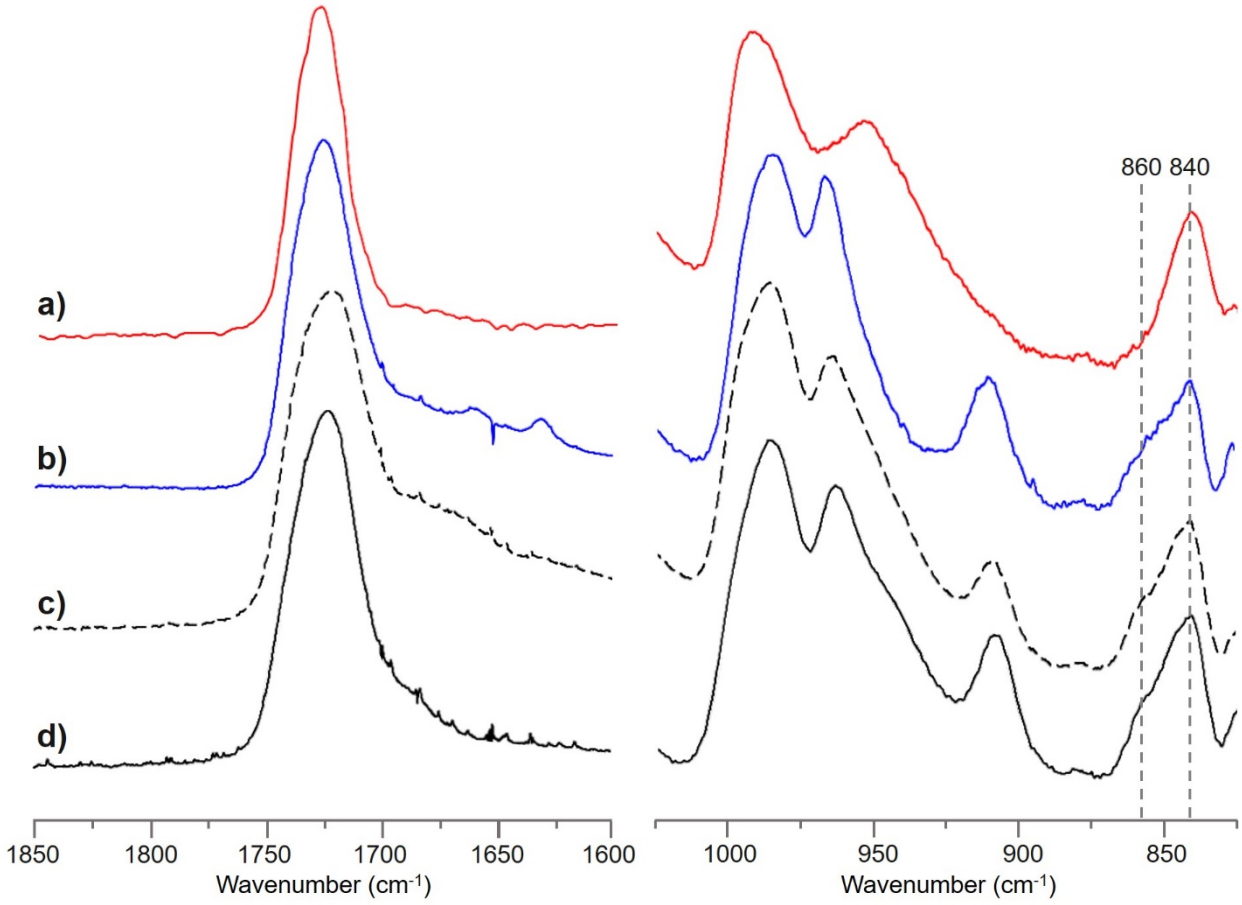


Figure A32. FTIR spectra of a) *it*-PMMA3K-Au NPs, b) *st*-PMMA6K-Au NPs, c) 1:1 *st*-PMMA6K-Au NPs + *it*-PMMA3K-Au NPs and d) 2:1 *st*-PMMA6K + *it*-PMMA3K cast from acetonitrile showing the main-chain CH_2-rocking band at 840 cm^{-1} for amorphous *st*-PMMA and both crystalline and amorphous states of *it*-PMMA.[9] In addition, a shoulder is observed at 860 cm^{-1} for both *st*- + *it*-PMMA nanoparticle and bulk polymer mixtures corresponding to the main-chain CH_2-rocking band of helical *st*-PMMA indicating partial stereocomplexation. The carbonyl stretch of PMMA at 1730 cm^{-1} was also examined however no distinct difference was observed between these bands for the samples in this work, similar with previous literature [9,10]

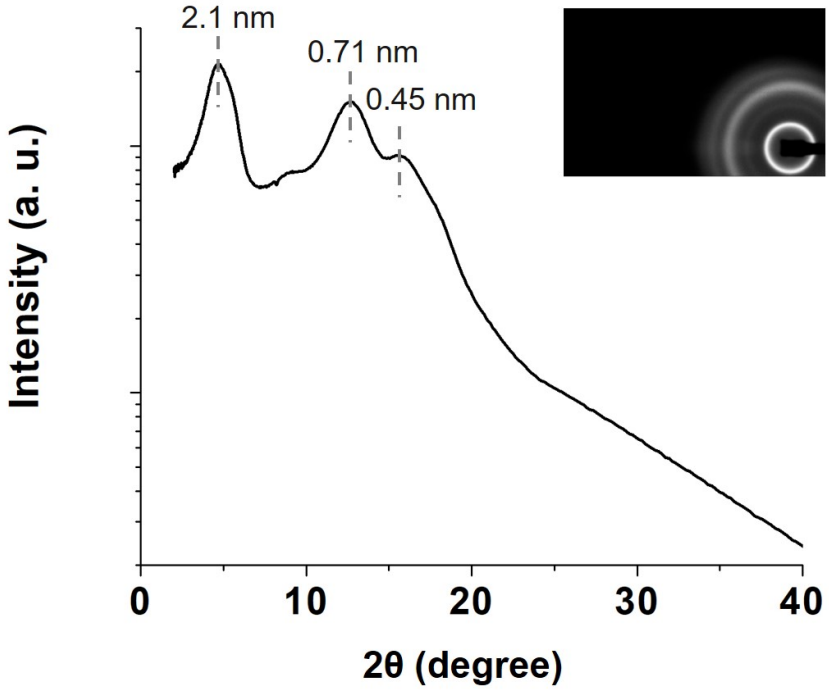


Figure A33. WAXS 1D plot (2D picture inset) of a 2:1 *st*-PMMA6K + *it*-PMMA3K mixture indicating triple-helix formation.[11,12]

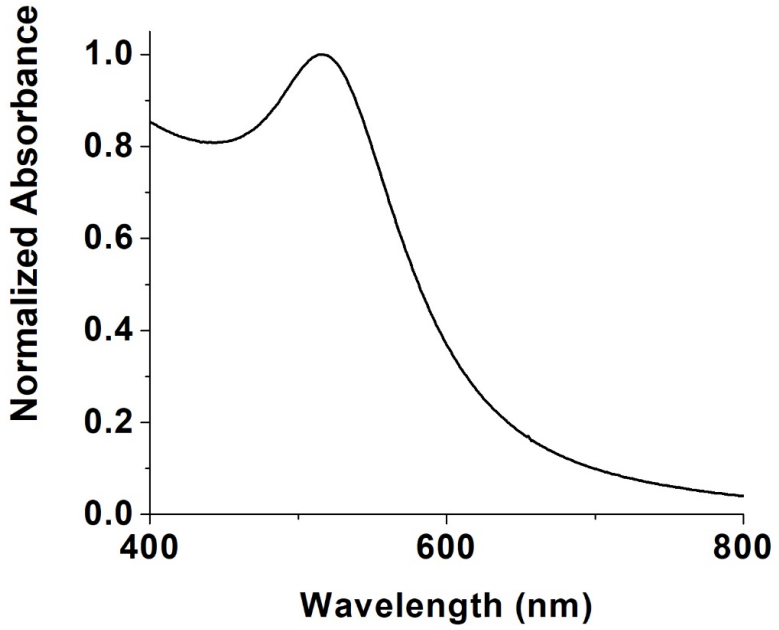


Figure A34. UV-Vis spectrum of *at*-PMMA6K-Au NPs.

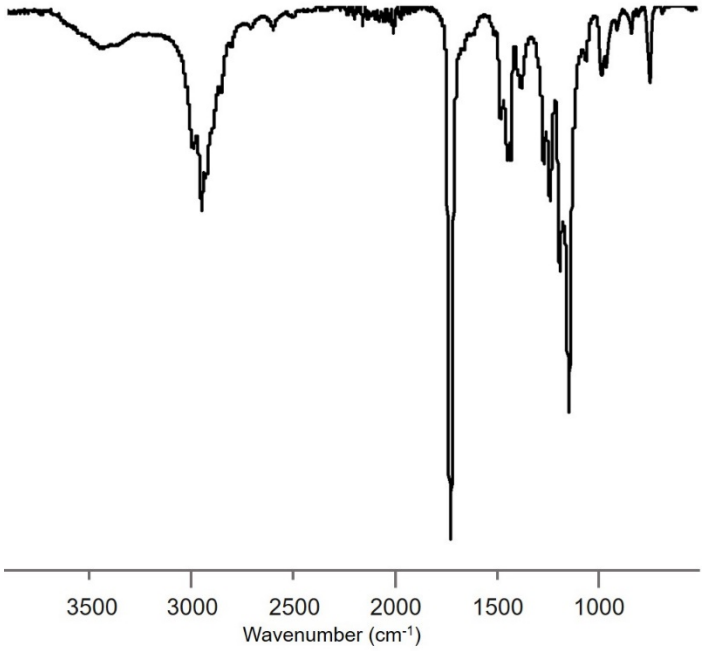


Figure A35. FT-IR spectrum of *at*-PMMA6K-Au NPs.

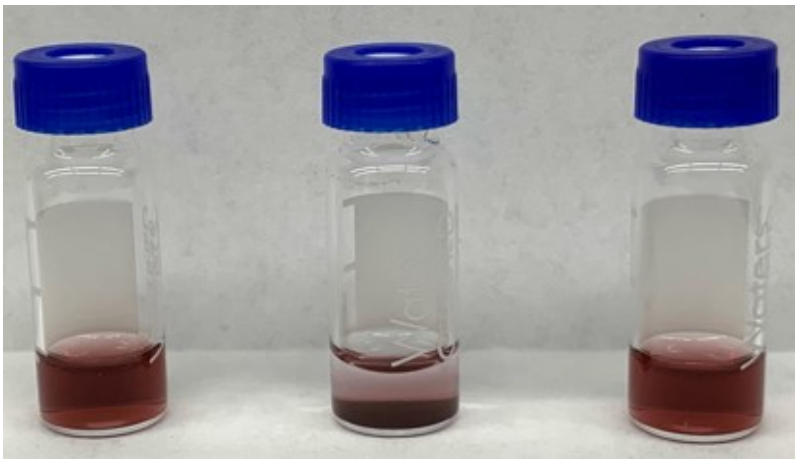


Figure A36. Image of 1:1 *st*-PMMA6K-Au NPs + *at*-PMMA6K Au NPs (left), 1:1 *st*-PMMA6K-Au NPs + *it*-PMMA3K Au NPs (center) and 1:1 *at*-PMMA6K-Au NPs + *it*-PMMA3K Au NPs (right).

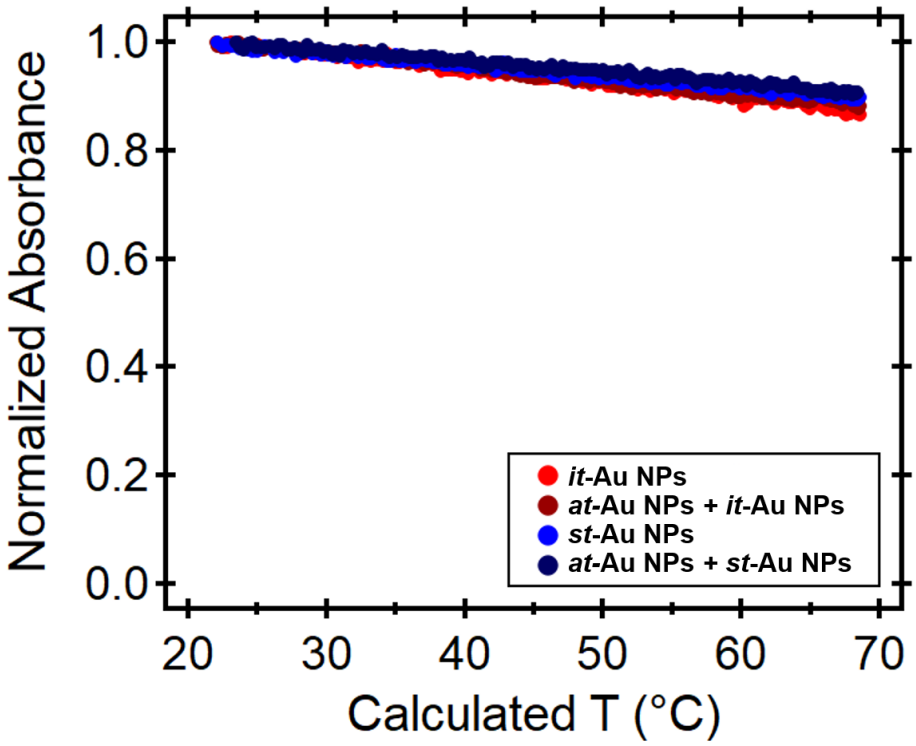


Figure A37. Normalized extinction of *st*-PMMA6K-Au NPs, *it*-PMMA3K-Au NPs and 1:1 mixture with *at*-PMMA6K-Au NPs while heating (heating rate: 1 °C/min) at 530 nm.

References

1. Ulrich, S.; Hemmer, J. R.; Page, Z. A.; Dolinski, N. D.; Rifaie-graham, O.; Bruns, N.; Hawker, C. J.; Boesel, L. F.; Read de Alaniz, J., *ACS Macro Lett.* **2017,** *6,* 738-742.
2. Zayas, M.; Dolinski, N. D.; Self, J.; Abdilla, A.; Hawker, C. J.; Bates, C. M.; Read de Alaniz, J., *ChemPhotoChem*, **2019**, *3*, 467-472.
3. Cao, Z. K.; Okamoto, Y.; Hatada, K., *KOBUNSHI RONBUNSHU* **1986**, *43*, 857-861.
4. Hatada, K.; Ute, K.; Tanaka, K.; Kitayama, T.; Okamoto, Y., *Polym. J.* **1985**, *17*, 977-980.
5. Ren, J. M.; Satoh, K.; Goh, T. K.; Blencowe, A.; Nagai, K.; Ishitake, K.; Christofferson, A. J.; Yiapanis, G.; Yarovsky, I.; Kamigaito, M.; Qiao, G. G., *Angew. Chem., Int. Ed.* **2014**, *53*, 459-464.
6. Zheng, N.; Fan, J.; Stucky, G. D., *J. Am. Chem. Soc.* **2006**, *128*, 6550-6551.
7. Scarabelli, L.; Sánchez-Iglesias, A.; Pérez-Juste, J.; Liz-Marzán, L. M., *J. Phys. Chem. Lett.* **2015**, *6*, 4270-4279.
8. Bae, W. K.; Char, K.; Hur, H.; Lee, S., *Chem. Mater.* **2008**, *20*, 531-539.
9. Kumaki, J.; Kawauchi, T.; Okoshi, K.; Kusanagi, H.; Yashima, E. *Angew. Chem. Int. Ed.* **2007**, *46*, 5348–5351.
10. J. Dybal, J. Štokr, B. Schneider, *Polymer,* **1983**, *24*, 971-980.
11. Ren, J. M.; Lawrence, J.; Knight, A. S.; Abdilla, A.; Zerdan, R. B.; Levi, A. E.; Oschmann, B.; Gutekunst, W. R.; Li, Y.; McGrath, A. J.; Bates, C. M.; Qiao, G. G.; Hawker, C. J. *J. Am. Chem. Soc.* **2018,** *140*, 1945-1951.
12. Kawauchi, T.; Kumaki, J.; Okoshi, K.; Yashima, E. *Macromolecules*, **2005**, *38*, 9155-9160.

Appendix B. Supporting Information for Chapter 3

GENERAL EXPERIMENTAL SECTION

Materials

Chlorodimethylsilane (TCI America, 95%), Ethylene glycol monoallyl ether (TCI America, 98%), Trimethylolpropane allyl ether (Sigma Aldrich), Vinyltrimethoxysilane (Sigma Aldrich, 98%), Allyl Glycidyl Ether (Sigma Aldrich, 98%), Allyl butyl ether (TCI America, 99%), Tetrakis(vinyldimethylsiloxy)silane (Gelest, 95%), 2-Bromoisobutyryl bromide (Alfa Aesar, 97%), Triethyamine (Alfa Aesar, 99%), Karstedt's Catalyst (Gelest, 2% Pt in xylenes), thiol-grafted PDMS (Gelest, SMS-141, 15 – 17 mol% thiol content), and Sodium Bicarbonate (Sigma Aldrich, 99.7%) were used as received. 3-Chloropropyldimethylchlorosilane (Gelest, 97%), Vinyldimethylchlorodsilane (Gelest), 3-Methacryloxypropyldimethylchlorosilane (Gelest, tech), and [(5-Bicyclo[2.2.1.]hept-2-enyl)ethyl]dimethylchlorosilane were purified by vacuum distillation before use. Hexamethylcyclotrisiloxane (D_3, TCI America, 98%) was dried with CaH_2 at 80 °C overnight prior to purification by sublimation. Lithium bis(trimethylsilyl)amide solution (Sigma Aldrich, 1M in Toluene), *n*-Butyllithium solution (Sigma Aldrich, 1.6M in hexanes), Acetonitrile (Sigma. Aldrich, 99.8%) and Diethyl ether (TCI America, Anhydrous) were purchased and used without purification. N,N-Dimethylformamide (DMF), Hexanes and Toluene were collected under an Ar atmosphere from a solvent purification system (PureSolv, Innovative Technology Inc.) for polymerization and hydrosilylation use.

Characterization Methods

^{1}H spectroscopy measurements were conducted in $CDCl_3$ at 20 °C on a Varian spectrometer operating at 600 MHz. ^{13}C and ^{29}Si NMR spectra were measured in $CDCl_3$ at 20 °C on a Bruker spectrometer operating at 125 MHz and 99 MHz. The number-average molecular weight (M_n), weight-average molecular weight (M_w) and dispersity ($Đ$) for PDMS homopolymers were determined by Size Exclusion Chromatography (SEC) in 0.25 wt% triethylamine/chloroform using a Waters e2695 separation module with a Waters 2414 differential refractive index detector. The columns were calibrated against PS standards (Agilent Technologies). Mass spectra measurments were conducted on a Bruker MALDI-TOF mass spectrometer in positive reflectron mode; the analyte, matrix (DCTB) and cationization agent (NaTFA) were dissolved in THF at concentrations of 10, 10 and 1 mg/mL, respectively, and then mixed in a volume ratio of 10 : 1 : 0.3 μL of this solution was spotted onto a ground steel target plate and the solvent was allowed to evaporate prior to analysis. FTIR spectra were recorded on a Perkin Elmer Spectrum 100 FT-IR Spectrometer.

Synthesis Procedures

H-Si_4-Cl

H-Si_4-Cl was prepared according to a previously reported procedure.[1] Hexamethylcyclotrisiloxane (D_3, 95 g, 430 mmol), and chlorodimethylsilane (50 mL, 450 mmol) were added into a 1 L round bottom flask under an argon atmosphere. Acetonitrile (22 mL) was added followed by DMF (1.1 mL) and stirred at room temperature for 72 hours. The reaction mixture was then purified by vacuum distillation (40 °C, 500 microns) and H-Si_4-Cl was isolated as a colorless oil (99 g, 75% yield). ^{1}H NMR (600 MHz, $CDCl_3$): δ = 4.71 (sept, 1H, H-Si,), 0.45 (s, 6H, Cl-Si-$(CH_3)_2$), 0.20 (d, 6H, H-Si-$(CH_3)_2$), 0.13 (s, 6H, CH_3), 0.09 ppm

(s, 6H, CH_3); ^{13}C NMR (125 MHz, CDCl3): δ = 4.02, 0.85, 0.77, 0.64 ppm. ^{29}Si NMR (99 MHz, CDCl3: δ = 3.69, -6.66, -18.98, -19.34 ppm.

H-Si_4-OH

H-Si_4-OH was prepared according to a previously reported procedure.[1] A solution of sodium bicarbonate (5.87 g, 70 mmol) in 100 mL water and 400 mL diethylether was stirred and was cooled to 0 °C in an ice bath. A solution of H-Si_4-Cl (21.3 mL, 20.0 g, 64 mmol) in 300 mL dry diethyl ether was added dropwise over 90 minutes and stirred for an additional 45 minutes. The ice bath was then removed to warm the reaction to room temperature while stirring for another 90 minutes. The reaction mixture was then washed with water followed by brine. After concentrating by rotary evaporation, 20 mL of toluene was added before freezing the mixture in liquid nitrogen and dried azeotropically overnight under high vacuum. H-Si_4-OH (18 g, 95%) was isolated as a clear, colorless oil. ^1H NMR (600 MHz, $CDCl_3$): δ = 2.10 (s, 1H, HO-Si- $(CH_3)_2$), 0.20 (s, 6H, HO-Si-$(CH_3)_2$)), 0.15 (s, 6H, CH_3), 0.10 (s, 6H, CH_3), 0.08 ppm (s, 6H, CH_3); ^{13}C NMR (125 MHz, $CDCl_3$): δ = 0.97, 0.84, 0.65, 0.31 ppm. ^{29}Si NMR (99 MHz, $CDCl_3$): δ = -6.31, -10.40, - 19.25, -20.64 ppm.

General Procedure for H-Si_4-OLi initiated polymerizations of D_3

H-Si_4-OH (0.23 g, 0.4 mmol, 50 wt% in hexanes) was added to a dried 100 mL 3-neck round bottom flask with a stir bar under an argon atmosphere and was cooled to 0 °C in an ice bath. LiHMDS (0.4 mL, 0.4 mmol, 1M in hexanes) was added while stirring and the ice bath was removed to slowly warm the reaction mixture to room temperature while stirring for 10 minutes. Hexamethylcyclotrisoloxane (D_3, 2.05 g, 9.0 mmol, 49 wt% in hexanes) was added followed by the rapid injection of DMF (0.4 mL) under heavy stirring to promote the polymerization. The reaction was then quenched after 30 minutes (77% conversion) by adding

methacryloxypropyldimethylchlorosilane (MAPrSiCl, 0.22 mL, 1.0 mmol) and stirring overnight. The crude reaction mixture was then diluted with hexanes and washed with water, saturated $NaHCO_3$, and water again then dried with $MgSO_4$. The hexanes layer was then concentrated by rotatory evaporation and washed three times with acetonitrile before drying under high vacuum overnight to give H-PDMS-MA (1.5g, 84% yield) as a clear, colorless viscous liquid. The same procedure was then repeated with varying amounts of D_3, shorter polymerizations times or quenched with different chlorosilanes to produce α-Si-H functionalized PDMS with varying molecular weights and ω- functional groups. Additionally, different initiation strategies where LiHMDS was substituted with *n*-BuLi or H-Si_4-OH was replaced with butoxypropyloctamethyltetrasilanol (*n*-BuOPr-Si_4-OH) were conducted via the above procedure.

General Procedure for the hydrosilylation of Si-H functionalized polymers

H-PDMS-PrCl (300 mg, 0.06 mmol), ethylene glycol monoallyl ether (10 mg, 0.10 mmol) and 0.5 mL of dry toluene were added to a 1 dram vial with a stir bar and degassed by argon bubbling for 10 minutes. Karstedt's catalyst (0.5 μL, 2 wt% Pt in xylenes) was added and the mixture was placed on a heating block at 60 °C while stirring. After 24 hours, the reaction was concentrated by rotary evaporation and unreacted excess olefin was removed under high-vacuum while heating at 50 °C overnight to isolate HO-PDMS-PrCl (303 mg, 99%) as a clear, colorless oil. The same procedure was repeated with different olefins to install different functionalities. *n*-BuOPr-Si_4-OH (1 g, 99%) was also synthesized via the procedure above by hydrosilylation of H-Si_4-OH with allyl butyl ether.

Synthesis of tetrahedral PDMS-Norbornene crosslinker

H-PDMS-Norbornene (1 g, 0.36 mmol), Tetrakis(vinyldimethylsiloxy)silane (39 mg, 0.09 mmol) and 1 mL of dry toluene were added to a 1-dram vial with a stir bar and degassed by argon bubbling for 20 minutes. Karstedt's catalyst (2 μL, 2 wt% Pt in xylenes) was added and the mixture was placed on a heating block at 60 °C while stirring. After 24 hours, the reaction diluted with hexanes and passed through a silica then concentrated by rotary evaporation. The mixture was dried overnight to isolate tetrahedral-PDMS-Norbornene (1 g, 99%) as a clear, colorless oil.

Formation of tetrahedral PDMS-Norbornene-thiol crosslinked gels

Tetrahedral-PDMS-Norbornene (100 mg, 0.04 mmol), thiol-grafted PDMS (100 mg, 0.04 mmol) and DMPA (2 mg in 100 μL DCM) were added to a 1 dram and mixed by a Vortex Mixer. Excess DCM was then removed under reduced pressure before irradiating the mixture under a UV-nail lamp for 10 minutes to form a thick and transparent crosslinked film.

CHARACTERIZATION DATA

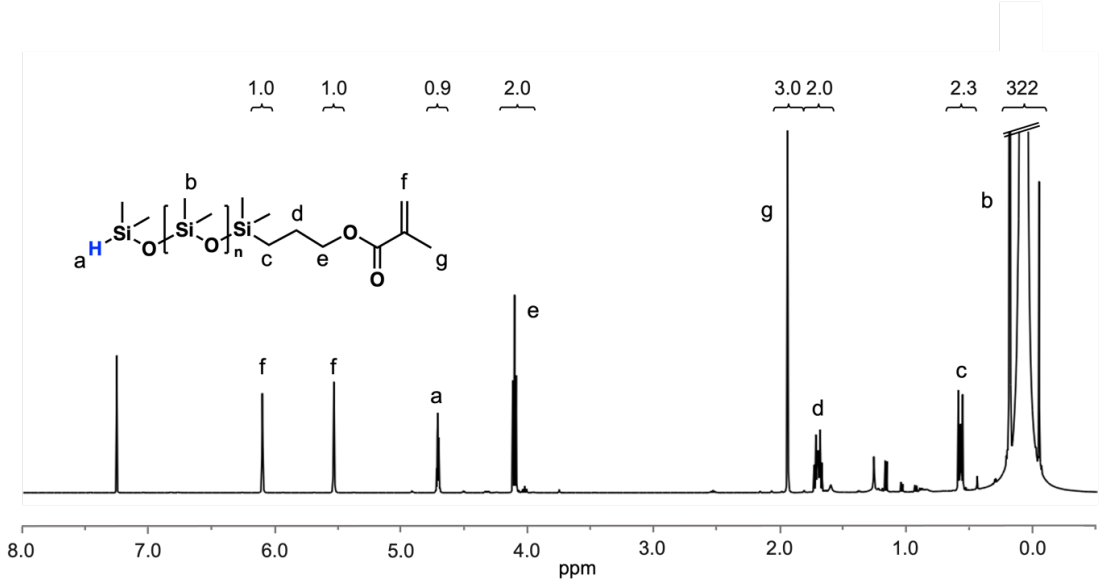


Figure B1. Representative ^{1}H NMR trace of H-PDMS-MA with LiHMDS as a Li agent

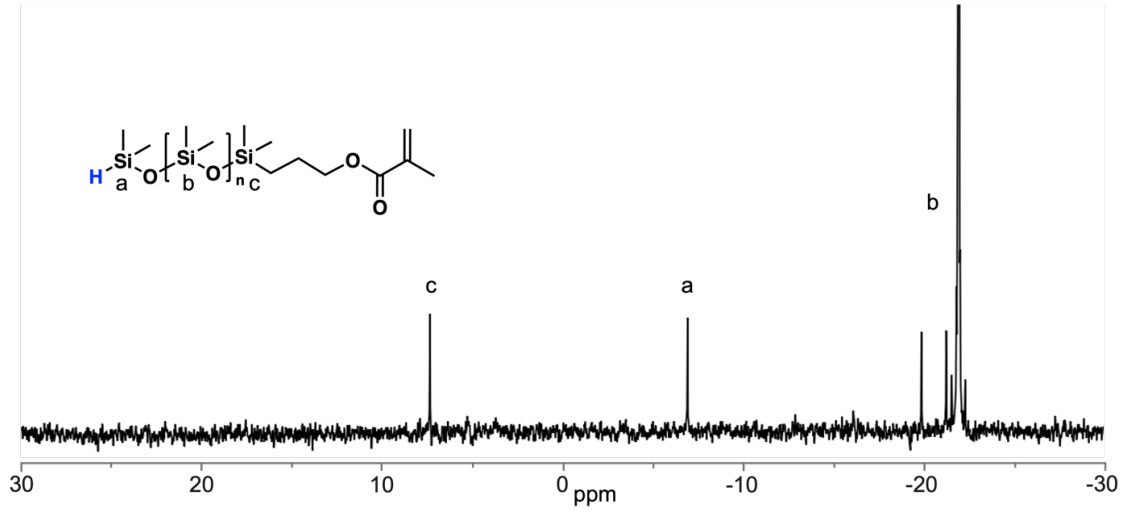


Figure B2. Representative ^{29}Si NMR trace of H-PDMS-MA with LiHMDS as a Li agent

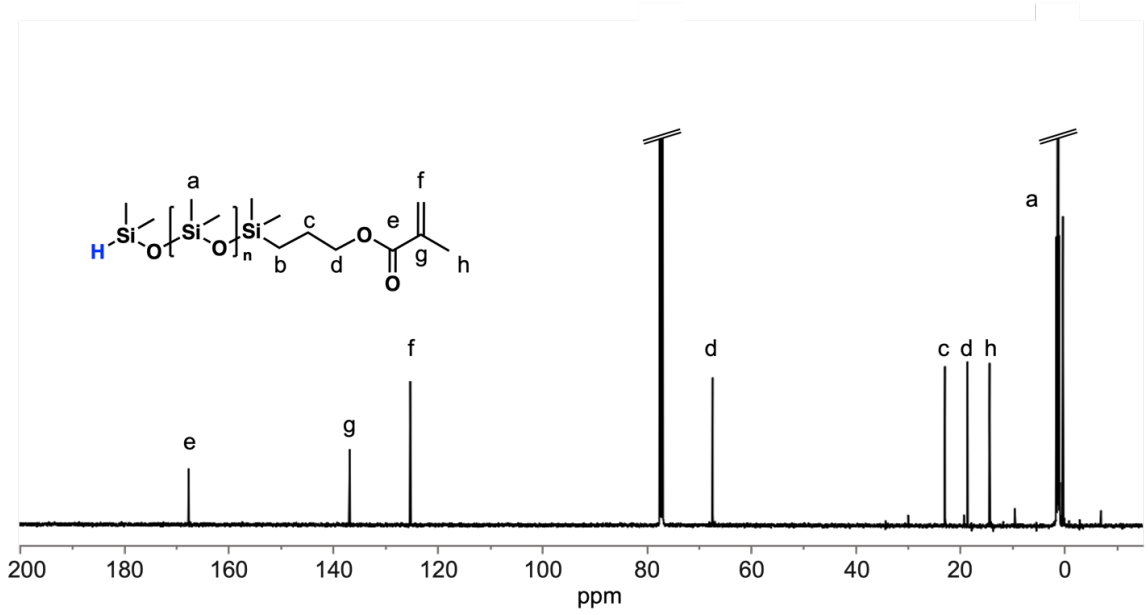


Figure B3. Representative ^{13}C NMR trace of H-PDMS-MA with LiHMDS as a Li agent

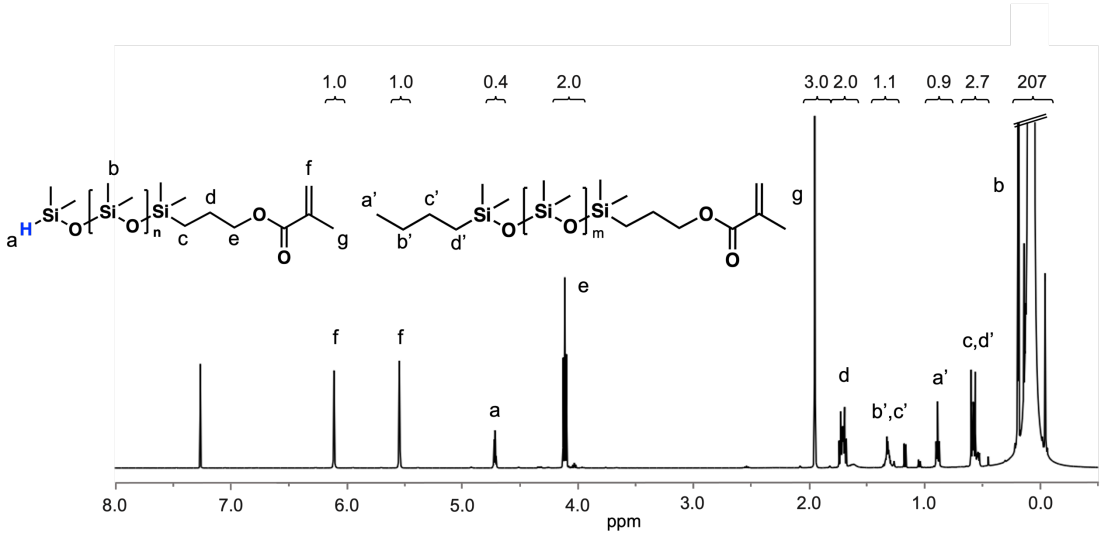


Figure B4. Representative ^{1}H NMR trace of H-PDMS-MA with *n*-BuLi as a Li agent

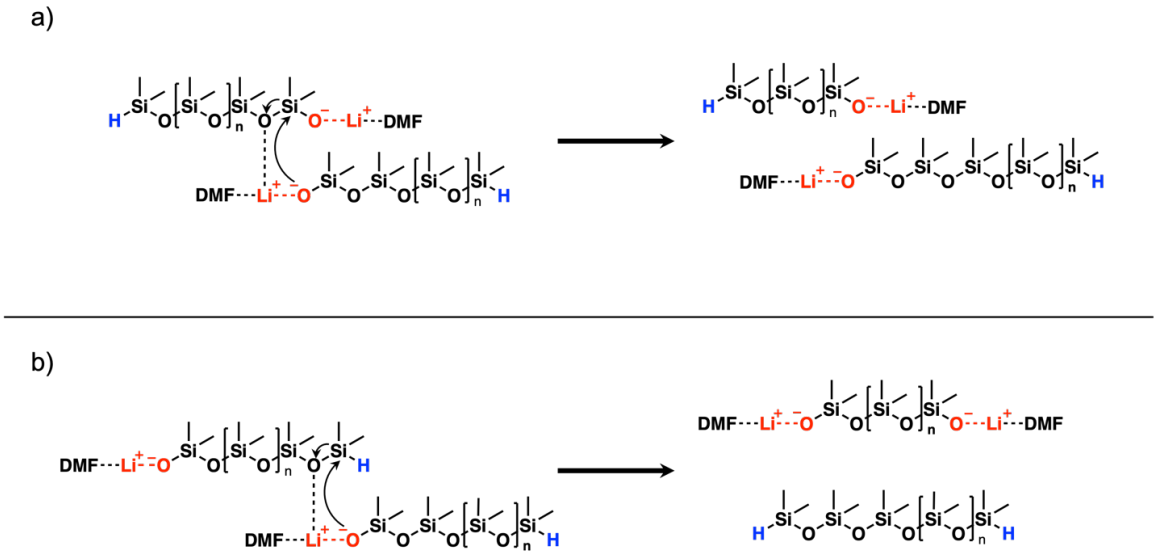


Figure B5. Reaction scheme showing chain-end exchange of a) Si-OLi groups and b) Si-OLi and Si-H groups

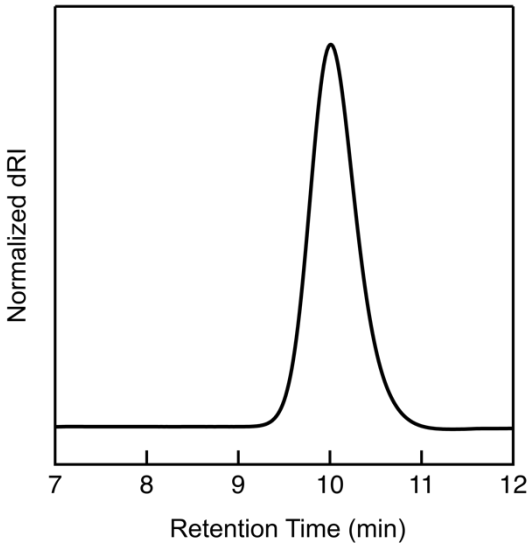


Figure B6. SEC-RI trace in chloroform AROPs initiated by H-Si$_4$-OLi with 92 eq of D_3 quenched after 5 minutes (20% conversion, M_n^{SEC} = 3.7 kDa, $Đ$ = 1.2). PDMS traces show negative RI values in chloroform and have been reversed for clarity.

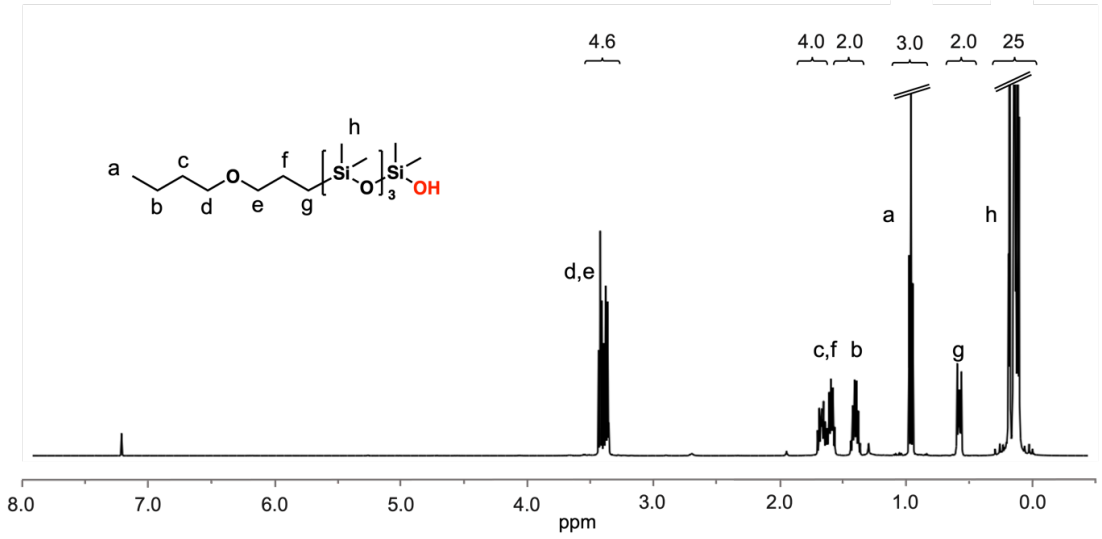


Figure B7. ^{1}H NMR trace of BuOPr-Si$_4$-OH

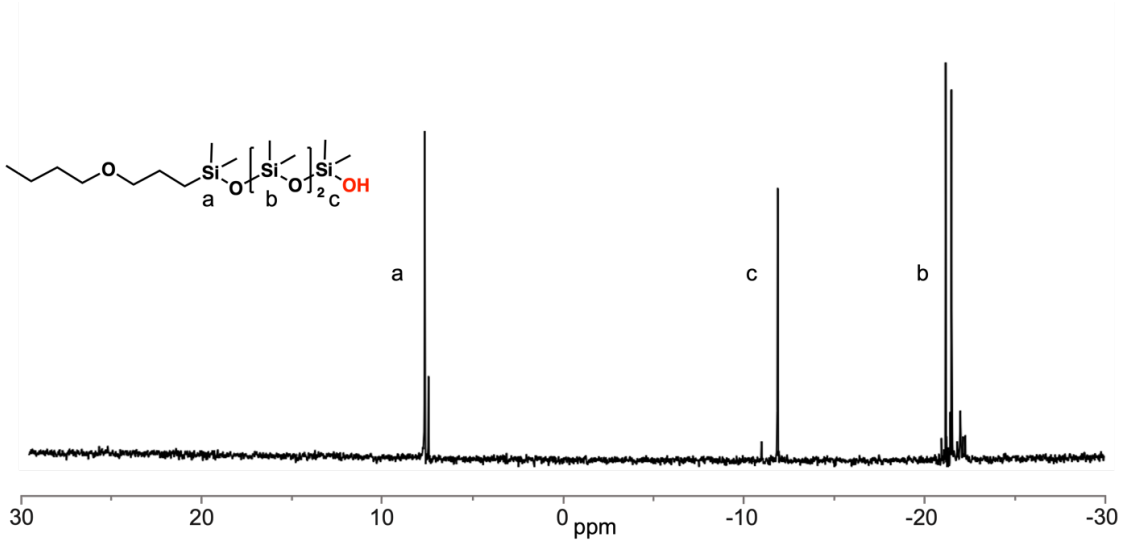


Figure B8. ^{29}Si NMR trace of BuOPr-Si$_4$-OH. The small second set of peaks arises from isomerization during hydrosilylation.[1]

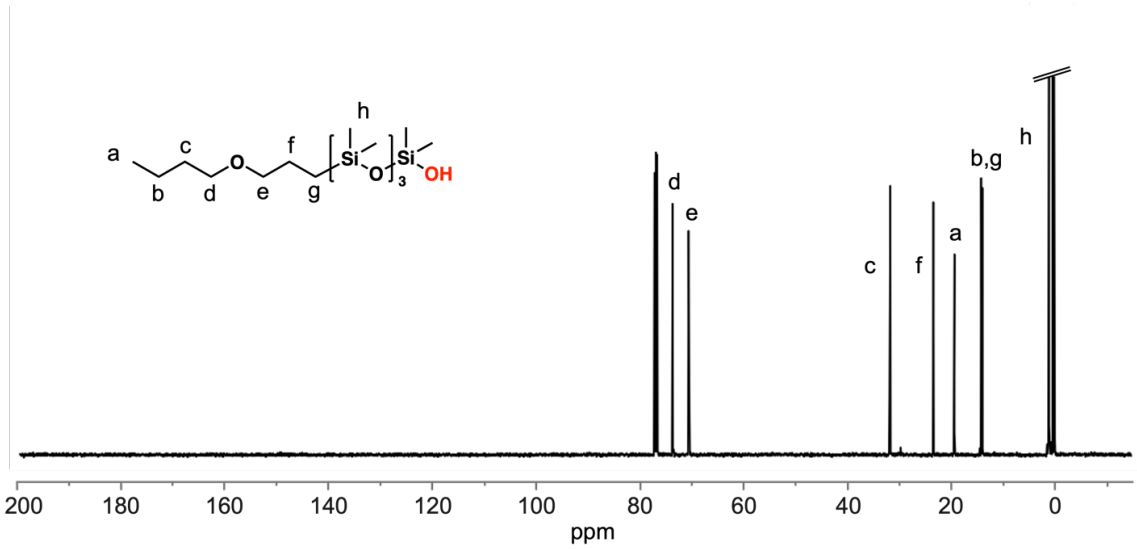


Figure B9.[13]C NMR trace of BuOPr-Si$_4$-OH.

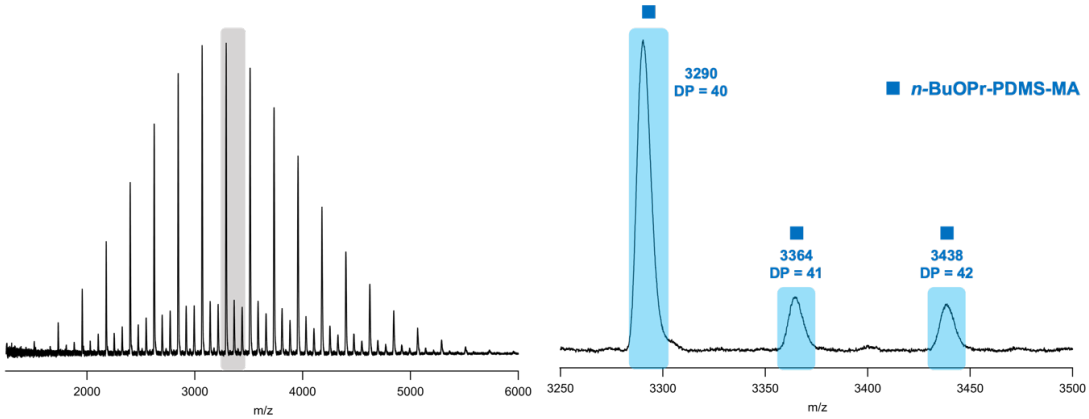


Figure B10. MALDI-ToF mass spectrum of BuOPr-PDMS-MA after 15 minutes polymerization (44% converson) showing the exchange of Si-OLi chain ends.

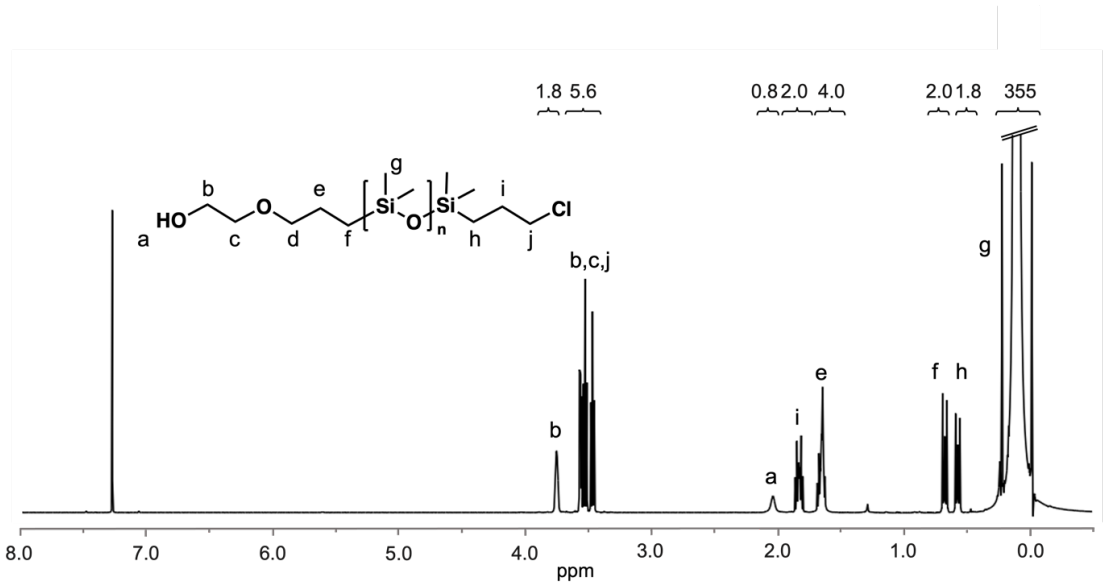


Figure B11. Representative ^{1}H NMR trace of HO-PDMS-PrCl after hydrosilylation

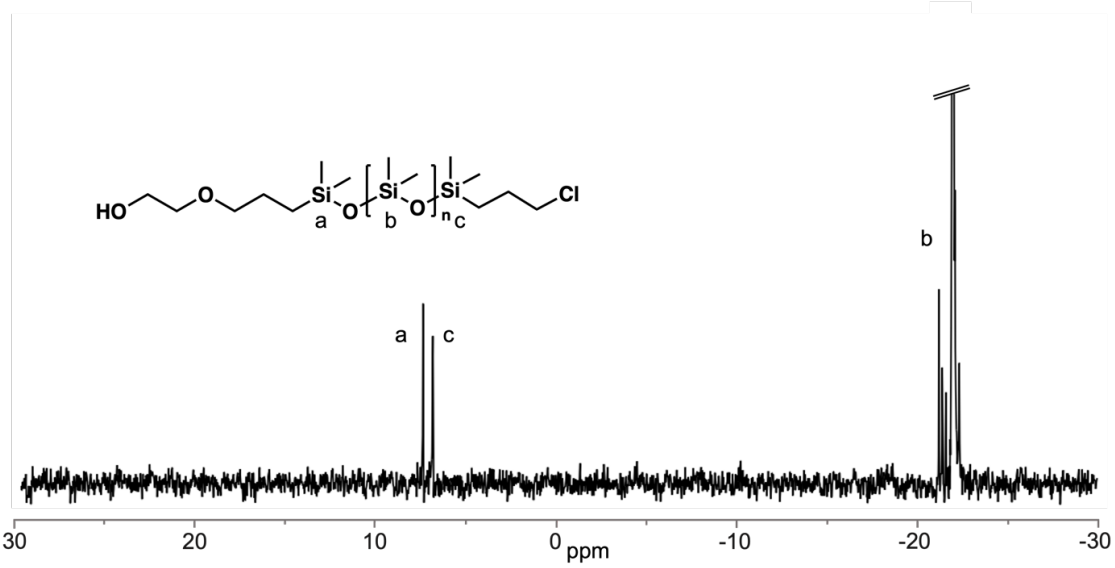


Figure B12. Representative ^{29}Si NMR trace of HO-PDMS-PrCl after hydrosilylation

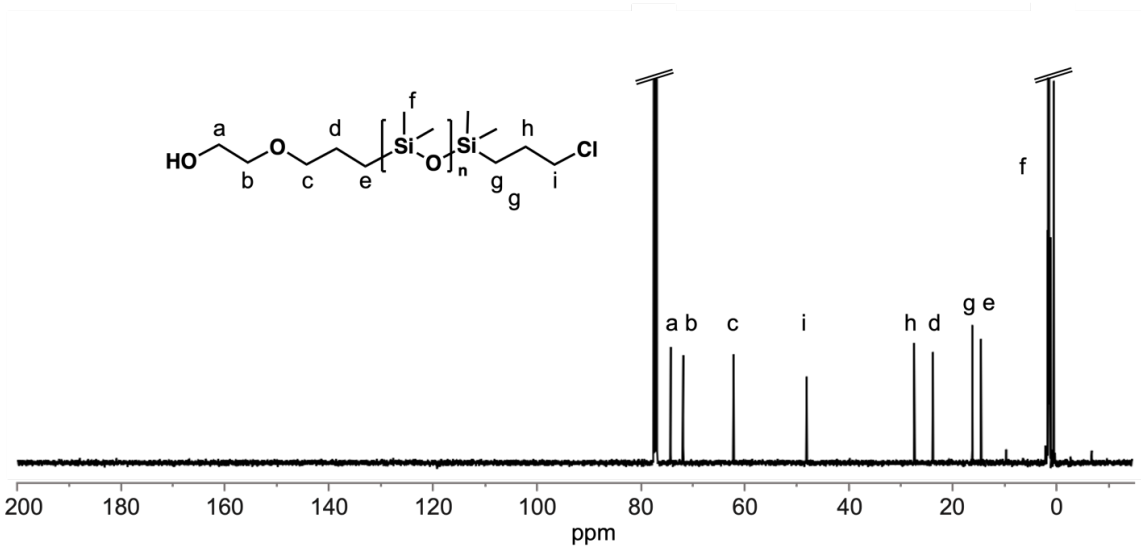


Figure B13. Representative ^{13}C NMR trace of HO-PDMS-PrCl after hydrosilylation

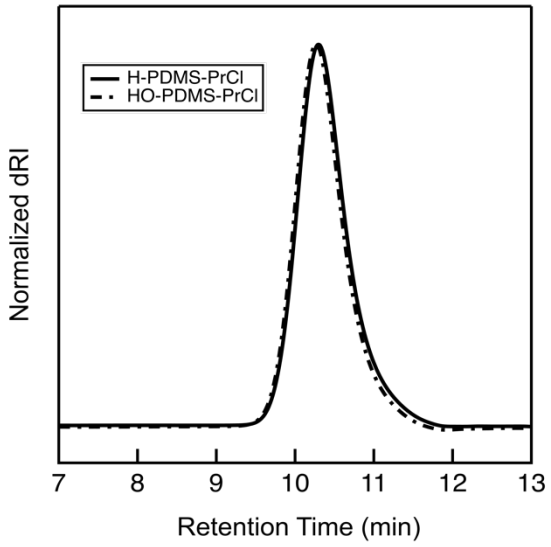


Figure B14. SEC-RI trace in chloroform of H-PDMS-ClPr (M_n^{SEC} = 4.9 kDa, $Đ$ = 1.2) and HO-PDMS-ClPr (M_n^{SEC} = 5.1 kDa, $Đ$ = 1.20). PDMS traces show negative RI values in chloroform and have been reversed for clarity.

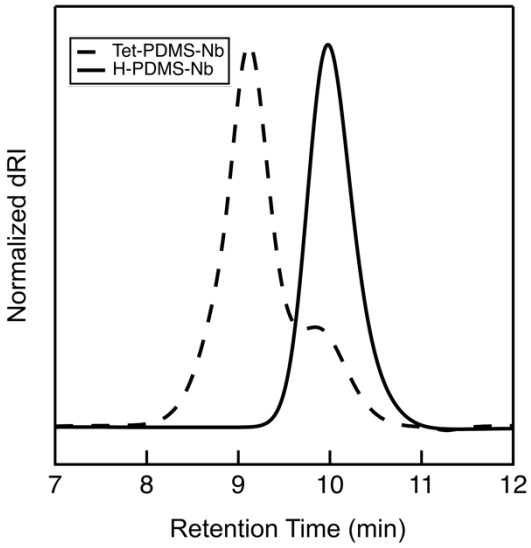


Figure B15. SEC-RI trace in chloroform of H-PDMS-Nb (M_n^{SEC} = 3.8 kDa, $Đ$ = 1.2) and tetrahedral PDMS-Nb (M_n^{SEC} = 10 kDa, $Đ$ = 1.4). PDMS traces show negative RI values in chloroform and have been reversed for clarity.

References

1. Lamers, B. A. G.; de Waal, B. F. M.; Meijer, E. W. *J. Polym. Sci.* **2020**, *59*, 1142.

Appendix C. Supporting Information for Chapter 4

GENERAL EXPERIMENTAL SECTION

Materials

Monocarbinol terminated poly(dimethylsiloxane) (PDMS-OH) with a molecular weight of 10 kDa (MCR-C22) was obtained from Gelest and used without purification. Ethyl 2-bromoisobutyrate (EBiB, Sigma Aldrich, 98%) 2-Bromoisobutyryl bromide (Alfa Aesar, 97%), Triethyamine (Alfa Aesar, 99%) and N,N,N',N'',N''-Pentamethyldiethylenetriamine (PMDETA, Sigma Alrich, 99%) were used as received. Methyl Methacrylate (Sigma Aldrich, 99%) and MD'M-ALMA (provided by Dow Chemical) were filtered through basic alumina (Aldrich, standard grade) before use. Dichloromethane (DCM) was collected under an Ar atmosphere from a solvent purification system (PureSolv, Innovative Technology Inc.) for chain-end functionalization use. Other solvents such as Chlorobenzene (Sigma Aldrich, 99%), N,N-Dimethylformamide (DMF, Sigma Aldrich, 99%), Methanol (Fisher Scientific, 99.8%) Acetonitrile (ACN, Sigma Aldrich, 99%), and Hexanes (Fisher Scientific, 98.5%) were used as received.

Characterization Methods

^{1}H spectroscopy measurements were conducted in $CDCl_3$ at 20 °C on a Varian spectrometer operating at 600 (or 500) MHz. The number-average molecular weight (M_n), weight-average molecular weight (M_w) and dispersity ($Đ_M$) for PDMS homopolymers were determined by Size Exclusion Chromatography (SEC) in 0.25 wt% triethylamine/chloroform using a Waters e2695 separation module with a Waters 2414 differential refractive index detector. The columns were calibrated against PS standards (Agilent Technologies). The M_n, M_w and $Đ_M$ for PDMS-b-P[MD'M-ALMA-r-MMA] copolymers were determined by SEC Waters

Alliance HPLC instrument using a refractive index detector and an Agilent PLgel 5 μm MiniMIX-D column at 35 °C with THF as the eluent, calibrated with Polystyrene standards (Agilent Technologies). Dynamic Scanning Calorimetry (DSC) was conducted by loading (∼5 mg) of each sample into Tzero Aluminum Hermetic DSC pans (TA instrument) and tested on a DSC2500 (TA instrument). The glass transition temperature (T_g) of each sample was measured based on the third heating cycle between −160 and 180 °C at 20 °C/min at the midpoint of the step transition. PMD'M-ALMA was thermally annealed at 60 °C in high vacuum (3×10^{-8} Torr) before cooling slowly to room temperature, producing homogeneous liquid devoid of air bubbles. The sample volume was measured at room temperature with a Micromeritics AccuPyc II 1340 gas pycnometer using the gas displacement technique with nitrogen. Ten purge cycles were followed by ten measurements. The density of PMD'M-ALMA was calculated to be 0.986 g/mL from the obtained average volume and separately measured mass. Small angle X-ray scattering (SAXS) measurements were conducted using a custom constructed SAXS instrument in the X-ray diffraction facility in the Materials Research Laboratory (MRL) at University of California, Santa Barbara (UCSB). The instrument used a 50 micron microfocus, Cu target X-ray source with a parallel beam multilayer optics and monochromator (Genix from XENOCS SA, France), high efficiency scatterless hybrid slits collimator developed in house,1 and Pilatus100k and Eiger 1M solid state detectors (Dectris, Switzerland). SAXS data was collected at a sample-to-detector distance of 1.7 m or 0.15 m and calibrated with a silver behenate standard. The 2D data were reduced by azimuthal averaging to give I(q), where I is intensity and q is the momentum transfer vector $q = (4\pi/\lambda) \sin \theta$. For SAXS measurements, data reduction was carried out using the NIKA and IRENA software packages developed at Argonne National Laboratory.

Synthesis Procedures

Bromoisobutryate terminated poly(dimethylsiloxane) macroinitiator (PDMS-Br)

PDMS-OH (10 kDa, 20 g, 2 mmol) and triethylamine (1.6 mL, 11 mmol) were added to an oven-dried round bottom flask with a stir bar and dissolved in dry DCM (100 mL). The reaction was cooled to 0 °C in an ice bath and 2-bromoisobutyryl bromide (1.2 mL, 20 mmol) was added dropwise while stirring. The ice bath was then removed to slowly warm the reaction mixture to room temperature and stirred for 1h. The reaction was then diluted with 200 mL DCM and washed with 200 mL 1M HCl, 200 mL saturated $NaHCO_3$, and 200 mL brine. After concentrating by rotary evaporation, the crude PDMS-Br was diluted with 300 mL hexanes and washed three times with 200 mL ACN. Hexanes was then removed by rotary evaporation to isolate 10k PDMS-Br (19.0 g, 95%**)** as a viscous colorless liquid. SEC-RI data and a ^{1}H NMR spectrum are provided in Figure C1 and C2.

General Procedure for ATRP of MD'M-ALMA

MD'M-ALMA (5.1 g, 14.7 mmol), PMDETA (41.7 μL, 0.2 mmol), Chlorobenzene (25.6 mL) and DMF (1.5 mL) were added to a Schlenk flask with a stir bar and purged by bubbling with Ar for 15 minutes. Afterwards CuBr (28.7 mg, 0.2 mmol) was added and degassed with Ar bubbling for an additional 5 minutes before heating the reaction mixture to 60 °C in an oil bath. A scintillation vial with 10k PDMS-Br (2.0 g, 0.2 mmol) was separately degassed with Ar bubbling for 15 minutes and quickly injected into the reaction mixture while stirring vigorously to initiate the polymerization. The polymerization was monitored by ^{1}H NMR stopped upon reaching 60-70% conversion (approximately 3h) by rapidly cooling the mixture in an ice bath and opening the Schlenk flask to air. The crude polymerization was then filtered through basic alumina and precipitated three times into methanol to isolate 10k PDMS-b-

PMD'M-ALMA (3.5 g, 87%) as a viscous colorless liquid. The same procedure was repeated with EBiB as an initiator following the procedure above to synthesize PMD'M-ALMA homopolymer for density measurements.

General Procedure for copolymerizations of MD'M-ALMA and MMA by ATRP

MD'M-ALMA (3.6 g, 10.3 mmol), MMA (2.0 mL, 18.3 mmol), PMDETA (41.7 μL, 0.2 mmol), Chlorobenzene (26.7 mL) and DMF (1.6 mL) were added to a Schlenk flask with a stir bar and purged by bubbling with Ar for 15 minutes. Afterwards CuBr (28.7 mg, 0.2 mmol) was added and degassed with Ar bubbling for an additional 5 minutes before heating the reaction mixture to 60 °C in an oil bath. A scintillation vial with 10k PDMS-Br (2.0 g, 0.2 mmol) was separately degassed with Ar bubbling for 15 minutes and quickly injected into the reaction mixture while stirring vigorously to initiate the polymerization. The polymerization was monitored by ^{1}H NMR stopped upon reaching 40% conversion of MD'M-ALMA (approximately 3h) by rapidly cooling the mixture in an ice bath and opening the Schlenk flask to air. The crude polymerization was then filtered through basic alumina and precipitated three times into methanol to isolate 10k PDMS-b-P[MD'M-ALMA-r-MMA] (3.5 g, 87%) as a waxy white solid. The same procedure was repeated with varying ratios of MD'M-ALMA and MMA to synthesize PDMS-b-P[MD'M-ALMA-r-MMA] copolymers ranging from viscous liquids to glassy solids depending on the composition of the methacrylate block.

CHARACTERIZATION DATA

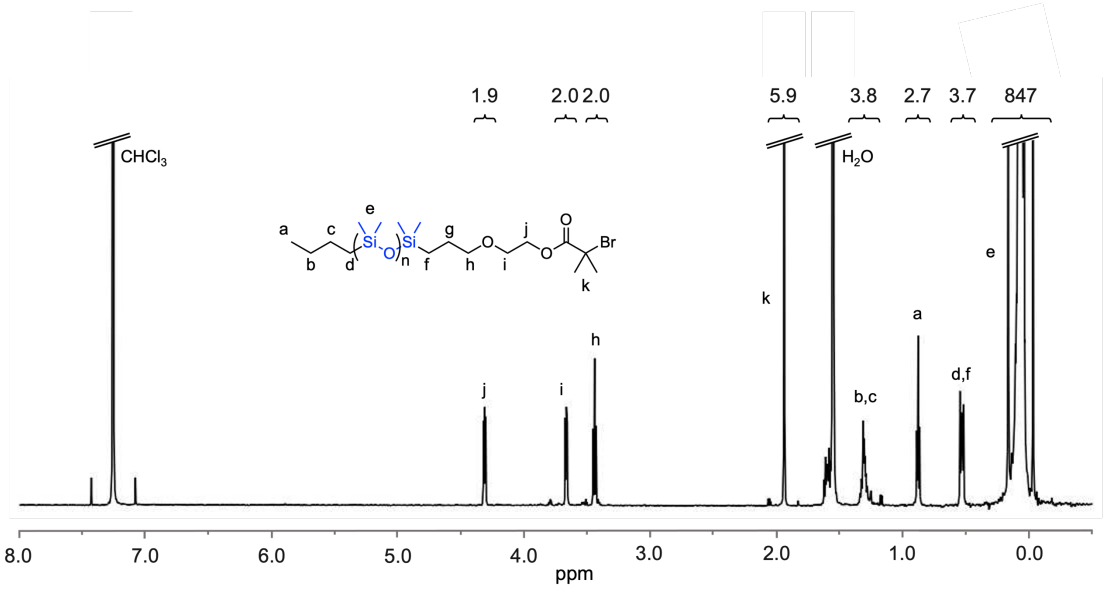


Figure C1. ^{1}H NMR trace of 10k PDMS-Br macroinitiator. The DMS backbone integration (peak e, 0.5 ppm) was used to calculate f_{PDMS} for the PDMS-based block copolymers.

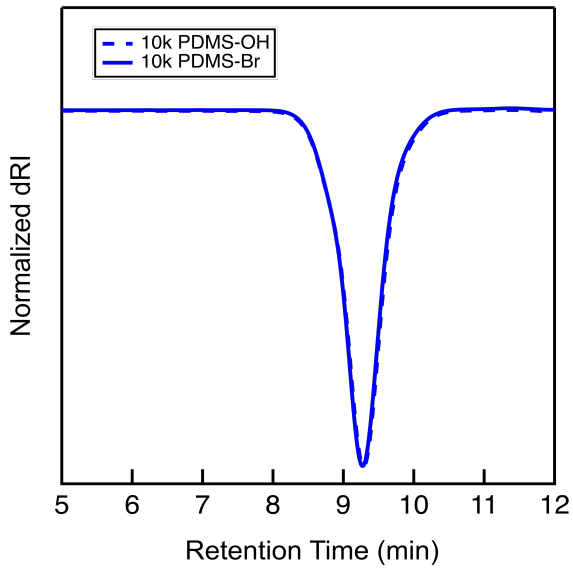


Figure C2. SEC-RI trace of 10k PDMS-OH (M_n^{SEC} = 10.6 kDa, $Đ$ = 1.2) and 10k PDMS-Br (M_n^{SEC} = 10.7 kDa, $Đ$ = 1.2) in chloroform after functionalization

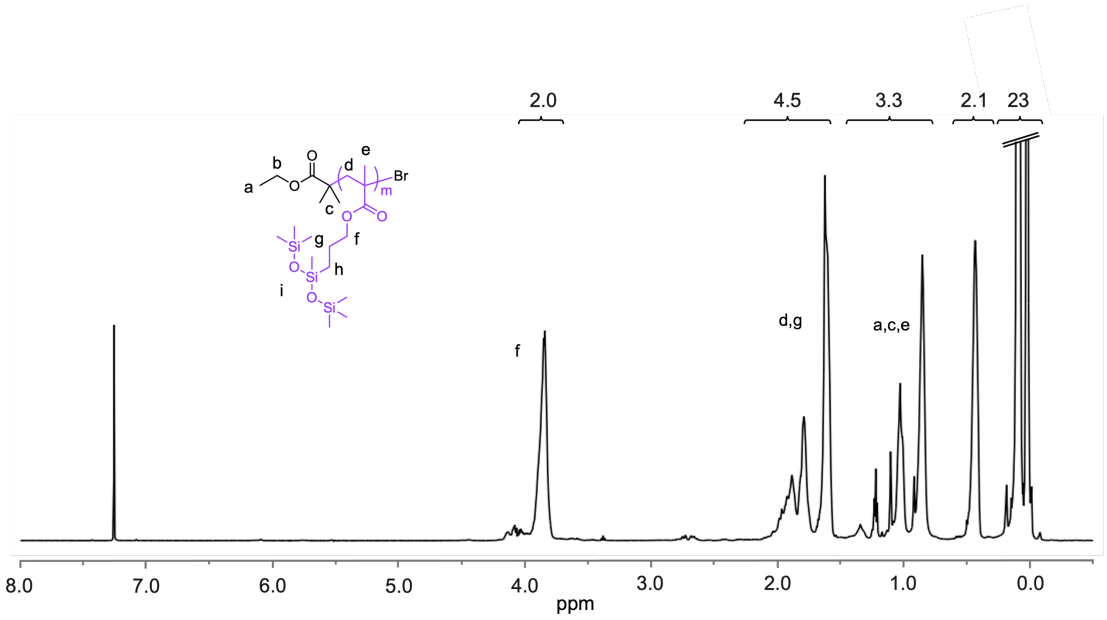


Figure C3. Representative ^{1}H NMR of PMD'M-ALMA made via ATRP.

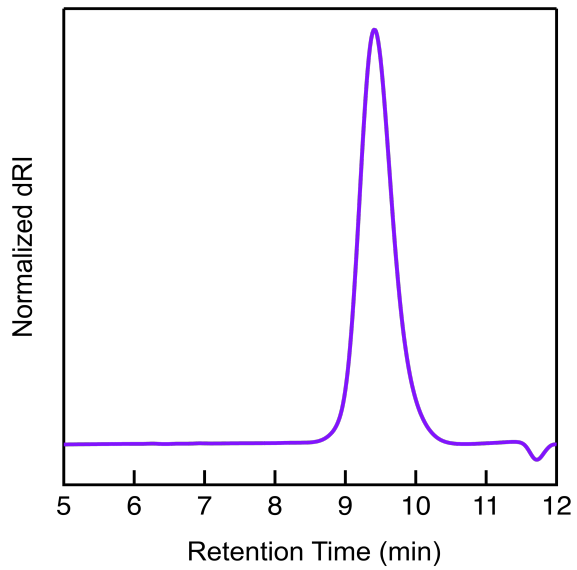


Figure C4. SEC-RI trace of PMD'M-ALMA (M_n^{SEC} = 9.4 kDa, $Đ$ = 1.2) in chloroform synthesized via ATRP.

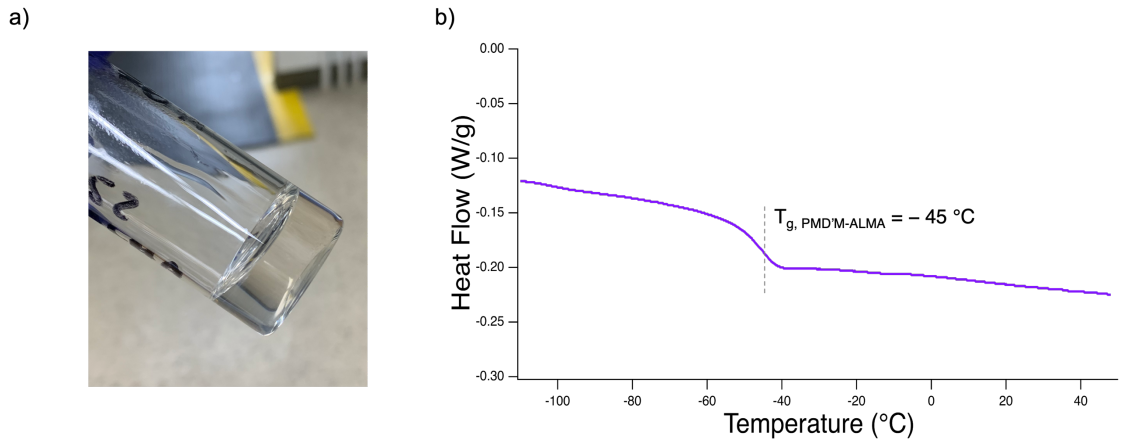


Figure C5. a) Image of and b) DSC trace of PMD'M-ALMA at 10 °C/min (Exo up).

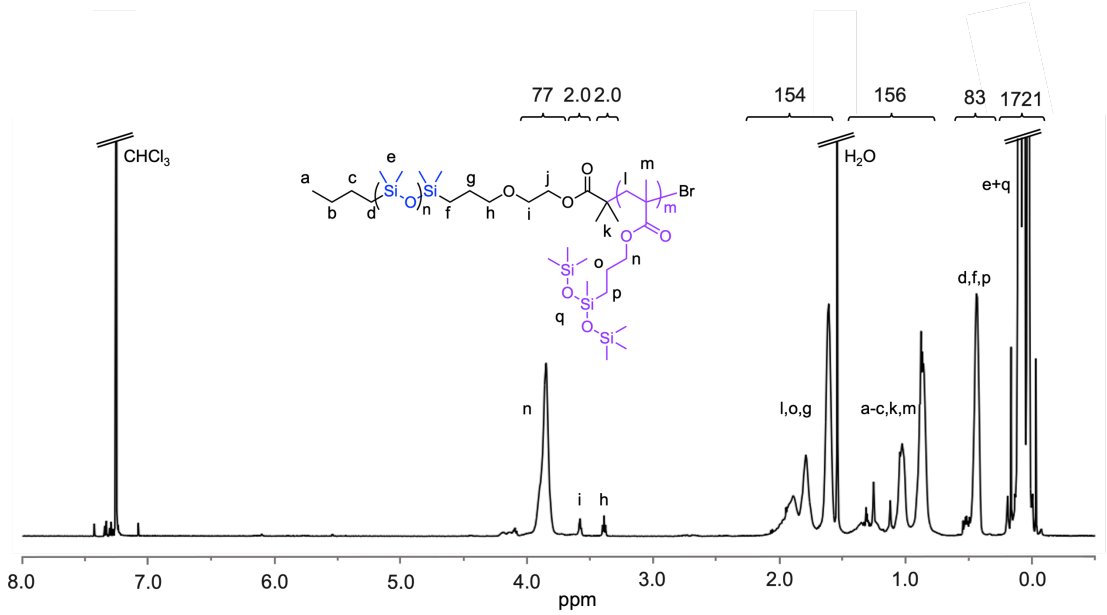


Figure C6. ^{1}H NMR of 10k PDMS-b-12k PMD'M-ALMA with integrations, the O-CH_2- of MD'M-ALMA (peak n, 3.8 ppm) was used to calculate $f_{MD'M\text{-}ALMA}$.

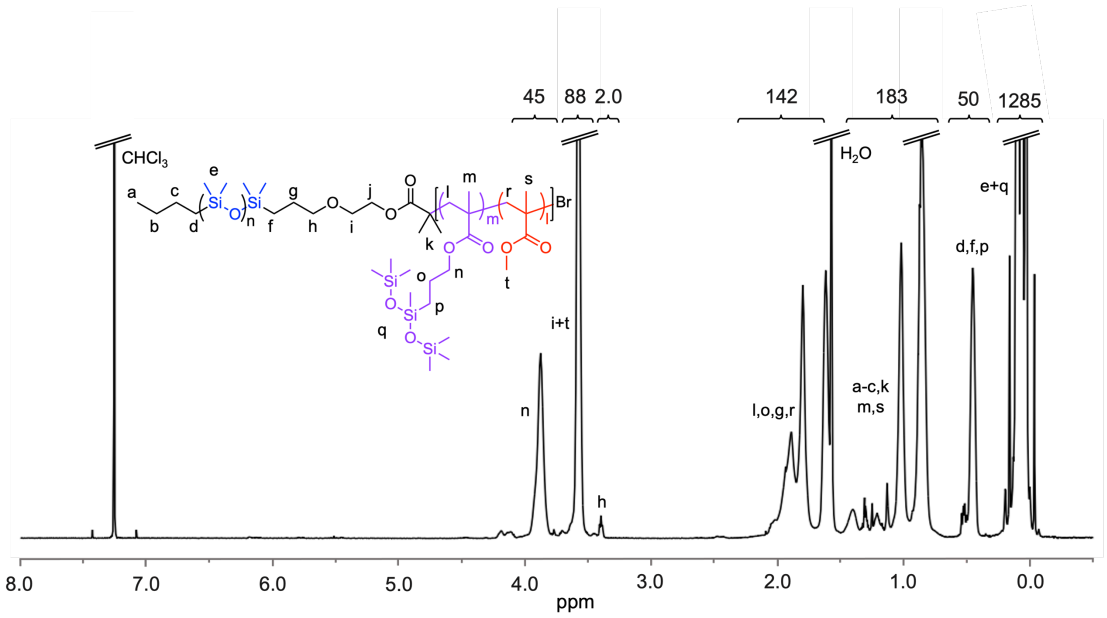


Figure C7. Representative ^{1}H NMR for PDMS-b-P[MD'M-ALMA-r-MMA] copolymers ($f_{MD'M\text{-}ALMA}$ = 0.37, Table 1, Entry 3 in main text). The O-CH_2- of MD'M-ALMA (peak n, 3.8 ppm) and O-CH_3- of MMA (peak t, 3.6 ppm) were used to calculate $f_{MD'M\text{-}ALMA}$ and f_{MMA} respectively.

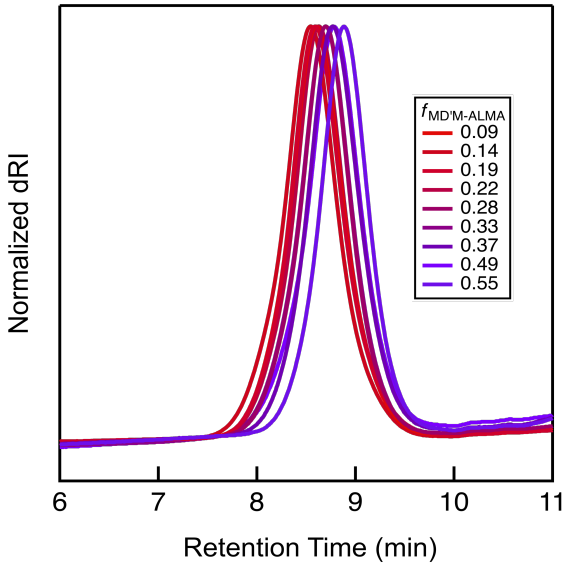


Figure C8. SEC-RI trace of the PDMS-b-P[MD'M-ALMA-r-MMA] copolymers with various $f_{MD'M\text{-}ALMA}$ in THF.

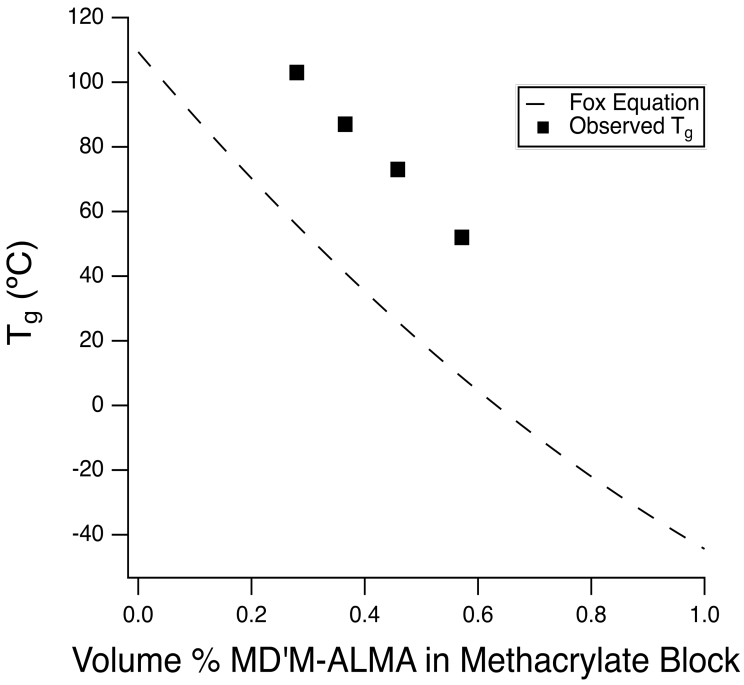


Figure C9. Calculated T_g values for random PMD'M-ALMA-r-MMA copolymers via the Fox equation relative to observed T_gs for the methacrylate blocks of PDMS-b-PMD'M-ALMA-r-MMA block random copolymers.

Appendix D. Silicone-based polymer blends: Enhancing Properties Through Compatibilization

This Appendix was initially published in *Journal of Polymer Science.*
Reprinted with permission from *J. Polym. Sci.* **2021**, *59*, 2114 – 2128.
Copyright 2021 John Wiley and Sons.

Received: 12 June 2021 | Revised: 12 July 2021 | Accepted: 13 July 2021

DOI: 10.1002/pol.20210453

REVIEW

JOURNAL OF POLYMER SCIENCE WILEY

Silicone-based polymer blends: Enhancing properties through compatibilization

Allison Abdilla[1] | Colton A. D'Ambra[2] | Zhishuai Geng[3] | Jaeman J. Shin[3,4] | Michael Czuczola[1] | David J. Goldfeld[3] | Souvagya Biswas[5] | Jodi M. Mecca[5] | Steven Swier[5] | Thomas D. Bekemeier[5] | David S. Laitar[5] | Morgan W. Bates[3] | Christopher M. Bates[1,2,3] | Craig J. Hawker[1,2,3]

[1]Department of Chemistry & Biochemistry, University of California, Santa Barbara, California, USA

[2]Materials Department, University of California, Santa Barbara, California, USA

[3]Materials Research Laboratory, University of California, Santa Barbara, California, USA

[4]Department of Organic Materials and Fiber Engineering, Soongsil University, Sangdo-ro, Seoul, South Korea

[5]Core R&D, The Dow Chemical Company, Midland, Michigan, USA

Correspondence
Morgan W. Bates, Christopher M. Bates, and Craig J. Hawker, Department of Chemistry & Biochemistry, University of California, Santa Barbara 93106, CA.
Email: morganbates@ucsb.edu (M. W. B.); cbates@ucsb.edu (C. M. B.); hawker@ucsb.edu (C. J. H.)

Funding information
UC Santa Barbara; Materials Research Science and Engineering Center; National Science Foundation; Natural Sciences and Engineering Research Council of Canada; Dow Materials Institute

Abstract

Polymer blending is a cost-effective way to control the properties of soft materials, but the propensity for blends to macrophase separate motivates the development of efficient compatibilization strategies. Across this broad area, compatibilization is particularly important for polysiloxanes, which exhibit strong repulsive interactions with most organic polymers. This review analyzes state-of-the-art polysiloxane compatibilization strategies for silicone–organic polymer blends. Emphasis is placed on chemical innovation in the design of compatibilization agents that may expedite the commercialization of new silicone–organic materials. We anticipate that hybrid silicone blends will continue to play an important role in fundamental and applied materials science across industry and academia.

KEYWORDS

compatibilization, PDMS, polymer blends

1 | INTRODUCTION

Blending polymers is a powerful technique to obtain materials with improved properties,[1–4] often at a lower cost than the design of novel monomers and/or polymerization routes. Procedurally, blending typically takes place using common processing equipment such as twin-screw extruders, further reducing the financial investment associated with developing new materials. An additional advantage is that a wide range of properties can be obtained by simply changing the composition of blends, leading to considerable interest in a variety of real-world applications.[3]

The exceptional properties of silicones,[5] like the chain flexibility imparted by the wide silicon-oxygen bond angle paired with high bond strength, are a key driver for investigating the preparation of polymer blends based on mixtures of silicones with a wide variety of organic polymers. These unique properties arise from the substantial dipolar character of Si–O–Si bonds situated along a polysiloxane backbone, coupled with an ability to readily control the organic substituents at each silicon atom.[6]

 © 2021 Wiley Periodicals LLC.

This versatile molecular design toolbox provides excellent tunability over surface properties, the glass transition temperature, flexibility, biocompatibility, chemical resistance, and thermal/oxidative stability.[7] Consequently, many polysiloxane-based materials have been manufactured in the form of fluids, resins, and as crosslinked elastomers for thousands of commercial products ranging from high performance aerospace adhesives to pharmaceuticals and advanced biomedical devices.[8–14]

Polysiloxanes have also been blended with various organic polymers to yield novel hybrid materials with improved mechanical properties.[15,16] One example is C-Flex™, a transparent, inexpensive, and biocompatible medical grade elastomer made from blends of polysiloxanes with styrene-ethylene-butylene-styrene (SEBS). Although the unique nature of Si–O bonds gives rise to the enhanced properties of silicones, polysiloxanes are known to be highly immiscible with other polymers, limiting their processing in blended materials.[16] When incorporated into blends, macrophase separation usually yields undesirable mechanical properties, and while good dispersions can sometimes be obtained with careful control of mixing conditions, the resulting blends are often thermodynamically unstable and undergo further phase separation over time.[17] Strategies to compatibilize polysiloxanes with organic polymers are therefore needed to develop novel, hybrid blends for advanced materials applications.

In this report, we review state-of-the-art polysiloxane compatibilization strategies as divided into four categories: (1) Block copolymer (BCP) compatibilization, (2) Reactive blending, (3) Interpenetrating polymer networks, and (4) End-group functionalization. The impact of these different approaches will be discussed in terms of phase behavior and properties.

2 | RESULTS AND DISCUSSION

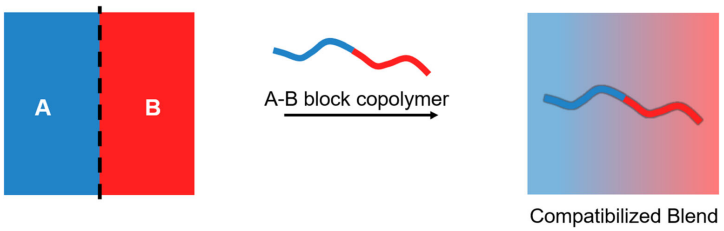
2.1 | Block copolymer compatibilization

The emulsification of immiscible polymer blends by the addition of an interfacial modifier can lead to controllable morphologies with good mechanical properties and thermal stability.[18] These modifiers, referred to as compatibilizers, are often BCPs where each block is miscible with one of the blend components.[19] BCP compatibilizers typically segregate to the interface between immiscible homopolymers, resulting in increased interfacial adhesion, decreased interfacial tension and domain size, and minimal coalescence during subsequent processing (Scheme 1).[20,21] BCP additives that sufficiently reduce interfacial tension can also prevent brittle fracture due to debonding, allowing for toughening mechanisms such as shear yielding and crazing to occur while limiting crack propagation.[21] This interfacial toughening effect can be enhanced if the molecular weight of the copolymer is high enough to form entanglements with the surrounding homopolymer matrix.

Ternary blends of two homopolymers with copolymer compatibilizers are frequently studied systems in statistical physics. Various theories can be used to calculate equilibrium and nonequilibrium phase behavior, modes of phase separation, and diffusion processes,[22] with significant experimental and theoretical work having been summarized in numerous in-depth reviews.[23–25] Traditionally, BCPs such as AB diblocks, ABA triblocks, or graft copolymers are used to manipulate the phase behavior of homopolymer blends as they segregate to A/B interfaces and suppress macroscopic phase separation.[2] The resulting blend morphology is governed by experimental factors including molecular weights, composition, and processing conditions.[26]

Useful insights regarding the miscibility and phase behavior of polymers can be inferred from the Flory–Huggins interaction parameter, χ, which captures the binary interactions between chemically dissimilar polymers.[22] Theoretically, χ reflects the enthalpy associated with mixing two dissimilar polymers (A and B) normalized by thermal energy, where positive values indicate repulsion, which drives phase separation. In practice, Flory–Huggins theory only accounts for the ideal combinatorial entropy of mixing with nonideal entropy contributions collapsed into an effective χ parameter which is modeled empirically as $\chi = A/T + B$, where T is absolute temperature and A and B are polymer specific parameters (note that additional terms with a higher-order temperature dependence can also be included).[27–29] Polysiloxanes are generally incompatible with organic materials and silicone-based BCPs are widely studied as strongly segregating, high-χ systems.[30–33] Table 1 provides a summary of χ values found in the literature for BCPs with polydimethylsiloxane (PDMS) as the A block and various organic components as the B block. We also note that experimentally measured values of χ can vary depending on the material system (e.g., blends vs. blocks) and measurement technique (e.g., scattering vs. rheology).[42]

While the high-χ nature of polysiloxanes with organic polymers facilitates the development of small features in applications such as photolithography and patterning, strong segregation presents a challenge for blend compatibilization.[8,37] Morse and coworkers have investigated the impact of adding premade BCPs to emulsify and stabilize PDMS droplets within an organic matrix.[43] The compatibility and morphology of the resulting blends were estimated by interfacial tension measurements,



SCHEME 1 Depiction of interfacial broadening in an immiscible polymer blend of homopolymers A and B after compatibilization by an AB block copolymer. The block copolymer segregates to the interface and lowers the interfacial tension

TABLE 1 $\chi(T)$ interaction parameters for AB diblock copolymers

B block	$\chi(T)$[a]	χ(298 K)	References
Poly(D,L-lactide)	$360/T + 0.21$	1.42	34
poly(3-hydroxystyrene)	$33.5/T + 0.31$	0.42	35
Poly(2-vinylpyridine)	$33.2/T + 0.14$	0.26	36
Poly(4-vinylpyridine)	$35.2/T + 0.18$[b]	0.30	36
Poly(methyl methacrylate)	$26.7/T + 0.11$ $20.8/T + 0.11$	0.19 0.18	37
Poly(ethylene oxide)	$19.3/T + 0.14$ $13.9/T + 0.14$	0.20 0.29	38
Polyethylene	$89.9/T - 0.094$	0.21	39
Polyisoprene	$43.6/T - 0.011$	0.14 0.19[c]	40,41
Poly(ethylene−propylene)	$41.0/T - 0.024$	0.12	39
Polystyrene	$5.80/T + 0.060$	0.076	37
Poly(ethyl ethylene)	$25.2/T - 0.021$	0.059	39

[a]values normalized to a monomer reference volume, v_0, of 118 Å^3 unless specified otherwise.
[b]reference volume not mentioned in source.
[c]only value given, not equation for $\chi(T)$.
Note: Where A, PDMS.

transmission electron microscopy, scanning electron microscopy, and calorimetry. Only minor amounts of a copolymer modifier, ranging from 0.01% to 5%, were required to compatibilize A/B blend interfaces. The addition of compatibilizer decreases the interfacial tension of a polymer blend until the A/B interface is saturated with BCP chains and the critical micellar concentration (CMC) is reached, beyond which BCP micelles lacking homopolymer begin to form and there is little change in bulk physical properties.

Leibler developed a theory to describe the interface between immiscible polymers and to predict the interfacial tension in highly immiscible A/B/AB ternary blends.[44] The theory models copolymer chains at the interface as brushes, with one brush in homopolymer A, the other brush in homopolymer B, and the interface separating the two brushes as a discrete plane. "Wet brush" and "dry brush" regimes are distinguished by the molecular weight ratio of a copolymer block relative to its homopolymer and the grafting density, σ, which is defined as the number of chains per unit area. A wet brush, where homopolymer chains intermingle with the copolymer, is obtained for small σ and relatively low homopolymer molecular weights relative to the block molecular weight. In contrast, a dry brush describes densely packed, highly extended copolymer interfaces where the brush resembles a neat BCP lamella. The ability to distinguish these regimes is critical as interfacial adhesion is dependent on the degree of homopolymer penetration and entanglement with the BCP brush.

Hu and coworkers explored this concept experimentally in immiscible polystyrene (PS), PDMS, and poly(styrene-*b*-dimethylsiloxane) (PS-*b*-PDMS) ternary blends (Figure 1).[45] The interfacial tension was measured using an automated drop tensiometer to evaluate the compatibilization as a function of diBCP concentration

and PDMS molecular weight. When a nearly symmetric PS-*b*-PDMS (M_n = 13 KDa, 50 wt% PS) was added into a PDMS homopolymer phase of a $PS_{4K}/PDMS_{4.5K}$ blend, the interfacial tension decreased as the copolymer concentration increased. A reduction in interfacial tension of 82% was achieved at the CMC (0.002 wt.%), above which no further change was observed. These results follow Leibler's theory for dry brush behavior and a calculated saturation concentration of 0.003 wt.%. In contrast, an approximately 70% reduction in interfacial tension was observed for a lower molecular weight PDMS blend ($PS_{4K}/PDMS_{1.6K}$) with a significantly higher CMC of 0.03%. In this case, the interfacial tension observed is larger than Leibler's theory predicts for a dry brush, suggesting lower molecular weight PDMS chains penetrate the copolymer brush layer, leading to repulsive interactions between the PDMS/PS homopolymers that increase interfacial tension. Furthermore, a higher interfacial tension was observed when the PS-*b*-PDMS compatibilizer was first mixed into the PS phase, likely due to the formation of micelles with diffusion also limited by viscosity effects.

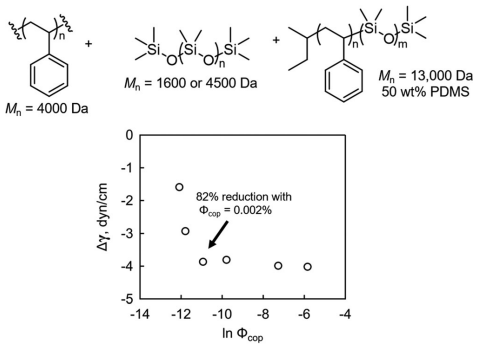


FIGURE 1 Reduction of interfacial tension (γ) for polystyrene (PS)/polydimethylsiloxane (PDMS) blends as a function of the mass concentration of a PS-*b*-PDMS copolymer additive (Φ_{cop}) formed at 180 °C. Adapted with permission.[45] 1995, American Chemical Society

In addition to the compatibilizer concentration, the phase behavior of ternary A/B/AB blends heavily depends on the composition of the AB diBCP additive.[46] Self-consistent field theory (SCFT) calculations predict that the interfacial tension, γ, for homopolymer mixtures with equal degrees of polymerization and statistical segment lengths should extrapolate to zero in the limit of a symmetric BCP and vary quadratically around the minimum of $f_A = 0.5$. To experimentally test these SCFT predictions, Chang and coworkers measured γ between polyisoprene (PI) and PDMS homopolymers mixed with a poly(isoprene-*b*-dimethylsiloxane) diBCP using a spinning drop tensiometer (Figure 2).[41] Measurements were

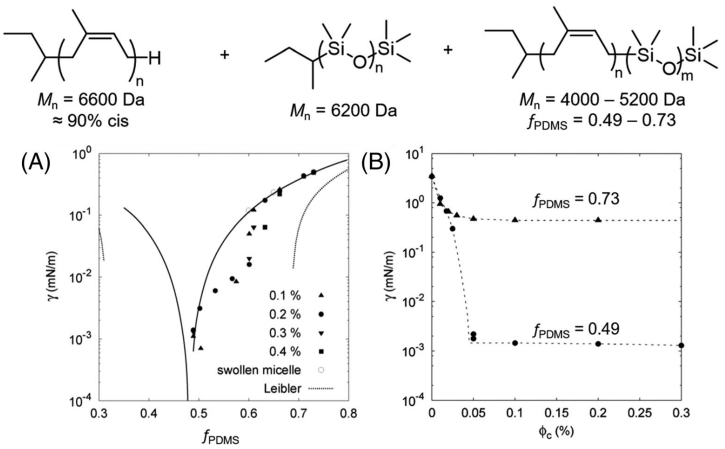


FIGURE 2 Reduction of interfacial tension (γ) between polyisoprene and polydimethylsiloxane (PDMS) through the addition of a poly(isoprene-*b*-dimethylsiloxane) copolymer. (A) Experimental data was gathered from a spinning drop tensiometer by varying the copolymer volume fraction (f_{PDMS}) and concentration (ϕ_c) and compared to Leibler's theory and self-consistent field theory (SCFT) predictions, denoted by the solid line. (B) Direct comparison of two different volume fractions shows a larger decrease in interfacial tension for a symmetric copolymer. Adapted with permission.[41] 2007, American Chemical Society

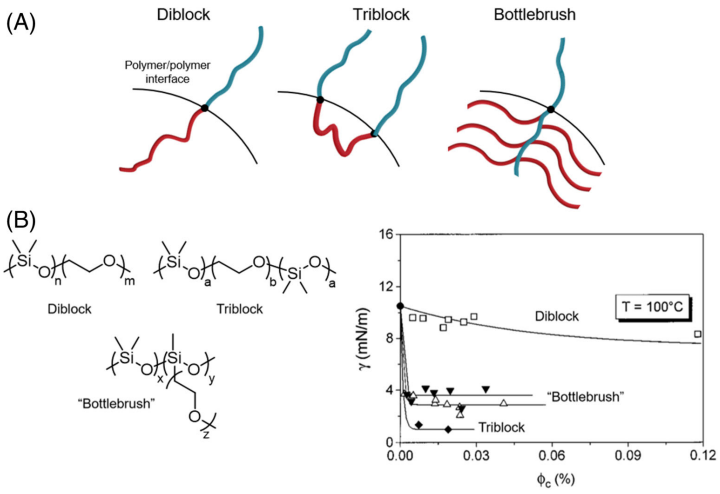


FIGURE 3
(A) Arrangement of block copolymer (BCP) compatibilizers with various architectures at an A/B interface. (B) Interfacial tension of compatibilized poly(ethylene oxide) (PEO)/polydimethylsiloxane (PDMS) blends for different copolymer architectures. Adapted with permission.[47] 1997, American Chemical Society

conducted on symmetric homopolymer mixtures with PDMS copolymer volume fractions, f_{PDMS}, ranging from 0.49 to 0.73. Mixtures containing nearly symmetric compatibilizers exhibited ultralow interfacial tension, up to three orders of magnitude less than observed for the homopolymer PI/PDMS interface. Optical microscopy and small-angle X-ray scattering confirmed that these symmetric mixtures form lamellar or bicontinuous microemulsion phases depending on the surfactant concentration. However, the equilibrium γ was found to be a discontinuous function of f_{PDMS}, particularly between $f_{PDMS} = 0.60–0.63$, where γ changes by an order of magnitude. Chang and coworkers concluded that the discrepancy with SCFT calculations may arise from the limiting rate at which micelles in the PDMS phase emulsify PI homopolymer chains as they approach the interface.

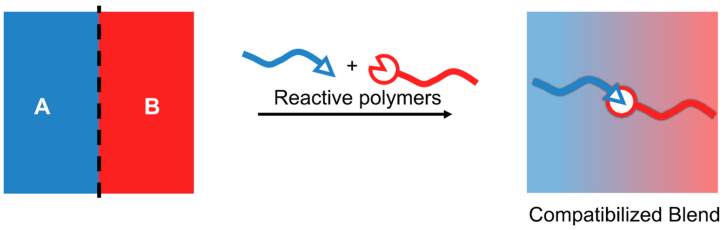
The architecture of copolymer compatibilizers also strongly impacts the interfacial structure of macrophase-separated polymer blends. Both theoretical and experimental studies have shown that a diBCP crosses the interface only once (Figure 3).[47–50] Notably, the number of interfacial crossings for blocky compatibilizers can be increased with multiBCPs,[50] for example, a triBCP can cross the interface twice, and a pentablock four times, creating multiple joints or "stitches" that improves interfacial adhesion. With low interfacial adhesion, brittle fracture can occur due to interfacial debonding, but when multiblock polymers are used as compatibilizers, the resulting blends are substantially tougher.[21] A caveat to the use of complex copolymer architectures is often the limited improvement in properties due to their poor entanglement with linear homopolymer chains and micelle formation that constrains diffusion to the homopolymer–homopolymer interface.[21]

The impact of compatibilizer architecture was also examined experimentally by Jorzik and Wolf, who measured the interfacial tension of poly(ethylene oxide) (PEO) blended with PDMS.[47] They compared the reduction in interfacial tension of diblock, triblock, and bottlebrush PEO-*b*-PDMS copolymers as a function of concentration (Figure 3).

The efficiency of the additives with respect to the maximum reduction of γ follows the sequence triblock > "bottlebrush" > diblock. However, caution should be exercised in generalizing this trend since it does not appear that total molecular weight nor block molecular weight of the copolymers were controlled or varied systematically in the investigation. This presents an opportunity for further theoretical and experimental studies as the connectivity of blocks in the compatibilizer can play a decisive role in reducing interfacial tension. Furthermore, insights from architectures beyond classic diBCPs such as tapered block, gradient or protein-like copolymers that have yet to be studied in silicone blends may guide future compatibilizer design.[51–53]

2.2 | Reactive blending

While copolymer modifiers have been shown to be an efficient means to lower the interfacial tension of blends, there are limitations related to cost, micelle formation and limited



SCHEME 2
Compatibilization of an immiscible A/B homopolymer blend by reactive compatibilization. Homopolymers containing reactive groups and/or reactive small molecules undergo in-situ coupling to form a block copolymer at the interface, which reduces interfacial tension

interfacial diffusion. Reactive compatibilization, the in-situ-formation of block or graft copolymers at the interface by coupling reactive polymers and that are miscible with at least one component of an immiscible polymer blend (Scheme 2), is an approach that circumvents some of these issues.[4] Moreover, reactive polymers avoid the potentially costly and complicated synthesis of BCPs.

Polymers with reactive comonomers or chain-ends can be mixed or added to unreactive homopolymers they are miscible with to generate polymer blends with BCPs at their interfaces. Coupling reactions between the reactive homopolymers must be rapid due to the short processing times (often <5 min) and enough copolymer must be formed to sufficiently compatibilize the final blend.[2,54] Thus, it is important to understand the yield of copolymer generated under specific processing conditions to design blends with specific material properties. Multiple factors controlling copolymer generation at the interface have been investigated, including reaction kinetics, fluid dynamics during processing, and thermodynamic interactions between immiscible polymers.[55–57] A key constraint of reactive compatibilization is reaction efficiency and kinetics. For efficient coupling, reactive species must be able to access phase boundaries and react in the melt during the short processing times associated with blending. The resulting covalent bond must also be sufficiently stable under the processing conditions, further limiting the range of potential functional groups. Additionally, unreacted functional groups left within the final blend can be prone to long term side reactions, causing significant material degradation and drifts in their properties. Despite these challenges, reactive blending has been widely successful for the compatibilization of immiscible polymers and is used in a variety of commercial materials.[58,59] One example is high-impact polystyrene (HIPS), a class of rubber toughened materials prepared by the free-radical polymerization of styrene in the presence of polybutadiene.[60,61]

Reactive blending has also been applied to compatibilize polysiloxanes with various organic polymers. Maric and coworkers studied the in-situ formation of BCPs with functionalized PDMS and PS bearing various amine (NH_2)/anhydride (Anh), NH_2/epoxy (Ep), and carboxylic acid (COOH)/Ep coupling partners using size exclusion chromatography (SEC) to probe copolymer formation and electron microscopy to determine the morphology.[62] Electron microscopy of the resulting blends showed a clear particle size dependence on the reactive functional groups (Figure 4). As expected, non-functional PDMS/PS blends produced large PDMS droplets that coarsened rapidly after annealing. The PDMS-Ep/PS-NH_2 and PDMS-Ep/PS-COOH blends were also coarse and unstable at elevated temperatures. In contrast, after only 5 min of mixing, PDMS-Anh/PS-NH_2 blends produced stable sub-micron droplets (< 0.5 μm) of PDMS in PS. SEC revealed that the final PDMS-Anh/PS-NH_2 blend contained 3 wt.% BCP, which is sufficient to saturate the interface, whereas the nonstable blends did not show evidence of copolymer formation. Maric and coworkers also noted that in-situ BCP formation was slower for the PDMS-Anh/PS-NH_2 blends compared to other Anh/NH_2 systems in the literature. They speculated that this lower reactivity may be due to the sharper PDMS/PS interface caused by their poor miscibility leading to decreased chain mixing.

Expanding on this concept, Jones and coworkers examined the impact of the polymer backbone chemistry on Anh/NH_2 reactions at the polymer–polymer interface to elucidate how χ impacts the reactivity (Figure 5).[57] The extent of interfacial reaction of anthracene labeled Anh-terminated poly(methyl methacrylate) (PMMA-Anh) or PS-Anh with a range of amine functional polymers was determined by annealing bilayer thin films and measuring the resulting copolymer concentration using SEC with ultraviolet light (UV), fluorescence and refractive index (RI) detectors. In addition, the interfacial roughness was characterized by atomic force microscopy. Two principal effects were observed with decreasing χ: an increase in the rate and extent of reaction at long times, as well as greater interfacial roughening. PDMS/

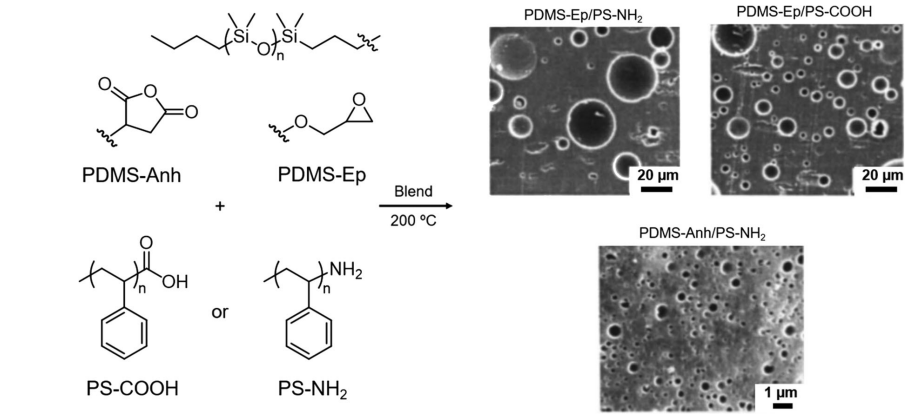


FIGURE 4 Compatibilization of polydimethylsiloxane (PDMS) and polystyrene (PS) through reactive blending with functional end groups. Adapted with permission.[62] 2004, John Wiley and Sons

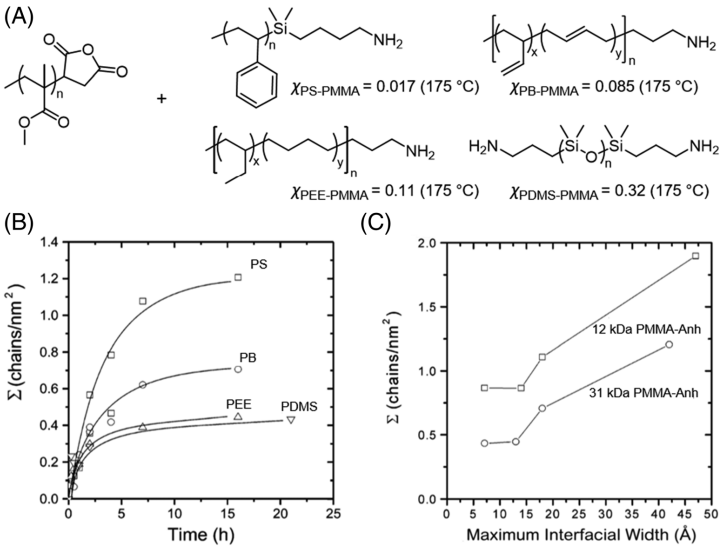


FIGURE 5 (A) Structure and χ values (at 175 °C) of Anh-terminated poly(methyl methacrylate) (PMMA-Anh) with different amine-terminated polymers. (B) Interfacial conversion versus time for reactive blends (at 200 °C) containing PMMA-Anh. (C) Interfacial width for 12 and 31 kDa PMMA-Anh with a range of amine functional polymers. Adapted with permission.[57] 2003, American Chemical Society

PS and PDMS/PMMA reactive films were found to have the lowest conversion due to a decreased interfacial volume in which reactions can occur. Furthermore, the maximum interfacial conversion was found to decrease for blends prepared with higher molecular weight PMMA components, likely due the lower concentration of functional groups limiting the number of chains that react at the PDMS/PMMA interface. In addition, the stronger segregation, suppressed internal fluctuations and increased BCP asymmetry at higher PMMA molecular weights may be important.

In addition to the Anh/NH_2 reaction, there are a wide variety of other potential reactive blending chemistries for the modification of silicone-based materials based on commercially-available polysiloxanes, including hydrosilylation, thiol–ene, and polycondensation.[63] Of these reactions, only a subset has been reported for the in-situ formation of compatibilizers, primarily in the form of graft copolymers.

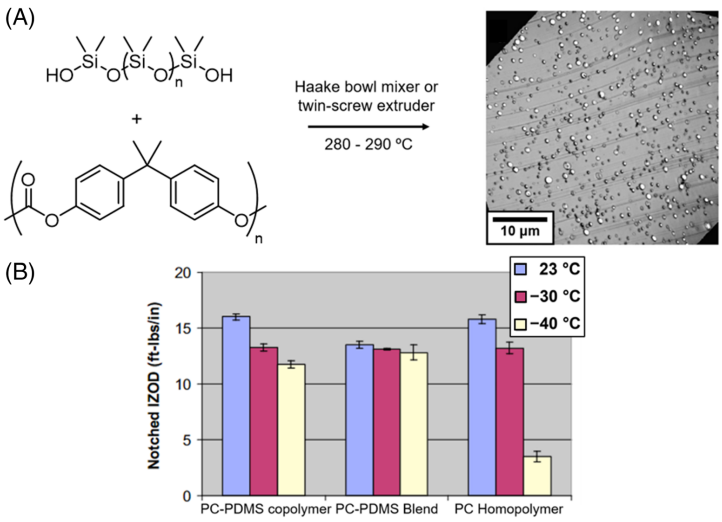


FIGURE 6 (A) Reactive blending and morphology of polycarbonate (PC) with polydimethylsiloxane (PDMS). (B) Notched Izod impact toughness for a PC-PDMS copolymer, PC-PDMS reactive blend, and PC homopolymer at various temperatures. Adapted with permission.[65] 2010, Elsevier

Although graft compatibilizers allow for more "crossings" at the polymer–polymer interface, the location of functional groups impacts the coupling kinetics for reactive polymers due to potential steric hindrance from the polymer backbone.[64] Significantly, the effect of compatibilizer architecture, that is, block versus graft compatibilizers, remains an open question for reactive polymer blends and warrants further investigation.

The promise of these studies is illustrated by the improved flow and impact toughness reported by Zhou and Osby for the modification of polycarbonate (PC) with a small amount of ultra-high molecular weight PDMS.[65] By promoting transesterification between the PC backbone and hydroxyl-terminated PDMS, a novel PC/PDMS/PC-*co*-PDMS polymer blend was prepared with superior flow and excellent performance at low temperatures (Figure 6). By carefully tuning the molecular weight of the base PC, the blend retained its impact toughness from room temperature down to as low as −40 °C. This change was attributed to the formation of a graft copolymer architecture through the incorporation of low-T_g PDMS chains, which reduced the ductile-to-brittle transition temperature of the final material. Analysis of the blend morphologies by electron microscopy revealed stable, sub-micron PDMS droplets dispersed within a PC matrix, with near optimum particle sizes between 0.2–0.9 µm for good impact toughening. This observation is in stark contrast to nearly identical blends prepared with nonreactive PDMS, where coalescence and macroscopic phase separation resulted in large PDMS domains and poor mechanical performance.

In principle, many functionalization reactions are available to prepare polysiloxanes with an array of architectures and well-defined chain ends, including hydrosilylation, thiol–ene, halogen substitution, and esterification.[7] Additionally, recent developments based on the Piers-Rubinsztajn, aza-Michael, condensation and azide-alkyne click reactions provide a wide scope of orthogonal chemistries to create precise siloxane small molecules, polymers and networks.[66–72] Although a variety of methods to modify polysiloxanes exist,[57,62,63,65–73] the hydrosilylation of Si–H-containing PDMS is by far the most versatile, allowing for efficient coupling to olefins, carbonyl groups, and other functionalities.[73] Indeed, this highly effective toolbox has enabled the development of various vulcanization strategies for the industrial production of silicone networks.[58] Nevertheless, only a few papers have explored the reactive compatibilization of silicone–organic blends via hydrosilylation chemistry. In 2012, Bonnet and coworkers reported the reactive blending of Si–H-terminated PDMS and poly(ethylene-*co*-vinyl acetate) (EVA) via metal-catalyzed carbonyl hydrosilylation (Figure 7).[74] The properties and morphology of the reactive EVA/PDMS blends could be tuned depending on the viscosity and stoichiometry of the homopolymer components. Specifically, a crosslinked material was obtained for low-viscosity PDMS with a high molar ratio of Si–H groups to vinyl acetate (VA) residues along the backbone of the EVA (Si-H/VA = 0.5). In contrast, a compatibilized blend was generated by increasing the PDMS/EVA viscosity ratio and decreasing the Si–H/VA ratio to 3.5×10^{-3}, allowing for the in-situ formation of EVA-*g*-PDMS copolymers at the interface between immiscible homopolymers. In the absence of the Ru catalyst, no graft formation was observed, resulting in a coarse

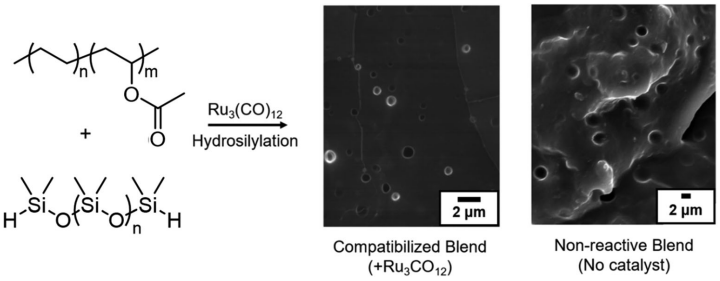
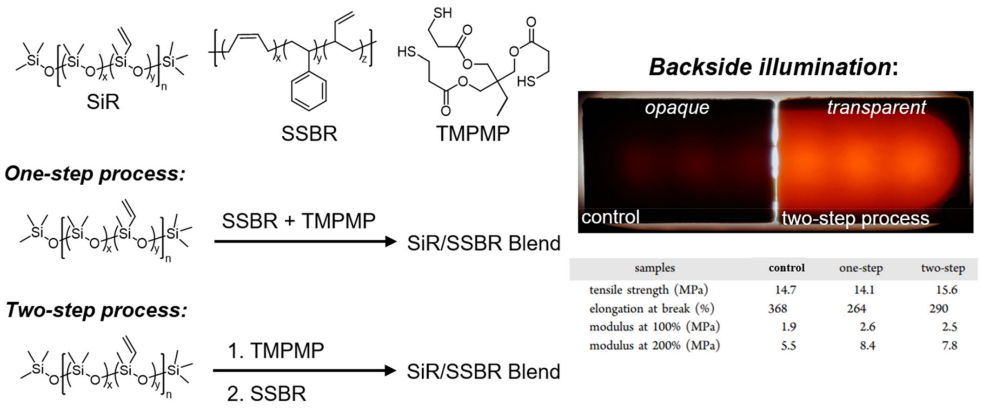


FIGURE 7 Morphology of reactive and nonreactive polydimethylsiloxane (PDMS)/poly(ethylene-*co*-vinyl acetate) (EVA) blends compatibilized through a metal-catalyzed carbonyl hydrosilylation reaction. Adapted with permission.[74] 2012, Elsevier



samples	control	one-step	two-step
tensile strength (MPa)	14.7	14.1	15.6
elongation at break (%)	368	264	290
modulus at 100% (MPa)	1.9	2.6	2.5
modulus at 200% (MPa)	5.5	8.4	7.8

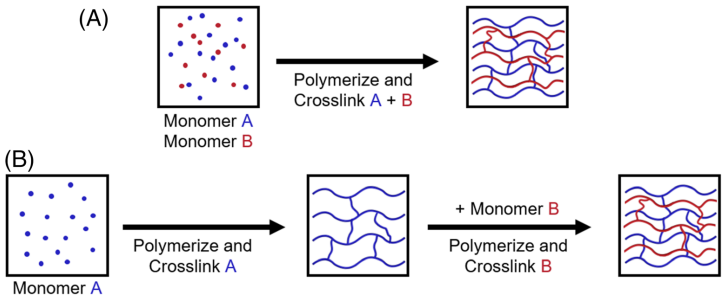
FIGURE 8 One-step and two-step process for forming SSBR/SiR reactive blends. Backside illuminated images of a control blend (without TMPMP) and a two-step SSBR/SiR blend. Mechanical properties are summarized in the table. Adapted with permission.[76] 2017, American Chemical Society

morphology with PDMS droplet sizes between 3–5 μm, compared to 0.5 μm in reactive blends. This approach was later expanded to the reactive compatibilization of polyamide/PDMS blends through amide hydrosilylation, which showed similar trends.[75]

The reactive compatibilization of silicones was also probed by Sun and coworkers by blending linear poly(dimethyl siloxane-*co*-vinylmethyl siloxane) chains, that is, silicone rubber (SiR), and soluble styrene–butadiene rubber (SSBR) compatibilized by thiol–ene click chemistry (Figure 8).[76] A trifunctional thiol trimethylolpropane (TMPMP) was chosen to compatibilize SiR and SSBR via an in-situ interfacial coupling during the mixing process. Although SiR and SSBR are both vinyl functionalized and can undergo a thiol–ene click reaction with TMPMP, SSBR contains a significantly higher vinyl content and tends to self-crosslink, inhibiting its coupling to SiR. Thus, a two-step process, where TMPMP was first reacted with SiR and then compounded with SSBR, was investigated to address the different reactivities. Blends prepared by a one-step process without TMPMP (referred to as blank) were also prepared for comparison. Both the one-step and two-step blends showed an increased tensile stiffness compared to the control. However, the tensile strength and elongation at break of the one-step blend decreased, indicating an increasing stress concentration from the tendency of TMPMP to internally crosslink the SSBR domains rather than coupling SSBR with SiR to form grafted/hyperbranched architectures. In contrast, the two-step process led to improved tensile strength and tensile modulus stemming from enhanced interfacial SiR and SSBR interactions. These results were supported by increased transparency and decreased SiR domain sizes within the two-step blends, characteristic of improved compatibilization.

2.3 | Interpenetrating polymer networks

Unlike compatibilized blends that are thermodynamically stabilized using BCPs, interpenetrating polymer networks



SCHEME 3 (A) Formation of an interpenetrating network by the single step method starting from a solution of monomer A (blue) and monomer B (red). Homopolymers A and B are also orthogonally crosslinked during polymerization. (B) Formation of an interpenetrating network by a sequential strategy starting from a matrix of monomer A. Monomer A is initially polymerized and crosslinked, followed by the addition and network formation of monomer B

(IPNs) are kinetically trapped structures containing two or more independently crosslinked networks.[77] Miscible lower molecular weight components (oligomers or monomers) are combined and crosslinked and/or polymerized. This strategy forces the compatibilization of two immiscible polymers by rapidly crosslinking the growing chains, limiting phase separation to produce materials with enhanced properties.[78,79] The domain size and degree of interpenetration are tunable depending on the blending process and the nature of the monomers/oligomers. For example, a simultaneous IPN can be prepared using orthogonal crosslinking reactions where the polymer components are crosslinked simultaneously to form both networks in a single step (Scheme 3(A)).[80] Alternatively, the formation of the first polymer network can be followed by swelling with an additional reactive component and subsequent polymerization or crosslinking of the second network in a process typically referred to as sequential IPN formation (Scheme 3(B)).

The formation of silicone-containing IPNs is attractive for silicone blends due to the wide variety of available crosslinking methods including alcoholysis, vulcanization, radiation, and hydrosilylation.[63] Careful control over the polymerization, crosslinking, and mixing during preparation prevents macroscopic phase separation, producing small domain sizes in otherwise incompatible polymer mixtures. In particular, the morphology and domain size of an IPN depends on the rate of phase separation and the crosslinking chemistry.[80] Phase separation can either occur by nucleation and growth, generating polymer droplets within a larger matrix, or by spinodal decomposition, which generally yields a bicontinuous structure with two interconnected domains.

Turner and Cheng prepared PDMS–poly(methacrylic acid) (PMAA) IPN membranes using sequential monomer immersion. Pre-IPN films were first produced by mixing vinyl-terminated PDMS with a multifunctional Si–H crosslinker, which was cured via hydrosilylation (Figure 9).[81] The crosslinked PDMS resin was then swollen in a methacrylic acid monomer solution containing triethylene glycol dimethacrylate as crosslinker and the IPN formed via free-radical polymerization upon exposure to UV radiation. Fluorescent labeling of the resulting PMAA domains by swelling in fluorescein enabled the direct visualization of the IPN morphology by laser scanning confocal microscopy. The morphology of these PDMS–PMAA sequential IPNs transitioned from a relatively homogeneous hydrogel near the glass surface to coarse phase separation and finally to a bicontinuous structure, indicative of spinodal decomposition, in the interior of the films. This change in film morphology was attributed to a concentration gradient created by monomer evaporation and substrate–surface thermodynamic effects. In contrast, the total immersion of pre-IPN films in a MAA solution ensured an even monomer concentration profile and produced a uniform bicontinuous morphology throughout the IPN. Interestingly, these homogeneous membranes were much more permeable to water-soluble compounds, with the dispersed hydrogels forming an impermeable layer at the air or glass–IPN interfaces.

Although sequential strategies provide well-disperse IPNs with unique morphologies, they are often not very practical for industrial applications. An interesting alternative to the sequential approach is IPN formation via simultaneous polymerization processes.[82] In these systems, the morphology depends on homopolymer incompatibility and the polymerization conditions, including mixing and the kinetics of each reaction.[16] Issues such as co-solubility and relative hydrophobicity between the polymers are major constraints in IPN formation and are

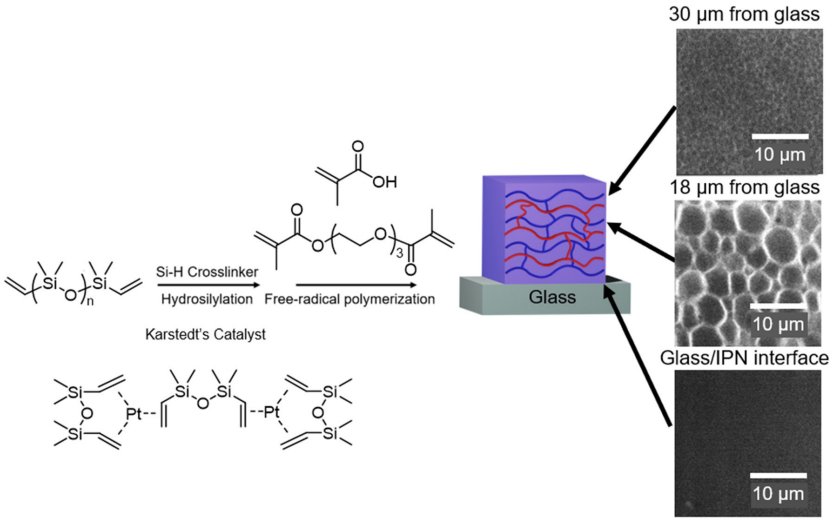


FIGURE 9 Sequential formation of a polydimethylsiloxane (PDMS)/methacrylic acid (MAA) interpenetrating polymer network (IPN) and laser scanning confocal microscopy depth profile images of an IPN prepared on a glass substrate. Adapted with permission.[81] 2000, American Chemical Society

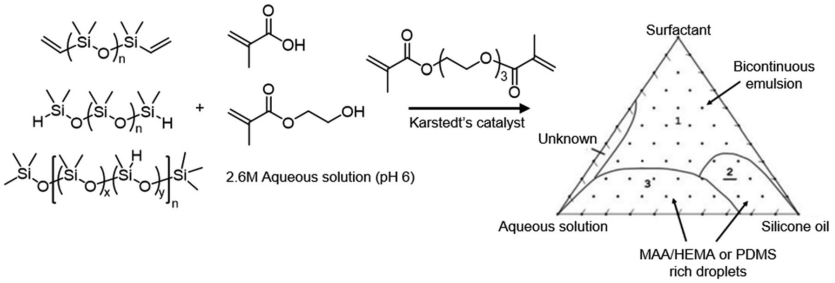


FIGURE 10 Simultaneous formation of a polydimethylsiloxane (PDMS)/methacrylic acid (MAA)/HEMA interpenetrating polymer network (IPN) and phase behavior of pre-IPN microemulsion templates with reactive surfactants. Adapted with permission.[83] 2012, Springer Nature

particularly evident when both hydrophobic and hydrophilic monomers are polymerized simultaneously. To circumvent these issues, Castellino and coworkers formed PDMS–poly(methacrylic acid-*stat*-hydroxyethyl methacrylate) (PDMS-P[MAA-HEMA]) IPNs simultaneously from bicontinuous emulsion templates that were stabilized with polymerizable silicone/ethylene-glycol-acrylate-functionalized surfactants (Figure 10).[83] This process provides a simpler one-step approach to form silicone IPNs with interpenetration at the nanoscale level. The phase behavior of these pre-IPN silicone microemulsions was evaluated using pseudo-ternary phase diagrams at different temperatures to identify compositional ranges for potential polymerization templates. Compositions with the desired morphology were then polymerized and crosslinked simultaneously to produce the final IPN. Confocal microscopy on samples swollen in aqueous sodium fluorescein confirmed that both phases were well distributed with domain sizes <1 μm, although for systems with nonreactive surfactants the

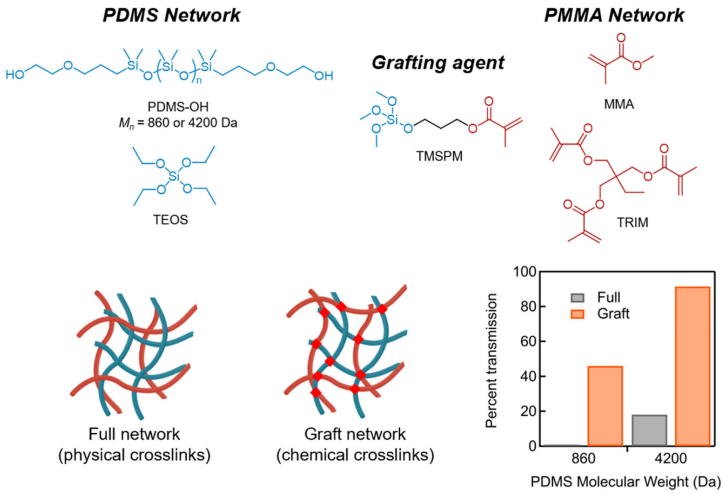
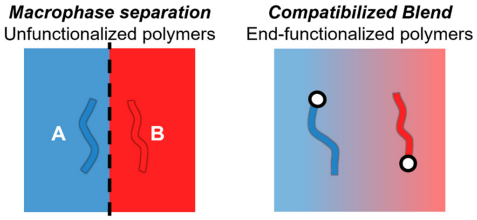


FIGURE 11 In-situ sequential synthesis and light transmission percentage for full and grafted polydimethylsiloxane (PDMS)/methacrylic acid (MAA) interpenetrating polymer networks (IPNs). Adapted with permission.[84] 1992, Elsevier



SCHEME 4 Compatibilization of immiscible homopolymer A and B through end-group effects

morphology was not uniform throughout the material. This nonuniformity may be a result of changes in the template microemulsion phase behavior and domain size during polymerization. In contrast, the bulk microstructure of IPNs produced from reactive surfactants was more uniform with reduced domain size down to <200 nm.

Although orthogonal chemistries are typically used to crosslink each domain during IPN formation, additional chemical grafts between the two immiscible polymers can increase the compatibility of the overall material. Meyer and coworkers explored this concept by synthesizing grafted and nongrafted IPNs based on PDMS and PMMA (Figure 11).[84] The IPNs were synthesized through an in-situ sequential strategy involving mixing dihydroxy-terminated PDMS, MMA, azobisisobutyronitrile (AIBN), 1,1,1-trimethylolpropane trimethacrylate (TRIM) and either tetraethyl orthosilicate (TEOS) or trimethoxysilylpropyl methacrylate (TMSPM) as a crosslinker for the PDMS domains. The PDMS network was initially formed by adding tin(II) octanoate to catalyze the polycondensation crosslinking, followed by heating to 60 °C to initiate the copolymerization of the vinyl network. Interestingly, the grafted PDMS/PMMA IPNs (crosslinked by TMSPM) were more transparent when compared to their nongrafted analogs, indicative of a decreased PDMS domain size within the composite material. In addition, differential scanning calorimetry (DSC) showed little change in the glass transition temperatures of the PDMS and PMMA networks, supporting phase separation in the graft IPNs. The stress–strain behavior of full and graft IPNs demonstrated that grafting and crosslinking significantly improved the tensile modulus E while reducing elongation at break ε_u.

2.4 | End-group interaction

Although the formation of stable polymer blends has primarily focused on the design of novel compatibilizers, several publications have demonstrated that interactions between chain ends can significantly impact interfacial properties.[85,86] This approach can lead to increased miscibility by incorporating end groups that have repulsive interactions with both blend homopolymers (Scheme 4). This phenomenon is primarily observed with low molecular weight polymers as end-group effects are diluted with increasing degrees of polymerization.[87]

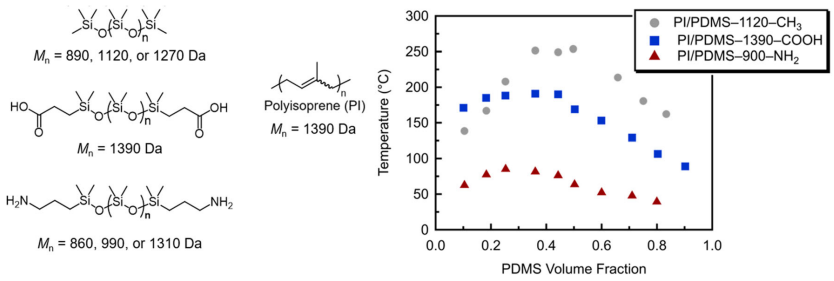


FIGURE 12 Experimental cloud point curves of nonreactive polyisoprene (PI)/polydimethylsiloxane (PDMS) blends with various chain ends. Adapted with permission.[89] 2001, Elsevier

While underexplored, a limited number of studies have shown significant end group effects on the miscibility of polysiloxanes with organic polymers.[85–89] In one example, the Koberstein group measured the interfacial tension of end-functionalized PDMS blended with polybutadiene (PBD).[85] For this study, the authors measured the interfacial tension between PBD blended with amine-terminated PDMS (PDMS-NH_2) or methyl-terminated PDMS (PDMS-CH_3). At molecular weights around 1300 Da, the interfacial tension of the PDMS-NH_2 blend was 20% lower than that of the PDMS-CH_3 blend. However, at molecular weights around 19 kDa, the change in interfacial tension was only ~5%. Unexpectedly, PDMS-NH_2 did not exhibit significant interfacial activity, indicating the reduction in interfacial tension cannot be attributed to a surfactant effect, but instead to changes in bulk thermodynamic interactions.

To understand this phenomenon, Qian et al. used a Flory–Huggins lattice model and molecular simulations to account for end group effects and their impact on the χ interaction parameter.[88] χ values of PDMS and poly(methylphenylsiloxane) (PMPS) blends were calculated for trimethylsilyl- or silanol-terminated polymers. The results indicate end groups in low molecular weight blends (particularly for oligomers with less than 20 repeat units) significantly impact χ and microphase separation, whereas end-group effects are inconsequential at higher molecular weights. Expanding on this study, Lee and coworkers measured the cloud point of low molecular weight blends of polyisoprene with PDMS—CH_3, PDMS—COOH, and PDMS—NH_2 (Figure 12).[89] For equivalent molecular weights, the cloud points of PI/PDMS—CH_3, PI/PDMS—COOH, and PI/PDMS—NH_2 dropped dramatically from 250 °C for the methyl-terminated polymer to 190 °C for PDMS—COOH and 85 °C for PDMS—NH_2, scaling inversely with the polarity of the PDMS end group. In particular, the polymer chain end had profound effects on χ, with the largest decrease associated with terminal amine groups on PDMS. Chain ends having repulsive interactions with both homopolymers force the functionalized polymers to interact, leading to increased miscibility as evidenced by lower cloud points. The phase diagrams of these end-functional blends can be modeled by a modified Flory–Huggins–Staverman lattice approach that includes binary interaction theory and group additivity concepts that capture the effect of end groups on the enthalpy of mixing.

3 | CONCLUSIONS AND FUTURE WORK

Advances in silicone chemistry have forged a remarkable toolbox for the preparation of novel BCPs, reactive coupling systems, and functionalized materials. This increased availability and versatility has allowed researchers the opportunity to design and tune the stability, morphology, and mechanical properties of immiscible polymer blends. The compatibilization of these materials has been achieved through four well-established approaches, namely the addition of silicone–organic BCPs, reactive blending, highly crosslinked interpenetrating polymer networks, and end-group effects in low molecular weight materials. With precise structural and functional group control, a wide array of silicone–organic blends can now be achieved from previously immiscible polymers despite their strong phase separation.

Although much progress has been made in the compatibilization of immiscible silicone–organic blends, several key areas are still poorly understood and would benefit from further theoretical and experimental studies. Most importantly, the impact of copolymer architecture on silicone-containing BCP additives needs more research despite noted architectural effects on the compatibilization and interfacial structure of immiscible polymer blends. Further studies are also required on reactive

blending as it does only form copolymers at the interface. There is a caveat in that a large portion of the added reactive groups on the siloxane and organic polymers are left unreacted and will be prone to degradation, further material drift (potential long term side reactions) and potential hazards as would be in the case of residual SiH containing PDMS (hydrogen formation). The BCP approach, on the other hand, could be classified as more inert but may also have issues since reaching the same level of silicone/organic polymer dispersion will require more (mixing) energy. Further fundamental studies exploring the effects of silicone-containing BCP architecture on the morphology and mechanical properties of blended polysiloxanes may allow these architecture effects to be more comprehensively evaluated. In addition, the impact of other BCP design concepts that are known to strongly influence the phase behavior of neat, nonblended materials—for example, conformational asymmetry—would provide an increased understanding of opportunities in blend compatibilization. Finally, the development of scalable, efficient, and cost-effective reactive systems that generate compatibilizers in situ will drastically aid in the commercialization of immiscible silicone–organic polymeric blends. We anticipate that polymeric silicone blends will continue to play a significant role in many areas of materials science with well-dispersed silicone–organic polymer blends being central to an increasing range of academic and industrial applications.

ACKNOWLEDGMENTS

All authors thank Dow for financial support of the Dow Materials Institute (DowMI) at UCSB. Allison Abdilla thanks the Natural Sciences and Engineering Research Council of Canada (NSERC) for financial support. Partial support by the National Science Foundation (NSF) through the Materials Research Science and Engineering Center at UC Santa Barbara (DMR-1720256, IRG-2) is gratefully acknowledged. We thank Lewis Manring (UCSB), Nikhil Fernandes (Dow), and Matthew Carter (Dow) for useful discussions.

ORCID

Craig J. Hawker https://orcid.org/0000-0001-9951-851X

REFERENCES

[1] K. Binder, *Theories and Mechanism of Phase Transitions, Heterophase Polymerizations, Homopolymerization, Addition Polymerization*, Springer-Verlag, Berlin, Germany **1994**, p. 4.
[2] C. Koning, M. van Duin, C. Pagnoulle, R. Jerome, *Prog. Polym. Sci.* **1998**, *23*, 707.
[3] D. R. Paul, J. W. Barlow, H. Keskkula, *Encyclopedia of Polymer Science and Engineering*, 2nd ed., Vol. 12, Wiley-Interscience, New York, USA **1988**.
[4] A. A. R. S. Thomas, *Compatibilization of Polymer Blends*, Elsevier, Amsterdam, Netherlands **2020**.
[5] We use silicone and polysiloxane interchangeably and use siloxane to refer to the Si–O functional group.
[6] M. G. Voronkov, V. P. Mileshkevich, Y. A. Yuzhelevskii, *Studies in Soviet Science. The Siloxane Bond*, Physical Properties and Chemical Transformations, Plenum Publishing Corporation, New York, USA **1978**.
[7] E. Pouget, J. Tonnar, P. Lucan, P. Lacroix-Desmazes, F. Ganachaud, B. Boutevin, *Chem. Rev.* **2010**, *110*(3), 1233.
[8] Centre Européen des Silicones, http://www.silicones.eu **2020**.
[9] C. G. Zimmermann, *MRS Bull.* **2010**, *35*, 48.
[10] T. Aziz, M. Waters, R. Jagger, *J. Dentist.* **2003**, *31*, 67.
[11] B. M. Holzapfel, J. C. Reichert, J.-T. Schantz, U. Gbureck, L. Rackwitz, U. Nöth, F. Jakob, M. Rubert, J. Groll, D. W. Hutmacher, *Adv. Drug Delivery Rev.* **2013**, *65*, 581.
[12] C. Hassler, T. Boretius, T. Stieglitz, *J. Polym. Sci., Part B: Polym. Phys.* **2011**, *49*, 18.
[13] F. Abbasi, H. Mirzadeh, A.-A. Katbab, *Polym. Int.* **2001**, *50*, 1279.
[14] K. Mojsiewicz-Pieńkowska, *Handbook of Polymers for Pharmaceutical Technologies*, Scrivener, Beverly, Massachusetts **2015**, p. 13.
[15] C. R. McMillin, *Rubber Chem. Technol.* **1994**, *67*, 417.
[16] P. Lucas, J. J. Robin, *Functional Materials and Biomaterials*, Springer, Berlin, Heidelberg **2007**, p. 3.
[17] U. Sundararaj, C. W. Macosko, *Macromolecules* **1995**, *28*, 2647.
[18] C. W. Macosko, P. Guégan, A. K. Khandpur, *Macromolecules* **1996**, *29*, 5590.
[19] J. Noolandi, K. M. Hong, *Macromolecules* **1982**, *15*, 482.
[20] A. V. Ruzette, L. Leibler, *Nat. Mater* **2005**, *4*, 19.
[21] C. Creton, E. J. Kramer, H. R. Brown, C. Y. Hui, *Adv. Polym. Sci* **2002**, *156*, 53.
[22] D. Schwahn, *Adv. Polym. Sci.* **2005**, *183*, 1.
[23] P. J. Flory, *Principles of Polymer Chemistry*, Cornell University Press, New York, USA **1971**.
[24] P. G. DeGennes, *Scaling Concepts in Polymer Physics*, Cornell University Press, New York, USA **1979**.
[25] D. Schwann, K. Mortensen, *Thermal Composition Fluctuations in Polymer Blends studied with Small Angle Neutron Scattering*, Gordon & Breach Science Publishers, Amsterdam, Netherlands **2000**.
[26] F. W. Bates, W. W. Maurer, P. M. Lipic, M. A. Hillmyer, K. Almdal, K. Mortensen, G. H. Fredrickson, T. P. Lodge, *Phys. Rev. Lett.* **1997**, *79*, 849.
[27] F. M. Bates, M. A. Hillmyer, T. P. Lodge, C. M. Bates, K. T. Delaney, G. H. Fredrickson, *Science* **2012**, *336*, 434.
[28] P. C. Hiemenz, T. P. Lodge, *Polymer Chemistry*, CRC Press, Boca Raton, Florida, USA **2007**.
[29] H. B. Eitouni, N. P. Balsara, in *Physical Properties of Polymer Handbook* (Ed: J. E. Mark), Springer, New York, USA **2007**, p. 19.
[30] L. M. Pitet, S. F. Wuister, E. Peeters, E. J. Kramer, C. J. Hawker, E. W. Meijer, *Macromolecules* **2013**, *46*, 8289.
[31] A. Tavakkoli, K. W. Gotrik, A. F. Hannon, A. Alexander-Katz, C. A. Ross, K. K. Berggren, *Science* **2012**, *336*, 1294.
[32] W. J. Durand, G. Blachut, M. J. Maher, S. Sirard, S. Tein, M. C. Carlson, Y. Asano, S. X. Zhou, A. P. Lane, C. M. Bates, C. J. Ellison, C. G. Willson, *J. Polym. Sci.* **2014**, *53*, 344.
[33] M. J. Maher, C. M. Bates, G. Blachut, S. Sirard, J. L. Self, M. C. Carlson, L. M. Dean, J. D. Cushen, W. J. Durand, C. O. Hayes, C. J. Ellison, C. G. Willson, *Chem. Mater.* **2014**, *26*(3), 1471.

[34] M. D. Rodwogin, C. S. Spanjers, C. Leighton, M. C. Hillmyer, *ACS Nano* **2010**, *4*, 725.
[35] K. Azuma, J. Sun, Y. Choo, Y. Rokhlenko, J. H. Dwyer, B. Schweitzer, T. Hayakawa, C. O. Osuji, P. Gopalan, *Macromolecules* **2018**, *51*, 6460.
[36] Y. H. Hur, S. W. Song, J. M. Kim, W. I. Park, K. H. Kim, Y. Kim, Y. S. Jung, *Adv. Funct. Mater.* **2018**, *28*, 1800765.
[37] Y. Luo, D. Montarnal, S. Kim, W. Shi, K. P. Barteau, C. W. Pester, P. D. Hustad, M. D. Christianson, G. H. Fredrickson, E. J. Kramer, C. J. Hawker, *Macromolecules* **2015**, *48*, 3422.
[38] Y. Luo, B. Kim, D. Montarnal, Z. Mester, C. W. Pester, A. J. McGrath, G. Hill, E. J. Kramer, G. H. Fredrickson, C. J. Hawker, *J. Polym. Sci., Part A: Polym. Chem.* **2016**, *54*, 2200.
[39] K. Almdal, M. A. Hillmyer, F. S. Bates, *Macromolecules* **2002**, *35*, 7685.
[40] E. W. Cochran, D. C. Morse, F. S. Bates, *Macromolecules* **2003**, *36*, 782.
[41] K. Chang, C. W. Macosko, D. C. Morse, *Macromolecules* **2007**, *40*, 3819.
[42] W. W. Maurer, F. S. Bates, T. P. Lodge, *J. Chem. Phys.* **1998**, *108*, 2989.
[43] K. Chang, C. W. Macosko, D. C. Morse, *Macromolecules* **2015**, *48*, 8154.
[44] L. Leibler, *Makromol. Chem., Macromol. Symp.* **1988**, *16*, 1.
[45] W. Hu, J. T. Koberstein, J. P. Lingelser, Y. Gallot, *Macromolecules* **1995**, *28*, 5209.
[46] K. Chang, C. D. Morse, *Macromolecules* **2006**, *39*, 7746.
[47] U. Jorzik, B. A. Wolf, *Macromolecules* **1997**, *30*, 4173.
[48] M. D. Dadmun, *Macromolecules* **1996**, *29*, 3868.
[49] M. D. Dadmun, *Mater. Res. Soc. Symp. Proc.* **1997**, *461*, 123.
[50] E. A. Eastwood, M. D. Dadmun, *Macromolecules* **2002**, *35*, 5069.
[51] R. Malik, C. K. Hall, J. Genzer, *Macromolecules* **2011**, *44*, 8284.
[52] J. Kim, M. K. Gray, H. Zhou, S. T. Nguyen, J. M. Torkelson, *Macromolecules* **2005**, *38*, 1037.
[53] C. Harrats, R. Fayt, R. Jérôme, S. Blacher, *J. Polym. Sci. Pol. Phys.* **2003**, *41*, 202.
[54] C. W. Macosko, H. K. Jeon, T. R. Hoye, *Prog. Polym. Sci.* **2005**, *30*, 939.
[55] C. A. Orr, J. J. Cernohous, P. Guegan, A. Hirao, H. K. Jeon, C. W. Macosko, *Polymer* **2001**, *42*, 8171.
[56] J. Zhang, J. Shengxiang, J. Song, T. P. Lodge, C. W. Macosko, *Macromolecules* **2010**, *43*, 7617.
[57] T. D. Jones, J. S. Schulze, C. W. Macosko, T. P. Lodge, *Macromolecules* **2003**, *36*, 7212.
[58] S. Y. Hobbs, M. E. J. Dekkers, V. H. Watkins, *J. Mater. Sci.* **1989**, *24*, 2025.
[59] B. N. Epstein, U.S. 4174358, **1979**.
[60] J. Rovere, C. A. Correa, V. G. Grassi, M. F. D. Pizzol, *J. Mater. Sci.* **2008**, *43*, 952.
[61] J. Lacoste, F. Delor, J. F. Pilichowski, R. P. Singh, A. Vishwa Prasad, S. Sivaram, *J. Appl. Polym. Sci.* **1996**, *59*, 953.
[62] M. Maric, N. Ahurov, C. W. Macosko, *Polym. Eng. Sci.* **2001**, *41*, 631.
[63] M. A. Brook, *Silicon in Organic, Organometallic and Polymer Chemistry*, Wiley, New York, USA **2000**.
[64] K. J. Hyun, C. W. Macosko, B. Moon, T. R. Hoye, Z. Yin, *Macromolecules* **2004**, *37*, 2563.
[65] W. Zhou, J. Osby, *Polymer* **2010**, *51*, 1990.
[66] M. A. Brook, J. B. Grande, F. Ganachaud, *Adv. Polym. Sci.* **2010**, *235*, 161.
[67] M. A. Brook, *Chem. – Eur. J.* **2018**, *24*, 8458.
[68] F. B. Madsen, I. Javakhishvili, R. E. Jensen, A. E. Daugaard, S. Hvilsted, A. L. Skov, *Polym. Chem.* **2014**, *5*, 7054.
[69] A. Genest, D. Portinha, E. Fleury, F. Ganachaud, *Prog. Polym. Sci.* **2017**, *72*, 61.
[70] F. Gonzaga, G. Yu, M. A. Brook, *Macromolecules* **2009**, *42*, 9220.
[71] F. B. Madsen, I. Dimitrov, A. E. Daugaard, S. Hvilsted, A. L. Skov, *Polym. Chem.* **2013**, *4*, 1700.
[72] A. Jurásková, S. M. Olsen, K. Dam-Johansen, M. A. Brook, A. L. Skov, *Molecules* **2021**, *26*, 82.
[73] C. S. Sample, S. H. Lee, S. Li, M. W. Bates, V. Lensch, B. A. Versaw, C. M. Bates, C. J. Hawker, *Macromolecules* **2019**, *52*, 7244.
[74] J. Bonnet, V. Bounor-Legaré, P. Alcouffe, P. Cassagnau, *Mater. Chem. Phys.* **2012**, *136*, 954.
[75] J. P. Li, P. Passagnau, F. Da Cruz-Boisson, F. Mélis, P. Alcouffe, V. Bounor-Legaré, *Polymer* **2017**, *112*, 10.
[76] Z. Sun, Q. Huang, Y. Wang, L. Zhang, Y. Wu, *Ind. Eng. Chem. Res.* **2017**, *56*, 1471.
[77] L. H. Sperling, V. Mishra, *IPNs Around the World*, Wiley, New York, USA **1997**.
[78] S. Murayama, S. Kuroda, Z. Osawa, *Polymer* **1993**, *34*, 2845.
[79] L. H. Sperling, V. Mishra, *Polym. Adv. Technol.* **1996**, *7*, 197.
[80] X. Xie, Y. Chen, Z. Zhang, A. Tanioka, M. Matsuoka, K. Takemura, *Macromolecules* **1999**, *32*, 4424.
[81] J. S. Turner, Y. L. Cheng, *Macromolecules* **2000**, *33*, 3714.
[82] A. J. Silvaroli, T. R. Heyl, Z. Qiang, J. M. Beebe, D. Ahn, S. Mangold, K. R. Shull, M. Wang, *ACS Appl. Mater. Inter.* **2020**, *12*, 44125.
[83] V. Castellino, E. Acosta, Y. L. Cheng, *Colloid Polym. Sci.* **2013**, *291*, 527.
[84] X. W. He, J. M. Widmaier, J. E. Herz, G. C. Meyer, *Polymer* **1992**, *33*, 866.
[85] C. A. Fleischer, J. T. Koberstein, V. Krukonis, P. Wetmore, *Macromolecules* **1993**, *26*, 4172.
[86] C. A. Fleischer, A. R. Morales, J. T. Koberstein, *Macromolecules* **1994**, *27*, 379.
[87] T. G. Fox, P. J. Flory, *J. Polym. Sci.* **1954**, *14*, 315.
[88] C. Qian, S. Grigoras, L. D. Kennan, *Macromolecules* **1996**, *29*, 1260.
[89] M. H. Lee, C. A. Fleischer, A. R. Morales, J. T. Koberstein, R. Koningsveld, *Polymer* **2001**, *42*, 9163.

How to cite this article: A. Abdilla, C. A. D'Ambra, Z. Geng, J. J. Shin, M. Czuczola, D. J. Goldfeld, S. Biswas, J. M. Mecca, S. Swier, T. D. Bekemeier, D. S. Laitar, M. W. Bates, C. M. Bates, C. J. Hawker, *J. Polym. Sci.* **2021**, *59*(19), 2114. https://doi.org/10.1002/pol.20210453

Appendix E. CC Chemokine Receptor 5 Targeted Nanoparticles Imaging the Progression and Regression of Atherosclerosis using PET/CT

This Appendix was initially published in *Molecular Pharmaceutics*.
Reprinted with permission from *Mol. Pharmaceutics*, **2021**, *18*, 3, 1386 – 1396.
Copyright 2021 American Chemical Society.

molecular pharmaceutics

pubs.acs.org/molecularpharmaceutics Article

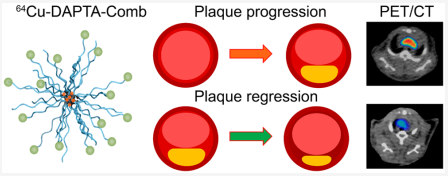
CC Chemokine Receptor 5 Targeted Nanoparticles Imaging the Progression and Regression of Atherosclerosis Using Positron Emission Tomography/Computed Tomography

Lisa Detering,[‖] Allison Abdilla,[‖] Hannah P. Luehmann, Jesse W. Williams, Li-Hao Huang, Deborah Sultan, Andrew Elvington, Gyu Seong Heo, Pamela K. Woodard, Robert J. Gropler, Gwendalyn J. Randolph, Craig J. Hawker,* and Yongjian Liu*

Cite This: *Mol. Pharmaceutics* 2021, 18, 1386−1396 Read Online

ACCESS | Metrics & More | Article Recommendations | Supporting Information

ABSTRACT: Chemokines and chemokine receptors play an important role in the initiation and progression of atherosclerosis by mediating the trafficking of inflammatory cells. Chemokine receptor 5 (CCR5) has major implications in promoting the development of plaques to advanced stage and related vulnerability. CCR5 antagonist has demonstrated the effective inhibition of atherosclerotic progression in mice, making it a potential biomarker for atherosclerosis management. To accurately determine CCR5 *in vivo*, we synthesized CCR5 targeted Comb nanoparticles through a modular design and construction strategy with control over the physiochemical properties and functionalization of CCR5 targeting peptide D-Ala-peptide T-amide (DAPTA-Comb). *In vivo* pharmacokinetic evaluation through ^{64}Cu radiolabeling showed extended blood circulation of ^{64}Cu-DAPTA-Combs conjugated with 10%, 25%, and 40% DAPTA. The different organ distribution profiles of the three nanoparticles demonstrated the effect of DAPTA on not only physicochemical properties but also targeting efficiency. *In vivo* positron emission tomography/computed tomography (PET/CT) imaging in an apolipoprotein E knockout mouse atherosclerosis model (ApoE$^{-/-}$) showed that the three ^{64}Cu-DAPTA-Combs could sensitively and specifically detect CCR5 along the progression of atherosclerotic lesions. In an ApoE-encoding adenoviral vector (AAV) induced plaque regression ApoE$^{-/-}$ mouse model, decreased monocyte recruitment, CD68+ macrophages, CCR5 expression, and plaque size were all associated with reduced PET signals, which not only further confirmed the targeting efficiency of ^{64}Cu-DAPTA-Combs but also highlighted the potential of these targeted nanoparticles for atherosclerosis imaging. Moreover, the up-regulation of CCR5 and colocalization with CD68+ macrophages in the necrotic core of *ex vivo* human plaque specimens warrant further investigation for atherosclerosis prognosis.



KEYWORDS: *nanoparticle, CCR5, atherosclerosis, positron emission tomography, macrophage*

Downloaded via UNIV OF CALIFORNIA SANTA BARBARA on March 10, 2022 at 05:27:22 (UTC).
See https://pubs.acs.org/sharingguidelines for options on how to legitimately share published articles.

INTRODUCTION

Atherosclerosis, the underlying cause of the majority of cardiovascular diseases (CVDs), is a chronic, systemic, primarily lipid driven inflammatory disease characterized by the development of multifocal plaque lesions within vessel walls, which extend into the vascular lumen.[1,2] During the progression of atherosclerosis, most atherosclerotic plaques remain asymptomatic, and for many clinical events, the first patient manifestation is stroke, myocardial infarction, or sudden cardiac death. The identification and detection of biomarkers closely associated with the progression or stability of advanced plaques would therefore provide invaluable information about the staging and vulnerability of disease, allowing for personalized therapy and monitoring of treatment response.[3−8]

Of the biomarkers studied in atherosclerosis, most have centered on addressing leukocyte influx in plaque initiation. This establishes a prime role for selectin family members in the capture, tethering, and rolling of circulating monocytes onto the inflamed endothelium and for endothelial adhesion molecules, which mediate leukocyte arrest by interacting with integrins on activated monocytes.[9−11] However, leukocyte influx in advanced plaque structures has shown large variability during the progression of atherosclerosis, which significantly affects the expression of associated biomarkers and requires further investigation to correlate expression with disease maturation.[6,12,13] Chemokines and their receptors are widely

Received: December 3, 2020
Revised: February 3, 2021
Accepted: February 4, 2021
Published: February 16, 2021



ACS Publications © 2021 American Chemical Society

expressed and prominently presented on cells that play a crucial role in atherosclerosis development, such as monocytes and macrophages.[14−21] Of the various chemokine/chemokine receptor pairs identified in atherosclerotic plaque, the CCL5/CCR5 axis is one of the most studied systems.[22,23] In an attempt to find the temporal expression of CCR5 during the progression of atherosclerosis, it was observed that CCR5 showed age-associated increase and played a central role in promoting late-stage plaque.[24] In CCR5 deleted apolipoprotein E ($ApoE^{-/-}$) mice fed with a high fat diet (HFD), the content of monocytes/macrophages and T-lymphocytes in the aorta region was substantially reduced compared to $ApoE^{-/-}$ mice. As a result, the atherosclerotic plaque was significantly reduced in size and showed improvement toward a less inflammatory phenotype, as evident by reduced T cell/monocyte infiltration and higher smooth muscle and IL-10 content.[25] With CCR5 antagonist Maraviroc treatment in $ApoE^{-/-}$ mice, the plaque size was decreased by 70%, and the monocyte/macrophage infiltration was attenuated by 50%,[26] in part because both monocyte subsets in the blood utilize CCR5 in trafficking to plaques.[23] In humans, CCR5 up-regulation in advanced plaque structures was identified and closely associated with plaque stability, demonstrating a significant role for CCR5 as a predictor of atherosclerosis diagnosis and treatment.[27−29]

In atherosclerosis imaging, due to the low abundance of biomarkers expressed on the lesion, the sensitivity and specificity of the imaging probe are essential for successful plaque diagnosis, which makes positron emission tomography (PET) a desirable imaging modality.[6−8] In contrast to monovalent imaging agents, multivalent nanoparticles have demonstrated superior performance based on tunable, high molecular weight structures, which promote targeting efficiency and favorable *in vivo* pharmacokinetics.[30,31] Core−shell amphiphilic comb copolymers are modular nanostructure designs, which provide for accurate control over functional groups for targeting and imaging, size, charge, and hydrophilicity for minimal nonspecific retention. These systems have been studied for the detection of atherosclerotic plaques across various systems, from preclinical research to human translation.[32−36] Of various CCR5 targeting molecules,[37] the DAPTA peptide was chosen due to its CCR5 binding specificity and straightforward conjugation strategy to nanoparticles. Previously, we have reported a DAPTA-Comb nanoparticle conjugated with 10% DAPTA for imaging CCR5 in a mouse vascular injury model.[35] Given the success of ongoing clinical study using a natriuretic peptide clearance receptor targeted Comb nanoparticle for human atherosclerosis PET imaging,[36] we aim to further improve the targeting efficiency of DAPTA-Comb for potential translation. We synthesized DAPTA-Comb nanoparticles conjugated with various amounts of DAPTA peptides and assessed the relationship between biodistribution and plaque imaging efficiency. Due to the extended blood retention of DAPTA-Comb, we chose ^{64}Cu as radiolabel owing to its appropriate nuclear properties such as decay half-life ($t_{1/2}$ = 12.7 h). We thoroughly assessed ^{64}Cu radiolabeled DAPTA-Combs (^{64}Cu-DAPTA-Combs) plaque imaging sensitivity and specificity in progressive and regressive $ApoE^{-/-}$ mouse atherosclerosis models using PET/CT and correlated the expression of CCR5 on plaques with PET signals. To further assess the potential of CCR5 as an imaging biomarker for human atherosclerosis management, we examined the up-regulation of CCR5 and related histopathological features of *ex vivo* human atherosclerotic specimens collected from carotid endarterectomy (CEA).

MATERIALS AND METHODS

Reagents and Instrumentation. All reagents were used as received unless otherwise specified. 2,5-Dioxopyrrolidin-1-yl pent-4-ynoate was purchased from Annova Chemical Inc. Poly(ethylene glycol)-N_3 (PEG-N_3) was purchased from Nanocs Inc.. Functionalized poly(ethylene glycol) (PEG) derivatives were purchased from Intezyne Technologies. 1,4,7,10-Tetraazacyclododecane-1,4,7-tris(*tert*-butyl acetate) (DOTA-*t*-Bu-ester), tris-*tert*-butylester-DOTA, 1,4,7,10-tetraazacyclododecane, and DOTA-*N*-hydroxysuccinimide ester were obtained from Macrocyclics. Amicon Centriplus YM-30 centrifugal filtrations tubes were obtained from Millipore. ^{64}Cu was produced at the Washington University cyclotron facility. D-Ala1-peptide T-amide (DAPTA, D-A1STTTNYT-NH_2) was synthesized by CPC Scientific. Zeba desalting spin columns were from Pierce. Polymeric materials were characterized by ^{1}H and ^{13}C nuclear magnetic resonance (NMR) spectroscopy using a Bruker 500 MHz spectrometer with the residual solvent signal as an internal reference. Gel permeation chromatography was performed in dimethylformamide on a Waters system equipped with four 5 mm Waters columns (300 mm × 7.7 mm) connected in series with increasing pore size (102, 103, 104, and 106 Å) and Waters 410 differential refractometer index and 996 photodiode array detectors. The molecular weights of the polymers were calculated relative to linear poly(methyl methacrylate) (PMMA) or PEG standards. Infrared spectra were measured with a PerkinElmer Spectrum 100 with a Universal ATR sampling accessory.

Mass spectrometry was carried out using matrix-assisted laser desorption/ionization techniques. Gel permeation chromatography (GPC) was carried out with a Waters Alliance HPLC system pump (2695 separation module) and four Visco Gel I series columns (7.8 mm × 30 cm, Viscotek). A Waters 2414 differential refractometer was used for analysis using dimethylformamide (DMF) with 0.1% LiBr as mobile phase. Chromatographic analyses were performed at room temperature and using poly(methyl methacrylate) (PMMA) as standards. Dynamic light scattering (DLS) was performed on a Wyatt Technology DynaPro NanoStar at room temperature to determine the hydrodynamic sized of as-prepared nanoparticles. Data were collected on 0.1 wt % aqueous solutions of nanoparticles filtered through a 0.2 μm filter.

Synthetic Procedures. The syntheses of *S*-methoxycarbonylphenylmethyl dithiobenzoate reversible addition−fragmentation chain-transfer (RAFT) agent,[38] macro- and small molecule monomers, DOTA methacrylate (DOTA-MA), PEG methacrylate (PEGMA), and DAPTA PEG methacrylate (DAPTA-PEGMA), DAPTA-Comb copolymers, and nanoparticles were adopted from previously published work with minor modifications.[32−35,39]

DAPTA-acetylene. Synthesis of DAPTA-acetylene was conducted as previously reported with the following modification: 2,5-Dioxopyrrolidin-1-yl pent-4-ynoate was used in the place of 4-pentynoic anhydride. MS (MALDI): calculated (M + Na) 960.5, observed (M + Na) 959.7.

Synthesis of DAPTA Poly(ethylene glycol) Methacrylate (DAPTA-PEGMA). DAPTA-PEGMA was synthesized as previously reported[35] with minor modification using a 0.01 M aqueous ethylenediaminetetraacetic acid (EDTA) solution

https://dx.doi.org/10.1021/acs.molpharmaceut.0c01183
Mol. Pharmaceutics 2021, 18, 1386−1396

Table 1. Characterization of Nontargeted Comb and 10%, 25%, and 40% DAPTA-Comb

polymer	M_n[a]	$Đ$[a]	hydrodynamic size (nm)[b]	ζ-potential (mV)	no. of DAPTA/nanoparticle[c]	no. of DOTA/nanoparticle[c]	^{64}Cu radiolabeling specificity activity (GBq/nmol)
Comb	220 000	1.2	20.0	−32.0	0	105	5.1
10% DAPTA-Comb	200 000	1.7	14.8	−6.24	14	105	4.5
25% DAPTA-Comb	300 000	2.5	15.2	−10.0	35	105	3.8
40% DAPTA-Comb	358 000	2.9	10.9	−14.7	56	105	4.6

[a]Determined by gel permeation chromatography in dimethylformamide, calibrated to poly(methyl methacrylate) standards (g/mol), $Đ = M_w/M_n$. [b]Measured by dynamic light scattering. [c]Predicted incorporation.

containing 0.02 M NaOH (×4) and Milli-Q water (×10) to wash the product.

Synthesis of DAPTA-Comb Copolymers. Synthesis of the comb copolymers was performed as previously reported.[34,35] Percent DAPTA (%DAPTA) is defined as the feed ratio of DAPTA-PEGMA to the total PEG containing monomers (DAPTA-PEGMA + PEGMA). GPC-DMF (PMMA standards): 10% DAPTA-Comb M_w = 200 000 g mol^{-1}, $Đ$ = 1.7; 25% DAPTA-Comb M_w = 300 000 g mol^{-1}, $Đ$ = 2.5; 40% DAPTA-Comb M_w = 358 000 g mol^{-1}, $Đ$ = 2.9.

DOTA Deprotection and Nanoparticle Assembly. Deprotection of the DOTA groups and particle assembly were performed as previously reported.[35] Briefly, after deprotection of the DOTA groups, the freeze-dried comb copolymers were dissolved in dimethyl sulfoxide (DMSO) (1 wt %) and heated to 50 °C until fully dissolved. The solution was cooled to room temperature, and an equal volume of Milli-Q water was added all at once while stirring to achieve assembly. By changing of the ratios of various copolymers, the number of targeting moieties could be controlled (Figure S1). To remove DMSO, the solution was transferred to two Amicon Centriplus YM-30 (molecular weight cutoff = 30 000 g mol^{-1}) centrifugal filtration tubes and concentrated and rediluted with Milli-Q water until the DMSO content was less than 0.5 mg/mL by ^{1}H NMR (~5×). The resultant particles were characterized by DLS and ζ potential with a Zetasizer nano ZS (ZEN3600, Malvern Instruments) (Table 1). 10% DAPTA-Comb: R_h = 14.8 nm, % dispersity = 13.2, ζ-potential = −6.24 mV. 25% DAPTA-Comb: R_h = 15.2 nm, % dispersity = 11.3, ζ-potential = −10.0 mV. 40% DAPTA-Comb: R_h = 10.9 nm, % dispersity = 11.1, ζ-potential = −14.7 mV. Nontargeted Comb: R_h = 20.0 nm, % dispersity = 10.1, ζ-potential = −32.0 mV. All the nanoparticle solutions were rediluted to 10 mg/mL and stored at −20 °C.

ApoE$^{-/-}$ Mouse Spontaneous Atherosclerosis Progression Model. All animal studies were performed in compliance with guidelines set forth by the National Institutes of Health Office of Laboratory Animal Welfare and approved by the Washington University Institutional Animal Care and Use Committee (IACUC). For the spontaneous atherosclerosis mouse model, 6-week-old male ApoE$^{-/-}$ mice were fed a high fat diet (HFD) (Harlan Teklad, 42% fat) for 40 weeks. Age-matched wild-type (WT) male C57BL/6 mice on normal chow were used as controls. Each mouse was anesthetized with a standard inhaled-anesthetic protocol (1.5−2% isoflurane) by induction in a chamber, and maintenance anesthesia was administered via a nose cone.

ApoE$^{-/-}$ Mouse Atherosclerosis Regression Model. ApoE$^{-/-}$ mouse atherosclerosis regression model was carried out in ApoE$^{-/-}$ mice following our previous report.[22] Six-week-old male ApoE$^{-/-}$ mice were first put on HFD for 9 weeks. ApoE$^{-/-}$ mice were injected iv with 1.0 × 10^{12} plaque-forming units per mouse of adeno-associated virus encoding mouse ApoE (AAV-252844, Vector Biolabs) or a control PBS solution in a volume of PBS not exceeding 200 μL. Mouse plasma was collected for the measurement of cholesterol levels at baseline and 1, 2, and 3 weeks after adeno-associated virus injection, as we previously reported.[22] To determine the monocyte recruitment during the plaque regression, classic Ly-6C^{hi} monocytes were labeled *in vivo* by retro-orbital iv injection of 1.0 μm Fluoresbrite green fluorescent plain microsphere (Polysciences Inc.) diluted 1:4 in sterile PBS at 3 days after iv injection of 250 μL of clodronate-loaded liposomes (Liposoma BV).

^{64}Cu Radiolabeling of DAPTA-Combs and Comb Nanoparticles. The radiolabeling of DAPTA-Comb and comb nanoparticles was as reported previously.[34,39] The nanoparticles (5 μg, 5 pmol) were heated with ^{64}Cu (~185 MBq) in 100 μL of ammonium acetate buffer (0.1 M, pH 5.5) at 80 °C for 1 h. EDTA (5 μL, 10 mM in 50 mM pH 7.4 phosphate buffer) was added to the solution and incubated for another 3 min to remove any nonspecifically bound ^{64}Cu from the nanoparticles. Then, the ^{64}Cu radiolabeled nanoparticles were purified using a 2 mL Zeba spin desalting column. The radiochemical purity (RCP) of the purified nanoparticles was determined by spotting a 2 μL aliquot of the solution on silica gel impregnated glass microfiber chromatography paper developed in a buffer composed of methanol and 10% ammonium acetate (volume ratio = 1:1) and measured by radioactive thin layer chromatography (Radio-TLC, Washington, DC). Repeated procedures would be performed to ensure the RCP was equal to or greater than 95% prior to *in vivo* studies. Mouse serum stability was performed by incubating 3.5 mCi 40% ^{64}Cu-DAPTA-Comb in 100 μL of 1× PBS with 100 μL of mouse serum at 37 °C with gentle shaking (350 rpm) using an Eppendorf thermomixer (Fisher Scientific, Pittsburgh, PA). At 0, 2, and 24 h after incubation, an aliquot of sample was taken out for radio-TLC analysis to determine radiochemical purity.

Biodistribution Studies. Purified ^{64}Cu-DAPTA-Comb nanoparticles were reconstituted in 0.9% sodium chloride (APP Pharmaceuticals) for intravenous injection. Male C57BL/6 mice weighing 20−25 g (n = 4/group) were anesthetized with inhaled isoflurane, and approximately 370 kBq of labeled nanoparticles (7.2−9.0 mg/kg of body weight) in 100 μL of saline was injected via the tail vein. The mice were reanesthetized before they were euthanized by cervical dislocation at each time point (1, 4, and 24 h) after injection. Organs of interest were collected, weighed, and counted in a well γ counter (Beckman 8000). Standards were prepared and measured along with the samples to calculate the percentage injected dose per gram of tissue (%ID/g).[35,39]

Small-Animal PET/CT Imaging. Small-animal PET/CT imaging with 10%, 25%, and 40% ^{64}Cu-DAPTA-Comb was

https://dx.doi.org/10.1021/acs.molpharmaceut.0c01183
Mol. Pharmaceutics 2021, 18, 1386−1396

performed with ApoE$^{-/-}$ mice on HFD to determine the uptake at the aortic arch along the progression and regression of atherosclerotic lesions. The wild-type C57BL/6 mice were used as controls and scanned following the same protocol. For PET/CT imaging with ^{64}Cu-DAPTA-Combs and ^{64}Cu-Comb, 3.7 MBq purified nanoparticles in 100 μL of saline was injected via tail vein. The imaging sessions were collected on the PET scanners at 24 h after injection using an Inveon PET/CT scanner (Siemens Healthcare). Competitive receptor blocking studies were performed on ApoE$^{-/-}$ mice for ^{64}Cu-DAPTA-Combs by co-injection of unlabeled DAPTA-Comb in 100-fold excess (n = 4) at 36 weeks after HFD, followed by PET scans at 24 h after injection. Data analysis of the PET images was performed using the manufacturer's software (IRW, Siemens Healthcare). The accumulation of the PET tracers at aortic arch was calculated as %ID/g.

Histology and Immunofluorescence of ApoE$^{-/-}$ Mouse Tissues. After the last scan, the mice were euthanized by cervical dislocation, and the hearts and aortic arches were perfusion-fixed in situ with freshly prepared 4% paraformaldehyde in 1× phosphate-buffered saline for histopathology and immunohistochemistry.

Serial sections of 10 μm in thickness were cut from paraformaldehyde-fixed (24 h), OCT-embedded specimens. Blocking serum was added (10% donkey serum in PBS-T) for 1 h to prevent nonspecific binding. The sections were then incubated overnight at 4 °C with primary antibody (anti-CD68, 1:100 in 1% blocking serum; Biorad, Hercules, CA, and anti-CCR5, 1:100 in 1% blocking serum, Bioss, Woburn, MA). Sections were washed in PBS, and secondary antibodies were applied for 1 h (donkey anti-rat Cy5, 1:300, and donkey anti-rabbit Cy3, 1:300, both from Jackson Laboratories, West Grove, PA). Sections were washed in PBS, and SMA-FITC conjugate was applied for 1 h at room temperature (1:500, Sigma, St. Louis, MO). Sections were washed again in PBS and coverslipped with DAPI mounting medium before being imaged with confocal microscopy. H&E was also obtained to analyze morphology of the tissues. Quantification of plaque area and area occupied by a particular stain was calculated with ImageJ software. Beads in plaques were counted manually by fluorescence microscopy.[22]

Histology and Immunostaining of Human Tissues. Human carotid endarterectomy (CEA) specimens were from Washington University Vascular Surgery Biobank Repository collected under Institutional Review Board. Deidentified CEA specimens were placed in sterile saline in the operating room and fixed in 10% formalin overnight, embedded in paraffin, and sectioned at a thickness of 5 μm for histology and immunohistochemistry. Whole specimen histologic evaluations were performed using H&E to examine tissue architecture. Paraffin embedded sections were deparaffinized in xylenes and rehydrated using alcohols and PBS. Tissues were boiled in buffer (pH 6.2 Diva Decloaker, 1×) to retrieve antigen. They were blocked with 10% donkey serum (EMD Millipore, St. Louis, MO) for 1 h to reduce nonspecific binding. The sections were then incubated with primary antibody (anti-CD68, 1:100 in 1% blocking serum; Biorad, Hercules, CA, and anti-CCR5, 1:100 in 1% blocking serum, Bioss, MA) overnight at 4 °C. Secondary antibody was applied (donkey anti-rat Cy5, 1:300, and donkey anti-rabbit Cy3, 1:300, both from Jackson Laboratories, West Grove, PA). Sections were washed again in PBS and coverslipped with DAPI mounting medium before being imaged with a Leica confocal microscope system.

Real-Time Reverse Transcription Polymerase Chain Reaction (RT-PCR). RNA isolated from aortic arteries was used for real-time RT-PCR. RNeasy microRNA kit (Qiagen; Germantown, MD) was used to isolate RNA following the manufacturer's instruction. Reverse transcription reactions used 300 ng of total RNA, random hexamer priming, and Superscript II reverse transcriptase (Invitrogen). Taqman assays (Invitrogen) were used to determine CCR5 and glyceraldehyde 3-phosphate dehydrogenase (GAPDH) with an Eco real-time PCR system (Illumina, San Diego, CA) in 48-well plates (n = 3). PCR cycling conditions were as follows: 50 °C for 2 min, 95 °C for 21 s, and 60 °C for 20 s. GAPDH expression was used as a comparator using ΔΔCt calculations.

Autoradiography. Fixed human CEA specimens (n = 10) were deparaffinized in Citrasolv and rehydrated with a series of graded alcohols and then PBS. The slides were incubated with 40% ^{64}Cu-DAPTA-Comb (0.75 MBq) for 15 min, followed by extensive wash with water. The slides were then covered with a phosphor-imaging film plate and exposed at −20 °C overnight. The film was imaged with a GE Typhoon FLA 9500 biomolecular imager. For blocking studies, similar procedures were performed in the presence of nonradiolabeled DAPTA-Comb in excess amount (DAPTA-Comb/^{64}Cu-DAPTA-Comb molar ratio = 100:1).

Statistical Analysis. Group variation is described as the mean ± SD. Groups were compared using one-way ANOVA with a Bonferroni adjustment. Individual group differences were determined using a two-tailed Mann−Whitney test. The significance level in all tests was a p value of 0.05 or less.

RESULTS AND DISCUSSION

***In Vivo* Pharmacokinetic Evaluation of DAPTA-Combs.** In contrast to other nanostructure agents reported for atherosclerosis imaging,[31,40−42] core−shell comb copolymer systems afford the design flexibility for strategically modifying the nanostructure size, morphology, composition, and surface properties through modular chemistry. This allows nanoparticle candidates to be screened for specific biomedical applications and future translation.[34] On the basis of our previous work imaging CCR5 in an ApoE$^{-/-}$ mouse vascular injury model[35] using 10% DAPTA-Comb (14 DAPTA peptides/Comb) radiolabeled with ^{64}Cu (^{64}Cu-DAPTA-Comb), we prepared 25% and 40% DAPTA-Comb with ∼35 and ∼56 DAPTA peptide units per comb nanostructure, respectively, following the modular construction strategies (Figure S1, Table 1), to compare and optimize the plaque imaging sensitivity and specificity. Representative mouse serum stability of 40% ^{64}Cu-DAPTA-Comb showed more than 80% intact tracer at 24 h after incubation (Figure S2), ensuring stable radiolabel for CCR5 imaging.

In contrast to previously reported CCR5 peptide targeting tracer ^{64}Cu-DOTA-DAPTA showing fast blood and renal clearance,[35] biodistribution of the three ^{64}Cu-DAPTA-Combs all showed largely extended blood retention, allowing enhanced targeting efficiency.[33−35] At 1 h postinjection (p.i.) in wild-type (WT) mice, the three ^{64}Cu-DAPTA-Combs showed comparable blood retention (10%, 33.6 ± 7.0 %ID/g; 25%, 32.4 ± 6.7 %ID/g; 40%, 27.2 ± 1.2 %ID/g, n = 4). At 4 h p.i., the blood retention of 25% and 40% ^{64}Cu-DAPTA-Comb decreased more than 40% from the value at 1 h, while the 10% counterpart was reduced by approximately 15%. At 24 h p.i., the blood retention of the 10% ^{64}Cu-DAPTA-Comb (21.8 ± 4.2 %ID/g) was almost 9 times (9×) higher than those of 25%

https://dx.doi.org/10.1021/acs.molpharmaceut.0c01183
Mol. Pharmaceutics 2021, 18, 1386−1396

and 40% ^{64}Cu-DAPTA-Comb (2.3 ± 0.2 %ID/g for both). This trend was also observed in other blood pool organs including heart, lung, and muscle (Figures 1 and S3). In the liver, the 10% ^{64}Cu-DAPTA-Comb had relatively stable accumulation during the 24 h study (5.2 ± 1.1−7.0 ± 0.6 % ID/g), while the 25% and 40% counterparts showed gradually increased uptake with approximately 2-, 4-, and 5-fold higher accumulations than the values for 10% ^{64}Cu-DAPTA-Comb at 1, 4, and 24 h. Compared to the progressively increased splenic uptake (3.1 ± 0.6 to 6.9 ± 0.7 %ID/g) of 10% ^{64}Cu-DAPTA-Comb, the uptake of the corresponding 25% and 40% derivatives in the spleen rapidly increased from 1 to 4 h. In both cases, the values were ∼20 times (20×) higher than for the 10% ^{64}Cu-DAPTA-Comb and remained stable up to 24 h. This trend was likely due to the increased concentration of DAPTA peptide units conjugated to the surface of the comb nanoparticle, leading to increased binding to the high levels of CCR5+ immune cells in spleen.[43] In the gastrointestinal tract, 25% and 40% ^{64}Cu-DAPTA-Comb showed slightly higher intestine accumulation at 4 h but at least doubled uptake at 24 h compared to the 10% counterpart, reasonably due to the hepatobiliary clearance. During the 24 h study, the renal clearance of all three nanoparticles remained constant, albeit the excretion of 40% ^{64}Cu-DAPTA-Comb was slightly higher than the other two (Figure 1).

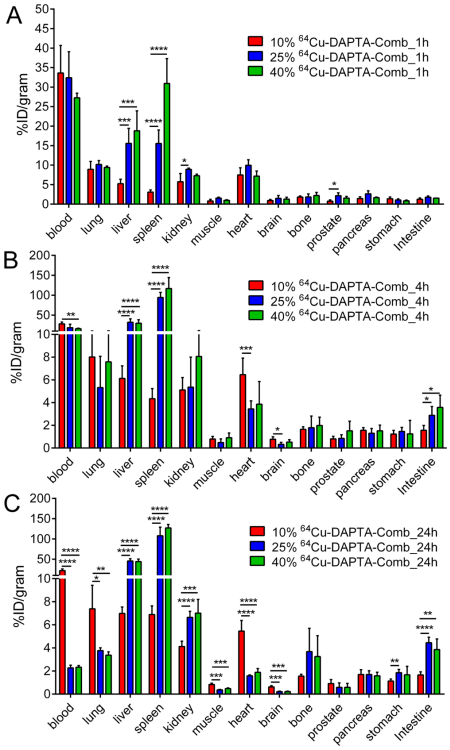


Figure 1. Biodistribution of 10%, 25%, and 40% ^{64}Cu-DAPTA-Comb in wild-type C57BL/6 mice (n = 4/group) at (A) 1 h, (B) 4 h, and (C) 24 h after intravenous injection: ****p < 0.0001, ***p < 0.001, **p < 0.01, *p < 0.05.

PET/CT Imaging CCR5 along the Progression of Atherosclerosis Using ^{64}Cu-DAPTA-Comb in an ApoE$^{-/-}$ Mouse Model. PET/CT imaging of CCR5 expression on atherosclerotic lesions was first performed in ApoE$^{-/-}$ mice fed with HFD using 10% ^{64}Cu-DAPTA-Comb along the progression of plaque. As shown in Figure S4, at 8 weeks after HFD, PET/CT images revealed strong uptake at aortic arch of ApoE$^{-/-}$ mouse with little retention observed in the heart, reasonably due to elevated clearance through liver and spleen. At 35 weeks after HFD in ApoE$^{-/-}$ mice, the CCR5 targeted nanoparticles continued to determine an intense PET signal at 24 h after injection in the aortic arch (Figure 2). Quantitative uptake analysis showed that the tracer uptake (7.06 ± 0.46 %ID/g, n = 4) was approximately 3 times as much as that determined from WT mice (2.39 ± 0.49 %ID/g, n = 4, p < 0.0001), which showed a weak signal in the aortic arch. Longitudinal PET/CT studies in ApoE$^{-/-}$ mice showed gradually increased uptake at aortic arch from 8 weeks (6.19 ± 0.24 %ID/g, n = 10) to 28 weeks (7.39 ± 1.15 %ID/g, n = 6) after HFD followed by a slow decrease to 6.78 ± 0.65 %ID/g at 40 weeks. In WT mice, due to the lack of atherosclerotic plaque, tracer accumulation at aortic arches was significantly lower than ApoE$^{-/-}$ mice at each time point and hardly changed during the 40 weeks' study (2.07 ± 0.3 %ID/g to 2.55 ± 0.41 %ID/g, p < 0.0001, n = 4−5 per group).

The CCR5 targeting specificity of 10% ^{64}Cu-DAPTA-Comb was confirmed through competitive receptor blocking in ApoE$^{-/-}$ mice. In the presence of excess nonradioactive DAPTA-Comb, accumulation of 10% ^{64}Cu-DAPTA-Comb was reduced by more than 50% (3.31 ± 0.71 %ID/g, n = 4, p < 0.0001) at 36 weeks after HFD compared to the signal acquired 1 week prior in the same group of mice, suggesting targeting specificity. To determine the CCR5 targeting positivity on plaques, the nonspecific retention of nanoparticles at atherosclerotic lesions was assessed with nontargeted ^{64}Cu-Comb nanoparticle. As shown in Figure 2, low uptake was demonstrated in ApoE$^{-/-}$ mice. Quantification showed the tracer accumulations (2.09 ± 0.66 %ID/g to 2.69 ± 0.98 %ID/g, n = 4 for all, p < 0.0001 for all) were approximately 2 times less than the results obtained with the targeted 10% ^{64}Cu-DAPTA-Comb at each time point despite the significant progression of atherosclerosis, confirming the targeting specificity of 10% ^{64}Cu-DAPTA-Comb. Interestingly, with the progression of plaque and decreased cellularity, the CCR5 targeting positivity of 10% ^{64}Cu-DAPTA-Comb gradually increased from 61% at 8 weeks to 70% at 40 weeks after HFD, which could be partially due to the elevated expression of CCR5 on late-stage plaques and reduced nonspecific retention,[24] making the tracer a useful tool to determine plaque stability. Moreover, quantitative RT-PCR measurement of CCR5 in aortic arteries of ApoE$^{-/-}$ mice at multiple time points revealed a close association with corresponding tracer uptake of 10% ^{64}Cu-DAPTA-Comb at aortic arch (Figure S5), which further confirmed the imaging specificity of this targeted nanoparticle.

Histopathological analysis of the aortic sinus of ApoE$^{-/-}$ mice at 12 weeks after HFD revealed significant development of atherosclerotic lesions characterized by substantial neo-

https://dx.doi.org/10.1021/acs.molpharmaceut.0c01183
Mol. Pharmaceutics 2021, 18, 1386−1396

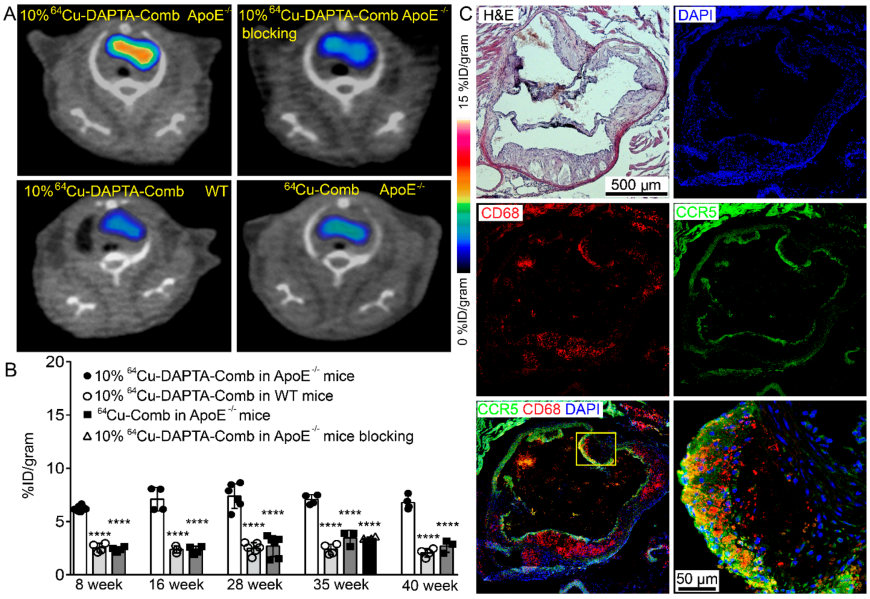


Figure 2. (A) Representative 10% ^{64}Cu-DAPTA-Comb PET/CT images at 24 h after injection showing specific targeting at aortic arch in ApoE$^{-/-}$ mice, significantly blocked signal with the co-injection of nonradiolabeled DAPTA-Comb, and minimum uptake in wild-type C57BL/6 mice. Nontargeted ^{64}Cu-Comb image showed low, nonspecific uptake at aortic arch. All the studies were performed in ApoE$^{-/-}$ mice at 35 weeks after HFD and WT mice on normal chow. (B) Quantitative uptake analysis of 10% ^{64}Cu-DAPTA-Comb in ApoE$^{-/-}$ and age-matched wild-type C57BL/6 mice and nontargeted ^{64}Cu-Comb in ApoE$^{-/-}$ mice in a time course study. Competitive receptor blocking study was performed in ApoE$^{-/-}$ mice (****p < 0.0001, n = 4−6/group). (C) H&E staining of aortic sinus of ApoE$^{-/-}$ mice on HFD for 12 weeks showing the development of atherosclerotic lesion with significant neointimal thickening, large lipid pool, and infiltration of foam cells. Immunofluorescent staining shows DAPI (blue), CD68 macrophage (red), CCR5 (green), and fused images. CD68 expression was largely throughout the plaques, while CCR5 was more on the surface of plaques and colocalized with CD68 (amplified image, yellow).

intima thickening, large lipid pool, extensive infiltration of foam cells, and a thin fibrous cap (Figure 2C). Immunofluorescent staining showed dense expression of CD68 macrophages throughout the plaques. Interestingly, CCR5 signals were mostly determined on the surface of plaque and largely colocalized with CD68 as illustrated in the magnified image (Figure 2C), further supporting the PET imaging data.

On the basis of biodistribution studies of the three nanoparticles and the PET/CT time-course study with 10% ^{64}Cu-DAPTA-Comb, we further explored the potential of CCR5 imaging using 25% and 40% ^{64}Cu-DAPTA-Combs to gain insight on the effect of DAPTA peptide conjugation on plaque targeting efficiency along the progression of atherosclerosis in ApoE$^{-/-}$ mice fed on HFD for 8, 16, and 28 weeks. As shown in Figure 3A, 25% ^{64}Cu-DAPTA-Comb nanoparticles showed a strong PET signal within the aortic arch of ApoE$^{-/-}$ mice at 28 weeks after HFD in contrast to weak accumulation in WT mice. Quantitative uptake analysis revealed a gradually increased uptake at plaques in ApoE$^{-/-}$ mice and progressively declining accumulation in WT mice during the time-course study, similar to what was determined using 10% ^{64}Cu-DAPTA-Comb. In contrast to the data acquired with 10% ^{64}Cu-DAPTA-Comb (∼14 DAPTA/Comb), the 25% ^{64}Cu-DAPTA-Comb (∼35 DAPTA/Comb) demonstrated approximately 20% higher uptake in plaques during the time-course study (p < 0.01 at both 8 and 28 weeks, n = 4−8 per group) (Figure S6). Importantly, 25% ^{64}Cu-DAPTA-Comb plaque uptake at 28 weeks (9.05 ± 0.67 %ID/g, n = 4) was significantly higher than those at 8 weeks (7.53 ± 0.31 %ID/g, n = 8, p < 0.0001) and 16 weeks (8.02 ± 0.38 %ID/g, n = 4, p < 0.05), suggesting its sensitivity to monitor the progression of plaque. ApoE$^{-/-}$/WT tracer uptake ratios at the three time points for 25% ^{64}Cu-DAPTA-Comb (3.8, 4.0, 5.1 for 8, 16, and 28 weeks, respectively) were all higher than those obtained with 10% counterpart (2.5, 2.9, 3.0) at the same time points, indicating DAPTA peptide mediated tracer uptake at atherosclerotic lesions (Figure 3B). Evaluation of the 40% ^{64}Cu-DAPTA-Comb demonstrated significantly increased uptake (approximately 25% higher, p < 0.01, p < 0.05, and p < 0.001 at 8, 16, and 28 weeks, respectively, n = 4−8 per group) and uptake ratios (3.8, 4.9, 5.6) at each time point relative to those obtained with 10% ^{64}Cu-DAPTA-Comb (Figure S6). Furthermore, 40% ^{64}Cu-DAPTA-Comb uptake at 16 weeks (8.80 ± 0.63 %ID/g, n = 4, p < 0.05) and 28 weeks (9.47 ± 0.72 %ID/g, n = 4, p < 0.005) was both significantly higher than those acquired at 8 weeks (7.61 ± 0.55 %ID/g, n = 8). Importantly, competitive receptor blocking at 28 weeks demonstrated more than 67% decreased uptake (3.10 ± 0.47

https://dx.doi.org/10.1021/acs.molpharmaceut.0c01183
Mol. Pharmaceutics 2021, 18, 1386−1396

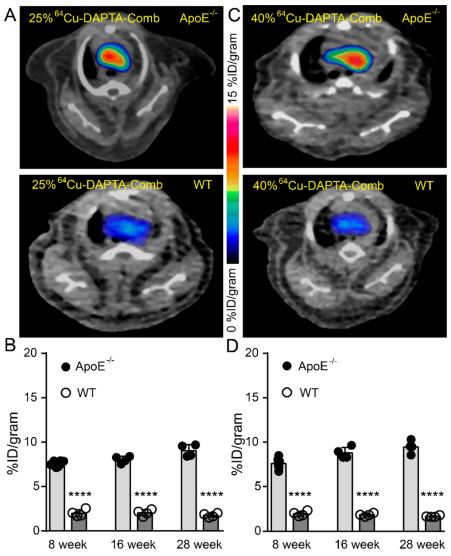


Figure 3. (A) PET/CT images of 25% and 40% ^{64}Cu-DAPTA-Comb in ApoE$^{-/-}$ mice at 28 weeks after HFD. Images acquired at 24 h after injection showed intensive PET signals at aortic arches compared to the low accumulation in WT mice on normal chow. (B) Quantitative uptake analysis of 25% and 40% ^{64}Cu-DAPTA-Comb showed significantly higher uptake in ApoE$^{-/-}$ mice than the age-matched WT C57BL/6 mice along the progression of atherosclerosis from 8 weeks to 28 weeks on HFD (****$p < 0.0001$, $n = 4$–6 per group).

%ID/g, $n = 4$, $p < 0.0001$), confirming the plaque targeting specificity of 40% ^{64}Cu-DAPTA-Comb. This is again in agreement with the conjugation of more DAPTA peptide units (~56 DAPTA/Comb) leading to more efficient CCR5 targeting (Figure 3C,D). These results are also consistent with the above biodistribution study and our previous report demonstrating the importance of nanoparticle's structure and functionalization for optimal targeting of atherosclerosis.[34]

PET/CT Imaging the Monocytes Recruitment Dynamics in Regressive Atherosclerosis. The development of atherosclerosis involves recruitment of monocytes from blood to plaques and local proliferation of macrophages,[1,44] which leads to dynamic variation of chemokine receptor concentrations. The sensitivity of an imaging agent for the detection of these dynamic changes is important for tracking the progression and regression of atherosclerosis to optimize treatment. Previously, we characterized plaque regression by treating ApoE$^{-/-}$ mice with ApoE-encoding adenoviral vector (AAV), showing significant decrease of cholesterol, considerable decrease of CD68+ macrophages at plaques, and effective reduction of plaque size.[22] To determine and compare the sensitivity of the three ^{64}Cu-DAPTA-Combs tracking plaque regression, we performed AAV treatment in 9-week-old ApoE$^{-/-}$ mice and imaged the mice at 3 weeks after treatment along with nontreated ApoE$^{-/-}$ mice on HFD. As shown in Figure 4A, plasma cholesterol levels in the AAV treated ApoE$^{-/-}$ mice (AAV group) were significantly decreased at 1 week after treatment and throughout the 3 weeks' study compared to the mice without treatment (no AAV group), which was consistent with our previous data.[22] PET/CT images with three ^{64}Cu-DAPTA-Combs all revealed intensive tracer accumulations at aortic arches in no AAV mice compared to the decreased uptake in the AAV group. Quantitative uptake analysis showed 45.8 ± 5.6%, 52.8 ± 8.3%, and 63 ± 6.4% decrease in AAV treated mice compared to the no AAV group ($p < 0.0001$ for all, $n = 4$–5 per group) for the 10%, 25%, and 40% ^{64}Cu-DAPTA-Comb, respectively (Figure 4B). The tracer uptake difference between the AAV and no AAV groups from 10% to 40% ^{64}Cu-DAPTA-Combs was consistent with the results above-mentioned in the progressive plaques, suggesting increased sensitivity of 40% ^{64}Cu-DAPTA-Comb in detecting atherosclerosis (Figure 4C).

Histopathological characterization of the impact of AAV treatment revealed decreased lipid pool, reduced infiltration of foam cells, and less neointimal thickening in the aortic sinus of AAV treated mice relative to the untreated group (Figure 4D). Immunofluorescent staining of the aortic sinus also showed reduced CD68+ macrophages and CCR5 signals in AAV treated mice compared to the ApoE$^{-/-}$ mice without AAV treatment. As we previously reported, through the transient depletion of monocytes using clodronate-loaded liposome followed by the introduction of fluorescent latex beads, the recruitment of proinflammatory monocytes from bone marrow to plaque can be determined by tracking these fluorescent beads.[23] As shown in Figure 4E, the fluorescence signals showed approximately 3-fold less latex+ cells in the AAV treated group compared to the untreated group, confirming decreased monocyte recruitment to plaques. Quantification of the atherosclerotic lesions demonstrated decreased plaque size from 0.46 ± 0.08 μm^2 in the no AAV group to 0.22 ± 0.08 μm^2 in AAV treated mice (Figure 4F), which was consistent with reduced monocyte recruitment. These characterizations strongly supported the PET imaging sensitivity and specificity of CCR5 targeted ^{64}Cu-DAPTA-Combs to determine plaque regression following AAV treatment in ApoE$^{-/-}$ mice.

Assessment of CCR5 Expression in Human Carotid Endarterectomy (CEA) Specimens. Though the expression of CCR5 has been reported in human atherosclerotic tissues,[45] we examined the level of CCR5 in human CEA specimens to further assess its potential as a biomarker for plaque imaging and therapy.[33,46] As shown in Figure 5, histological analysis of representative CEA tissue showed significant neointimal thickening, a large lipid-rich necrotic core (NC), high infiltration of foam cells, and some regions with a thin fibrous cap, suggesting a vulnerable phenotype.[47,48] Immunofluorescent staining revealed dense expression of CD68+ macrophages throughout the tissue, with most signals residing in the necrotic core. CCR5 staining showed high expression in the NC region, largely colocalized with CD68 (Figure 5E,F), suggesting its potential for further investigation in human atherosclerosis. *Ex vivo* autoradiography using 40% ^{64}Cu-DAPTA-Comb revealed significant binding to human CEA in a similar profile to CCR5 immunostaining, suggesting its binding specificity (Figure 5G). Competitive autoradiography blocking using nonradioactive 40% DAPTA-Comb showed largely reduced signal in CEA specimen (Figure 5H), confirming the binding specificity.

https://dx.doi.org/10.1021/acs.molpharmaceut.0c01183
Mol. Pharmaceutics 2021, 18, 1386–1396

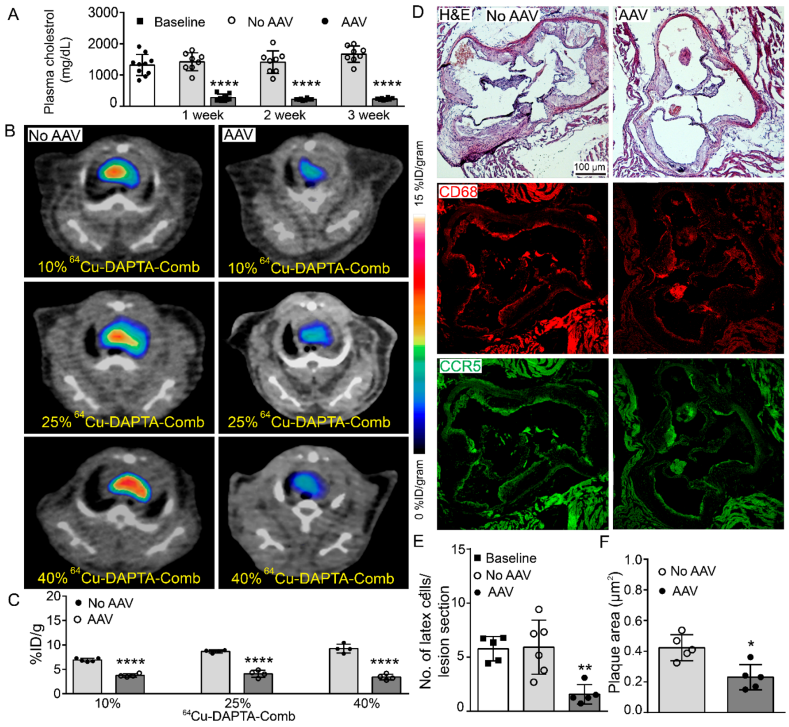


Figure 4. (A) Measurement of plasma cholesterol levels in ApoE$^{-/-}$ mice at 9 weeks after HFD (baseline) and 1, 2, and 3 weeks after AAV treatment. The nontreated (no AAV) ApoE$^{-/-}$ mice were also measured at the same time points. (B) PET/CT images of 10%, 25%, and 40% ^{64}Cu-DAPTA-Comb showed strong PET signals in the untreated group and weak uptake in AAV treated ApoE$^{-/-}$ mice (n = 4/group). (C) Quantification of tracer uptake of the three nanoparticles at 3 weeks after treatment showed significantly decreased uptake in AAV group compared to the untreated group. (D) Comparison of H&E, CD68 (red), and CCR5 (green) immunostaining between AAV and no AAV mice. H&E showed decreased lipid pool, less neointimal thickening, and reduced foam cells on plaques. Immunostaining showed less CD68 and CCR5 in the AAV treated ApoE$^{-/-}$ mice. (E) Counting of latex+ cells at baseline, no AAV, and AAV groups. Decreased signals in the AAV group confirmed the reduced recruitment of monocytes (n = 4/group). (F) Quantification of plaque area between AAV and no AAV groups (n = 4/group): *p < 0.05, **p < 0.01, ****p < 0.0001.

CONCLUSIONS

Through the modular design and construction of multifunctional nanostructures, we have synthesized and optimized three CCR5 targeted ^{64}Cu-DAPTA-Comb nanoparticles with accurate control over the physicochemical properties and surface functionalization for atherosclerosis imaging using PET/CT. *In vivo* pharmacokinetic evaluation demonstrated extended blood circulation and a correlation between the level of the conjugated DAPTA peptide units and organ distribution. All three targeting nanoparticles showed sensitive and specific detection of CCR5 in plaques not only along the progression of atherosclerotic lesions but also during plaque regression in an ApoE$^{-/-}$ mouse model. In contrast to the 10% and 25% ^{64}Cu-DAPTA-Combs, the 40% ^{64}Cu-DAPTA-Comb revealed superior sensitivity and specificity for imaging of CCR5 up-regulation on atherosclerotic lesions. Biological characterization of AAV treatment effect in ApoE$^{-/-}$ mice and its association with PET signals further confirmed the plaque targeting efficiency of these multifunctional nanoparticles. *Ex vivo* characterization of CCR5 in human CEA specimens highlighted its potential as a prognostic biomarker for atherosclerosis mangement. However, there are some limitations for the current study. Mouse serum stabily study showed significant dissociation of ^{64}Cu from DOTA at 24 h. A more stable chelator such as 5-(8-methyl-3,6,10,13,16,19-hexaazabicyclo[6.6.6]icosan-1-ylamino)-5-oxopentanoic acid (MeCOSar) needs to be used to further improve the biodistributin profile and reduce liver uptake.[49] Compared to the acute AAV treatment, future studies are warranted using a more clinically relevant treatment such as statin-based therapy or cessation of HFD in ApoE$^{-/-}$ mice to assess the sensitivity of 40% ^{64}Cu-DAPTA-Comb detecting the subtle variation of the plaques. Moreover, comparing to human plaques, it is known that ApoE$^{-/-}$ model does not rupture, and the as-

https://dx.doi.org/10.1021/acs.molpharmaceut.0c01183
Mol. Pharmaceutics 2021, 18, 1386−1396

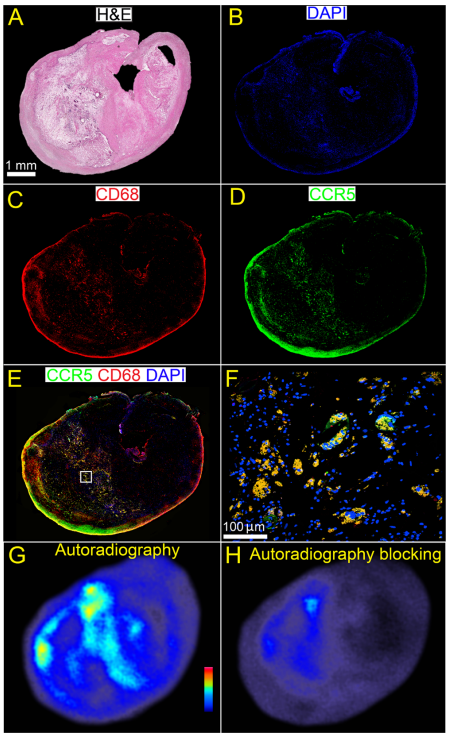


Figure 5. *Ex vivo* characterization of human CEA specimen. (A) H&E showed large lipid pool, necrotic core, significant neointimal thickening, and regions with thin fibrous cap. Immunofluorescent staining of (B) DAPI (blue), (C) CD68 (red), and (D) CCR5 (green) showed overexpression of CD68+ macrophages and CCR5 in the necrotic core. DAPI, CD68, and CCR5 fused (E) and amplified (F) immunofluorescent images showed that most CCR5 signals colocalized (yellow) with CD68+ macrophages. (G) Representative autoradiography of 40% ^{64}Cu-DAPTA-Comb binding to CEA specimen *ex vivo* showing similar profile to CCR5 signals in (D). (H) Competitive *ex vivo* autoradiography blocking of 40% ^{64}Cu-DAPTA-Comb using 100× nonradioactive 40% DAPTA-Comb. Note that (A) H&E was from ref 33 due to the use of same human CEA specimen.

developed nanoprobe may need to be further assessed in ApoE$^{-/-}$Fbn1$^{C1039G+/-}$ mice with vulnerable atherosclerotic lesions that eventually rupture.[50] Results acquired from these studies will promote the translation of as-developed ^{64}Cu-DAPTA-Combs to diagnose high-risk patients for surgical intervention or serve as a companion imaging approach for targeted treatment given the availability of CCR5 antagonists used in the clinic.

■ ASSOCIATED CONTENT

Supporting Information

The Supporting Information is available free of charge at https://pubs.acs.org/doi/10.1021/acs.molpharmaceut.0c01183.

Synthetic scheme of 10%, 25%, and 40% ^{64}Cu-DAPTA-Combs (Figure S1); mouse serum stability of of 40% ^{64}Cu-DAPTA-Comb determined by radio-TLC at 1, 2, and 24 h after incubation (Figure S2); biodistribution of 10%, 25%, and 40% ^{64}Cu-DAPTA-Comb in wild-type C57BL/6 mice at 1, 4, and 24 h after intravenous injection (Figure S3); PET/CT images of 10% ^{64}Cu-DAPTA-Comb in ApoE$^{-/-}$ mice at 8 weeks after HFD at 24 h after injection showing the uptake at aortic arch (Figure S4); association between 10% ^{64}Cu-DAPTA-Comb uptake in plaques at 16, 28, 35, and 40 weeks after high fat diet and CCR5 RT-PCR data for aortic arteries of ApoE$^{-/-}$ mice (Figure S5); summary of PET uptake of 10%, 25%, and 40% ^{64}Cu-DAPTA-Comb in ApoE$^{-/-}$ mice at 8, 16, and 28 weeks after high fat diet (Figure S6) (PDF)

■ AUTHOR INFORMATION

Corresponding Authors

Craig J. Hawker − *Materials Department, University of California, Santa Barbara, California 93106, United States;* orcid.org/0000-0001-9951-851X; Email: hawker@mrl.ucsb.edu

Yongjian Liu − *Mallinckrodt Institute of Radiology, Washington University, St. Louis, Missouri 63110, United States;* orcid.org/0000-0002-1118-1535; Email: yongjianliu@wustl.edu

Authors

Lisa Detering − *Mallinckrodt Institute of Radiology, Washington University, St. Louis, Missouri 63110, United States*

Allison Abdilla − *Materials Department, University of California, Santa Barbara, California 93106, United States*

Hannah P. Luehmann − *Mallinckrodt Institute of Radiology, Washington University, St. Louis, Missouri 63110, United States*

Jesse W. Williams − *Department of Pathology and Immunology, Washington University, St. Louis, Missouri 63110, United States*

Li-Hao Huang − *Department of Pathology and Immunology, Washington University, St. Louis, Missouri 63110, United States*

Deborah Sultan − *Mallinckrodt Institute of Radiology, Washington University, St. Louis, Missouri 63110, United States*

Andrew Elvington − *Department of Pathology and Immunology, Washington University, St. Louis, Missouri 63110, United States*

Gyu Seong Heo − *Mallinckrodt Institute of Radiology, Washington University, St. Louis, Missouri 63110, United States;* orcid.org/0000-0001-6200-4742

Pamela K. Woodard − *Mallinckrodt Institute of Radiology, Washington University, St. Louis, Missouri 63110, United States*

Robert J. Gropler − *Mallinckrodt Institute of Radiology, Washington University, St. Louis, Missouri 63110, United States*

Gwendalyn J. Randolph − *Department of Pathology and Immunology, Washington University, St. Louis, Missouri 63110, United States*

Complete contact information is available at: https://pubs.acs.org/10.1021/acs.molpharmaceut.0c01183

Author Contributions

[||]L.D. and A.A. contributed equally to this work.

Notes

The authors declare no competing financial interest.

■ ACKNOWLEDGMENTS

This work was supported by Grants 1R35HL145212 and R01HL138163 from the National Heart, Lung, and Blood Institute of the National Institutes of Health. The characterization of nanoparticles was performed in the Shared Facilities of the National Science Foundation (NSF) Materials Research and Engineering Center at UC Santa Barbara, Grant DMR-1720256. We thank Nicole Fettig, Margaret Morris, Amanda Klaas, and Lori Strong for their assistance with the biodistribution and imaging studies in animals, Alaina McGrath for synthesis help, and Thomas Voller, Evelyn Madrid, and Paul Eisenbeis for ^{64}Cu production.

■ REFERENCES

(1) Tuttolomondo, A.; Di Raimondo, D.; Pecoraro, R.; Arnao, V.; Pinto, A.; Licata, G. Atherosclerosis As an Inflammatory Disease. *Curr. Pharm. Des.* **2012**, *18*, 4266−4288.

(2) Libby, P. Inflammation in Atherosclerosis. *Arterioscler., Thromb., Vasc. Biol.* **2012**, *32*, 2045−2051.

(3) Wildgruber, M.; Swirski, F. K.; Zernecke, A. Molecular Imaging of Inflammation in Atherosclerosis. *Theranostics* **2013**, *3*, 865−884.

(4) Orbay, H.; Hong, H.; Zhang, Y.; Cai, W. Positron Emission Tomography Imaging of Atherosclerosis. *Theranostics* **2013**, *3*, 894−902.

(5) Quillard, T.; Libby, P. Molecular Imaging of Atherosclerosis for Improving Diagnostic and Therapeutic Development. *Circ. Res.* **2012**, *111*, 231−244.

(6) Piri, R.; Gerke, O.; Hoilund-Carlsen, P. F. Molecular Imaging of Carotid Artery Atherosclerosis with PET: A Systematic Review. *Eur. J. Nucl. Med. Mol. Imaging* **2020**, *47*, 2016−2025.

(7) Hoilund-Carlsen, P. F.; Moghbel, M. C.; Gerke, O.; Alavi, A. Evolving Role of PET in Detecting and Characterizing Atherosclerosis. *PET Clin.* **2019**, *14*, 197−209.

(8) Daghem, M.; Bing, R.; Fayad, Z. A.; Dweck, M. R. Noninvasive Imaging to Assess Atherosclerotic Plaque Composition and Disease Activity: Coronary and Carotid Applications. *JACC Cardiovasc. Imaging.* **2020**, *13*, 1055−1068.

(9) Dong, Z. M.; Brown, A. A.; Wagner, D. D. Prominent Role of P-selectin in the Development of Advanced Atherosclerosis in Apoe-deficient Mice. *Circulation* **2000**, *101*, 2290−2295.

(10) Libby, P.; DiCarli, M.; Weissleder, R. The Vascular Biology of Atherosclerosis and Imaging Targets. *J. Nucl. Med.* **2010**, *51* (Suppl. 1), 33S−37S.

(11) Nakashima, Y.; Raines, E. W.; Plump, A. S.; Breslow, J. L.; Ross, R. Upregulation of VCAM-1 and ICAM-1 at Atherosclerosis-prone Sites on the Endothelium in the Apoe-deficient Mouse. *Arterioscler., Thromb., Vasc. Biol.* **1998**, *18*, 842−851.

(12) Foss, C. A.; Sanchez-Bautista, J.; Jain, S. K. Imaging Macrophage-associated Inflammation. *Semin. Nucl. Med.* **2018**, *48*, 242−245.

(13) Miteva, K.; Madonna, R.; De Caterina, R.; Van Linthout, S. Innate and Adaptive Immunity in Atherosclerosis. *Vasc. Pharmacol.* **2018**, *107*, 67−77.

(14) John, A. E.; Channon, K. M.; Greaves, D. R. Chemokines, Chemokine Receptros and Atherosclerosis. In *Chemokines, Chemokine Receptors, and Disease*; Schwiebert, L. M., Ed.; Elsevier: Amesterdam, The Netherlands, 2005; pp 223−253.

(15) Kraaijeveld, A. O.; de Jager, S. C.; van Berkel, T. J.; Biessen, E. A.; Jukema, J. W. Chemokines and Atherosclerotic Plaque Progression: Towards Therapeutic Targeting? *Curr. Pharm. Des.* **2007**, *13*, 1039−1052.

(16) Bursill, C. A.; Channon, K. M.; Greaves, D. R. The Role of Chemokines in Atherosclerosis: Recent Evidence from Experimental Models and Population Genetics. *Curr. Opin. Lipidol.* **2004**, *15*, 145−149.

(17) White, G. E.; Iqbal, A. J.; Greaves, D. R. CC Chemokine Receptors and Chronic Inflammation−Therapeutic Opportunities and Pharmacological Challenges. *Pharmacol. Rev.* **2013**, *65*, 47−89.

(18) Zernecke, A.; Shagdarsuren, E.; Weber, C. Chemokines in Atherosclerosis: An update. *Arterioscler., Thromb., Vasc. Biol.* **2008**, *28*, 1897−1908.

(19) Weber, C.; Schober, A.; Zernecke, A. Chemokines: Key Regulators of Mononuclear Cell Recruitment in Atherosclerotic Vascular Disease. *Arterioscler., Thromb., Vasc. Biol.* **2004**, *24*, 1997−2008.

(20) Liu, Y.; Woodard, P. K. Chemokine Receptors: Key for Molecular Imaging of Inflammation in Atherosclerosis. *J. Nucl. Cardiol.* **2019**, *26*, 1179−1181.

(21) Li, W.; Luehmann, H. P.; Hsiao, H. M.; Tanaka, S.; Higashikubo, R.; Gauthier, J. M.; Sultan, D.; Lavine, K. J.; Brody, S. L.; Gelman, A. E.; Gropler, R. J.; Liu, Y.; Kreisel, D. Visualization of Monocytic Cells in Regressing Atherosclerotic Plaques by Intravital 2-Photon and Positron Emission Tomography-Based Imaging-Brief Report. *Arterioscler., Thromb., Vasc. Biol.* **2018**, *38*, 1030−1036.

(22) Potteaux, S.; Gautier, E. L.; Hutchison, S. B.; van Rooijen, N.; Rader, D. J.; Thomas, M. J.; Sorci-Thomas, M. G.; Randolph, G. J. Suppressed Monocyte Recruitment Drives Macrophage Removal from Atherosclerotic Plaques of Apoe−/− Mice During Disease Regression. *J. Clin. Invest.* **2011**, *121*, 2025−2036.

(23) Tacke, F.; Alvarez, D.; Kaplan, T. J.; Jakubzick, C.; Spanbroek, R.; Llodra, J.; Garin, A.; Liu, J.; Mack, M.; van Rooijen, N.; Lira, S. A.; Habenicht, A. J.; Randolph, G. J. Monocyte Subsets Differentially Employ Ccr2, Ccr5, and Cx3cr1 to Accumulate within Atherosclerotic Plaques. *J. Clin. Invest.* **2007**, *117*, 185−194.

(24) Quinones, M. P.; Martinez, H. G.; Jimenez, F.; Estrada, C. A.; Dudley, M.; Willmon, O.; Kulkarni, H.; Reddick, R. L.; Fernandes, G.; Kuziel, W. A.; Ahuja, S. K.; Ahuja, S. S. CC Chemokine Receptor 5 Influences Late-Stage Atherosclerosis. *Atherosclerosis* **2007**, *195*, e92−e103.

(25) Braunersreuther, V.; Zernecke, A.; Arnaud, C.; Liehn, E. A.; Steffens, S.; Shagdarsuren, E.; Bidzhekov, K.; Burger, F.; Pelli, G.; Luckow, B.; Mach, F.; Weber, C. Ccr5 But Not Ccr1 Deficiency Reduces Development of Diet-induced Atherosclerosis in Mice. *Arterioscler., Thromb., Vasc. Biol.* **2007**, *27*, 373−379.

(26) Cipriani, S.; Francisci, D.; Mencarelli, A.; Renga, B.; Schiaroli, E.; D'Amore, C.; Baldelli, F.; Fiorucci, S. Efficacy of The Ccr5 Antagonist Maraviroc in Reducing Early, Ritonavir-induced Atherogenesis and Advanced Plaque Progression in Mice. *Circulation* **2013**, *127*, 2114−2124.

(27) Fernandez-Sender, L.; Alonso-Villaverde, C.; Rull, A.; Rodriguez-Gallego, E.; Riera-Borrull, M.; Hernandez-Aguilera, A.; Camps, J.; Beltran-Debon, R.; Aragones, G.; Menendez, J. A.; Joven, J. A Possible Role for Ccr5 in the Progression of Atherosclerosis in HIV-infected Patients: A Cross-sectional Study. *AIDS Res. Ther.* **2013**, *10*, 11.

(28) Papaspyridonos, M.; Smith, A.; Burnand, K. G.; Taylor, P.; Padayachee, S.; Suckling, K. E.; James, C. H.; Greaves, D. R.; Patel, L. Novel Candidate Genes in Unstable Areas of Human Sthereosclerotic Plaques. *Arterioscler., Thromb., Vasc. Biol.* **2006**, *26*, 1837−1844.

(29) Lin, C. S.; Hsieh, P. S.; Hwang, L. L.; Lee, Y. H.; Tsai, S. H.; Tu, Y. C.; Hung, Y. W.; Liu, C. C.; Chuang, Y. P.; Liao, M. T.; Chien, S.; Tsai, M. C. The Ccl5/ccr5 Axis Promotes Vascular Smooth Muscle Cell Proliferation and Atherogenic Phenotype Switching. *Cell. Physiol. Biochem.* **2018**, *47*, 707−720.
(30) Bejarano, J.; Navarro-Marquez, M.; Morales-Zavala, F.; Morales, J. O.; Garcia-Carvajal, I.; Araya-Fuentes, E.; Flores, Y.; Verdejo, H. E.; Castro, P. F.; Lavandero, S.; Kogan, M. J. Nanoparticles for Diagnosis and Therapy of Atherosclerosis and Myocardial Infarction: Evolution Toward Prospective Theranostic Approaches. *Theranostics* **2018**, *8*, 4710−4732.
(31) Flores, A. M.; Ye, J.; Jarr, K. U.; Hosseini-Nassab, N.; Smith, B. R.; Leeper, N. J. Nanoparticle Therapy for Vascular Diseases. *Arterioscler., Thromb., Vasc. Biol.* **2019**, *39*, 635−646.
(32) Luehmann, H. P.; Detering, L.; Fors, B. P.; Pressly, E. D.; Woodard, P. K.; Randolph, G. J.; Gropler, R. J.; Hawker, C. J.; Liu, Y. Pet/ct Imaging of Chemokine Receptors in Inflammatory Atherosclerosis Using Targeted Nanoparticles. *J. Nucl. Med.* **2016**, *57*, 1124−1129.
(33) Liu, Y.; Luehmann, H. P.; Detering, L.; Pressly, E. D.; McGrath, A. J.; Sultan, D.; Nguyen, A.; Grathwohl, S.; Shokeen, M.; Zayed, M.; Gropler, R. J.; Abendschein, D.; Hawker, C. J.; Woodard, P. K. Assessment of Targeted Nanoparticle Assemblies for Atherosclerosis Imaging with Positron Emission Tomography and Potential for Clinical Translation. *ACS Appl. Mater. Interfaces* **2019**, *11*, 15316−15321.
(34) Woodard, P. K.; Liu, Y.; Pressly, E. D.; Luehmann, H. P.; Detering, L.; Sultan, D. E.; Laforest, R.; McGrath, A. J.; Gropler, R. J.; Hawker, C. J. Design and Modular Construction of A Polymeric Nanoparticle for Targeted Atherosclerosis Positron Emission Tomography Imaging: A Story of 25% (64)Cu-canf-comb. *Pharm. Res.* **2016**, *33*, 2400−2410.
(35) Luehmann, H. P.; Pressly, E. D.; Detering, L.; Wang, C.; Pierce, R.; Woodard, P. K.; Gropler, R. J.; Hawker, C. J.; Liu, Y. PET/CT Imaging of Chemokine Receptor CCR5 in Vascular Injury Model Using Targeted Nanoparticle. *J. Nucl. Med.* **2014**, *55*, 629−934.
(36) PET Imaging of Natriuretic Peptide Receptor C (npr-c) in Carotid Atherosclerosis. https://clinicaltrials.gov/ct2/show/NCT02417688?term=woodard&draw=2&rank=7.
(37) Aldinucci, D.; Borghese, C.; Casagrande, N. The CCL5/CCR5 Axis in Cancer Progression. *Cancers* **2020**, *12*, 1765.
(38) Perrier, S.; Takolpuckdee, P.; Westwood, J.; Lewis, D. M. Versatile Chain Transfer Agents for Reversible Addition Fragmentation Chain Transfer (raft) Polymerization to Synthesize Functional Polymeric Architectures. *Macromolecules* **2004**, *37*, 2709−2717.
(39) Pressly, E. D.; Pierce, R. A.; Connal, L. A.; Hawker, C. J.; Liu, Y. Nanoparticle PET/CT Imaging of Natriuretic Peptide Clearance Receptor in Prostate Cancer. *Bioconjugate Chem.* **2013**, *24*, 196−204.
(40) Beldman, T. J.; Malinova, T. S.; Desclos, E.; Grootemaat, A. E.; Misiak, A. L. S.; van der Velden, S.; van Roomen, C.; Beckers, L.; van Veen, H. A.; Krawczyk, P. M.; Hoebe, R. A.; Sluimer, J. C.; Neele, A. E.; de Winther, M. P. J.; van der Wel, N. N.; Lutgens, E.; Mulder, W. J. M.; Huveneers, S.; Kluza, E. Nanoparticle-aided Characterization of Arterial Endothelial Architecture during Atherosclerosis Progression and Metabolic Therapy. *ACS Nano* **2019**, *13*, 13759−13774.
(41) Lariviere, M.; Lorenzato, C. S.; Adumeau, L.; Bonnet, S.; Hemadou, A.; Jacobin-Valat, M. J.; Noubhani, A.; Santarelli, X.; Minder, L.; Di Primo, C.; Sanchez, S.; Mornet, S.; Laroche-Traineau, J.; Clofent-Sanchez, G. Multimodal Molecular Imaging of Atherosclerosis: Nanoparticles Functionalized with Scfv Fragments of An Anti-Alphaiibbeta3 Antibody. *Nanomedicine* **2019**, *22*, 102082.
(42) Banik, B.; Surnar, B.; Askins, B.; Banerjee, M.; Dhar, S. Dual Targeted Synthetic Nanoparticle for Cardiovascular Diseases. *ACS Appl. Mater. Interfaces* **2020**, *12*, 6852−6862.
(43) Bronte, V.; Pittet, M. J. The Spleen in Local and Systemic Regulation of Immunity. *Immunity* **2013**, *39*, 806−818.
(44) Robbins, C. S.; Hilgendorf, I.; Weber, G. F.; Theurl, I.; Iwamoto, Y.; Figueiredo, J. L.; Gorbatov, R.; Sukhova, G. K.; Gerhardt, L. M.; Smyth, D.; Zavitz, C. C.; Shikatani, E. A.; Parsons, M.; van Rooijen, N.; Lin, H. Y.; Husain, M.; Libby, P.; Nahrendorf, M.; Weissleder, R.; Swirski, F. K. Local Proliferation Dominates Lesional Macrophage Accumulation in Atherosclerosis. *Nat. Med.* **2013**, *19*, 1166−1172.
(45) Jones, K. L.; Maguire, J. J.; Davenport, A. P. Chemokine Receptor Ccr5: From Aids to Atherosclerosis. *Br. J. Pharmacol.* **2011**, *162*, 1453−1469.
(46) Heo, G. S.; Kopecky, B.; Sultan, D.; Ou, M.; Feng, G.; Bajpai, G.; Zhang, X.; Luehmann, H.; Detering, L.; Su, Y.; Leuschner, F.; Combadière, C.; Kreisel, D.; Gropler, R. J.; Brody, S. L.; Liu, Y.; Lavine, K. J. Molecular Imaging Visualizes Recruitment of Inflammatory Monocytes and Macrophages to the Injured Heart. *Circ. Res.* **2019**, *124*, 881−890.
(47) van Lammeren, G. W.; Moll, F. L.; De Borst, G. J.; de Kleijn, D. P. V.; de Vries JP, J.-P.P. M.; Pasterkamp, G. Atherosclerotic Plaque Biomarkers: Beyond the Horizon of the Vulnerable Plaque. *Curr. Cardiol. Rev.* **2011**, *7*, 22−27.
(48) Koenig, W.; Khuseyinova, N. Biomarkers of Atherosclerotic Plaque Instability and Rupture. *Arterioscler., Thromb., Vasc. Biol.* **2007**, *27*, 15−26.
(49) Keinänen, O.; Fung, K.; Brennan, J. M.; Zia, N.; Harris, M.; van Dam, E.; Biggin, C.; Hedt, A.; Stoner, J.; Donnelly, P. S.; Lewis, J. S.; Zeglis, B. M. Harnessing 64 Cu/ 67 Cu for a theranostic approach to pretargeted radioimmunotherapy. *Proc. Natl. Acad. Sci. U. S. A.* **2020**, *117*, 28316−28327.
(50) von Scheidt, M.; Zhao, Y.; Kurt, Z.; Pan, C.; Zeng, L.; Yang, X.; Schunkert, H.; Lusis, A. J. Applications and Limitations of Mouse Models for Understanding Human Atherosclerosis. *Cell Metab.* **2017**, *25*, 248−261.

https://dx.doi.org/10.1021/acs.molpharmaceut.0c01183
Mol. Pharmaceutics 2021, 18, 1386−1396